



SAPIENZA
UNIVERSITÀ DI ROMA

From high-fidelity high-order to reduced-order modeling for unsteady shock wave/boundary layer interactions

Scuola di dottorato in Tecnologie e sistemi aeronautici, elettromagnetici, elettronici, spaziali e di telerilevamento

Dottorato di ricerca in Ingegneria Aeronautica e Spaziale (XXXVI cycle)

Nicolas Goffart

ID number 1982612

Advisors

Prof. Sergio Pirozzoli

Dr. Benoît Tartinville

Academic Year 2022/2023


Thesis defended on 24/01/2024
in front of a Board of Examiners composed by:
Prof. Maurizio Quadrio (Politecnico di Milano)
Prof. Umberto Iemma (Università Roma Tre)
Prof. Christian Paravan (Politecnico di Milano)

External reviewers:

Prof. Dr. Marius Swoboda (Rolls-Royce Deutschland)
Dr. Lionel Larchevêque (IUSTI Laboratory, Aix-Marseille University)

From high-fidelity high-order to reduced-order modeling for unsteady shock wave/boundary layer interactions

PhD thesis. Sapienza University of Rome

© 2024 Nicolas Goffart  (0000-0001-9810-8332). All rights reserved.

This thesis is part of a project that has received funding from the European Union's Horizon 2020 research and innovation programme under the Marie Skłodowska-Curie grant agreement No 860909.

This thesis has been typeset by \LaTeX and the Sapthesis class.

Author's email: nicolas.goffart@hotmail.fr

*Dedicated to
Sarah*

Abstract

From high-fidelity high-order to reduced-order modeling for unsteady shock wave/boundary layer interactions

In transonic turbomachinery flows, the shock wave/boundary layer interaction is the primary aerodynamic performance-limiting factor. For the next-generation engines, improvements in efficiency can be achieved, provided that the computational fluid dynamics tools used for the design are able to properly capture this phenomenon. While high-fidelity simulations would be required, their cost is still prohibitive, and industry therefore relies mostly on low-fidelity methods. Besides (unsteady) Reynolds-Averaged Navier-Stokes simulations, frequency-domain approaches, such as the Non-Linear Harmonic method, are also employed. Special care must, however, be taken for the harmonic turbulence closure assumption, in particular in shock-induced separated flows. In this context, the present work intends to carry out high-fidelity simulations shock wave/boundary layer interactions, using a high-order solver, to obtain an accurate database of harmonic turbulence and improve its modeling in frequency-domain approaches for turbomachinery applications.

The first milestone of this dissertation is the development of a robust high-order solver, able to perform high-fidelity simulations of shock wave/boundary layer interactions. A scheme based on the flux reconstruction approach is chosen for the spatial discretization. To handle shock waves but avoid damping turbulent fluctuations within the boundary layer, the solver is supplemented with an artificial viscosity method combined with the Ducros sensor. Further stabilization is obtained thanks to a positivity-preserving limiter. A digital filtering technique is adopted to provide a realistic turbulent boundary layer within a reasonable distance from the inlet. For validation purposes, the capabilities of the high-order solver are demonstrated for the canonical case of an oblique shock reflection on a turbulent boundary layer. The results from a wall-resolved implicit large-eddy simulation, performed at the experimental Reynolds number, are thoroughly compared to the abundant literature, and an excellent agreement is reported. Especially, the typical low-frequency broadband unsteadiness of the reflected shock is captured. Conditional averaging is put in place and allows to identify coherent structures of turbulence kinetic energy. This successful experience gives confidence in the use of the high-order solver.

The second stage is the study of harmonic turbulence in shock-induced separated flows, for which the investigation is led on the transonic flow over a bump, using wall-resolved implicit large-eddy simulations. To replicate rotor/stator interactions occurring in turbomachinery, harmonic forcing of the back pressure is imposed at the outlet. Various perturbation frequencies are prescribed and encompass different regimes, from a fully locked configuration to a decoupling between the unperturbed and forced flows. The mean solution is, however, found to be independent of the perturbation. In a triple decomposition framework, the coherent component of the flow is extracted by phase-averaging. Organized structures of streamwise velocity

and turbulence kinetic energy are highlighted. Whereas of similar shapes beneath the shock system, their extent in the downstream boundary layer is controlled by the frequency of the perturbation. Mean and harmonic turbulent stress budgets are presented. A typical three-peaks distribution of mean turbulent diffusion is reported, which is also found to appear for the coherent turbulent diffusion. Harmonic production arises mainly from the mean shear and its modulation.

Finally, the Non-Linear Harmonic method is employed on the same bump configuration. Its inaccurate predictions of the harmonic content of the flow are emphasized and are attributed to the freezing of turbulence, or the neglect of harmonic turbulence. In an attempt to address this issue, the findings related to harmonic production are exploited to derive a simple and analytical model for a harmonic eddy viscosity. Its *a priori* performance is assessed and a satisfactory quantitative and qualitative match is reported with respect to the reference at the lowest forcing frequencies. These encouraging results give credibility to the methodology developed and applied throughout this work to eventually overcome the frozen turbulence assumption of the Non-Linear Harmonic method.

Acknowledgments

There is only one author to this thesis, but a lot of people actually contributed to its completion. They might not have noticed it, and if they did, perhaps they did not exactly know how, and therefore these first paragraphs are for them to realize or to understand better.

I would like first of all to thank Benoît. Throughout this project, I realized how lucky I was to have you as a supervisor. Your involvement in the project, your excitement when I had new results to share, your availability and your guidance clearly showed how much you enjoy to train people, and it added enormously to my motivation. It has been inspiring to work alongside you over the last three years and I evolved a lot thanks to that, both professionally and humanly speaking. I am glad to know that you did not have enough with me and that you will be looking for another PhD student in the coming years.

I would also like to express my gratitude to Prof. Pirozzoli. Thanks first of all for the time you took to host me at La Sapienza for the PhD. I was really pleased to receive your academic point of view, which helped to broaden mine, and your advice oriented this work to make it undoubtedly richer. Maybe we should have started to meet fortnightly earlier. I am also very grateful for the secondment I spent in Rome.

The perks of participating to the TEAMAero project cannot be stressed enough in my opinion. Many thanks first to all the other researchers I had the chance to meet and work with during these meetings, trainings, secondments and conferences. I had a lot of pleasure hanging out with you Jane, Andrea, César, Mari and Nikhil. Thanks also to Prof. Flaszynski and Dr. Wasilczuk for the smooth organization and for leading the project with such a caring spirit. My secondment in Marseille could not have been better thanks to the IUSTI team. Thanks to Dr. Larchevêque and Prof. Swoboda for kindly accepting to take the time to review this dissertation. Finally, I wanted to acknowledge Prof. Hirsch, without whom NUMECA would not have been involved in this project.

My gratitude also goes to my colleagues from Cadence Design Systems. To start with the DBS team (Guy, Stéphane, Benoît L., Raphaël, Éric, Mohamed, Lionel, François, Félix, Cristian), to which I wanted to say that I greatly appreciated your warm welcome and your goodwill to me. Being part of the team and benefiting from the good atmosphere you bring in there was truly stimulating. From other teams but as important to me, I think also of Alexandre, Omid, Shine, Dirk, Ray, to cite only a few. And I will not forget to thank you Gerasimos. I am very glad of the friendship we grew. Our discussions clearly helped me to take care of my mental health (as you recommended).

To my friends, I have never had the opportunity to tell you how grateful I am to have met all of you and to thank you for the wonderful memories we have together. So thank you Thibaut, Baptiste, Adrien, Thomas, Clémentine, Coline, Vincent, Mérédith, Tom, Arnaud for everything.

I could not have achieved this work without the support of my family. To my parents, who have always been encouraging me, under any circumstances. You

trusted me in every thing I wanted to undertake and made sure that transitions happened smoothly every time. You always made sure that I could feel as comfortable as possible, even when it was not as much for you. And for that I cannot thank you enough, but I can definitely tell that I could not have thought of better parents.

And last but clearly not least, I wanted to address a special thank to Jane. Your presence since the very beginning has enlightened this adventure. You supported me in the good and sometimes less good times, to always bring the best out of it, and in ways that I could not have imagined beforehand. I put a lot of value to the moments we could spend together so far and I simply hope we could share more of these in the future. Orada olduđun için ok teřekkür ederim.

Contents

Acronyms	ix
List of Figures	xi
List of Tables	xviii
1 Introduction	1
1.1 Context	1
1.1.1 Harmonic methods	5
1.1.2 High-order methods	8
1.2 Thesis objectives and outline	10
1.3 Publications and conference presentations	11
1.3.1 Journal publications	11
1.3.2 Conference proceedings papers and presentations	11
2 Governing Equations	13
2.1 Compressible Navier-Stokes equations	13
2.2 Triple decomposition for incompressible flows	14
3 High-Fidelity High-Order Solver	18
3.1 Spatial discretization	18
3.1.1 Flux Reconstruction approach in one dimension	18
3.1.2 Extension to multiple dimensions	22
3.1.3 Application to the Navier-Stokes equations	24
3.2 Temporal discretization	25
3.3 Shock-capturing technique	25
3.3.1 Basic artificial viscosity method	27
3.3.2 Combination with Ducros sensor	29
3.4 Positivity-preserving limiter	30
3.5 Turbulent inflow generator	31
4 Oblique Shock Wave/Boundary Layer Interaction	36
4.1 Introduction	36
4.2 Flow conditions and computational setup	41
4.3 Results	44
4.3.1 Basic flow validation	44
4.3.2 Shock-capturing technique performance	52

4.3.3	Conditional averaging	55
4.4	Summary	61
5	Transonic Bump	62
5.1	Introduction	62
5.2	Flow conditions and computational setup	65
5.3	Results	68
5.3.1	Influence of Reynolds number	68
5.3.2	Baseline flow	71
5.3.3	Forced flow	83
5.3.4	Coherent flow	92
5.3.4.1	Reference oscillator	92
5.3.4.2	Effect on the mean flow	93
5.3.4.3	Streamwise velocity	94
5.3.4.4	Turbulent stresses	97
5.3.4.5	Mean turbulent stress budgets	101
5.3.4.6	Coherent turbulent stress budgets	104
5.3.4.7	Turbulence production	108
5.4	Summary	111
6	Reduced-Order Modeling for the Non-Linear Harmonic Method	113
6.1	The Non-Linear Harmonic method	113
6.2	Comparison between URANS and NLH	116
6.3	A first model for the harmonic turbulence	120
6.4	Summary	124
7	Conclusions	126
A	Triple Decomposition for Incompressible Flows	129
A.1	Definitions and properties	129
A.2	Mean and coherent governing equations	130
A.3	Practical computation of the turbulent stress budgets	140
A.3.1	Double and triple correlations	140
A.3.2	Application to the coherent turbulent stress budgets	142
B	Turbulent Boundary Layer at Mach 2	144
B.1	Flow conditions and computational setup	144
B.2	Results	145
B.3	Summary	149
	Bibliography	150

Acronyms

ATAG Air Transport Action Group.

CFD Computational Fluid Dynamics.

CFL Courant-Friedrichs-Lewy.

CPR Correction Procedure via Reconstruction.

CTU Convective Time Unit.

DF Digital Filtering.

DFR Direct Flux Reconstruction.

DG Discontinuous Galerkin.

DNS Direct Numerical Simulation.

EARSM Explicit Algebraic Reynolds-Stress Model.

ENO Essentially Non Oscillatory.

FFT Fast Fourier Transform.

FR Flux Reconstruction.

GPU Graphical Processing Unit.

ICCT International Council on Clean Transportation.

ILES Implicit Large-Eddy Simulation.

IUSTI Institut Universitaire des Systèmes Thermiques Industriels.

LCP Lifting Colocation Penalty.

LES Large-Eddy Simulation.

NLFD Non-Linear Frequency Domain.

NLH Non-Linear Harmonic.

PDF Probability Density Function.

PIV Particle Image Velocimetry.

PSD Power Spectral Density.

RANS Reynolds-Averaged Navier-Stokes.

SD Spectral Difference.

SGS Subgrid Scale.

SRA Strong Reynolds Analogy.

SST Shear Stress Transport.

SWBLI Shock Wave/Boundary Layer Interaction.

TENO Targeted Essentially Non Oscillatory.

TSHB Time Spectral Harmonic Balance.

URANS Unsteady Reynolds-Averaged Navier-Stokes.

VCJH Vincent-Castonguay-Jameson-Huynh.

WENO Weighted Essentially Non Oscillatory.

WMLES Wall-Modeled Large-Eddy Simulation.

List of Figures

1.1	Double bubble D8 aircraft design concept, using boundary layer ingestion. Credits: NASA/MIT/Aurora Flight Sciences.	2
1.2	Rotor 37 - simulation of a single blade passage, highlighted on the full annulus (<i>left</i>) and relative Mach number at 70% span, featuring a shock wave/boundary layer interaction (<i>right</i>).	3
1.3	IDAC3 - simulation of a single blade passage in a multistage configuration, relative Mach number at 70% span. Two blade passages are shown for illustration purposes.	4
3.1	One-dimensional standard element at polynomial order $p = 2$, with associated solution points (<i>red</i> \circ) and flux points (<i>blue</i> \square).	19
3.2	Two-dimensional standard element at polynomial order $p = 2$, with associated solution points (<i>red</i> \circ) and flux points (<i>blue</i> \square).	23
3.3	Activation function for the artificial viscosity, with $s_0 = -4.5$ and $\kappa = 1.5$ (<i>left</i>) and activation for the Ducros sensor, with $s_{D,0} = 0.2$ (<i>right</i>).	28
4.1	Short time exposure Schlieren visualization of the interaction, flow deviation of 8° (Dupont et al., 2008).	37
4.2	Side view of the computational domain with some of the main flow features: incident shock wave (ISW), reflected show wave (RSW) and expansion fan (EF).	42
4.3	Instantaneous density gradient magnitude at mid-span (<i>top</i>) and instantaneous streamwise velocity u/U_∞ near the bump wall, $y^+ \approx 10$ (<i>bottom</i>).	44
4.4	Boundary layer profiles at $(x-\bar{x}_{imp})/L = -1.66$ - van Driest-transformed mean velocity profile (<i>left</i>) and density-scaled Reynolds stress profiles (<i>right</i>). <i>black</i> symbols refers to the DNS data of Bernardini et al. (2023) and <i>red</i> symbols to experimental measurements of Dupont et al. (2008).	45
4.5	Two-point streamwise velocity correlation coefficient in the spanwise direction, C_{uu} . Spatial distribution at $y/\delta_0 = 0.5$ (<i>left</i>) and spanwise evolution at four streamwise locations (<i>right</i>) - upstream of the interaction (<i>solid</i>), in the separated region (<i>dashed</i> and <i>dashdot</i>) and downstream of the interaction (<i>dotted</i>).	46

4.6	Streamwise evolution of mean friction coefficient (<i>left</i>) compared with simulation results from Bernardini et al. (2023) (\square) and from Morgan et al. (2013) (\circ) - Spatial distribution of flow reversal probability (<i>right</i>), with contour of null mean streamwise velocity (<i>solid white</i>). The inset shows the contour of null streamwise velocity (<i>black</i> with \triangleleft symbols) with an exponential best-fit line (<i>red</i>).	47
4.7	Streamwise evolution of mean wall pressure (<i>left</i>) and wall pressure fluctuations (<i>right</i>). Present case (<i>solid</i>), experimental data from Dupont et al. (2006) (<i>red</i> \square), simulation results from Bernardini et al. (2023) (<i>black</i> \square) and from Morgan et al. (2013) (<i>black</i> \circ). The <i>dashed</i> line represents the variance evaluated up to a cutoff frequency of 20kHz.	48
4.8	Comparison of mean velocity and Reynolds stress components between the present simulation results (<i>black</i> contours) and PIV measurements from Dupont et al. (2008) (<i>filled</i> contours). 15 equally-spaced contours of, from top to bottom, \bar{u}/U_∞ , \bar{v}/U_∞ , $\sqrt{u'u'}/U_\infty$, $\sqrt{v'v'}/U_\infty$ and $-\overline{u'v'}/U_\infty^2$	50
4.9	Weighted premultiplied Power Spectral Density of wall pressure - streamwise evolution (<i>left</i>) and four selected stations (<i>right</i>) corresponding to the upstream boundary layer (<i>blue</i>), the separation point (<i>green</i>), the minimum of friction coefficient (<i>purple</i>) and the relaxation zone (<i>orange</i>).	51
4.10	Spatial distribution of correlation coefficients - $R_{u,v_{ref}}$ (<i>top</i>), $R_{v,v_{ref}}$ (<i>center</i>) and $R_{p,v_{ref}}$ (<i>bottom</i>).	52
4.11	Averaged shock sensor s_e with $s_0 - \kappa = -5.0$ contour line (<i>left</i>), averaged Ducros sensor s_D with $s_{D,0} = 0.2$ contour line (<i>center</i>) and averaged artificial viscosity normalized by the local kinematic viscosity ε/ν (<i>right</i>).	53
4.12	Streamwise evolution of the averaged shock sensor (<i>left</i>), Ducros sensor (<i>center</i>) and artificial viscosity (<i>right</i>) in the potential flow, at $y/\delta_0 = 3.0$. Threshold values for the shock sensor and Ducros sensor are indicated by <i>thin dashed</i> lines.	54
4.13	Averaged static pressure evolution in the potential flow, at $y/\delta_0 = 3.0$.	54
4.14	Streamwise evolution of the averaged shock sensor (<i>left</i>), Ducros sensor (<i>center</i>) and artificial viscosity (<i>right</i>) in the boundary layer, at $y/\delta_0 = 0.2$. Threshold values for the shock sensor and Ducros sensor are indicated by <i>thin dashed</i> lines.	55
4.15	Mid-span slice of instantaneous density ρ/ρ_∞ with extracted incident shock (<i>dashed white</i>) and reflected shock (<i>solid white</i>).	56
4.16	Temporal evolution of incident shock foot displacement (<i>top</i>) and reflected shock foot displacement (<i>bottom</i>). <i>red</i> lines are obtained by applying a Savitzky-Golay filter with a window length corresponding to $10L/U_\infty$. <i>dashed</i> lines represent the standard deviations.	57
4.17	Comparison of Power Spectral Densities of the reflected shock foot displacement (<i>black</i>) and incident shock foot displacement (<i>red</i>).	57

4.18	Probability density function of reflected shock foot position with superimposed Gaussian distribution (<i>left</i>) and conditional averages of the oblique shock wave/boundary layer interaction: best-fit lines of incident and reflected shock waves and sonic lines (<i>right</i>). \bar{x}_0 is the streamwise location of the mean reflected shock impingement point.	58
4.19	Coherent streamwise velocity \tilde{u}/U_∞ for each bin. The bin index is indicated in the top left corner of each subfigure.	59
4.20	Mean turbulence kinetic energy \bar{k}/U_∞^2 (<i>left</i>) and differential coherent turbulence kinetic energy $\Delta\tilde{k}/U_\infty^2$ between bins 2 and 9 (<i>right</i>). . . .	60
4.21	Mean shear stress $\overline{u'v'}/U_\infty^2$ (<i>left</i>) and differential coherent shear stress $\Delta\overline{u'v'}/U_\infty^2$ between bins 2 and 9 (<i>right</i>).	61
5.1	Computational domain and mesh. One gridline out of two is represented in the full domain view.	66
5.2	Labeling of the bins with respect to a reference oscillator	68
5.3	Comparison of mean friction coefficient (<i>left</i>) and mean wall pressure coefficient (<i>right</i>) on the bump wall from RANS simulations - $Re_{B_l} = 3.81 \times 10^6$ (<i>solid</i>), $Re_{B_l} = 1.91 \times 10^5$ (<i>dashed</i>) and results from Bron (2004) (<i>symbols</i>). The <i>thin dashed</i> line represents the bump geometry.	69
5.4	Mean ρ/ρ_∞ from RANS simulations, 40 equally-spaced contours between 0.4 and 1.1 - $Re_{B_l} = 3.81 \times 10^6$ (<i>left</i>) and $Re_{B_l} = 1.91 \times 10^5$ (<i>right</i>).	70
5.5	Instantaneous density gradient magnitude at mid-span (<i>top</i>) and instantaneous streamwise velocity u/U_∞ near the bump wall, $y^+ \approx 10$ (<i>bottom</i>).	71
5.6	Mesh resolution at the bump wall - y_w^+ (<i>left</i>), Δx^+ and Δz^+ , respectively, <i>solid</i> and <i>dashed</i> lines (<i>right</i>). The <i>thin dashed</i> line represents the bump geometry.	72
5.7	Ratio between local grid size and estimated Kolmogorov length scale Δ/η in the region downstream of the bump.	73
5.8	Boundary layer profiles at $x/\delta_0 = -15$ - Streamwise velocity, incompressible (<i>solid blue</i>) and Van Driest normalization (<i>dashed black</i>) (<i>left</i>) and Reynolds stresses (<i>right</i>), compared to DNS data for incompressible boundary layers from Schlatter and Örlü (2010) at $Re_\theta = 1000$ (<i>symbols</i>).	74
5.9	Distribution of turbulence Mach number M_t	74
5.10	Two-point streamwise velocity correlation coefficient in the spanwise direction at $y/\delta_0 = 0.5$ - upstream of the bump, $x/\delta_0 = -15$ (<i>solid</i>) and downstream of the interaction, $x/\delta_0 = 16.67$ (<i>dashed</i>).	75
5.11	Averaged shock sensor s_e with $s_0 - \kappa = -6.0$ contour line (<i>left</i>), averaged Ducros sensor s_D with $s_{D,0} = 0.2$ contour line (<i>center</i>) and averaged artificial viscosity normalized by the local kinematic viscosity ε/ν (<i>right</i>).	75
5.12	Mean friction coefficient (<i>solid red</i>) with superimposed PDF, 8 equally-spaced contours between 0.02 and 0.40 (<i>left</i>) and mean wall pressure coefficient (<i>right</i>) on the bump wall. The <i>dashed</i> line represents the bump geometry.	76

5.13	Mean turbulence intensities, 15 equally-spaced contours between 0 and 15. The friction velocity u_τ is evaluated based on upstream conditions.	77
5.14	(<i>left</i>) Streamwise evolution of the acceleration parameter (<i>solid</i>) with threshold value (<i>dashdot</i>) and (<i>right</i>) streamwise evolution of maximum of mean turbulent stresses ($u'u'$ <i>solid</i> , $v'v'$ <i>dashed</i> , $w'w'$ <i>dotted</i> and $u'v'$ <i>dashdot</i>), the grey area represents the extent over which the acceleration parameter is higher than the threshold. On both figures, the <i>thin dashed</i> line represents the bump geometry.	78
5.15	Mean shock position superimposed on mean p/p_∞ contours (<i>left</i>) and weighted premultiplied Power Spectral Density map of shock position (<i>right</i>).	80
5.16	Shock motion amplitude (<i>left</i>) and phase (<i>right</i>) of dominant contributions for the baseline case - 200Hz (<i>solid</i>), 350Hz (<i>dashed</i>) and 800Hz (<i>dashdot</i>).	80
5.17	Streamwise evolution, at $y/L_y = 0.5$, of static pressure amplitude (<i>left</i>) and phase (<i>right</i>) of the three most dominant frequencies contributing to the shock motion - 200Hz (<i>solid</i>), 350Hz (<i>dashed</i>) and 800Hz (<i>dashdot</i>).	81
5.18	Weighted premultiplied PSD maps of bottom (<i>left</i>) and top (<i>right</i>) wall pressure for the baseline case - $N_{bl} = 7$ with 50% overlap. The <i>vertical</i> lines indicate from left to right the beginning of the bump, the bump throat, the end of the region of stable recirculation, the reattachment point and the end of the bump.	82
5.19	Amplitude of motion of separation point (<i>left</i>) and the reattachment point (<i>right</i>) for the baseline case.	83
5.20	Streamwise evolution of the amplification factor (<i>left</i>) and cumulative harmonic content (<i>right</i>) of the three first harmonics at mid-height, for the forced case at 500Hz.	84
5.21	Evolution of the amplification level of harmonics at the shock as a function of the frequency.	85
5.22	Comparison of mean friction coefficient (<i>left</i>) and mean wall pressure coefficient (<i>right</i>) on the bump wall between the baseline and the forced cases. The <i>dashed</i> line represents the geometry.	85
5.23	Weighted premultiplied Power Spectral Density map of shock motion for the forced cases - 250Hz (<i>left</i>), 500Hz (<i>center</i>) and 1000Hz (<i>right</i>).	86
5.24	Amplitude (<i>left</i>) and phase (<i>right</i>) of shock motion at the forcing frequencies - 250Hz (<i>dashdot</i>), 500Hz (<i>solid</i>) and 1000Hz (<i>dashed</i>). The inset shows the evolution of amplitude depending on the frequency at $y/L_y = 0.4$	87
5.25	Evolution of the shock position at $y/L_y = 0.4$ with respect to the outlet static pressure - forced case 250Hz (<i>left</i>), 500Hz (<i>center</i>) and 1000Hz (<i>right</i>). The <i>black dot</i> is the mean shock position from the baseline case.	88
5.26	Instantaneous density gradient magnitude at mid-span at eight regularly spaced instants over a period for the forced case at 250Hz.	89

5.27	Weighted pre-multiplied PSD maps of top (<i>top</i>) and bottom (<i>bottom</i>) wall pressure for the forced cases - 250Hz, $N_{bl} = 9$ with 50% overlap (<i>left</i>), 500Hz, $N_{bl} = 9$ with 50% overlap (<i>center</i>) and 1000Hz, $N_{bl} = 7$ with 50% overlap (<i>right</i>). The <i>vertical</i> lines indicate from left to right the beginning of the bump, the bump throat, the end of the region of stable recirculation, the reattachment point and the end of the bump.	90
5.28	Normalized wall pressure amplitude at the forcing frequencies - <i>left</i> , comparison of streamwise evolution between ILES (<i>solid</i>), URANS (<i>dashed</i>) and experiments (<i>symbols</i>) from Bron (2004). The <i>vertical</i> lines indicate from left to right the bump throat, the end of the region of stable recirculation, the reattachment point and the end of the bump.	91
5.29	Comparison of Power Spectral Densities of the separation point (<i>left</i>) and reattachment point (<i>right</i>).	92
5.30	Time evolution of separation point (<i>solid black</i>) and reconstructed signal at the forcing frequency (<i>solid blue</i>) for the 250Hz (<i>top</i>) and 500Hz (<i>bottom</i>) cases.	93
5.31	Budgets of mean x - (<i>top</i>) and y -momentum (<i>bottom</i>) equations for the 500Hz case at $x/B_l = 0.33$ (<i>left</i>) and $x/B_l = 0.38$ (<i>right</i>) - Convection (\square), pressure force (\triangle), viscous force (\triangleleft), turbulent force from $-\overline{u'_i u'_j}$ (\diamond), turbulent force from $-\overline{\tilde{u}_i \tilde{u}_j}$ (\times) and balance (<i>solid black</i> line).	94
5.32	Time history of \tilde{u}/U_∞ for the case forced at 500Hz. The bin index is indicated in the top right corner of each subfigure.	95
5.33	Amplitude $A_{\tilde{u},1}/U_\infty$ (<i>left</i>) and phase $\phi_{\tilde{u},1}$ (<i>right</i>) of the first harmonic of \tilde{u} - 250Hz (<i>top</i>), 500Hz (<i>center</i>) and 1000Hz (<i>bottom</i>). Amplitude is bounded between 0 and, respectively, 0.3, 0.1 and 0.05.	96
5.34	Evolution of the coherent streamwise velocity in the mixing layer over a period - Phase-averaged values (<i>symbols</i>) and first harmonic reconstruction (<i>solid</i>).	97
5.35	Amplitude $A_{\tilde{k},1}/U_\infty^2$ (<i>left</i>) and phase $\phi_{\tilde{k},1}$ (<i>right</i>) of the first harmonic of \tilde{k} - 250Hz (<i>top</i>), 500Hz (<i>center</i>) and 1000Hz (<i>bottom</i>). Amplitude is bounded between 0 and, respectively, 0.05, 0.02 and 0.005.	97
5.36	First harmonic phase of turbulence kinetic energy with superimposed contours of first harmonic amplitude of turbulence kinetic energy (250Hz case) - 6 contours at $A_{\tilde{k},1}/U_\infty^2 = \{0.004, 0.012, 0.018, 0.021, 0.036, 0.05\}$. The <i>solid straight white</i> lines indicate the stations $x/B_l = 0.33$ and $x/B_l = 0.38$, respectively. The <i>symbols</i> are located at the structure cores C_1 to C_4 .	98
5.37	Profiles of the three first harmonics (first: <i>solid</i> , second: <i>dashed</i> , third: <i>dashdot</i>) of \tilde{k} for the 500Hz case - Amplitude (<i>top</i>) and phase (<i>bottom</i>) at stations $x/B_l = 0.33$ (<i>left</i>) and $x/B_l = 0.38$ (<i>right</i>).	99
5.38	Profiles of the first amplitude of $\overline{u'_i u'_j}$ - normalized by reference velocity (<i>top</i>) and compared to local mean (<i>bottom</i>) at station $x/B_l = 0.33$ (<i>left</i>) and $x/B_l = 0.38$ (<i>right</i>) for the 500Hz case.	100

5.39	Budgets of mean turbulence kinetic energy and mean turbulent normal stresses at $x/B_l = 0.33$ (<i>left</i>) and $x/B_l = 0.38$ (<i>right</i>) for the 500Hz case - Convection (\square), production (\triangle), pressure strain (\triangleleft), dissipation (\diamond), viscous diffusion (\circ), pressure diffusion (\times), turbulent diffusion (+) and balance (<i>solid black</i>).	102
5.40	Budgets of mean turbulent shear stress at $x/B_l = 0.33$ (<i>left</i>) and $x/B_l = 0.38$ (<i>right</i>) for the 500Hz case - Convection (\square), production (\triangle), pressure strain (\triangleleft), dissipation (\diamond), viscous diffusion (\circ), pressure diffusion (\times), turbulent diffusion (+) and balance (<i>solid black</i>).	103
5.41	Budgets of mean turbulence kinetic energy (<i>left</i>) and turbulent shear stress (<i>right</i>) at $x/B_l = 1.05$ for the 500Hz case - Convection (\square), production (\triangle), pressure strain (\triangleleft), dissipation (\diamond), viscous diffusion (\circ), pressure diffusion (\times), turbulent diffusion (+) and balance (<i>solid black</i>).	104
5.42	Budgets of coherent turbulence kinetic energy and coherent turbulent normal stresses for bin 2 at $x/B_l = 0.33$ (<i>left</i>) and $x/B_l = 0.38$ (<i>right</i>) for the 500Hz case - Convection (\square), production (\triangle), pressure strain (\triangleleft), dissipation (\diamond), viscous diffusion (\circ), pressure diffusion (\times), turbulent diffusion (+) and balance (<i>solid black</i>).	105
5.43	Budgets of coherent turbulent shear stress for bin 2 at $x/B_l = 0.33$ (<i>left</i>) and $x/B_l = 0.38$ (<i>right</i>) for the 500Hz case - Convection (\square), production (\triangle), pressure strain (\triangleleft), dissipation (\diamond), viscous diffusion (\circ), pressure diffusion (\times), turbulent diffusion (+) and balance (<i>solid black</i>).	106
5.44	Budgets of coherent turbulence kinetic energy (<i>left</i>) and turbulent shear stress (<i>right</i>) for bin 2 at $x/B_l = 1.05$ for the 500Hz case - Convection (\square), production (\triangle), pressure strain (\triangleleft), dissipation (\diamond), viscous diffusion (\circ), pressure diffusion (\times), turbulent diffusion (+) and balance (<i>solid black</i>).	107
5.45	Comparison of budgets of coherent turbulence kinetic energy for bin 2 at $x/B_l = 0.33$ (<i>left</i>) and $x/B_l = 0.38$ (<i>right</i>) between the 250Hz (<i>dashed</i>) and the 500Hz (<i>solid</i>) cases - Convection (\square), production (\triangle), dissipation (\diamond) (<i>top</i>) and viscous diffusion (\circ), pressure diffusion (\times) and turbulent diffusion (+) (<i>bottom</i>). The gray area represents the region of the flow for which $A_{k,1}/U_\infty^2 < 0.004$	108
5.46	Coherent production of $\widetilde{u'u'}$ at $x/B_l = 0.33$ (<i>left</i>) and $x/B_l = 0.38$ (<i>right</i>) for the 500Hz case - Total production (<i>solid</i>), $-2\overline{u'v'}\partial\widetilde{u}/\partial y$ (<i>dashed</i>), $-2\overline{u'v'}\partial\overline{u}/\partial y$ (<i>dashdot</i>), $-2\overline{u'v'}\partial\widetilde{u}/\partial y - 2\overline{u'v'}\partial\overline{u}/\partial y$ (<i>light blue</i>).	110
5.47	Coherent production of $-\widetilde{u'v'}$ at $x/B_l = 0.33$ (<i>left</i>) and $x/B_l = 0.38$ (<i>right</i>) for the 500Hz case - Total production (<i>solid</i>), $-\overline{v'v'}\partial\widetilde{u}/\partial y$ (<i>dashed</i>), $-\overline{v'v'}\partial\overline{u}/\partial y$ (<i>dashdot</i>), $-\overline{v'v'}\partial\widetilde{u}/\partial y - \overline{v'v'}\partial\overline{u}/\partial y$ (<i>light blue</i>).	110
6.1	Mean ρ/ρ_∞ from URANS (<i>left</i>) and NLH (<i>right</i>) simulations at $Re_{B_l} = 3.81 \times 10^6$ and $f = 500\text{Hz}$, 40 equally-spaced contours between 0.4 and 1.1.	117

6.2	Comparison of mean friction coefficient (<i>left</i>) and mean wall pressure coefficient (<i>right</i>) on the bump wall between RANS, URANS and NLH simulations at $Re_{B_i} = 3.81 \times 10^6$. For the forced cases, $f = 500\text{Hz}$. The <i>thin dashed</i> line represents the bump geometry.	117
6.3	Amplitude $A_{\tilde{p},1}/A_{\tilde{p}_o}$ (<i>left</i>) and phase $\phi_{\tilde{p},1}$ (<i>right</i>) of the first harmonic of \tilde{p} at $Re_{B_i} = 3.81 \times 10^6$ and $f = 500\text{Hz}$ - URANS (<i>top</i>) and NLH (<i>bottom</i>) simulations.	118
6.4	Normalized wall pressure amplitude at the forcing frequencies - comparison of streamwise evolution between URANS (<i>dashed</i>) and NLH (<i>solid</i>) simulations at $Re_{B_i} = 3.81 \times 10^6$	119
6.5	Mean ρ/ρ_∞ from URANS (<i>left</i>) and NLH (<i>right</i>) simulations at $Re_{B_i} = 1.91 \times 10^5$ and $f = 500\text{Hz}$, 40 equally-spaced contours between 0.4 and 1.1.	119
6.6	Comparison of mean friction coefficient (<i>left</i>) and mean wall pressure coefficient (<i>right</i>) on the bump wall between RANS, URANS and NLH simulations at $Re_{B_i} = 1.91 \times 10^5$. For the forced cases, $f = 500\text{Hz}$. The <i>thin dashed</i> line represents the bump geometry.	120
6.7	Normalized wall pressure amplitude at the forcing frequencies - comparison of streamwise evolution between URANS (<i>dashed</i>) and NLH (<i>solid</i>) simulations at $Re_{B_i} = 1.91 \times 10^5$	120
6.8	Comparison of harmonic eddy viscosity $\tilde{\nu}_T$ for the case at $Re_{B_i} = 1.91 \times 10^5$ with $f = 250\text{Hz}$ (<i>left</i>), $f = 500\text{Hz}$ (<i>center</i>) and $f = 1000\text{Hz}$ (<i>right</i>) - from URANS (<i>top</i>) and from the model (<i>bottom</i>).	123
6.9	Comparison of harmonic eddy viscosity $\tilde{\nu}_T$ for the case at $Re_{B_i} = 3.81 \times 10^6$ with $f = 250\text{Hz}$ (<i>left</i>), $f = 500\text{Hz}$ (<i>center</i>) and $f = 1000\text{Hz}$ (<i>right</i>) - from URANS (<i>top</i>) and from the model (<i>bottom</i>).	124
B.1	Instantaneous density ρ/ρ_∞ at mid-span (<i>top</i>) and instantaneous streamwise velocity u/U_∞ near the bottom wall, $y^+ \approx 10$ (<i>bottom</i>).	146
B.2	Streamwise evolution of Reynolds numbers based on the friction velocity Re_τ (<i>left</i>) and on the boundary layer momentum thickness Re_θ (<i>right</i>), present case (<i>black</i>) and DNS results (<i>red</i>).	147
B.3	Evolution of friction coefficient, present case (<i>black</i>) and DNS results (<i>red</i>). The results from simulations with an extended domain are shown in <i>dashed</i> . The <i>thin dashed</i> line represents the correlation from Ceci et al. (2022).	147
B.4	Evolution of peak $\overline{\rho u' u'}$ (<i>left</i>) and peak $\overline{\rho u' v'}$ (<i>right</i>), present case (<i>black</i>) and DNS results (<i>red</i>). The <i>thin dashed</i> lines represent the correlations from Ceci et al. (2022).	148
B.5	Evolution of static pressure fluctuations, present case (<i>black</i>) and DNS results (<i>red</i>). The <i>thin dashed</i> line represents the correlations from Ceci et al. (2022).	148
B.6	Boundary layer profiles at $x/\delta_0 = 15$ - van Driest-transformed mean velocity profile (<i>left</i>) and density-scaled Reynolds stress profiles (<i>right</i>), present case (<i>black</i>) and DNS results (<i>red</i>).	149

List of Tables

3.1	Coefficients for the Runge-Kutta scheme.	26
4.1	Comparison of high-fidelity simulation setups for the oblique SWBLI configuration from IUSTI. The column BC refers to the type of lateral boundary condition employed, with P, S and W standing for Periodic, Slip and Wall, respectively. ϕ is the deflection angle. T is the total integration time of the simulation.	39
4.2	Comparison of domain dimensions, numbers of degrees of freedom and grid resolutions for high-fidelity simulations of the oblique SWBLI configuration from IUSTI. $-x_{in}/\delta_0$ gives the location of the inlet plane, considering the location of the theoretical impingement point of the incident shock to be at $x_{imp}/\delta_0 = 0$. ^a Dimension originally given in terms of the inlet boundary layer thickness δ_{in} , but rescaled here by δ_{in}/δ_0	40
4.3	Boundary layer characteristics upstream of the interaction. The reference station is located at $(x - \bar{x}_{imp})/L \approx -1.66$. Experimental values are taken from Dupont et al. (2008) or Piponnier et al. (2009) depending on the available data. δ^* , θ and θ_i are the compressible displacement thickness and the compressible and incompressible momentum thicknesses, respectively.	45
4.4	Comparison of the length of interaction and length of separation. ^a value estimated assuming $L_{sep} = 0.8L$ (Clemens & Narayanaswamy, 2009). ^b value estimated from the friction coefficient curve.	49
5.1	Comparison of flow conditions for studies on the bump of Bron (2004). p_t and T_t are inlet total pressure and total temperature, respectively. p_o is the outlet static pressure. The integration time in convective time units n_{CTU} is given for high-fidelity simulations only.	63
5.2	Comparison of unsteady flow conditions for studies on the bump of Bron (2004).	64
5.3	Comparison of domain size and inlet location for high-fidelity simulations of the bump of Bron (2004).	66
5.4	Comparison of number of degrees of freedom and grid resolution for high-fidelity simulations of the bump of Bron (2004). ^a values taken from figures 11 and 12 in Wollblad et al. (2006). ^b values estimated using the Blasius law.	67

5.5	Comparison of separation and reattachment points location as well as shock position at mid-height for various turbulence models.	70
5.6	Comparison of separation bubble characteristics.	79
5.7	Comparison of the effectiveness of the forcing conditions at the outlet boundary.	83
5.8	First harmonic energy content at the four structure cores depending on the forcing frequency.	99

Chapter 1

Introduction

1.1 Context

Air travel is nowadays a popular means of transport, allowing to connect people from all around the world in less than a day. It also facilitates the transport of goods and the provision of services, and stimulates development by empowering businesses to collaborate on an international scale. The contribution of the aviation sector to the society and the economy is undoubtedly considerable. In Europe for example, 3.6% of all employment is directly or indirectly related to aviation and 4.4% of all gross domestic product is generated by the air transport industry (ATAG, 2020). Big aircraft manufacturers recently published their market outlooks for the next two decades, giving some insights on the future of aviation. A global air traffic growth of 3.6% (Airbus, 2023) and 6.1% (Boeing, 2023) is forecasted per year over the next 20 years. Past history also showed that air traffic growth is resilient to external events and quickly recovers from crises, making these predictions most likely to occur. As a result, the fleet in service is expected to approximately double compared to current numbers.

Alongside these perspectives, the rising awareness about climate change brings scrutiny on the role played by the aviation sector. Its environmental impact cannot be denied as worldwide flights produced around 2.1% of the global CO₂ emissions in 2019 (ATAG, 2020), with an average yearly increase of 4.5% since 2013 (ICCT, 2020). In 2015, an international treaty on climate change, referred to as the Paris Agreement, was adopted by a vast majority of world leaders. To mitigate the severity of climate change impacts, it established goals of limiting the increase in global average temperature. The aviation industry has actually continuously made efforts to reduce the environmental footprint of aviation over the last decades. Nevertheless, meeting the requirements from the Paris Agreement imply to pursue and push these efforts further. Through various initiatives, the actors of the aviation sector shared their vision, their path toward a climate neutral air mobility by 2050, to reach the targets set by the Paris Agreement (see for example *Waypoint 2050* (2021) and *Fly the Green Deal* (2022), the continuity of the *Flightpath 2050* (2011)).

Several solutions were suggested by the aforementioned initiatives. Besides the use of sustainable fuels, technology is the other lever that will allow to attain the objectives the industry committed to. Substantial research is focused on breakthrough concepts that completely reinvent the way aircraft are imagined (Bravo-Mosquera et al., 2022). Often, they feature an enhanced level of component integration. The boundary layer ingestion concept, for instance, consists in the integration of the engines in the fuselage (see figure 1.1), and the resulting distorted inflow is difficult to consider in the design of the engines. While being part of the solutions for climate neutral aviation, the development process of such alternatives, from the proof of concept to industrial maturity, is long and the environmental challenge cannot wait.



Figure 1.1. Double bubble D8 aircraft design concept, using boundary layer ingestion. Credits: NASA/MIT/Aurora Flight Sciences.

Persisting with the current paradigm involves to incrementally, but significantly, improve both aircraft and engines efficiency, the designs of which have already been optimized for decades. In turbomachinery, one of the challenge resides in the transonic regime, where shock waves appear and interact with the boundary layers developing on the blades (see figure 1.2, *right*). The resulting shock wave/boundary layer interaction is currently the primary aerodynamic performance-limiting factor. It leads indeed to flow separation, flow distortion and also exhibits large-scale unsteadiness at low-frequency. This behavior can threaten the structural integrity of the blades and its origin is still an open question that is motivating numerous works on the topic (see the reviews of Clemens and Narayanaswamy (2014) and Gaitonde and Adler (2023)). A better knowledge of the phenomenon, a better understanding of the underlying physics would indeed help to develop better design tools. The subsequent enhanced predictability would therefore allow to extend the design space and push the efficiency limits further with confidence.

Even though experiments will always occupy a position in the industrial design chain, the need for a quick assessment of a broad range of designs, together with the advancements in computer technology, led to the development of numerical methods to simulate fluid flows. Fluid flows are governed by the Navier-Stokes equations, a set of non-linear partial differential equations, which do not have an analytical solution for the general case. They can, however, be solved on computers using the theory of numerical analysis and the associated research field is commonly called Computational Fluids Dynamics (CFD).

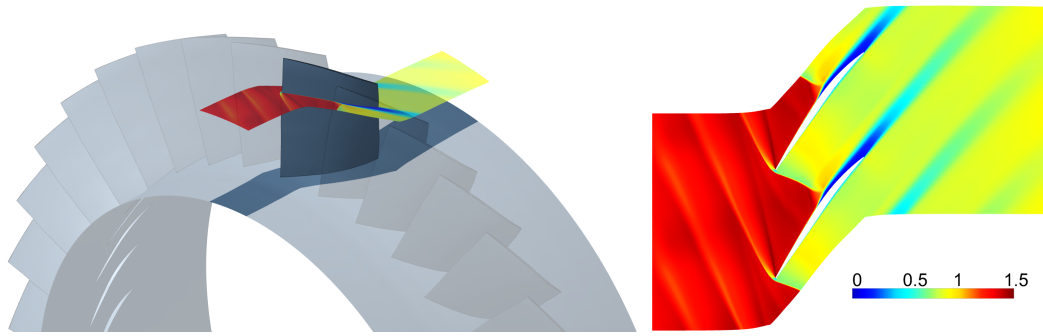


Figure 1.2. Rotor 37 - simulation of a single blade passage, highlighted on the full annulus (*left*) and relative Mach number at 70% span, featuring a shock wave/boundary layer interaction (*right*).

A wide variety of methods were developed for turbomachinery CFD (Denton & Dawes, 1998) and their adoption in the industry is closely related to the progress in computational power. Early numerical models were based on two-dimensional blade-to-blade and hub-to-tip surfaces, the latter being referred to as throughflow calculations. The fully three-dimensional simulations started to be used in the industry as a routine design tool in the 1980s. To benefit from a drastic reduction of the computing cost, the whole wheel was truncated to a single blade passage, owed to the periodicity of the flow (see figure 1.2, *left*). Simulations were using steady models and were carried over a single blade row. Beginning of the 1990s, computer power enabled the extension to multistage configurations, see figure 1.3 for an example. The limitation due to the imposition of boundary conditions was therefore lifted and let place to the development of various treatments for rotor/stator interactions. Turbomachinery flows are fundamentally unsteady and three-dimensional unsteady simulations across multiple blade rows started to be performed at that time, first on a subset of the full annulus and then eventually for the complete annulus, thanks to the rising power of computing resources. At present, all these methods are routinely employed in the design chain. They are indeed mature, robust and quickly evaluate the performance of a design.

The obtainment of unsteady flow solutions in multistage, full annulus configurations definitely brought a clearer understanding of the complex flow physics occurring in turbomachinery. Nevertheless, their cost with respect to their steady, single passage and single row counterpart is several orders of magnitude higher. The unsteady phenomena in turbomachinery (such as forced response or flutter) do not necessarily have the same periodicity than the blade count and therefore the restriction of the full annulus to a single passage is not valid if such features are to be predicted. This played in the favor of the development of Fourier (or harmonic) methods, with the idea of capturing unsteady features by keeping the mesh of a single blade, to benefit from the inherent periodicity of turbomachinery flows. An unsteady solution is provided, but with a considerable reduction of cost compared to full unsteady simulations.

The non-linearity of the Navier-Stokes equations brings in a chaotic behavior known as turbulence. Turbulent flows are intrinsically three-dimensional, exhibit

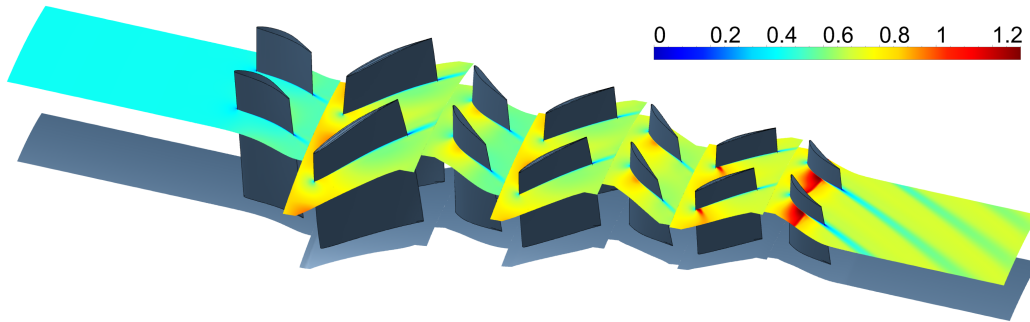


Figure 1.3. IDAC3 - simulation of a single blade passage in a multistage configuration, relative Mach number at 70% span. Two blade passages are shown for illustration purposes.

enhanced dissipative, diffusive and mixing effects and are characterized by a large spectrum of scales (also called eddies) in space and time. Turbomachinery flows are highly turbulent, and therefore the inclusion of turbulence plays a critical role in the design. The cheapest methods are obtained by solving the time-averaged Navier-Stokes equations, the Reynolds-Averaged Navier-Stokes (RANS) equations, in which turbulence manifests itself by an additional viscous stress term. In all the methodologies cited so far, this extra term is modeled. An immensity of turbulence models exist in CFD and their defects and palliatives in a turbomachinery context were outlined in Tucker (2013). With respect to shock wave/boundary layer interactions, the turbulence model was found to play a significant role in the prediction of the flow features (DeBonis et al., 2012). Unsteady RANS (or URANS) simulations are also inefficient at reproducing their low-frequency unsteadiness. Methods relying on turbulence models are often referred to as low-fidelity methods. Nevertheless, they have been the backbone of industrial turbomachinery design so far, thanks to their efficiency and robustness, and will continue to be employed as such for the foreseeable future (Rumsey & Coleman, 2022).

Instead of modeling all the scales of turbulence, other approaches consist in actually resolving all or most of them. In contrast, they are therefore called high-fidelity methods. In Large-Eddy Simulations (LES), only the large scales of turbulence are captured by the computational grid, while the behavior of the smallest eddies, being more universal, is still handled by a model. In Direct Numerical Simulations (DNS), the Navier-Stokes equations are solved as such, without any model, providing the closest representation of the reality. These methods are profitable for predicting features that fall in the shortcomings of RANS-based methods, such as separation, transition and heat transfer. However, the more scales are captured, the more the computational cost increases as the mesh needs to be refined. Such methods are consequently costly, but the continuously increasing computational power makes them slowly affordable for the industry (Tyacke et al., 2019) in late design stages. Their use for a routine design work remains nevertheless out of reach.

A second application of high-fidelity simulations is to extract knowledge to develop low-fidelity approaches. High-fidelity simulations allow indeed to generate gigantic data sets and to provide insightful information that cannot necessarily be

obtained from experiments. Because of the tremendous amount of data, the learning process is difficult to handle for a human and tools from artificial intelligence, such as machine learning, become the way to proceed. Among the various developments from machine learning for turbomachinery CFD (see Hammond et al. (2022)), the most relevant in this context is related to turbulence modeling. Turbulence models contains numerous coefficients, which can be tuned for specific cases, or entirely new turbulence models can be devised.

The rising interest in high-fidelity simulations also calls for the development of high-order methods. State-of-the-art industrial solvers are typically second-order accurate, because it yields robustness and reliability. The good robustness is actually associated to the larger dissipation of low-order schemes, which therefore does not make them suitable if a fine description of all the turbulent eddies is desired. For scale resolving simulations, the use of high-order schemes (the order of accuracy of which is by definition greater than two) is preferred for their inherent low dissipation. High-order means also that the same accuracy will be obtained as a second order scheme, but for a reduced cost (or a reduced number of degrees of freedom). On the other side, high-order schemes are known to suffer from a lack of robustness, which has slowed down their adoption in the industry. This is particularly true in the presence of discontinuities such as shock waves. Developing high-order schemes with better properties and/or finding strategies to stabilize the simulations is the motivation of intensive research.

The context being introduced, the present work, entitled *From high-fidelity high-order to reduced-order modeling for unsteady shock wave/boundary layer interactions*, aims first at contributing to the development of a high-order solver in order to perform high-fidelity simulations of shock wave/boundary layer interactions. These will be used to study periodically forced interactions and improve low-fidelity methods in that regard, and more particularly aspects related to turbulence modeling in harmonic methods for turbomachinery applications. Before presenting in more details and better understand the objectives and the methodology employed to address this topic, further context is now brought about harmonic methods and high-order methods.

1.1.1 Harmonic methods

Harmonic methods have the ambitious goal of predicting unsteady flows as in full unsteady simulations, but with the advantage of steady simulations, that is to say the restriction of the computational domain to a single blade passage. This can be achieved by employing the inherent periodicity of turbomachinery flows.

Different ways exist to take advantage of this inherent periodicity with harmonic models. Periodicity can be exploited either in space or in time, and the equations can be solved in the time or in the frequency domain. A short, non-exhaustive overview of these methods is given hereafter but for a more detailed review, the reader is invited to refer to the works of Sicot (2009) and He (2010).

The first methods to appear were the time-linearized harmonic models. The basic idea is the decomposition of the flow variables into a mean component and a small periodic perturbation around that mean. Using this decomposition in the flow equations allows to derive two sets of equations, one for the mean flow and one for the perturbation, which are solved with the same algorithms as for steady simulations. A one-way coupling exists in the sense that the mean equations are independent of the solution for the perturbations. These methods were applied to three-dimensional Euler and Navier-Stokes equations in the context of turbomachinery, for example in Hall and Lorence (1993) and Sbardella and Imregun (2001).

Even though linear harmonic models are computationally efficient, their applicability is limited because of the linear assumption. Turbomachinery flows are indeed highly turbulent and non-linear, which motivated the development of non-linear harmonic models. Different methods resulted from this effort. By casting the discretized URANS equations into the frequency domain and solving for the Fourier coefficients of the conservative variables, the non-linearity is accounted for through the direct treatment of the non-linear residual. This corresponds to the Non-Linear Frequency Domain (NLFD) method introduced by McMullen et al. (2001). If now these equations are transformed back and solved into the temporal domain for the time instants, the Time Spectral Harmonic Balance method (TSHB) developed by Hall et al. (2002) is obtained. Both approaches were successfully applied to industrial configurations. For instance, Frey et al. (2014) reported the results for a 1.5-stage transonic axial compressor using the NLFD approach and Sicot et al. (2013) employed a solver based on the TSHB method to study a 3.5-stages axial compressor.

Another way to bring non-linearity is by time-averaging the flow equations after introducing the decomposition. The procedure indeed generates additional terms in the mean equations, called the deterministic stresses (Adamczyk, 1984), which enable a two-ways coupling between the mean flow and the harmonic perturbations. The resulting approach, the one employed in this work, is referred to as the Non-Linear Harmonic (NLH) method, originally proposed by He and Ning (1998). The most ambitious test case illustrated was then an oscillating compressor cascade. Vilmin et al. (2006) successfully implemented the NLH in commercial software and presented a treatment for rotor/stator interface. The solver was validated against several industrially-relevant test cases, amongst them a radial turbine and a 4-stages transonic compressor. Many improvements were made to extend the range of application of the method, further popularizing the NLH for industrial uses. Real gases (Vilmin et al., 2007), clocking effects (Vilmin et al., 2009), multi-row interactions (Vilmin et al., 2013), moving bodies (Debrabandere et al., 2013), interactions between harmonics (Debrabandere, 2014), incompressible or low Mach number flows (Tartinville & Hirsch, 2015) and conjugate heat transfer (Mehdizadeh et al., 2017) were addressed.

All these methods share a drastic reduction of computing time with respect to full unsteady simulations, owed to the fact that only a single blade passage is meshed, but also that the sets of equations are solved as in steady mode. These methods can, however, be distinguished by several aspects.

The power of the NLH method resides in its inherent ability to manage multiple perturbations, a key aspect for the design of multistage turbomachinery configurations. Perturbations can indeed come from multiple sources: neighboring rows with different blade-passing frequencies, inlet/outlet distortion or modal deformations for instance. The choice of the number of perturbations and related number of harmonics, as well as the selection of the number of rows that the perturbations can travel across, makes the method highly flexible, as demonstrated by Tartinville and Vilmin (2023). In contrast, NLFD and TSHB approaches suffer from the selection of the discrete instants or Fourier coefficients for which solving the equations.

On the other hand, the direct treatment of the residual in the NLFD and TSHB methods allows them to automatically account for interactions between harmonics, not necessarily originating from the same perturbation. These effects are, however, not considered in the basic formulation of the NLH.

Another important aspect is related to how turbulence is handled. While the effects of the perturbations on the turbulence are automatically embedded in the frameworks of harmonic balance methods (NLFD and TSBH), this is not the case for the linearized models and the NLH, which require an analytical expression. Keeping the sole contribution of the time-mean turbulence model equations, for instance a turbulent eddy viscosity evaluated based on the averaged flow variables, is called the frozen turbulence assumption. On the opposite is the harmonic turbulence approach, including the effects of the perturbations in the treatment of the turbulence. The frozen turbulence assumption is often adopted as it is a straightforward way to close the equations. It was shown to give reliable predictions in many cases (Borm & Kau, 2012; Hembera et al., 2009; Hildebrandt et al., 2014; Y. Liu et al., 2023; Marlier et al., 2016; Mathison et al., 2011; Sugimoto et al., 2014; Tartinville & Vilmin, 2023). Nevertheless, it remains inaccurate for some configurations. Using a fully-linearized solver, Philit et al. (2012) illustrated the latter fact for the forced transonic flow over a bump with a massive shock-induced separation. Harmonic turbulence was found to be indispensable to recover the same results as in a full unsteady computation. As expected, results from the TSHB method were also shown to be accurate without any modification.

As a first solution to that problem, several works incorporated the linearized turbulence model into linearized harmonic solvers. Clark and Hall (2000) and Sbardella and Imregun (2001) derived the perturbation equation for the Spalart-Allmaras model. Holmes and Lorence (1998) and Philit et al. (2012) dealt with the $k-\omega$ model. This could be integrated in the NLH method as well. However, the path toward a robust implementation of such a solution is not elementary. Besides the challenging arithmetic work of developing the linearized equation(s), the translation into code brings additional complexity and difficulties to the debugging. On top of that, turbulence models contain numerous calibrated variables, which would require further adjustments. Holmes and Lorence (1998) raised the question of the clips of turbulence quantities, for example. Moreover, the linearization should be performed for each turbulence model, multiplying the effort. It should also be achieved for each equation, regardless of the number of equations involved in the model. As a consequence, the cost of the simulation can drastically increase. This is

particularly true if Reynolds-stress models are employed, let alone the combination with a transition model. Finally, and more importantly, turbulence is inherently non-linear and this solution still suffers from the linearity assumption. In practical terms, the reconstruction of an unsteady solution based on the mean and harmonic solutions could give negative values of turbulent quantities that are by definition positive.

Apart from linearizing the turbulence model, no other mean has been found to account for the harmonic turbulence. A more elegant solution, which would be valid for any turbulence model and which would account for non-linearity properly has not been found but would definitely improve the predictions given by harmonic methods such as the NLH and therefore widen their range of application.

1.1.2 High-order methods

A method is categorized as being high-order if its order of accuracy is greater than two. The order of accuracy is by definition controlling the solution error, that is to say a method is said to be p^{th} -order accurate if the error is proportional to H^p , with H being the mesh size. Compared to lower-order methods, a high-order method will therefore provide a better accuracy on the same mesh, or the same accuracy on a coarser mesh.

High-order accuracy can be achieved in several ways. In finite difference and finite volume methods, this can be done by extending the stencil, meaning increasing the number of neighboring cells involved in the evaluation of the fluxes. Examples can be found in Pirozzoli (2010) and Kok (2009), respectively. Because the neighbors are readily available, this approach works well for structured grids, whereas the lack of compactness makes the handling of unstructured grids more difficult. Compact schemes can, however, be obtained by considering a polynomial representation of the solution within each cell. The most popular and mature class of schemes originates from the work of Reed and Hill (1973) to solve the neutron transport equation. From this have arisen mainly two methods, abbreviated DG for Discontinuous Galerkin (Bassi & Rebay, 1997; Cockburn & Shu, 1998) and SD for Spectral Difference (Kopriva & Koliass, 1996; Y. Liu et al., 2006).

The method that will be employed here in the high-order solver is called the Flux Reconstruction (FR) approach, and is closely related to DG and SD methods. It was introduced first in Huynh (2007) for the advection equation. When representing the solution within each cell by a polynomial, the global solution function and, similarly, the global flux function, are discontinuous across cell interfaces. The idea of FR schemes is to apply correction functions to the discontinuous flux function by taking into account the information at the cell interfaces so that the global flux function becomes continuous across cell interfaces. The flux function can then be differentiated in order to advance the solution in time. The FR approach is actually a unifying framework. Depending on the correction function chosen, it is possible to recover DG or SD, but also to derive entirely new schemes. The schemes developed are simpler and more economical than the original DG or SD methods as the equations are solved in their differential form and only one set of points is used.

The schemes are also simpler in the way the approach is formulated and conceived. A straightforward extension to 2D quadrilateral meshes based on tensor product was proposed and is valid for 3D hexahedral grids as well. The evaluation of second order derivatives and therefore the extension of the approach to diffusion problems was presented later by the same author (Huynh, 2009).

Whereas quadrilateral and hexahedral meshes are easily supported by the original FR approach, the extension to triangular elements is not straightforward since tensor product is not available. Z. J. Wang and Gao (2009) suggested a correction for the derivative of the flux, appearing as a penalty term in the equations. It led to the Lifting Collocation Penalty (LCP) formulation. Results were shown for the 2D Euler equations (Z. J. Wang & Gao, 2009) and further for the 2D Navier-Stokes equations (Gao & Wang, 2009) on mixed elements meshes. The corresponding 3D development, including tetrahedra and triangular prisms, was demonstrated in Haga et al. (2011). Because of the close relationship between FR and LCP, both are often combined into what is called the CPR method (for Correction Procedure via Reconstruction). Finally, Huynh (2011) expanded the FR approach to consider triangular elements. Both a derivative correction (as in the LCP formulation) and a flux correction (or reconstruction) were derived.

Following the mathematical background of Jameson (2010) for a SD scheme, Vincent et al. (2011a) devised energy stable FR schemes for linear advection problems, known as the VCJH schemes (for Vincent-Castonguay-Jameson-Huynh). This range of schemes is parameterized by a single scalar parameter, analytically defining the correction functions, and some of the original schemes derived by Huynh (2007) can be retrieved. Early applications consisted in the simulation of the 2D Euler equations (Castonguay, Vincent, et al., 2011), 2D (Williams et al., 2011) and 3D Navier-Stokes equations (Castonguay, Williams, et al., 2011) on mixed unstructured grids, after the method was extended to diffusion problems by Ou et al. (2011). Contrary to the Fourier stability analysis, the power of energy-based stability proofs lies in their validity for all orders of accuracy and on arbitrary (nonuniform) meshes. Rigorous theoretical proofs of energy stability were further extended to triangles (Castonguay et al., 2012) and given for linear advection-diffusion equations in 1D (Castonguay et al., 2013), on triangles (Williams et al., 2013) and tetrahedra (Williams & Jameson, 2014).

Romero et al. (2016) devised a simplified formulation for the FR approach, called the Direct Flux Reconstruction (DFR), in which the use of correction functions to ensure continuity is replaced by a single Lagrange interpolation. It was later extended to advection-diffusion problems on triangular elements (Romero et al., 2017) and further studied in Huynh (2020).

Schemes based on FR are highly suitable for parallel computing and more particularly GPU acceleration. Indeed, high-order methods generally involve more work per degree of freedom than low-order methods, and only a few operations involve coupling between elements, especially with explicit time-stepping techniques. The first high-order 3D compressible Navier-Stokes solver supporting mixed unstructured grid and running on multiple GPUs was presented in Castonguay, Williams, et al. (2011). It was moreover based on the FR approach and used the VCJH correction

functions. Another GPU porting of FR was performed by Witherden et al. (2014) on Python (hence the solver name PyFR) and later on heterogeneous platforms in Witherden et al. (2015). A comparison between PyFR and an industrial solver confirmed the benefit of high-order methods and the use of GPUs (Vermeire et al., 2017). A GPU-accelerated solver based on the DFR method was finally presented in Romero et al. (2020).

Solvers using a flux reconstruction scheme were employed for various applications. To give a non-exhaustive list, the suitability of the FR approach to perform simulations of turbulent flows was demonstrated in Vermeire et al. (2016) using ILES. Also with ILES, the flow over an NACA0021 airfoil was investigated by Park et al. (2017). The laminar and turbulent shock wave/boundary layer interactions in a transonic passage were studied by means of ILES in Priebe et al. (2020). A DNS of a low pressure turbine blade was reported by Iyer et al. (2021). Z. J. Wang and Rahmani (2021) used ILES on the NASA CRM high-lift configuration near stall. Finally, Rahmani and Wang (2022) presented the results of ILES of the transonic flow over a hump.

The potential of high-order methods was demonstrated mainly in academia. Even though the industry also showed interest, several pacing items need to be addressed in order to develop high-order tools suitable for a routine design work (Z. Wang, 2014). In relation to shock wave/boundary layer interactions, an efficient shock-capturing strategy is needed to properly handle discontinuities and avoid robustness issues. Several approaches exist, as it will be emphasized in a later chapter, but none is considered to be preminent. Another issue is attributed to inlet turbulence (Tyacke et al., 2019), or how to prescribe realistic inflow conditions for turbulent flows.

1.2 Thesis objectives and outline

From the picture brought by the context, the objectives of the thesis are now detailed. The first aim is to contribute to the development of a high-order solver, so that it becomes robust and accurate enough to be employed to perform high-fidelity simulations of shock wave/boundary layer interactions. To this effect, a particular attention will be given to the shock-capturing technique and the prescription of inflow turbulence. The capabilities of the solver will be assessed on a canonical oblique shock reflection on a turbulent boundary layer.

The second goal is to bring insights on the physics of periodically forced transonic flows and to shed some light on harmonic turbulence. The test case investigated, simpler but representative of turbomachinery configurations, will be the transonic flow over a two-dimensional bump. High-fidelity simulations will be performed at various forcing frequencies using the freshly validated high-order solver.

Finally, the last objective refers to the need of a better handling of harmonic turbulence in the Non-Linear Harmonic method. Instead of implementing a linearized turbulence model, the idea is to derive a reduced-order model to include this effect in a more general and flexible manner, which would also preclude the issues related

to the non-linearity of turbulent quantities. The data generated to study the forced transonic flow over a bump will be employed in an attempt to answer that need.

The structure of the dissertation is the following. In chapter 2, the governing equations are presented. The chapter begins with the compressible Navier-Stokes equations and further introduces the triple decomposition (and subsequent equations) as a tool to analyze periodic flows. In chapter 3, the solver based on the high-order flux reconstruction scheme is described, from the spatial scheme and the temporal discretization to the shock-capturing strategy and the turbulent inflow generator. The results obtained for the validation case of the canonical oblique shock wave/boundary layer interaction are presented in chapter 4. The results of the forced transonic flow over a bump and the study of the harmonic turbulence are given in chapter 5. In chapter 6, the results from the Non-Linear Harmonic method for the forced transonic flow over a bump and the attempt to model harmonic turbulence are introduced. Finally, some conclusions are drawn in chapter 7. Two appendices then follow. In appendix A, the complete derivation of the governing equations for incompressible flows with a triple decomposition, together with some practical aspects to compute the budgets of harmonic turbulent stress, are detailed. Appendix B gives the results from the simulation of a supersonic turbulent boundary layer as a validation for the turbulent inflow.

1.3 Publications and conference presentations

A part of the methods and results presented in this thesis were presented in international conferences or published in peer-reviewed journals. They are listed hereunder.

1.3.1 Journal publications

- Goffart, N., Tartinville, B., & Pirozzoli, S. (2024). Harmonic Turbulent Stress Budgets in Forced Transonic Flow over a Bump. *AIAA Journal*, 62(3), 940–955. <https://doi.org/10.2514/1.J063417>

1.3.2 Conference proceedings papers and presentations

- Goffart, N., Tartinville, B., Puri, K., Hirsch, C., & Pirozzoli, S. (2022). High-Order, High-Fidelity Simulation of Unsteady Shock-Wave/Boundary Layer Interaction Using Flux Reconstruction. *8th European Congress on Computational Methods in Applied Sciences and Engineering*. <https://doi.org/10.23967/eccomas.2022.138>
- Goffart, N., Tartinville, B., Hirsch, C., & Pirozzoli, S. (2022). Coherent Turbulent Stresses in Transonic Nozzle with Shock-Wave/Turbulent Boundary Layer Interaction. *ERCOFTAC Direct and Large-Eddy Simulation Workshop 13*

- Goffart, N., Tartinville, B., Hirsch, C., & Pirozzoli, S. (2023). Investigation of Forced Shock-Induced Separation in a Transonic Channel. *15th European Conference on Turbomachinery Fluid Dynamics and & Thermodynamics*. <https://doi.org/10.29008/ETC2023-155>
- Goffart, N., Tartinville, B., & Pirozzoli, S. (2023). Coherent Turbulent Stresses in Unsteady Forced Transonic Nozzle with Shock-Induced Separation. *ASME Turbo Expo: Power for Land, Sea, and Air, Volume 13D: Turbomachinery — Multidisciplinary Design Approaches, Optimization, and Uncertainty Quantification; Radial Turbomachinery Aerodynamics; Unsteady Flows in Turbomachinery*, V13DT36A009. <https://doi.org/10.1115/GT2023-101925>

Chapter 2

Governing Equations

In this chapter, the different governing equations are presented. The first section deals with the Navier-Stokes equations governing compressible flows, equations which will be discretized in the high-order solver. The second section introduces the triple decomposition, a tool for the analysis of oscillatory flows, and the various systems of governing equations deriving from it.

2.1 Compressible Navier-Stokes equations

The equations considered here are the three-dimensional compressible Navier-Stokes equations governing the conservation of mass, momentum and energy. In conservative form and using the convention of repeated indices, the system of equations is given by

$$\frac{\partial \rho}{\partial t} + \frac{\partial}{\partial x_i}(\rho u_i) = 0 \quad (2.1)$$

$$\frac{\partial}{\partial t}(\rho u_i) + \frac{\partial}{\partial x_j}(\rho u_i u_j) = -\frac{\partial p}{\partial x_i} + \frac{\partial \sigma_{ij}}{\partial x_j} \quad (2.2)$$

$$\frac{\partial}{\partial t} \left[\rho \left(e + \frac{1}{2} u_i u_i \right) \right] + \frac{\partial}{\partial x_j} \left[\rho u_j \left(h + \frac{1}{2} u_i u_i \right) \right] = \frac{\partial}{\partial x_j} (u_i \sigma_{ij}) - \frac{\partial q_j}{\partial x_j}, \quad (2.3)$$

where ρ is the density, u_i the velocity components, p the static pressure, e the specific internal energy and $h = e + p/\rho$ the specific enthalpy. The fluid is air assumed to be a perfect gas, so that the equation of state is written

$$p = \rho R T \quad (2.4)$$

with R the perfect gas constant and T the static temperature. The viscous stress tensor σ_{ij} for compressible flow is defined following

$$\sigma_{ij} = 2\mu \left(s_{ij} - \frac{1}{3} \frac{\partial u_k}{\partial x_k} \delta_{ij} \right) \quad (2.5)$$

where δ_{ij} is the Kronecker delta and s_{ij} is the instantaneous strain rate tensor given by

$$s_{ij} = \frac{1}{2} \left(\frac{\partial u_i}{\partial x_j} + \frac{\partial u_j}{\partial x_i} \right). \quad (2.6)$$

The fluid is also presumed to be calorically perfect. As a consequence, the specific heat coefficients are constant and the specific internal energy e is computed with

$$e = c_v T \quad (2.7)$$

with c_v the specific heat coefficient for constant volume. The heat flux vector q_j is expressed as

$$q_j = \lambda \frac{\partial T}{\partial x_j} \quad (2.8)$$

in which λ is the thermal conductivity.

Fluid properties are evaluated as follows. From the specific heat ratio $\gamma = 1.4$ and the specific heat capacity for constant pressure $c_p = 1006 \text{J}/(\text{kg}\cdot\text{K})$, the specific heat capacity for constant volume c_v and the perfect gas constant R are obtained with

$$c_v = \frac{c_p}{\gamma} \quad (2.9)$$

$$R = c_p - c_v. \quad (2.10)$$

The dynamic viscosity is computed according to Sutherland's law,

$$\mu(T) = \mu_{ref} \left(\frac{T}{T_{ref}} \right)^{3/2} \frac{T_{ref} + S}{T + S} \quad (2.11)$$

with the reference dynamic viscosity $\mu_{ref} = 1.716 \times 10^{-5} \text{Pa}\cdot\text{s}$ at the reference static temperature $T_{ref} = 293.111 \text{K}$ and $S = 110.555 \text{K}$. Finally, knowing the dynamic viscosity, the thermal conductivity is evaluated with

$$\lambda = \frac{c_p \mu}{Pr} \quad (2.12)$$

where the laminar Prandtl number Pr is assumed to be constant and equal to 0.708.

2.2 Triple decomposition for incompressible flows

To conveniently analyze the oscillatory flows that will be investigated in the later chapters, the triple decomposition of Reynolds and Hussain (1972) is adopted. This section provides an introduction and summarizes the equations that arise from this decomposition, for both the mean flow and its oscillatory component. The detailed derivation is given in appendix A.

The triple decomposition states that any instantaneous quantity a may be written as the sum of three components,

$$a(x, y, z, t; T) = \bar{a}(x, y, z) + \tilde{a}(x, y, z, t/T) + a'(x, y, z, t) \quad (2.13)$$

where \bar{a} is the mean component, \tilde{a} is the coherent (also called periodic or harmonic) component and a' is the incoherent (or random) component. Both the coherent and incoherent components depend on time but, for this decomposition to be meaningful, their time scales must differ by several orders of magnitude. Typically, the coherent component is related to a single low frequency, whereas the incoherent component corresponds to broadband phenomena at higher frequencies.

After introducing this decomposition into the incompressible Navier-Stokes equations, taking the time average allows to derive the equations ruling the mean flow. The mean equations of conservation of mass and momentum are given by

$$\frac{\partial \bar{u}_i}{\partial x_i} = 0 \quad (2.14)$$

$$\bar{u}_j \frac{\partial \bar{u}_i}{\partial x_j} = -\frac{1}{\rho} \frac{\partial \bar{p}}{\partial x_i} + \nu \frac{\partial^2 \bar{u}_i}{\partial x_j^2} - \frac{\partial}{\partial x_j} \left(\overline{\tilde{u}_i \tilde{u}_j} + \overline{u'_i u'_j} \right) \quad (2.15)$$

with ν being the kinematic viscosity. These equations are almost identical to the mean equations obtained by the classical Reynolds, double, decomposition. The only difference lies in the additional term in the conservation of momentum which represents the feedback of the coherent motion on the mean flow. As it takes a similar form as the turbulent force from the Reynolds stress $-\overline{u'_i u'_j}$, this represents the turbulent force from the wave Reynolds stress $-\overline{\tilde{u}_i \tilde{u}_j}$.

The equations of the coherent flow are obtained by taking the difference between the phase- and time-averaged Navier-Stokes equations, after introduction of the triple decomposition. These are therefore

$$\frac{\partial \tilde{u}_i}{\partial x_i} = 0 \quad (2.16)$$

$$\frac{\partial \tilde{u}_i}{\partial t} + \bar{u}_j \frac{\partial \tilde{u}_i}{\partial x_j} + \tilde{u}_j \frac{\partial \bar{u}_i}{\partial x_j} = -\frac{1}{\rho} \frac{\partial \tilde{p}}{\partial x_i} + \nu \frac{\partial^2 \tilde{u}_i}{\partial x_j^2} - \frac{\partial}{\partial x_j} \left(\tilde{u}_i \tilde{u}_j - \overline{\tilde{u}_i \tilde{u}_j} + \overline{u'_i u'_j} \right) . \quad (2.17)$$

A particular attention will be given to the turbulent stresses $u'_i u'_j$, to which the triple decomposition can also be applied. The influence of the low-frequency oscillation on the turbulence is quantified through the coherent turbulent stress $\overline{u'_i u'_j}$, obtained from

$$\overline{u'_i u'_j} = \langle u'_i u'_j \rangle - \overline{u'_i u'_j} , \quad (2.18)$$

with $\langle u'_i u'_j \rangle$ the phase average and $\overline{u'_i u'_j}$ the usual Reynolds stress. The transport equations for these two components of turbulent stresses can be derived as well and, following Brereton and Reynolds, 1991, can be re-organized to highlight the contributions of production P_{ij} , pressure strain T_{ij} , dissipation D_{ij} and diffusion

flux $J_{ij,k}$ (combining the turbulent transport, pressure diffusion and viscous diffusion terms). For the mean turbulent stress, the transport equation is given by

$$\overline{u_k \frac{\partial u'_i u'_j}{\partial x_k}} + \overline{\widetilde{u_k \frac{\partial u'_i u'_j}{\partial x_k}}} = \overline{P}_{ij} + \overline{T}_{ij} - \overline{D}_{ij} - \overline{J}_{ij,k} , \quad (2.19)$$

with

$$\overline{P}_{ij} = - \left(\overline{u'_j u'_k \frac{\partial \overline{u}_i}{\partial x_k}} + \overline{u'_i u'_k \frac{\partial \overline{u}_j}{\partial x_k}} + \overline{\widetilde{u'_j u'_k \frac{\partial \overline{u}_i}{\partial x_k}}} + \overline{\widetilde{u'_i u'_k \frac{\partial \overline{u}_j}{\partial x_k}}} \right) \quad (2.20)$$

$$\overline{T}_{ij} = \frac{1}{\rho} \left(\overline{p' \frac{\partial u'_i}{\partial x_j}} + \overline{p' \frac{\partial u'_j}{\partial x_i}} \right) \quad (2.21)$$

$$\overline{D}_{ij} = 2\nu \overline{\frac{\partial u'_i}{\partial x_k} \frac{\partial u'_j}{\partial x_k}} \quad (2.22)$$

$$\overline{J}_{ij,k} = \overline{J}_{ij,k}^T + \overline{J}_{ij,k}^p + \overline{J}_{ij,k}^\nu , \quad (2.23)$$

and in which the three contributions to the diffusive flux include turbulent diffusion, pressure diffusion and viscous terms, given by, respectively,

$$\overline{J}_{ij,k}^T = \frac{\partial}{\partial x_k} \left(\overline{u'_i u'_j u'_k} \right) \quad (2.24a)$$

$$\overline{J}_{ij,k}^p = \frac{\partial}{\partial x_k} \left(\frac{1}{\rho} \overline{u'_j p' \delta_{ik}} + \frac{1}{\rho} \overline{u'_i p' \delta_{jk}} \right) \quad (2.24b)$$

$$\overline{J}_{ij,k}^\nu = - \frac{\partial}{\partial x_k} \left(\nu \overline{\frac{\partial u'_i u'_j}{\partial x_k}} \right) . \quad (2.24c)$$

As a consequence of the triple decomposition, additional contributions appear in the convection and production terms compared to the transport equations arising from the typical Reynolds decomposition.

For the coherent turbulent stress, the transport equation is written

$$\frac{\partial \widetilde{u'_i u'_j}}{\partial t} + \overline{u_k \frac{\partial \widetilde{u'_i u'_j}}{\partial x_k}} + \overline{\widetilde{u_k \frac{\partial u'_i u'_j}{\partial x_k}}} = \widetilde{P}_{ij} + \widetilde{T}_{ij} - \widetilde{D}_{ij} - \widetilde{J}_{ij,k} , \quad (2.25)$$

with

$$\begin{aligned} \widetilde{P}_{ij} = & - \left(\overline{\widetilde{u'_i u'_k \frac{\partial \widetilde{u}_j}{\partial x_k}}} - \overline{\widetilde{u'_i u'_k \frac{\partial \overline{u}_j}{\partial x_k}}} + \overline{u'_i u'_k \frac{\partial \widetilde{u}_j}{\partial x_k}} + \overline{\widetilde{u'_i u'_k \frac{\partial \overline{u}_j}{\partial x_k}}} \right) \\ & - \left(\overline{\widetilde{u'_j u'_k \frac{\partial \widetilde{u}_i}{\partial x_k}}} - \overline{\widetilde{u'_j u'_k \frac{\partial \overline{u}_i}{\partial x_k}}} + \overline{u'_j u'_k \frac{\partial \widetilde{u}_i}{\partial x_k}} + \overline{\widetilde{u'_j u'_k \frac{\partial \overline{u}_i}{\partial x_k}}} \right) \end{aligned} \quad (2.26)$$

$$\widetilde{T}_{ij} = \frac{1}{\rho} \left(\overline{\widetilde{p' \frac{\partial u'_i}{\partial x_j}}} + \overline{\widetilde{p' \frac{\partial u'_j}{\partial x_i}}} \right) \quad (2.27)$$

$$\widetilde{D}_{ij} = 2\nu \overline{\widetilde{\frac{\partial u'_i}{\partial x_k} \frac{\partial u'_j}{\partial x_k}}} \quad (2.28)$$

$$\widetilde{J}_{ij,k} = \widetilde{J}_{ij,k}^T + \widetilde{J}_{ij,k}^p + \widetilde{J}_{ij,k}^\nu \quad (2.29)$$

and turbulent diffusion, pressure diffusion and viscous diffusion are, respectively,

$$\tilde{J}_{ij,k}^T = \frac{\partial}{\partial x_k} \left(\widetilde{u'_i u'_j u'_k} \right) \quad (2.30a)$$

$$\tilde{J}_{ij,k}^p = \frac{\partial}{\partial x_k} \left(\frac{1}{\rho} \widetilde{u'_j p'} \delta_{ik} + \frac{1}{\rho} \widetilde{u'_i p'} \delta_{jk} \right) \quad (2.30b)$$

$$\tilde{J}_{ij,k}^\nu = -\frac{\partial}{\partial x_k} \left(\nu \frac{\partial \widetilde{u'_i u'_j}}{\partial x_k} \right) . \quad (2.30c)$$

All the terms are essentially the same as in the mean budgets, with the exception of the coherent production which contains twice more contributions compared to the mean production.

Chapter 3

High-Fidelity High-Order Solver

This chapter describes the numerical schemes implemented in the high-order solver employed to perform the high-fidelity simulations presented in the subsequent chapters. The spatial and temporal discretizations of the compressible Navier-Stokes equations are first discussed. Then, some stabilization techniques are introduced, namely the shock-capturing strategy and the positivity-preserving limiter. Finally, the treatment of the turbulent inflow is addressed.

3.1 Spatial discretization

The flux reconstruction (FR) approach, introduced in section 1.1.2, is adopted to evaluate the spatial derivatives of the compressible Navier-Stokes equations. A summary of the algorithm is presented here, first for a one-dimensional scalar conservation law, and then for its extension to multiple dimensions. The section ends with the application of the algorithm to the governing equations and with a discussion on the type of simulation that are targeted with the high-order solver.

3.1.1 Flux Reconstruction approach in one dimension

Consider the following one-dimensional scalar conservation law

$$\frac{\partial u}{\partial t} + \frac{\partial f}{\partial x} = 0 \quad (3.1)$$

where x is the spatial coordinate, t is the time, $u = u(x, t)$ is a conserved scalar quantity and f is the flux in the x direction. For this equation to be representative of the Navier-Stokes equations, f depends on both u and its gradient, that is to say $f = f(u, \partial u / \partial x)$.

The conservation law is solved on a computational domain denoted Ω , which is further partitioned into N non-overlapping, conforming elements. Each element is

defined by $\Omega_n = \{x | x_n < x < x_{n+1}\}$, from which it follows that

$$\Omega = \bigcup_{n=1}^N \Omega_n . \quad (3.2)$$

The exact solution u is then represented within each of these separate elements by a polynomial of degree p in x . This approximate solution is denoted by $u_n^\delta = u_n^\delta(x, t)$. In a similar manner, the exact flux is represented within each Ω_n by a function denoted $f_n^\delta = f_n^\delta(x, t)$, which is a polynomial of degree $p + 1$, to ensure consistency in equation 3.1 with respect to the representation of u . Outside Ω_n , both u_n^δ and f_n^δ are identically zero, in such a way that the total approximate solution $u^\delta = u^\delta(x, t)$ and flux $f^\delta = f^\delta(x, t)$ over the entire domain Ω are given by

$$u^\delta = \sum_{n=1}^N u_n^\delta \approx u, \quad f^\delta = \sum_{n=1}^N f_n^\delta \approx f . \quad (3.3)$$

A common description of each element being more convenient for the implementation, each Ω_n is further transformed into a standard element Ω_S defined on the interval $[-1, 1]$. The mapping function is defined as

$$x = \Theta_n(\xi) = \left(\frac{1 - \xi}{2}\right) x_n + \left(\frac{1 + \xi}{2}\right) x_{n+1} . \quad (3.4)$$

The corresponding transformed equation within the standard element Ω_S is therefore written as

$$\frac{\partial \hat{u}^\delta}{\partial t} + \frac{\partial \hat{f}^\delta}{\partial \xi} = 0 \quad (3.5)$$

with the approximate solution and approximate flux given by

$$\hat{u}^\delta = \hat{u}^\delta(\xi, t) = u_n^\delta(\Theta_n(\xi), t), \quad \hat{f}^\delta = \hat{f}^\delta(\xi, t) = \frac{1}{J_n} f_n^\delta(\Theta_n(\xi), t) \quad (3.6)$$

and are a polynomial of degree p and $p + 1$, respectively. $J_n = (x_{n+1} - x_n)/2$ is the Jacobian of the transformation.

The FR algorithm to solve equation 3.5 consists then of seven steps.

1. To allow for a polynomial representation of degree p for \hat{u}^δ , a set of $p + 1$ points ξ_i , called the *solution points*, is prescribed. Many different sets of points exist, and the one actually selected in the solver is given at the end of the subsection. The edges of the standard element are also marked by two *flux points*. A reference one-dimensional element with its associated solution points and flux points at polynomial order $p = 2$ is illustrated in figure 3.1.



Figure 3.1. One-dimensional standard element at polynomial order $p = 2$, with associated solution points (red \circ) and flux points (blue \square).

On this set of solution points, a polynomial representation of \hat{u}^δ is obtained through Lagrange interpolation, such that

$$\hat{u}^\delta(\xi, t) = \sum_{i=1}^{p+1} \hat{u}^\delta(\xi_i, t) l_i(\xi) \quad (3.7)$$

with $\hat{u}^\delta(\xi_i, t)$ being the evaluation of \hat{u}^δ at the i^{th} solution point and l_i the associated Lagrange basis polynomial. With this representation, the approximate solution at the flux points is given by extrapolation

$$\hat{u}_L^\delta = \hat{u}^\delta(-1, t), \quad \hat{u}_R^\delta = \hat{u}^\delta(1, t) . \quad (3.8)$$

2. Because the extrapolated values are generally different at the edge shared by two neighboring cells, the second step is the calculation of a common solution at the flux points (that is to say at $\xi = \pm 1$). These will be denoted $\hat{u}_L^{\delta I}$ and $\hat{u}_R^{\delta I}$ for the left and right element interface, respectively, and are computed by taking the average of the extrapolated values from the left and right elements.
3. The next step is to obtain an approximation of the solution gradient within the reference element, denoted \hat{q}^δ . For this purpose, a continuous solution polynomial across element interfaces is built through the application of correction functions. These will ensure that the approximate solutions on each element will take the common values at the flux points and therefore that the gradient will be well defined. Two correction functions $g_L(\xi)$ and $g_R(\xi)$ are considered, for the left and right boundaries, respectively. They are defined such that

$$g_L(-1) = 1, \quad g_L(1) = 0 \quad (3.9)$$

$$g_R(-1) = 0, \quad g_R(1) = 1 \quad (3.10)$$

and approximate the zero function within the element. They also satisfy a symmetry condition,

$$g_L(\xi) = g_R(-\xi) . \quad (3.11)$$

Consequently, a continuous solution polynomial across element interfaces is given by

$$\begin{aligned} \hat{u}_C^\delta(\xi, t) &= \hat{u}^\delta(\xi, t) + (\hat{u}_L^{\delta I} - \hat{u}_L^\delta) g_L(\xi) + (\hat{u}_R^{\delta I} - \hat{u}_R^\delta) g_R(\xi) \\ &= \sum_{i=1}^{p+1} \hat{u}^\delta(\xi_i, t) l_i(\xi) + (\hat{u}_L^{\delta I} - \hat{u}_L^\delta) g_L(\xi) + (\hat{u}_R^{\delta I} - \hat{u}_R^\delta) g_R(\xi) . \end{aligned} \quad (3.12)$$

Practically speaking, this continuous solution is actually not computed as such since the gradient is directly obtained with

$$\hat{q}^\delta(\xi, t) = \sum_{i=1}^{p+1} \hat{u}^\delta(\xi_i, t) \frac{dl_i(\xi)}{d\xi} + (\hat{u}_L^{\delta I} - \hat{u}_L^\delta) \frac{dg_L(\xi)}{d\xi} + (\hat{u}_R^{\delta I} - \hat{u}_R^\delta) \frac{dg_R(\xi)}{d\xi} . \quad (3.13)$$

It further allows to evaluate the gradient at the $p + 1$ solution points, and therefore to build a polynomial representation, following

$$\hat{q}^\delta(\xi, t) = \sum_{i=1}^{p+1} \hat{q}^\delta(\xi_i, t) l_i(\xi) . \quad (3.14)$$

4. Knowing the solution and the gradient at the solution points, the approximate flux is also evaluated at the solution points, since

$$\hat{f}^\delta(\xi_i, t) = \hat{f}^\delta(\hat{u}^\delta(\xi_i, t), \hat{q}^\delta(\xi_i, t)) . \quad (3.15)$$

Note that in equation 3.15, the solution is not the corrected one. The flux polynomial is then obtained by Lagrange interpolation,

$$\hat{f}^\delta(\xi, t) = \sum_{i=1}^{p+1} \hat{f}^\delta(\xi_i, t) l_i(\xi) \quad (3.16)$$

and is called the discontinuous flux polynomial as it is computed from quantities which are generally piecewise discontinuous across element interfaces.

5. The fifth step consists in the evaluation of the common fluxes $\hat{f}_L^{\delta I}$ and $\hat{f}_R^{\delta I}$ at, respectively, the left and right interfaces of the standard element Ω_s . It first requires to calculate the approximate flux at the flux points, namely \hat{f}_L^δ and \hat{f}_R^δ . To be able to apply boundary conditions on the gradients of the solution, these are obtained by using

$$\hat{f}_L^\delta = \hat{f}^\delta(\hat{u}_L^\delta, \hat{q}_L^\delta), \quad \hat{f}_R^\delta = \hat{f}^\delta(\hat{u}_R^\delta, \hat{q}_R^\delta) \quad (3.17)$$

instead of the Lagrange interpolation of equation 3.16, with \hat{u}_L^δ and \hat{u}_R^δ coming from step 1 (see equation 3.8) and equivalently, from equation 3.14,

$$\hat{q}_L^\delta = \hat{q}^\delta(-1, t), \quad \hat{q}_R^\delta = \hat{q}^\delta(1, t) . \quad (3.18)$$

6. To ensure a continuous flux polynomial across cell interfaces, two correction functions are employed, similarly to the procedure followed in step 3 to build the continuous solution polynomial. For the general case, they are denoted $h_L(\xi)$ and $h_R(\xi)$.
7. The last step of the algorithm is to compute the derivative of the continuous flux polynomial. It is given by

$$\frac{\partial \hat{f}_C^\delta}{\partial \xi}(\xi, t) = \sum_{i=1}^{p+1} \hat{f}^\delta(\xi_i, t) \frac{dl_i(\xi)}{d\xi} + (\hat{f}_L^{\delta I} - \hat{f}_L^\delta) \frac{dh_L(\xi)}{d\xi} + (\hat{f}_R^{\delta I} - \hat{f}_R^\delta) \frac{dh_R(\xi)}{d\xi} \quad (3.19)$$

and is finally evaluated at the solution points ξ_i in order to advance the solution in time,

$$\frac{d\hat{u}^\delta(\xi_i, t)}{dt} = -\frac{\partial \hat{f}_C^\delta}{\partial \xi}(\xi_i, t) . \quad (3.20)$$

The boundary conditions are directly enforced at the corresponding flux points of the boundary elements. Referring to the algorithm described above, it means that they replace the just extrapolated values \hat{u}_L^δ and \hat{q}_L^δ (or \hat{u}_R^δ and \hat{q}_R^δ , accordingly). For conditions involving the solution, the treatment is applied between step 1 and step 2. When gradients of the solution are concerned, the process takes place during step 5.

A particular FR scheme is defined by three characteristics, specifically the type of solution points, the type of correction functions and the way the common solutions and common fluxes are evaluated. In the present implementation, Gauss points are selected. They correspond to the zeros of the associated Legendre polynomials. The left and right correction functions are defined, respectively, by the right and left Radau polynomials so that a nodal Discontinuous Galerkin scheme is recovered (Huynh, 2007). Moreover, they are chosen to be identical whether they are to build the continuous solution or the continuous flux polynomials (that is to say, $g_L = h_L$ and $g_R = h_R$). Doing so ensures energy stability for linear advection-diffusion problems for all orders of accuracy on nonuniform grids (Castonguay et al., 2013). Finally, common advective fluxes are computed with Roe's approximate Riemann solver (Roe, 1981) and common viscous fluxes employ the Local Discontinuous Galerkin approach of Cockburn and Shu (1998) with $\beta = 0$ and $\tau = 1$ (Castonguay et al., 2013).

3.1.2 Extension to multiple dimensions

Now that the FR algorithm has been presented in the one-dimensional case, it is here extended to multiple dimensions. In particular, the two-dimensional case for quadrilateral elements is treated, from which the adaptation to hexahedral elements is straightforward. The other types of elements are not covered since only hexahedra will be used to generate the meshes in this work.

The two-dimensional scalar conservation law is given by

$$\frac{\partial u}{\partial t} + \nabla_{xy} \cdot \mathbf{f} = 0 \quad (3.21)$$

where $\mathbf{f} = (f, g)$ is the vector formed by the fluxes in the x and y directions, respectively, $f = f(u, \nabla u)$ and $g = g(u, \nabla u)$.

Each element of the computational domain is now transformed from the physical reference space (x, y) into the reference space (ξ, η) , with the standard element being defined on the biunit square $[-1, 1] \times [-1, 1]$. The transformed equation to solve on each standard element is then written

$$\frac{\partial \hat{u}^\delta}{\partial t} + \nabla_{\xi\eta} \cdot \hat{\mathbf{f}}^\delta = 0 \quad (3.22)$$

with

$$\hat{u}^\delta = \hat{u}^\delta(\xi, \eta, t) = u_n^\delta(\Theta_n(\xi, \eta), t) \quad (3.23)$$

$$\hat{\mathbf{f}}^\delta = \hat{\mathbf{f}}^\delta(\xi, \eta, t) = (\hat{f}^\delta, \hat{g}^\delta) \quad (3.24)$$

$$= \frac{1}{J_n} \left(\frac{\partial y}{\partial \eta} f_n^\delta - \frac{\partial x}{\partial \eta} g_n^\delta, -\frac{\partial y}{\partial \xi} f_n^\delta + \frac{\partial x}{\partial \xi} g_n^\delta \right). \quad (3.25)$$

The solution points within the reference quadrilateral element are obtained by tensor product of the one-dimensional solution points. There are therefore $(p+1)^2$ (and $(p+1)^3$ for hexahedra) solution points at polynomial order p . Flux points are generated accordingly on each edge, leading to a total of $4 \times (p+1)$ flux points. Similarly, a set of $(p+1)^2$ flux points are obtained on each face of a hexahedral element. An illustration is provided in figure 3.2 for a standard quadrilateral element at polynomial order 2.

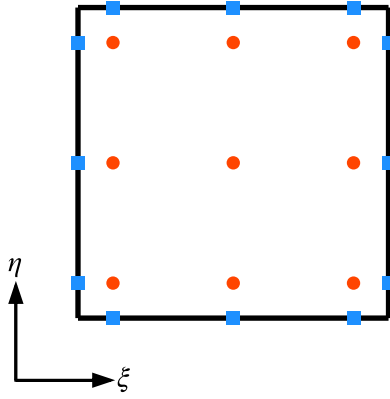


Figure 3.2. Two-dimensional standard element at polynomial order $p = 2$, with associated solution points (red \circ) and flux points (blue \square).

The approximate solution on each standard element is derived from tensor product, using the one-dimensional Lagrange basis polynomials, such that

$$\hat{u}^\delta(\xi, \eta, t) = \sum_{i,j=1}^{p+1} \hat{u}^\delta(\xi_i, \eta_j, t) l_i(\xi) l_j(\eta) \quad (3.26)$$

and based on this representation, the components of the corrected gradient $\hat{\mathbf{q}}^\delta = (\hat{q}_\xi^\delta, \hat{q}_\eta^\delta)$ are computed independently with one-dimensional correction functions,

$$\hat{q}_\xi^\delta(\xi, \eta, t) = \frac{\partial \hat{u}^\delta}{\partial \xi}(\xi, \eta, t) + (\hat{u}_L^{\delta I} - \hat{u}_L^\delta) \frac{dg_L(\xi)}{d\xi} + (\hat{u}_R^{\delta I} - \hat{u}_R^\delta) \frac{dg_R(\xi)}{d\xi} \quad (3.27)$$

$$\hat{q}_\eta^\delta(\xi, \eta, t) = \frac{\partial \hat{u}^\delta}{\partial \eta}(\xi, \eta, t) + (\hat{u}_B^{\delta I} - \hat{u}_B^\delta) \frac{dg_B(\eta)}{d\eta} + (\hat{u}_T^{\delta I} - \hat{u}_T^\delta) \frac{dg_T(\eta)}{d\eta} \quad (3.28)$$

where the indices B and T refer to the bottom and top edges, respectively. The corresponding correction functions are simply $g_B(\eta) = g_L(\xi = \eta)$ and $g_T(\eta) = g_R(\xi = \eta)$. Using tensor product, the solution gradient within the cell is obtained by

$$\hat{\mathbf{q}}^\delta(\xi, \eta, t) = \sum_{i,j=1}^{p+1} \hat{\mathbf{q}}^\delta(\xi_i, \eta_j, t) l_i(\xi) l_j(\eta) \quad (3.29)$$

and is used to evaluate the flux and then construct the discontinuous flux polynomial,

$$\hat{\mathbf{f}}^\delta(\xi, \eta, t) = \sum_{i,j=1}^{p+1} \hat{\mathbf{f}}^\delta(\xi_i, \eta_j, t) l_i(\xi) l_j(\eta). \quad (3.30)$$

Finally, following the same correction procedure, the flux is made continuous across cell interfaces and its divergence is given by

$$\nabla_{\xi, \eta} \cdot \hat{\mathbf{f}}_C^\delta(\xi, \eta, t) = \frac{\partial \hat{f}_C^\delta}{\partial \xi} + \frac{\partial \hat{g}_C^\delta}{\partial \eta} \quad (3.31)$$

$$\begin{aligned} &= \frac{\partial \hat{f}^\delta}{\partial \xi} + (\hat{f}_L^{\delta I} - \hat{f}_L^\delta) \frac{dh_L(\xi)}{d\xi} + (\hat{f}_R^{\delta I} - \hat{f}_R^\delta) \frac{dh_R(\xi)}{d\xi} \\ &+ \frac{\partial \hat{g}^\delta}{\partial \eta} + (\hat{g}_B^{\delta I} - \hat{g}_B^\delta) \frac{dh_B(\eta)}{d\eta} + (\hat{g}_T^{\delta I} - \hat{g}_T^\delta) \frac{dh_T(\eta)}{d\eta} \end{aligned} \quad (3.32)$$

which is ultimately evaluated at the solution points to update the solution following

$$\frac{d\hat{u}^\delta(\xi_i, \eta_j, t)}{dt} = -\nabla_{\xi, \eta} \cdot \hat{\mathbf{f}}_C^\delta(\xi_i, \eta_j, t). \quad (3.33)$$

3.1.3 Application to the Navier-Stokes equations

The FR approach is directly applicable to the three-dimensional compressible Navier-Stokes equations described in section 2.1. They can indeed be formulated as

$$\frac{\partial \mathbf{W}}{\partial t} + \nabla \cdot \mathbf{F}(\mathbf{W}, \nabla \mathbf{W}) = 0 \quad (3.34)$$

where $\mathbf{W} = (\rho, \rho u, \rho v, \rho w, \rho E)$, with $E = e + u_i u_i / 2$, is the vector of conservative variables and $\mathbf{F} = (F, G, H)$ is the flux vector. The latter is usually decomposed into its advective (or inviscid) and viscous components, such that $(F, G, H) = (F_I - F_V, G_I - G_V, H_I - H_V)$, with,

$$F_I = \begin{pmatrix} \rho u \\ \rho u^2 + p \\ \rho uv \\ \rho uw \\ \rho E u + p u \end{pmatrix}, G_I = \begin{pmatrix} \rho v \\ \rho uv \\ \rho v^2 + p \\ \rho vw \\ \rho E v + p v \end{pmatrix}, H_I = \begin{pmatrix} \rho w \\ \rho vw \\ \rho vw \\ \rho w^2 + p \\ \rho E w + p w \end{pmatrix} \quad (3.35)$$

$$F_V = \begin{pmatrix} 0 \\ \sigma_{xx} \\ \sigma_{xy} \\ \sigma_{xz} \\ u_i \sigma_{ix} - q_x \end{pmatrix}, G_V = \begin{pmatrix} 0 \\ \sigma_{xy} \\ \sigma_{yy} \\ \sigma_{yz} \\ u_i \sigma_{iy} - q_y \end{pmatrix}, H_V = \begin{pmatrix} 0 \\ \sigma_{xz} \\ \sigma_{yz} \\ \sigma_{zz} \\ u_i \sigma_{iz} - q_z \end{pmatrix}. \quad (3.36)$$

In turbulent flows, the smallest scales are responsible for the dissipation of turbulence kinetic energy. Failing to capture this process results in an undesired accumulation of energy at the highest wave numbers that the grid allows to resolve.

By performing a Direct Numerical Simulation (DNS), the equations are solved as presented here above and the mesh is fine enough to resolve all the scales of the flow. Dissipation is then accurately reproduced but at the expense of the computing cost, rising because of the strict grid resolution needed. An alternative is to perform a Large-Eddy Simulation (LES), in which only the large scales are resolved, and the small scale dissipation is accounted for through a subgrid scale (SGS) model, giving an additional term in the viscous flux. A coarser mesh is therefore employed, reducing the cost of the simulation.

The approach adopted for the present simulations lies in between these two methods. The mesh is not fine enough to capture the smallest scales but is finer than for a LES, while no SGS model is employed. For these reasons, the approach is referred to as under-resolved DNS or Implicit LES (ILES). The small scale dissipation is implicitly taken care of by the numerical scheme, instead of using an explicit SGS model. Such an approach is justified if the scheme is able to provide the dissipation necessary to avoid the build-up of turbulence kinetic energy, which is deemed to be the case for FR schemes. Vincent et al. (2011b) indeed showed, using Von Neumann analysis, that FR schemes are effectively dissipative at high wave numbers, regardless of the order of accuracy. Vermeire et al. (2016) further demonstrated that this dissipation was sufficient by performing ILES on a various set of cases, ranging from the Taylor-Green vortex to a turbulent channel flow and a transitional and turbulent flow over an airfoil. Finally, using other spatial discretization techniques, ILES were also found to be suitable for shock wave/boundary layer interactions at low or moderate Reynolds numbers (Larsson et al., 2022; Morgan et al., 2013; Vyas et al., 2019a). In practice, ILES offer a reduced computing cost with respect to DNS and avoid the use of a SGS model, and its inherent assumptions.

3.2 Temporal discretization

The temporal derivative of the Navier-Stokes equations is computed by using a five stages fourth-order accurate explicit low-storage Runge-Kutta scheme from Carpenter and Kennedy (1994). The algorithm is given by

$$d\mathbf{W}_n = A_n d\mathbf{W}_{n-1} + \Delta t \mathbf{R}(\mathbf{W}_{n-1}) \quad (3.37)$$

$$\mathbf{W}_n = \mathbf{W}_{n-1} + B_n d\mathbf{W}_n \quad (3.38)$$

where n is the stage index, $\mathbf{R}(\cdot) = -\nabla \cdot \mathbf{F}(\cdot)$ is the residual and Δt is the time step. The coefficients of the method A_n and B_n are given in table 3.1 and yield an optimal stability envelope. This justifies the additional stage, while fourth-order accuracy can be reached with four stages only. The computing cost of the fifth stage is compensated by the increased time step the method allows.

3.3 Shock-capturing technique

The improved accuracy promised by the use of high-order methods is counterbalanced by their lack of robustness with respect to lower-order schemes, which has been

$$\begin{aligned}
A_1 &= 0 & B_1 &= \frac{1432997174477}{9575080441755} \\
A_2 &= -\frac{567301805773}{1357537059087} & B_2 &= \frac{5161836677717}{13612068292357} \\
A_3 &= -\frac{2404267990393}{2016746695238} & B_3 &= \frac{1720146321549}{2090206949498} \\
A_4 &= -\frac{3550918686646}{2091501179385} & B_4 &= \frac{3134564353537}{4481467310338} \\
A_5 &= -\frac{1275806237668}{842570457699} & B_5 &= \frac{2277821191437}{14882151754819}
\end{aligned}$$

Table 3.1. Coefficients for the Runge-Kutta scheme.

preventing them to be widely adopted in the industry. A typical issue is related to the handling of shock waves. The step discontinuity imposed by shock waves is indeed badly represented by polynomials employed in high-order methods. This is known as the Gibbs phenomenon, ultimately resulting in spurious oscillations around the shock. If not treated properly, these oscillations pollute the solution, destroy accuracy and make the simulation unstable. To investigate shock wave/boundary layer interactions, care must therefore be given to the shock-capturing technique.

Various ways to stabilize numerical methods in the presence of shocks were investigated in the literature. The first idea is to limit the solution to meet properties such as Total Variation Diminishing or Total Variation Bounded. A popular scheme was proposed for instance by Cockburn and Shu (1989) in a high-order Discontinuous Galerkin framework for structured grids. While being very efficient, the accuracy can, however, be drastically reduced in smooth regions near local extrema. These methods are also difficult to extend to unstructured grids.

Closely related are the reconstruction procedures called Essentially Non Oscillatory (ENO) schemes, and their weighted (WENO) and targeted (TENO) extensions. The general concept is to replace the solution (or the solution polynomial) using the information from smooth neighbouring cells. In ENO schemes (Harten et al., 1987), the stencil giving the best smoothness among a set of candidates is solely considered for the reconstruction. To increase the order of accuracy, WENO schemes were introduced by X.-D. Liu et al. (1994). They provide a reconstruction of the solution from a combination of all the candidate stencils, weighted by their local smoothness. They were, however, found to be excessively dissipative in smooth regions of the flow and therefore not suitable for high-fidelity simulations. To tackle this issue, many improvements were proposed, among them are the TENO schemes (see the review of Fu (2023)). An adaptation of a WENO scheme for the FR approach was proposed by Du et al. (2015).

An alternative stabilization technique employs filtering. Taking advantage of the modal decomposition of the solution within each cell, the application of a low-pass filter, cutting the highest modes of the decomposition, allows to remove the spurious oscillations. The treatment can also be made locally, for example by considering criteria based on kinetic energy (Flad et al., 2016) or concentration property (Sheshadri, 2016).

Yet another strategy, the one exploited here, is based on the concept of artificial viscosity, described first by VonNeumann and Richtmyer (1950). It relies on the fact that shocks are smeared out in the presence of dissipative mechanisms. By artificially

increasing viscous effects, the sharp and discontinuous evolution of flow variables across shocks becomes smoother. Eventually, it will be possible to fit a polynomial representation of the solution and therefore to remove the spurious oscillations from the Gibbs phenomenon.

Two approaches were proposed depending on the way the extra viscous effects are considered. In physics-based approaches, the physical viscosity is directly supplemented by the artificial viscosity. The procedure can also be extended to account for an artificial thermal conductivity. Examples of this approach can be found in Fernandez et al. (2018) and references therein. The second approach is called Laplacian artificial viscosity. The idea is to add a dissipative term to the governing equations that takes the form of a Laplacian. Formally, the new system of equations is written

$$\frac{\partial \mathbf{W}}{\partial t} + \nabla \cdot \mathbf{F}(\mathbf{W}, \nabla \mathbf{W}) = \nabla \cdot (\varepsilon \nabla \mathbf{W}) \quad (3.39)$$

with ε the artificial viscosity.

The method employed in the solver is a combination of the Laplacian artificial viscosity method of Persson and Peraire (2006) with the sensor of Ducros (Ducros et al., 1999). For the sake of completeness, the original method is first recalled and the usefulness of the Ducros sensor is then explained.

3.3.1 Basic artificial viscosity method

Most of artificial viscosity methods consist of two steps. The first step is to detect the troubled cells, in which there might be a discontinuity. It allows a local treatment, since artificial viscosity is unnecessary and actually harmful in smooth regions of the flow. Various shock sensors were proposed in the literature to detect shocks. In the method of Persson and Peraire (2006), the sensor is a modal resolution-based indicator. It uses the modal decomposition of the solution to assess if a discontinuity exists in the considered cell. The sensor is defined as follows. First, consider the expansion in a modal basis of the solution of order p within a cell,

$$q = \sum_{i=1}^{N(p)} q_i \psi_i \quad (3.40)$$

with $N(p)$ the total number of terms in the expansion of order p , q_i the coefficients of the expansion and ψ_i the basis functions. The quantity q can be any flow quantity, the most often used being density or entropy. For smooth solutions, the coefficients q_i are expected to decrease quickly whereas for non-smooth solutions the decay rate of the coefficients will be affected by the discontinuity.

Taking a truncated expansion \hat{q} of the same solution, up to order $p - 1$, the smoothness indicator is defined as

$$s_e = \log_{10} \left(\frac{(q - \hat{q}, q - \hat{q})_e}{(q, q)_e} \right) \quad (3.41)$$

in which $(\cdot, \cdot)_e$ refers to the standard inner product in the cell. The sensor is therefore an image of the ratio between the energy content of the highest order mode and the energy content of all the modes together. The Gibbs phenomenon generating higher order modes, a high sensor value indicates the presence of a discontinuity.

Secondly, the value of the artificial viscosity is computed, taking into account the value of the shock sensor, with a smooth activation function

$$\varepsilon_e = \begin{cases} 0 & \text{if } s_e < s_0 - \kappa \\ \frac{\varepsilon_0}{2} \left(1 + \sin \frac{\pi(s_e - s_0)}{2\kappa} \right) & \text{if } s_0 - \kappa < s_e < s_0 + \kappa \\ \varepsilon_0 & \text{if } s_e > s_0 + \kappa \end{cases} \quad (3.42)$$

illustrated in figure 3.3 (left). The maximum ε_0 is given by

$$\varepsilon_0 = C_T \frac{\hat{h}}{p} \lambda_{max} \quad (3.43)$$

in which \hat{h} is the reference grid spacing of the cell and λ_{max} is the maximum eigenvalue among all the solution points of the considered cell. Practically speaking, \hat{h} is computed as twice the maximum distance between the cell center and the cell face centers whereas $\lambda_{max} = \sqrt{\mathbf{u}^2} + c$ with \mathbf{u} the velocity vector and c the speed of sound.

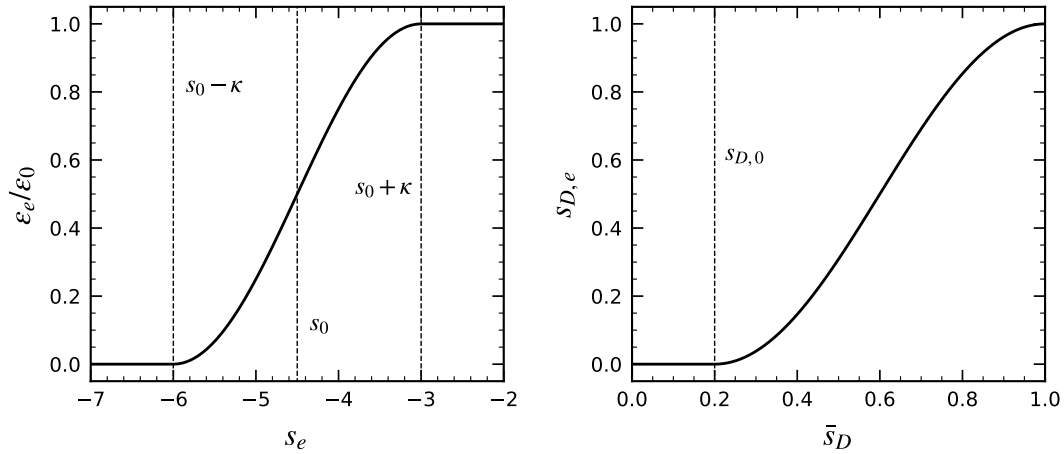


Figure 3.3. Activation function for the artificial viscosity, with $s_0 = -4.5$ and $\kappa = 1.5$ (left) and activation for the Ducros sensor, with $s_{D,0} = 0.2$ (right).

Three parameters have been introduced so far, namely s_0 , κ and C_T . While s_0 and κ define the range of shock sensor values for which artificial viscosity will be triggered, C_T directly scales the value of artificial viscosity. These parameters are user-defined and case dependent. They are usually adapted empirically or automatically based on manufactured solutions (Tonicello et al., 2020).

3.3.2 Combination with Ducros sensor

An issue with the shock sensor s_e defined above is its inability to distinguish shocks from turbulence. Early tests showed indeed that artificial viscosity was also triggered in the unsteady viscous regions of the flow, such as boundary layers. As mentioned by Mani et al. (2009), there are conflicting requirements between capturing shocks and resolving turbulence. While artificial viscosity is needed to smear out the shock profile, it can also totally damp turbulent fluctuations. As a result, the boundary layer would not develop realistically and the shock wave/boundary layer interaction would not be predicted correctly by the solver.

To further differentiate shocks from boundary layers, the artificial viscosity method is combined with the Ducros sensor (Ducros et al., 1999). It is defined as

$$s_D = \frac{(\nabla \cdot \mathbf{u})^2}{(\nabla \cdot \mathbf{u})^2 + (\nabla \wedge \mathbf{u})^2 + \epsilon} \quad (3.44)$$

with $\nabla \cdot \mathbf{u}$ the velocity divergence and $\nabla \wedge \mathbf{u}$ the vorticity. ϵ is a small positive constant to avoid division by zero in regions where both velocity divergence and vorticity are close to zero. By definition, the Ducros sensor is able to identify regions of high vorticity (such as boundary layers and wakes for example), taking values near zero, and shock regions, in which it approaches unity.

The combination is performed through the direct multiplication of the artificial viscosity field,

$$\varepsilon = \varepsilon_e s_{D,e} \quad (3.45)$$

where $s_{D,e}$ is the output of an activation function given by

$$s_{D,e} = \begin{cases} 0 & \text{if } \bar{s}_D < s_{D,0} \\ \frac{1}{2} \left(1 + \sin \left(\pi \left(\frac{\bar{s}_D - s_{D,0}}{1 - s_{D,0}} - \frac{1}{2} \right) \right) \right) & \text{if } s_{D,0} < \bar{s}_D < 1 \\ 1 & \text{if } \bar{s}_D > 1 \end{cases} \quad (3.46)$$

and depicted in figure 3.3 (*right*). To comply with the cell-wise constant artificial viscosity field ε_e , \bar{s}_D is the cell-averaged Ducros sensor. $s_{D,0}$ is a suitable threshold value under which the artificial viscosity is explicitly set to zero. This fourth parameter can also be user-defined even though, in practice, a value of 0.2 has been found to work in any case. By doing so, the shock-capturing technique will let the boundary layer untouched by the artificial viscosity.

The original method of Persson and Peraire (2006) combined with the Ducros sensor provides with a cell-wise constant artificial viscosity field. Several authors showed the shortcomings of such an approach. It was found by Barter and Darmofal (2010) to lead to spurious oscillations in the state gradients that can convect downstream and pollute the solution. Moreover, Glaubitz et al. (2019) demonstrated that even the principle of conservation is not fulfilled for a cell-wise constant artificial viscosity field. This is why a smoothing operation is necessary. Although both suggested very different strategies to obtain a smooth artificial viscosity, the method implemented here is inspired from Persson (2013) and follows these steps:

1. For each mesh vertex, find the maximum value of artificial viscosity among all direct neighbouring cells.
2. For each cell, interpolate back from the vertices to the solution points using the three-dimensional first order shape functions.

The result is a C^0 -continuous artificial viscosity field. As explained in Persson (2013) and Klöckner et al. (2011), there is no advantage in ensuring a higher degree of continuity. Nevertheless, a weak point of such a smoothing method is that the localization of the artificial viscosity is destroyed (Glaubitz et al., 2019). Shocks are now spread over several cells whereas sub-cell resolution was the initial goal (Persson & Peraire, 2006).

Finally, in the FR algorithm, the Laplacian term added to the governing equations is treated as any other flux. The artificial viscosity in itself is computed between steps 3 and 4 (see section 3.1.1).

3.4 Positivity-preserving limiter

For additional robustness, the solver is supplemented by a positivity-preserving limiter. Its aim is to ensure that, as the simulation evolves in time, both density and pressure remain positive, as they should be physically speaking. Getting unphysical solutions might indeed appear independently of the presence of shock waves, for example in regions of low pressure or density.

The limiter is based on the work of Zhang and Shu (2010). Developed for Runge-Kutta Discontinuous Galerkin methods and valid for arbitrary orders, its use in the context of the present Runge-Kutta Flux Reconstruction approach is therefore straightforward. It also complies with conservation and maintains the accuracy.

The implementation is the following. For each cell (indexed K),

1. Find the minimum density $\rho_{K,min}$ among all the solution points and all the flux points.
2. Compute

$$\theta_{K,1} = \min \left\{ 1, \frac{\bar{\rho}_K - \epsilon}{\bar{\rho}_K - \rho_{K,min}} \right\} \quad (3.47)$$

where $\bar{\rho}_K$ is the cell-averaged density and ϵ a small number, typically $\epsilon = 10^{-13}$.

3. Limit the density at all solution points and flux points, by applying

$$\dot{\rho} = \theta_{K,1}(\rho - \bar{\rho}_K) + \bar{\rho}_K \quad (3.48)$$

which has no effect if $\rho_{K,min} > \epsilon$ since in that case $\theta_{K,1} = 1$.

4. Evaluate the pressure based on the conservative solution with limited density $\dot{\rho}$ at all the solution points and flux points.

5. For all the solution points and all the flux points, if $p \geq 0$, define $\theta_2 = 1$, otherwise, set

$$\theta_2 = \frac{\bar{p}_K}{\bar{p}_K - p} \quad (3.49)$$

with \bar{p}_K is the pressure computed using the cell-averaged conservative solution. In the original implementation (Zhang & Shu, 2010), finding θ_2 implies the resolution of a quadratic equation in each point. Because of round-off errors, the numerical solution obtained does not necessarily ensure the strict positivity of pressure and therefore, equation 3.49 is preferred here as it improves the robustness of the limiter (C. Wang et al., 2012).

6. Find $\theta_{K,2} = \min \theta_2$ over all the solution points and flux points.
7. Finally, limit the conservative solution with

$$\dot{\mathbf{W}} = \theta_{K,2}(\mathbf{W} - \overline{\mathbf{W}}_K) + \overline{\mathbf{W}}_K \quad (3.50)$$

at all solution points and flux points.

In the FR algorithm, the limiter is applied after step 1 (see section 3.1.1) and before the application of the boundary conditions. It is used at each stage of the Runge-Kutta method, as recommended in Zhang and Shu (2010).

3.5 Turbulent inflow generator

With the use of LES or DNS comes the problem of imposing realistic inflow conditions, especially when dealing with turbulent flows. The literature related to inflow turbulence generation is vast and the interested reader is invited to refer to Wu (2017) and Dhamankar et al. (2018) for reviews on the topic. A short description of the main methods is nevertheless provided in this section, followed by a more detailed view of the chosen approach.

The two major categories of methods are the precursor methods and the synthetic turbulence methods. In the precursor methods, an auxiliary simulation is run, preferably in the same flow conditions, and is used to extract the information for the inlet of the actual simulation. The auxiliary simulation consists typically of a flow periodic in the streamwise direction, so that the inlet boundary condition is not a problem. It was extended to what is called recycling/rescaling methods, in which the outflow of the auxiliary simulation is fed to the inlet after a rescaling to account for a non-homogeneity in the streamwise direction. The benefit in using precursor methods comes from the high degree of fidelity of the field provided at the inflow. Also, it is easier to reproduce target quantities, such as the friction coefficient for example. On the drawbacks side, these methods are more complex to put in place and more costly as they basically require to run an additional simulation. More importantly, they are suffering from the introduction of a spurious low-frequency component in the flowfield because of the recycling process, which is harmful for the study of shock wave/boundary layer interactions (known to exhibit a low-frequency

behavior). This can also be detrimental for the study of forced flow. For this reason in particular, this family of method will not be used in this work.

In synthetic turbulence methods, the basic idea is to add artificial velocity perturbations to the prescribed mean velocity profiles. These artificial perturbations are meant to mimic real turbulence and, as a consequence, the flow needs a certain distance from the inlet to recover from this unrealistic treatment. This adaptation length is dependent on the fidelity of the perturbations and therefore the level of approximation employed. A longer domain is needed and leads to an increase of computing cost. Nevertheless, synthetic turbulence generation techniques are known for their ease of implementation, their efficiency and flexibility, which makes them greatly suitable for industrial applications of high-fidelity simulations.

The most straightforward way to proceed is to consider random fluctuations, or white noise. However, the energy of white noise is equally distributed over the entire wave number range, therefore not complying with the energy cascade of turbulence (Pope, 2000). The usual consequence is an undesired re-laminarization of the flow shortly downstream of the inlet because of the lack of energy in the low wave numbers corresponding to the energy-carrying turbulent eddies. This issue can be circumvented by providing some coherence to the random fluctuations in order to recover some known statistics of the flow. Various methods exist again (see in particular the review of Dhamankar et al. (2018) for more details), depending on the way this coherence is imposed and, among all of them, the digital filtering (DF) technique, originally designed by Klein et al. (2003), has been selected. In the context of shock wave/boundary layer interactions, many works employed the digital filtering technique successfully, supporting this choice. One can for example cite Toubert (2010), Vyas et al. (2019a), Larsson et al. (2022) and Bernardini et al. (2023).

The aim of the digital filtering technique is to add spatial and temporal coherence to the random fluctuations through the application of filters, in such a way that the turbulence length scales are recovered. To better illustrate, consider the one-dimensional example of a line consisting of N equally-spaced grid points. To each grid point is assigned a random value r selected from a set of uncorrelated and normally distributed random numbers r_m with a zero mean ($\overline{r_m} = 0$) and a unit variance ($\overline{r_m r_m} = 1$). The filtered value \hat{r}_k , at the position index k , is written as

$$\hat{r}_k = \sum_{l=-W}^W b_l r_{k+l} \quad (3.51)$$

with b_l the filter coefficients and W the filter stencil half-width. It can be shown that the auto-correlation function of the filtered value is given by

$$\frac{\overline{\hat{r}_k \hat{r}_{k+j}}}{\overline{\hat{r}_k \hat{r}_k}} = \sum_{l=-W+j}^W b_l b_{l-j} / \sum_{l=-W}^W b_l^2 \quad (3.52)$$

and provides a relation with the filter coefficients. By matching the auto-correlation of equation 3.52 with the auto-correlation typically obtained in turbulent flows, the

coefficients of the filter can therefore be computed. Originally, Klein et al. (2003) assumed a Gaussian function,

$$R_{uu}(d) = \exp\left(-\frac{\pi d^2}{4I^2}\right) \quad (3.53)$$

where I is the desired turbulence length scale. In discretized form, considering $I = n\Delta x$ and $d = k\Delta x$, this gives

$$R_{uu}(k\Delta x) = \exp\left(-\frac{\pi k^2}{4n^2}\right) \quad (3.54)$$

and therefore the filter coefficients are obtained by solving

$$\sum_{l=-W+j}^W b_l b_{l-j} / \sum_{l=-W}^W b_l^2 = \exp\left(-\frac{\pi k^2}{4n^2}\right). \quad (3.55)$$

An approximated solution is given by

$$b_j \approx \tilde{b}_j / \left(\sum_{l=-W}^W \tilde{b}_l^2\right)^{1/2}, \quad \tilde{b}_l = \exp\left(-\frac{\pi l^2}{2n^2}\right) \quad (3.56)$$

and by this methodology, a one-dimensional inlet field with zero mean, unit variance and a prescribed length scale has been generated.

From this one-dimensional example, some notable changes are needed for real applications. First, turbulence is inherently three-dimensional and, as a consequence, the inlet data should be filtered in the three dimensions. A straightforward but computationally expensive extension, based on the convolution of three one-dimensional filters, was proposed by Klein et al. (2003). Despite a further improvement suggested by Kempf et al. (2012), this method remains costly. The issue was addressed by Xie and Castro (2008) in which a two-dimensional filter is put in place by convolution and is correlated in time using an exponential function. Avoiding the third dimension filtering operation resulted in a drastic reduction of computing time.

Moreover, the DF technique in the way it has been initially developed is suitable mainly for finite difference discretizations using uniformly spaced Cartesian structured grids. An extension to unstructured non-uniform grids, applied to the high-order FR method, was presented in Duan and Wang (2022). A separate digital filter grid is employed to compute the fluctuations which are then interpolated back on the flux points of the actual computational grid. This two-step procedure is, however, laborious and the approach of Adler et al. (2018) is preferred here. The convolution of one-dimensional filters is replaced by an inherently two-dimensional filter which makes it valid for unstructured and non-uniform meshes.

Practically, the DF algorithm is the following. As pre-processing steps,

1. For each flux point in the inlet plane (consider the yz plane), get the associated turbulence length scales I_y and I_z and look for all the flux points, called the neighbors, within an ellipse of semi-axes I_y and I_z .

2. Evaluate and store the filter coefficients for each neighbor of each flux point. A two-dimensional, elliptical filter with an exponential correlation function is defined, in a similar way as in Adler et al. (2018). For a neighbor located at (y, z) of the flux point located at (y_0, z_0) , the coefficient is given by

$$b(y, z; y_0, z_0) = \frac{\exp \left[-\pi \sqrt{\left(\frac{y - y_0}{I_y(y_0, z_0)} \right)^2 + \left(\frac{z - z_0}{I_z(y_0, z_0)} \right)^2} \right]}{\left(\sum \exp \left[-2\pi \sqrt{\left(\frac{y - y_0}{I_y(y_0, z_0)} \right)^2 + \left(\frac{z - z_0}{I_z(y_0, z_0)} \right)^2} \right] \right)^{1/2}} \quad (3.57)$$

where the sum applies on all the neighbors.

Then, during the simulation, at each update of the boundary conditions,

1. A set of independent, normally distributed random numbers with zero mean and unit variance is generated for each velocity component and each flux point is associated to one number of the set. The Box-Muller theorem (Box & Muller, 1958) is used for this purpose. From two independent sets of random numbers a and b following a uniform distribution between 0 and 1 (a distribution typically acquired when using pseudo-random number generators), two sets c and d , independent and normally distributed, also with zero mean and unit variance, are obtained by

$$c = \cos(2\pi b) \sqrt{-2 \ln a}, \quad d = \sin(2\pi b) \sqrt{-2 \ln a}. \quad (3.58)$$

Either one is actually used for the flux points.

2. The turbulence length scales I_y and I_z are imposed by applying the two-dimensional filter, the coefficients of which were obtained in the pre-processing (see equation 3.57).
3. Following Xie and Castro (2008), the two-dimensional slice is correlated in time to the previous time step in order to impose the streamwise turbulence length scale. An exponential correlation function of the form

$$v_k^t = \hat{r}_k^{t-\Delta t} \exp\left(-\frac{\pi \Delta t}{2t_L}\right) + \hat{r}_k^t \sqrt{1 - \exp\left(-\frac{\pi \Delta t}{t_L}\right)} \quad (3.59)$$

is employed, where t_L is the Lagrangian time scale, or $t_L = I_x/U$ with U the prescribed inlet mean streamwise velocity.

4. The perturbations are then scaled according to the transformation of Lund et al. (1998) to recover a prescribed distribution of Reynolds stress tensor and superimposed to the mean prescribed velocity profiles.

$$u_i = \bar{u}_i + u' = \bar{u}_i + L_{ij} v^t \quad (3.60)$$

with

$$L_{ij} = \begin{bmatrix} \sqrt{\overline{u'u'}} & 0 & 0 \\ \frac{u'v'}{L_{11}} & \sqrt{v'v'} - L_{21}^2 & 0 \\ \frac{u'w'}{L_{11}} & (v'w' - L_{21}L_{31})/L_{22} & \sqrt{w'w'} - L_{31}^2 - L_{32}^2 \end{bmatrix}. \quad (3.61)$$

Note that in turbulent boundary layers, the matrix is simpler since $\overline{u'w'} = \overline{v'w'} = 0$.

5. If compressibility effects have to be accounted for, the methodology of Touber (2010) is considered. Invoking the Strong Reynolds Analogy (Gaviglio, 1987), temperature fluctuations are computed using

$$\frac{T'}{\overline{T}} = -(\gamma - 1)M^2 \frac{u'}{\overline{u}}, \quad M^2 = \frac{\overline{u}^2}{\gamma R \overline{T}} \quad (3.62)$$

and, assuming negligible pressure fluctuations in the boundary layer, density fluctuations follow with

$$\frac{\rho'}{\overline{\rho}} = -\frac{T'}{\overline{T}}. \quad (3.63)$$

To complete the presentation of the digital filter technique, two comments are addressed to clarify some choices made in the algorithm. Firstly, an exponential correlation function is used to define the filter, instead of a Gaussian function as initially suggested by Klein et al. (2003). Xie and Castro (2008) indeed recommended the former as it is more appropriate for turbulent shear flows. Kim et al. (2013) further modified it to better match turbulent channel flows.

Secondly, as precised by Touber (2010), the validity of the SRA is arguable. Adler et al. (2018) makes use of an extended SRA, the assumptions of which are also dubious. In any case, providing an approximation of temperature fluctuations is better than considering them to be negligible, and both approaches showed successful applications.

Chapter 4

Oblique Shock Wave/Boundary Layer Interaction

In this chapter, the results of an implicit Large-Eddy Simulation (ILES) of a canonical oblique shock wave/boundary layer interaction (SWBLI) are presented. Such flow configurations are challenging on the numerical point of view since it requires to handle multiple, unsteady shocks but also to resolve turbulence appropriately. It constitutes therefore a good validation case to assess the numerical methodology employed to develop the high-fidelity high-order solver introduced in chapter 3. Besides this main objective, the case is also an opportunity to introduce the triple decomposition adopted for the analysis of coherent flows and to test the conditional averaging technique.

The chapter begins with an introduction of the configuration and a literature review of experimental and numerical works. The flow conditions and the computational setup are then described. The results section is divided into three sub-parts. A validation of the flow is first undertaken to assess if the basic features of the flow can be reproduced. Afterwards, the performance of the shock-capturing technique is evaluated. Finally, the results from conditional averaging are discussed.

4.1 Introduction

The first test case to be investigated is a canonical oblique shock wave/boundary layer interaction. The general flow arrangement from experiments is depicted in figure 4.1. An oblique shock wave, called the *incident shock*, is generated by the deflection imposed through a flat plate inclined in a supersonic flow and impinges on the turbulent boundary layer developed on the floor of the wind tunnel. In inviscid conditions, the *reflected shock* would originate from the impingement point on the bottom wall. However, in viscous flows, the presence of the boundary layer translates into a reflected shock that is positioned more upstream. The information of adverse pressure gradient carried by the incident shock can indeed travel upstream through the subsonic part of the boundary layer. It provokes in turn a thickening

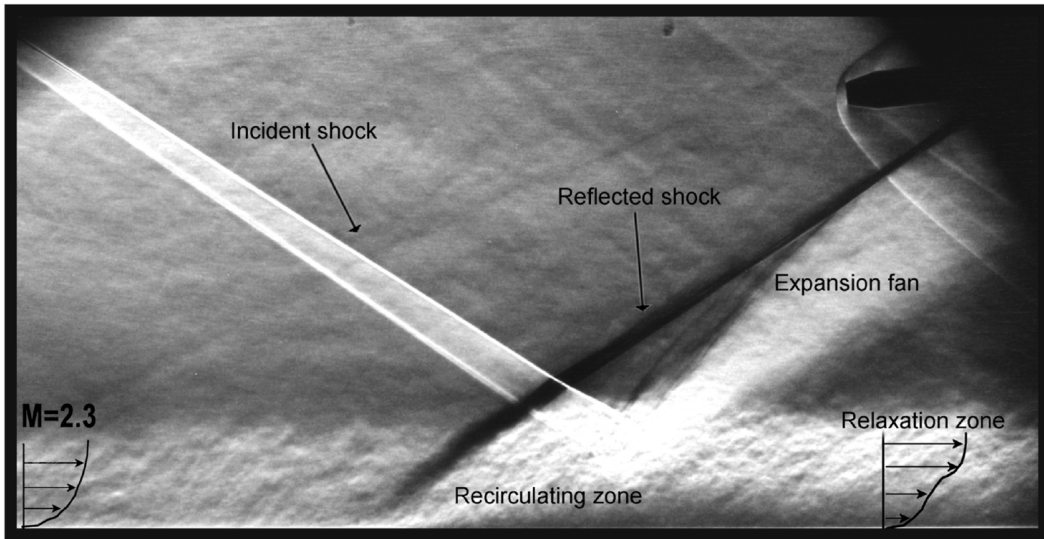


Figure 4.1. Short time exposure Schlieren visualization of the interaction, flow deviation of 8° (Dupont et al., 2008).

of the boundary layer that is seen as an obstacle by the upstream supersonic flow. As a consequence, a series of compression waves that eventually merge into a single reflected shock is generated upstream of its inviscid location. For a strong interaction, that is to say for a large pressure gradient, the boundary layer separates and a *recirculating zone* appears right downstream of the reflected shock. Further downstream of the interaction is the *relaxation zone*, in which the boundary layer slowly recovers its original, undisturbed state. Pressure being constant on the sonic line, the incident shock is reflected there as an *expansion fan*. Finally, a *reattachment shock* develops from the reattachment point to turn back the flow parallel to the wall. Being rather weak, it is, however, not easily observable in Schlieren visualizations as in figure 4.1.

This configuration was extensively studied experimentally by the *Institut Universitaire des Systèmes Thermiques Industriels* (IUSTI) in Marseille, France, for a supersonic flow at Mach 2.3. Various shock intensities (with deflection angles ranging from 7° to 9.5°) were investigated using wall pressure, hot-wire anemometry or particle image velocimetry (PIV) measurements (Dupont et al., 2005; Dupont et al., 2006; Dupont et al., 2008; Dussauge et al., 2006). Several zones were distinguished in the flow, each of them related to specific time scales. The first one is the upstream boundary layer, with a frequency scale of the order of U_∞/δ_0 and related to the energetic turbulent structures (U_∞ being the free stream velocity and δ_0 the reference boundary layer thickness). Then, the reflected shock was shown to exhibit a large-scale low-frequency motion. The associated frequency is two orders of magnitude lower than for the upstream boundary layer. The Strouhal number, defined as $St_L = fL/U_\infty$ is around 0.03. The characteristic length scale employed is the length of interaction L , that will be defined in the results section. In the interaction region, large convective scales are developing in the mixing layer and correspond to an intermediate frequency range, one order of magnitude lower than in

the incoming boundary layer. Together with this, low frequencies of the same range as the reflected shock were also observed in the interaction zone and were found to contribute up to around 20% of the total energy content of the wall pressure fluctuations. Finally, the relaxation zone displays intermediate frequencies persisting far downstream.

The low-frequency unsteadiness is a typical feature of strong shock wave/boundary layer interactions with flow separation. Moreover, it appears not only for oblique shock reflection but in other configurations as well, such as compression corners (Dolling, 2001). Discovering its source has been the motivation of numerous works over the past decades, the findings of which were compiled by Clemens and Narayanaswamy (2014). Two main categories of mechanisms were suggested. In upstream mechanisms, the low-frequency motion is explained by events occurring in the upstream boundary layer, whereas downstream mechanisms consider the influence of the separated flow. Piponnier et al. (2009) developed, for example, a model predicting the low-frequency unsteadiness derived from the breathing motion of the separated bubble. On the numerical side, the low-frequency motion cannot be reproduced by unsteady Reynolds-Averaged Navier-Stokes simulations and therefore requires the use of high-fidelity simulations to be captured.

Numerous high-fidelity simulations were performed on the IUSTI configuration. This popularity comes from the relatively low experimental Reynolds number, $Re_\theta \approx 5 \times 10^3$ based on the compressible momentum thickness. A short overview of the different studies found in the literature and their outcomes is given in the following paragraphs. A detailed comparison of the simulation setups can be found in tables 4.1 and 4.2. Early efforts of Garnier et al. (2002) demonstrated the ability of Large-Eddy Simulation (LES) to reproduce the experimental results, opening the way for such tools to study the physics of oblique SWBLI. The computing time was, however, too short to put in light the low-frequency unsteadiness of the reflected shock. Further insights were gained with Pirozzoli and Grasso (2006), who performed a Direct Numerical Simulation (DNS) of the interaction at a reduced Reynolds number ($Re_\theta = 3.7 \times 10^3$). They suggested a mechanism based on acoustic resonance to explain the origin of the shock motion. The integration time was again too short with respect to the time scale of the low-frequency oscillation observed experimentally. The low-frequency motion of the reflected shock was finally reproduced in the reference conditions by Toubert (2010) using LES, with a simulation time covering more than 25 low-frequency cycles. A first-order stochastic model was derived to predict wall-pressure spectra and showed that the coupled system - shock/boundary layer - acts as a low-pass filter. Pirozzoli and Bernardini (2011) developed a numerical DNS database for the 8° case at $Re_\theta \approx 2.3 \times 10^3$, providing reference data for the development of turbulence models. Efforts were made to extend the duration of the computation. Agostini et al. (2012) performed a LES to study the regions of influence of the shock motion. A low frequency range and a medium frequency range are identified and it is concluded that both are related to phenomena occurring in the separated zone. A LES database was presented in Morgan et al. (2013), considering various domain size, grid resolution, Reynolds number and wedge angle. Several popular plausible mechanisms proposed to explain the low-frequency motion of the reflected shock were assessed. The defects of selected

Table 4.1. Comparison of high-fidelity simulation setups for the oblique SWBLI configuration from IUSTI. The column BC refers to the type of lateral boundary condition employed, with P, S and W standing for Periodic, Slip and Wall, respectively. ϕ is the deflection angle. T is the total integration time of the simulation.

	Re_θ	Type	BC	ϕ [°]	TU_∞/δ_0
Garnier et al. (2002)	5.0×10^3	LES	P	8	85
Pirozzoli and Grasso (2006)	3.7×10^3	DNS	P	8	32
Touber (2010)	5.0×10^3	LES	P	8	2650
Pirozzoli and Bernardini (2011)	2.3×10^3	DNS	P	8	231
Agostini et al. (2012)	5.0×10^3	LES	P	6.3/8/9.5	6250-25000
Hadjadj (2012)	5.3×10^3	LES	P/S	8	/
Morgan et al. (2013)	$1.5/2.3/4.8 \times 10^3$	ILES	P	6.5-9.5	172
Aubard et al. (2013)	3.7×10^3	LES	P	8/9	900
Bermejo-Moreno et al. (2014)	5.5×10^3	WMLES	P/W	9.5	3500
Yang et al. (2016)	5.0×10^3	LES	P	8	/
Vyas et al. (2019a)	4.6×10^3	ILES	P	8	1820
Vyas et al. (2019b)	4.6×10^3	ILES	W	8	1600
Di Renzo et al. (2022)	0.85×10^3	DNS	P	5/10.4	560
Larsson et al. (2022)	$0.85 - 2.2 \times 10^3$	ILES	P	10.4	19000
Céci et al. (2023)	0.85×10^3	DNS	P	8/10.4	1200
Bernardini et al. (2023)	6.9×10^3	DNS	P	8	2000
Present case	5.2×10^3	ILES	P	8	1000

Table 4.2. Comparison of domain dimensions, numbers of degrees of freedom and grid resolutions for high-fidelity simulations of the oblique SWBLI configuration from IUSTI. $-x_{in}/\delta_0$ gives the location of the inlet plane, considering the location of the theoretical impingement point of the incident shock to be at $x_{imp}/\delta_0 = 0$. ^a Dimension originally given in terms of the inlet boundary layer thickness δ_{in} , but rescaled here by δ_{in}/δ_0 .

	L_x/δ_0	L_y/δ_0	L_z/δ_0	$-x_{in}/\delta_0$	N_x	N_y	N_z	N	Δx^+	Δz^+	y_w^+
Garnier et al. (2002)	17.1	6.4	1.4	7.6	255	151	55	2.1×10^6	50	18	1
Pirozzoli and Grasso (2006)	74.7	6.5	2.2	58.2	2650	111	255	7.5×10^7	15	6.5	1
Touber (2010)	20.3	4.1	4.7		451	151	281	1.9×10^7	33	12	1.3
Pirozzoli and Bernardini (2011)	44.4 ^a	7.1 ^a	3.6 ^a	29.6 ^a	3841	344	261	3.4×10^8	5.6	6.6	0.93
Agostini et al. (2012)	≥ 20	/	1.6	≥ 10	/	/	/	5.5×10^6	40	16	0.9
Hadjadj (2012)	20	10	5	/	375	160	461	2.8×10^7	40	16	1
Morgan et al. (2013)	12	10.2	3.6	/	530	443	214	5.0×10^7	29-16-29	14	1
Aubard et al. (2013)	58	17.6	2.9	/	1100	250	150	4.1×10^7	40-9-40	14	1.8
Bermejo-Moreno et al. (2014)	41.8	10.9	6	29.7	/	/	/	/	100	50	20
Yang et al. (2016)	23.3	4.6	5.4	17.1	451	151	281	1.9×10^7	33	12	1.3
Vyas et al. (2019a)	30	4	5	15	1025	257	513	1.4×10^8	15	7	0.68
Vyas et al. (2019b)	30	4	17	15	1025	395	1489	6.0×10^8	15	10	0.68
Di Renzo et al. (2022)	56.9 ^a	10.7 ^a	9.5 ^a	37.9 ^a	2560	256	448	2.9×10^8	< 5	< 5	< 0.65
Larsson et al. (2022)	64.8 ^a	24.2 ^a	4.8 ^a	30.3 ^a	2560	320	192	1.6×10^8	< 13	< 13	< 0.6
Ceci et al. (2023)	65.4 ^a	13.6 ^a	65.4 ^a	43.6 ^a	1920	240	2016	9.3×10^8	8	6	0.6-0.7
Bernardini et al. (2023)	70	12	6.5		8192	1024	1024	8.6×10^9	7	5	0.6-1.1
Present case	23	9.5	5	17	1024	388	304	1.2×10^8	16	12	0.3

RANS turbulence models were also addressed and the analysis showed that turbulent transport in particular was not well represented. Yang et al. (2016) studied the effectiveness of a control device in order to mitigate the flow separation, using LES. The detailed Reynolds stress budgets, obtained from ILES in the reference conditions, were reported in Vyas et al. (2019a) and stressed out the importance of pressure strain and pressure diffusion terms. Finally, Bernardini et al. (2023) performed a DNS at moderate Reynolds number and presented an analysis of the shock unsteadiness using a wavelet transform. The shock movement was found to be described by a collection of intermittent events, some of them being related to the breathing of the separation bubble.

Most of the numerical studies prescribed periodic lateral boundaries, therefore assuming a statistically two-dimensional flow. In the experiment, confinement effects are actually expected because of the presence of sidewalls. The latter was clearly reported by Dupont et al. (2005) for the strongest interaction case, with a deflection angle of 9.5° . Some works treated that aspect. Hadjadj (2012) presented the results from LES and provided a comparison between periodic and slip wall lateral boundaries for the 8° deflection case. The confinement of the flow produced a strengthened interaction because of the generation of near-wall vortices. Bermejo-Moreno et al. (2014) made use of wall-modeled LES to be able to consider the full cross-section of the wind tunnel, while reaching the experimental Reynolds number. Their study of the 9.5° case indicated that the correct characterization of the strong interaction is obtained with sidewalls, the simulation with periodic spanwise boundary conditions under-predicting the length of interaction. A peculiar feature of the computational domain was also the inclusion of the shock generator as the top boundary. A full-span, wall-resolved simulation of the 8° case was performed by Vyas et al. (2019b). The obtained length of interaction was longer than in the experiment. A detailed analysis of the spanwise variation of the turbulent stress budgets was also carried out and highlighted different behavior between the core span and the corner bisector.

The addition of a spanwise velocity component was examined by Di Renzo et al. (2022) and Larsson et al. (2022) using, respectively, DNS and ILES. The main effect of crossflow was shown to be an increase in the size of the separation bubble compared to the purely two-dimensional case. An extension of the two-dimensional model of Piponniau et al. (2009) to include crossflow effects was then derived by Ceci et al. (2023) based on DNS results collected on very wide computational domains.

4.2 Flow conditions and computational setup

The flow conditions are chosen to replicate the experiment of the oblique shock wave/boundary layer interaction performed at the IUSTI on the 8° deflection case. The incoming boundary layer, developing in a supersonic flow at Mach 2.3, is fully turbulent. Its experimental characteristics, that are to be matched in the simulation, are given in table 4.3 at a reference station upstream of the interaction. In particular, the reference boundary layer thickness $\delta_0 = 11\text{mm}$ and the Reynolds number based on the compressible momentum thickness $Re_\theta \approx 5.1 \times 10^3$. The upstream total

temperature and total pressure are, respectively, 300K and 50kPa. The fluid is assumed to be a perfect gas.

A side view of the computational domain is shown in figure 4.2 together with some of the main flow features. Contrary to most of the high-fidelity simulations presented in the literature review, the shock generator is modeled and is part of the top boundary, which is therefore inclined by 8° . However, the upper part of the wind tunnel, above the shock generator, is not included in the computational domain. The lengths of the domain in the streamwise and spanwise directions are, respectively, $L_x \approx 23\delta_0$ and $L_z = 5\delta_0$. Based on past studies (for example Toubert (2010)), the width is *a priori* sufficiently large to avoid any artificially confined flow. This will be formally checked in the results section. The inlet is located $\approx 17\delta_0$ upstream of the inviscid impingement point of the incident shock wave so that the upstream turbulence can develop properly before reaching the interaction region. Finally, the domain height is $L_y \approx 9.5\delta_0$ at the inlet and $L_y \approx 7.5\delta_0$ at the outlet. The dimensions of the domain and the location of the inlet are recapitulated in table 4.2 together with the setups found in the literature.

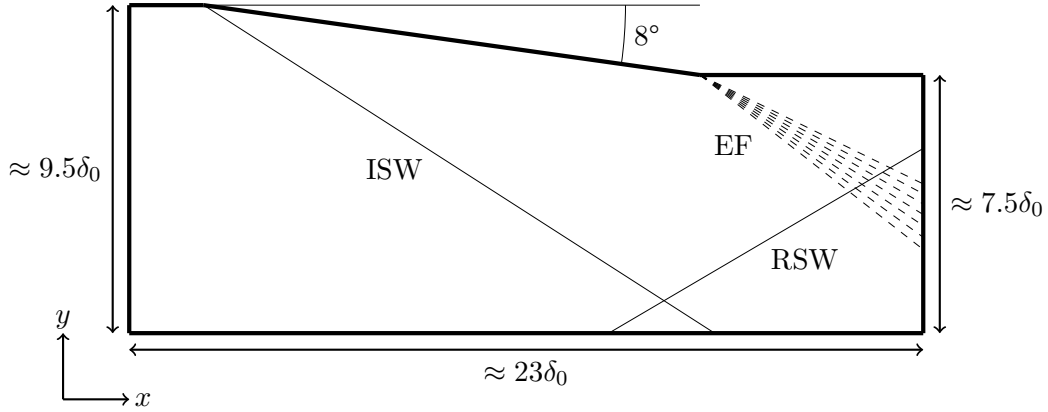


Figure 4.2. Side view of the computational domain with some of the main flow features: incident shock wave (ISW), reflected show wave (RSW) and expansion fan (EF).

The mesh is entirely composed of hexahedra. The number of cells is $256 \times 97 \times 76$ in the streamwise, wall-normal and spanwise directions, respectively. The simulation is performed at polynomial order 3, leading to a total number of solution points of $N_x \times N_y \times N_z = 1024 \times 388 \times 304 \approx 121 \times 10^6$. A constant grid spacing is used in the x and z directions giving in wall units based on the upstream conditions $\Delta x^+ = 16$ and $\Delta z^+ = 12$. In the wall-normal direction, the boundary layer comprises exactly 25 cells (or 100 solution points at polynomial order 3), which are stretched according to a hyperbolic tangent law. The first cell height is imposed such that the first solution point lies below $y^+ = 1$. Outside the boundary layer, the grid spacing is kept practically constant and equal to the grid spacing in the streamwise direction. Therefore, $\Delta y^+ = 16$. Table 4.2 summarizes the mesh parameters and compares them with the literature.

The grid resolutions given here above are evaluated with respect to the solution points. Using a high-order representation of the solution within each cell, the effective

grid spacing h is related to the cell size H through

$$h = \frac{H}{p+1}, \quad (4.1)$$

where p is the polynomial order. This equation assumes that the solution points are uniformly distributed within the cell, which is not the case for Gaussian solution points. The zeros of the Legendre polynomials are indeed located much closer to the cell face than their uniformly distributed equivalent and tend to get closer as the polynomial order increases. Equation 4.1 will therefore give an averaged effective grid spacing.

Regarding the boundary conditions, the inlet is fully supersonic with prescribed velocity components, static temperature and static pressure profiles coming from a precursor ILES of a turbulent boundary layer performed in the same flow conditions. To configure the digital filter used to generate the inflow turbulence, the turbulence length scales in the streamwise I_x and spanwise I_z directions are set constant and equal to $0.5\delta_0$ and $0.2\delta_0$, respectively. The Lagrangian time scale t_L (see equation 3.59) is evaluated with a velocity equal to $0.9U_\infty$, with U_∞ being the free stream velocity upstream of the interaction. The profile for the turbulence length scale I_y in the wall-normal direction is obtained so that it gives a constant number of points constituting the filter of around 350 across the inlet plane. Furthermore, I_y matches I_z at the edge of the boundary layer. Reynolds stress profiles are prescribed to scale the filtered perturbations and are extracted from the precursor simulation too. The outlet boundary is supersonic with a specific treatment for the subsonic part of the boundary layer in which the static pressure is imposed. The specified value is taken from a separate RANS simulation of the interaction, at the first supersonic point in the outlet boundary layer. The bottom boundary is a no-slip adiabatic wall. The top boundary is divided into three parts. The central part, modeling the shock generator, is a slip wall so that the boundary layer is not resolved, which allows to reduce the computational cost. The other parts of the top boundary are external boundaries with Riemann invariants. In the spanwise direction, periodic boundary conditions are prescribed.

The parameters of the shock-capturing technique described in subsection 3.3 are $s_0 = -4.5$, $\kappa = 0.5$, $C_T = 0.03$ and $s_{D,0} = 0.2$. Density is used as the sensor variable.

The explicit time step is $2.5 \cdot 10^{-8}$ s, giving a CFL number of around 2.5. The simulation is first restarted from an initial RANS solution for about $225\delta_0/U_\infty$ to get rid of the transient. Samples of the flow are then collected for a duration of $1000\delta_0/U_\infty$. Instantaneous span-averaged, instantaneous mid-span, as well as bottom wall data are extracted at a sampling rate of 500kHz. The flow is also probed at various locations. The probes record the primitive variables at each time step, hence a sampling rate of 40MHz. The frequency associated to the energy-carrying eddies in the upstream boundary layer is $\mathcal{O}(U_\infty/\delta_0) \approx 50$ kHz. Both sampling rates are consequently high enough to capture all the frequencies involved in the flow. The shock unsteadiness is expected to correspond to a frequency two orders of magnitude lower than the characteristic frequency of the upstream boundary layer. The simulation time therefore covers around 10 cycles of the reflected shock motion.

4.3 Results

4.3.1 Basic flow validation

A first insight into the flow field is given in figure 4.3 displaying an instantaneous view of the density gradient magnitude at mid-span and of the streamwise velocity near the bottom wall (at a distance $y^+ \approx 10$). The different flow features introduced previously in figure 4.1 are easily recognized, beginning with the oblique incident shock. Its reflection as an expansion fan on the sonic line is also discerned. As expected, the reflected shock wave stands slightly upstream of its inviscid location. The weak reattachment shock wave, turning back the flow parallel to the wall after the interaction, is also captured. Turbulent streaks are clearly highlighted in the upstream boundary layer and are largely influenced by the interaction. A sudden and sharp drop in streamwise velocity occurs as soon as the boundary layer meets with the reflected shock, which provokes the separation of the flow. Further downstream, turbulent streaks develop again, progressively, as the boundary layer recovers from the interaction.

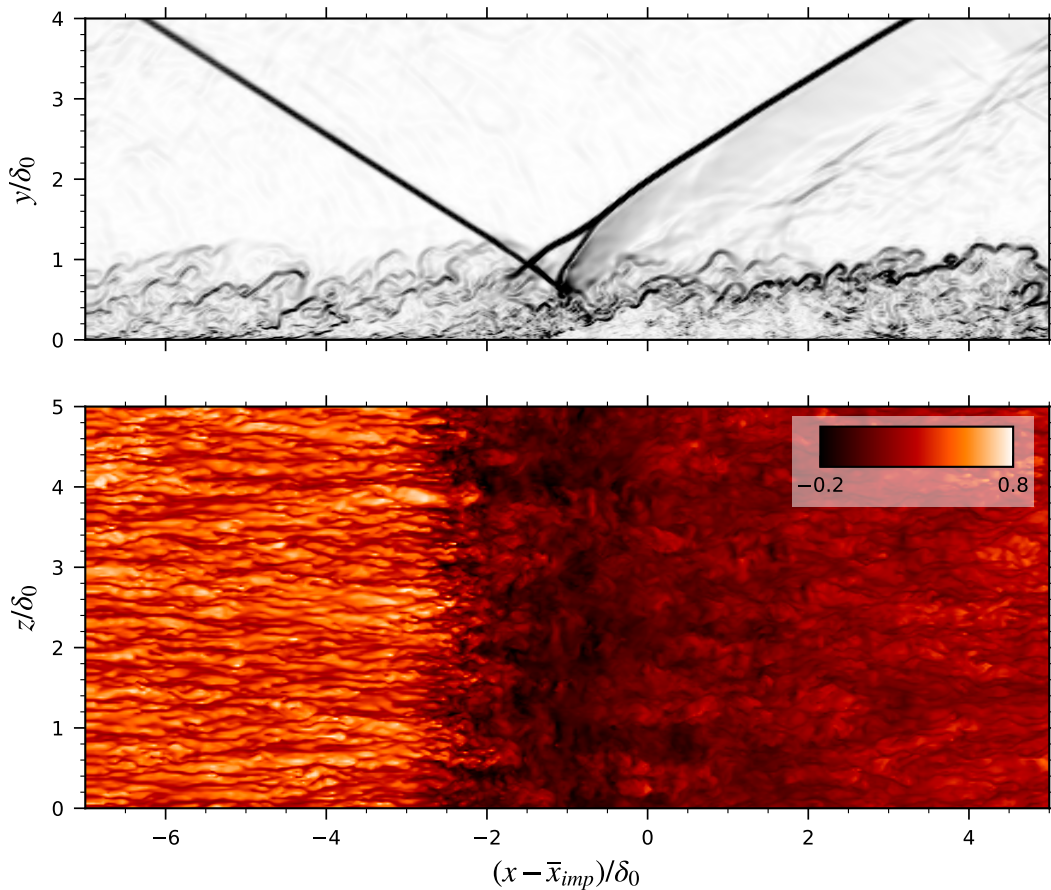


Figure 4.3. Instantaneous density gradient magnitude at mid-span (*top*) and instantaneous streamwise velocity u/U_∞ near the bump wall, $y^+ \approx 10$ (*bottom*).

To begin with, table 4.3 summarizes the characteristics of the boundary layer, at a reference station upstream of the interaction, and compares them to the experimental ones. Note that the location of the reference station is scaled to account for the different interaction length (as it will be shown later). The boundary layer thickness, the Reynolds number and the friction coefficient are all nicely matched.

	Experiment	Present case
δ_0 [mm]	11	11.4
δ^* [mm]	3.4	3.42
θ [mm]	0.96	0.93
θ_i [mm]	1.28	1.28
Re_θ	5.1×10^3	5.2×10^3
Re_{θ_i}	6.9×10^3	6.9×10^3
C_f	2×10^{-3}	2.04×10^{-3}

Table 4.3. Boundary layer characteristics upstream of the interaction. The reference station is located at $(x - \bar{x}_{imp})/L \approx -1.66$. Experimental values are taken from Dupont et al. (2008) or Piponniau et al. (2009) depending on the available data. δ^* , θ and θ_i are the compressible displacement thickness and the compressible and incompressible momentum thicknesses, respectively.

The boundary layer profile upstream of the interaction is shown in figure 4.4 together with PIV measurements from Dupont et al. (2008) and DNS data of Bernardini et al. (2023). Regarding the van Driest-transformed mean velocity profile (*left* figure), a very good agreement is found between the present results and the DNS. The curves are on top of each other in both the viscous sublayer and in the logarithmic region. The typical law of the wall is matched, with $\kappa = 0.41$ and $C = 5.3$. A slight departure from DNS is observed in the defect layer. With respect to experimental results, an offset is reported in the logarithmic layer. It comes from the use of a different friction velocity in the van Driest transform. The experimental value is around 25.4m/s (as indicated by Touber (2010)) whereas the simulation gives here 24.5m/s. Scaling the experimental profile with the latter reduced the gap.

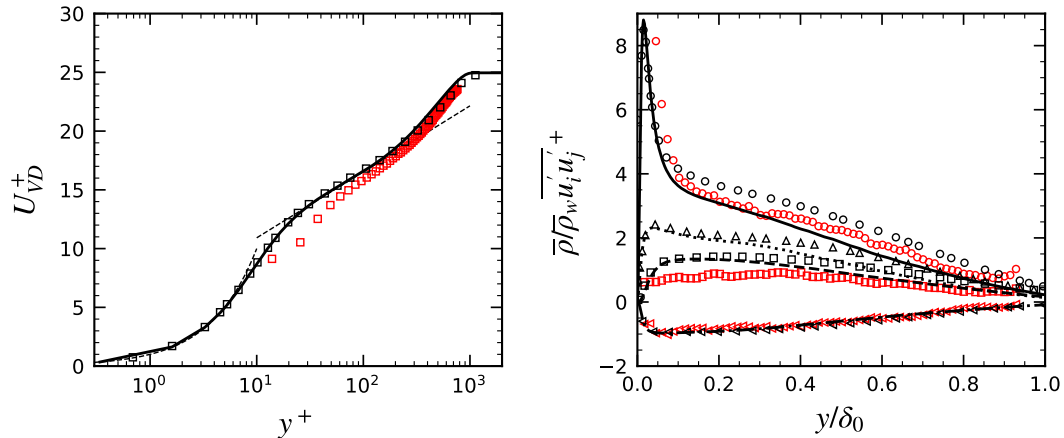


Figure 4.4. Boundary layer profiles at $(x - \bar{x}_{imp})/L = -1.66$ - van Driest-transformed mean velocity profile (*left*) and density-scaled Reynolds stress profiles (*right*). *black* symbols refers to the DNS data of Bernardini et al. (2023) and *red* symbols to experimental measurements of Dupont et al. (2008).

In figure 4.4, *right*, Reynolds stress profiles are presented and compared again with the available PIV data from Dupont et al. (2008) and the DNS results reported in Bernardini et al. (2023). A digital filtering approach was also employed to provide

a turbulent inflow. A good agreement is again found between the different numerical results. In particular, the peaks of the normal stresses are very well predicted. The agreement with experimental data is satisfactory, the under-prediction of the wall normal velocity fluctuations being typical in measurements.

A key point in the computational setup is the width of the domain, which has to be sufficiently large to guarantee the de-correlation of the turbulent structures before reaching the lateral boundary. Failing this requirement leads to a virtually confined flow and therefore mimics the presence of sidewalls. Ultimately, this can result in a stronger interaction and, as a consequence, in a larger separation bubble. The domain width is typically checked by considering the two-point streamwise velocity correlation coefficient in the spanwise direction, computed following

$$C_{uu}(x, y, \Delta z) = \overline{u'(x, y, z)u'(x, y, z + \Delta z)} / \overline{u'(x, y, z)u'(x, y, z)}. \quad (4.2)$$

Figure 4.5 presents the results at a distance $y/\delta_0 = 0.5$ from the bottom wall. The spatial distribution (*left*) indicates that C_{uu} quickly drops to zero, at $\Delta z/L_z \approx 0.1$, regardless of the streamwise location. A more detailed view at four selected stations (*right*) shows moreover that, within the separated region, the integral length scale first increases and then immediately decreases. A similar observation was reported by Morgan et al. (2013). Upstream and downstream of the interaction region, the integral length scale is identical. In any case, the flow is de-correlated much before a distance of half the span. It is therefore concluded that the domain is wide enough. Touber (2010) reached the same conclusion using the same domain width.

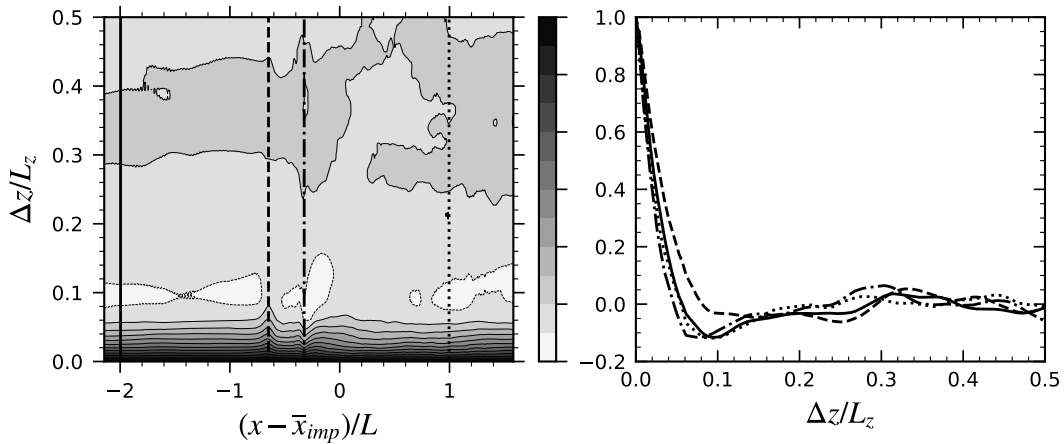


Figure 4.5. Two-point streamwise velocity correlation coefficient in the spanwise direction, C_{uu} . Spatial distribution at $y/\delta_0 = 0.5$ (*left*) and spanwise evolution at four streamwise locations (*right*) - upstream of the interaction (*solid*), in the separated region (*dashed* and *dashdot*) and downstream of the interaction (*dotted*).

Figure 4.6 (*left*) illustrates the streamwise evolution of the friction coefficient, compared with the simulation results of Morgan et al. (2013) and Bernardini et al. (2023). Upstream of the interaction, the friction coefficient is steadily decreasing, as it is expected for a developed turbulent boundary layer. Together with the boundary layer profiles showed in figure 4.4, this is comforting the idea that the inlet is located far upstream enough from the interaction region to let the boundary layer retrieve

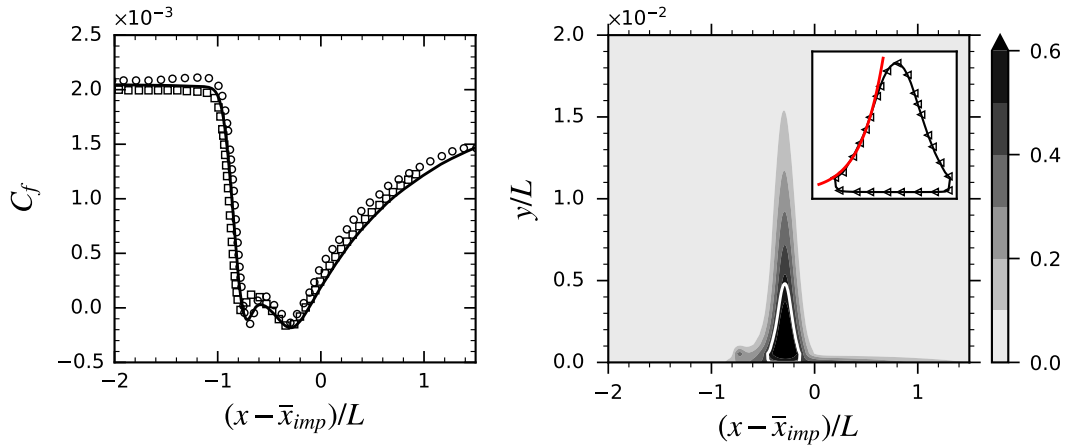


Figure 4.6. Streamwise evolution of mean friction coefficient (*left*) compared with simulation results from Bernardini et al. (2023) (\square) and from Morgan et al. (2013) (\circ) - Spatial distribution of flow reversal probability (*right*), with contour of null mean streamwise velocity (*solid white*). The inset shows the contour of null streamwise velocity (*black* with \triangleleft symbols) with an exponential best-fit line (*red*).

its main features but also that the digital filtering is correctly configured. Within the interaction region, two negative lobes are observed, which is in agreement with other high-fidelity predictions. Whereas the absolute magnitude of the second minimum is identical among the different results, the depth of the first lobe decreases with increasing Reynolds number. This effect was already reported by Morgan et al. (2013).

To further comment on the complex pattern of the friction coefficient in the interaction region, figure 4.6 (*right*) shows the flow reversal probability (that is to say the probability for the flow to exhibit a negative streamwise velocity component). Interestingly, the second lobe displays a high probability of reverse flow (above 60%), while the first lobe barely exceeds 30%. Besides, a clear recirculation bubble is highlighted for the second lobe only (see *white* contour) and matches the contour at 50% probability of flow reversal. The fact that the first lobe is not associated to a high probability of flow reversal means that it corresponds to rare events during which the friction coefficient is strongly negative. The maximum height of the bubble in wall unit is $h^+ \approx 11$, which is almost four times lower than the value reported by Touber (2010) ($h^+ \approx 41$) but, however, compares well with Morgan et al. (2013) ($h^+ \approx 7$). The inset reproduces the contour of the recirculation bubble and shows that its front part can be approximated by an exponential curve, a fit suggested by Touber (2010).

The streamwise evolution of mean wall pressure is depicted in figure 4.7 (*left*) together with experimental measurements given in Dupont et al. (2006) and simulation results of Morgan et al. (2013) and Bernardini et al. (2023). Scaled by the length of interaction, the results are practically all on top of each other. The sharp pressure gradient imposed by the shock system in the potential flow is smeared in the boundary layer, giving a smooth increase of pressure as soon as the flow enters the interaction region. Downstream of the interaction region, pressure slowly reaches

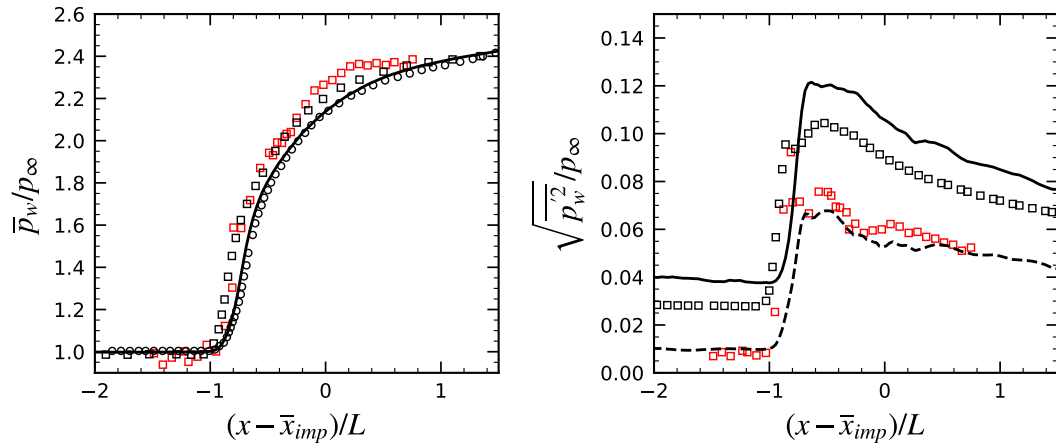


Figure 4.7. Streamwise evolution of mean wall pressure (*left*) and wall pressure fluctuations (*right*). Present case (*solid*), experimental data from Dupont et al. (2006) (*red* \square), simulation results from Bernardini et al. (2023) (*black* \square) and from Morgan et al. (2013) (*black* \circ). The *dashed* line represents the variance evaluated up to a cutoff frequency of 20kHz.

the imposed value.

On the *right* of figure 4.7 is illustrated the streamwise evolution of wall pressure fluctuations. In the present case, it was obtained from a series of probes recording static pressure at the sampling rate of 40MHz. Upstream of the interaction, the level is approximately equal to 4% of the upstream static pressure, an offset of 1% with respect to the DNS of Bernardini et al. (2023), who reported slightly less than 3%. In the interaction region and downstream of it, the same trend as the DNS is observed but the offset is still present. The reason for the additional noise might come from the relatively short domain in comparison to Bernardini et al. (2023), preventing the level of fluctuation to sufficiently decrease to reach the DNS result. The results from the turbulent boundary layer case presented in appendix B also demonstrated that the digital filter introduces additional acoustic disturbances, resulting in an over-prediction of the wall pressure variance. Measurements from Dupont et al. (2006) are known to under-estimate the pressure fluctuations because of the cutoff frequency of the pressure transducers employed to acquire the data. By integrating the PSD up to that cutoff frequency (20kHz), a much better agreement is found between simulation and experiment, as witnessed by the *dashed* line. It indicates therefore that the additional noise does not affect the low-frequency content (that is to say below the cutoff frequency) in the interaction region.

Two length scales of interest in shock wave/boundary layer interactions are the length of interaction L and the length of separation L_{sep} . The former is defined by the distance between the reflected shock foot and the incident shock foot, the positions of which result from the extrapolation of the shocks down to the wall. Table 4.4 compares the length scales found in the experiment and also in various high-fidelity simulations. The length of interaction in the present case is much shorter than in the experiment. It is actually consistently under-predicted by ILES and DNS when using periodic boundary conditions. The experiment suffers indeed from three-dimensional effects, strengthening the interaction at the centerline and

therefore resulting in a longer length of interaction. The present result falls in line with similar simulations and L follows an increasing trend with increasing Reynolds number. Toubert (2010) and Agostini et al. (2012) managed to obtain a value closer to the experiment but the results are affected by the choice of a particular subgrid-scale model. Including the sidewalls, Vyas et al. (2019b) reported a length of interaction longer than the experiment.

For separated interactions, the length of separation L_{sep} is simply defined by the extent of the separation bubble. Figure 4.6 revealed, however, the existence of two smaller separated regions in the mean field. From an instantaneous perspective, these can actually merge into a single bubble, such that the length of separation is taken here as the distance between the first and the last location of null C_f . The present result is indicated in table 4.4 and again conforms with ILES and DNS data. Also, following the interaction length, the separation bubble is much shorter than in the experiment and increases with increasing Reynolds number.

Table 4.4. Comparison of the length of interaction and length of separation. ^avalue estimated assuming $L_{sep} = 0.8L$ (Clemens & Narayanaswamy, 2009). ^bvalue estimated from the friction coefficient curve.

	Re_θ	L/δ_0	L_{sep}/δ_0
Vyas et al. (2019a)	4.6×10^3	2.94	1.51^b
Morgan et al. (2013)	4.8×10^3	3.02	1.61
Present case	5.2×10^3	3.12	2.09
Bernardini et al. (2023)	6.9×10^3	3.30	2.16
Agostini et al. (2012)	5.0×10^3	3.45	2.76^a
Experiment (Dupont et al., 2005)	4.5×10^3	4.18	3.34^a
Toubert (2010)	5.0×10^3	4.80	3.90
Vyas et al. (2019b)	4.6×10^3	5.20	4.70^b

A qualitative comparison between simulation and experimental results is provided in figure 4.8. Qualitatively, the thickening of the boundary layer downstream of the interaction is reproduced and the amplification of turbulence in the interaction region is highlighted as well. Quantitatively, a mismatch is observed. More particularly, u' is under-predicted whereas v' is over-estimated.

One of the shortcomings of low-fidelity methods when simulating oblique SWBLI is their inability to reproduce the low-frequency motion of the reflected shock, the flow feature at the origin of the research effort on SWBLI. As detailed in the literature review of this case, high-fidelity methods were proven to succeed in doing so and it is therefore of prime interest to check if the high-order solver employed in this work does not escape the rule. Figure 4.9 shows the weighted premultiplied Power Spectral Densities (PSD) obtained from a series of probes recording the wall pressure at mid-span. The PSDs are computed by using the Welch's method (Welch, 1967) with 7 blocks, Hamming windows and a typical overlap of 50%. The left figure reports the streamwise evolution of the PSDs, as a map. Several zones are discriminated beginning with the upstream boundary layer, characterized by the ridge centered at around $St_L \approx 10$. Near the mean separation point, an energetic

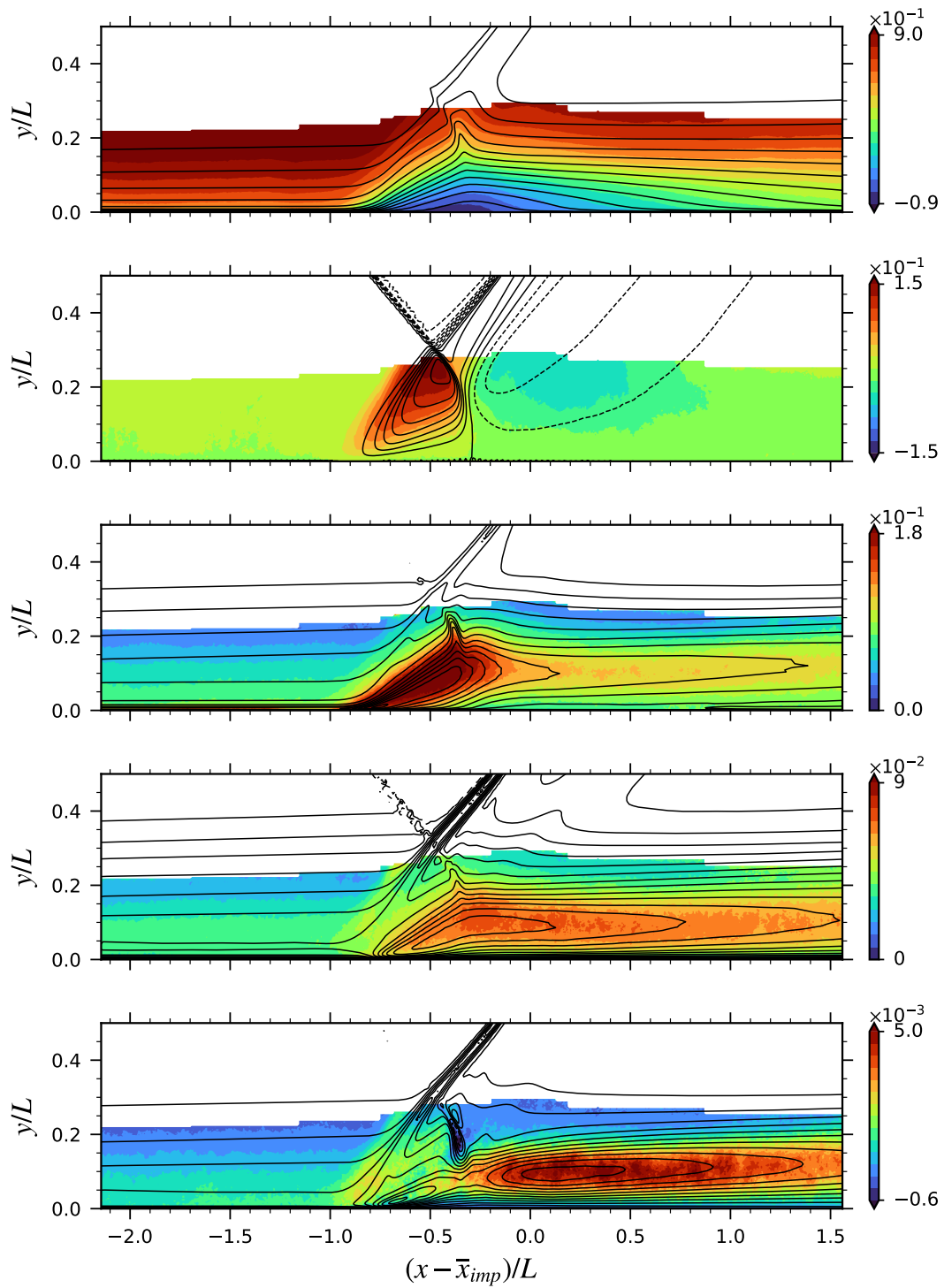


Figure 4.8. Comparison of mean velocity and Reynolds stress components between the present simulation results (*black* contours) and PIV measurements from Dupont et al. (2008) (*filled* contours). 15 equally-spaced contours of, from top to bottom, \bar{u}/U_∞ , \bar{v}/U_∞ , $\sqrt{u'u'}/U_\infty$, $\sqrt{v'v'}/U_\infty$ and $-u'v'/U_\infty^2$.

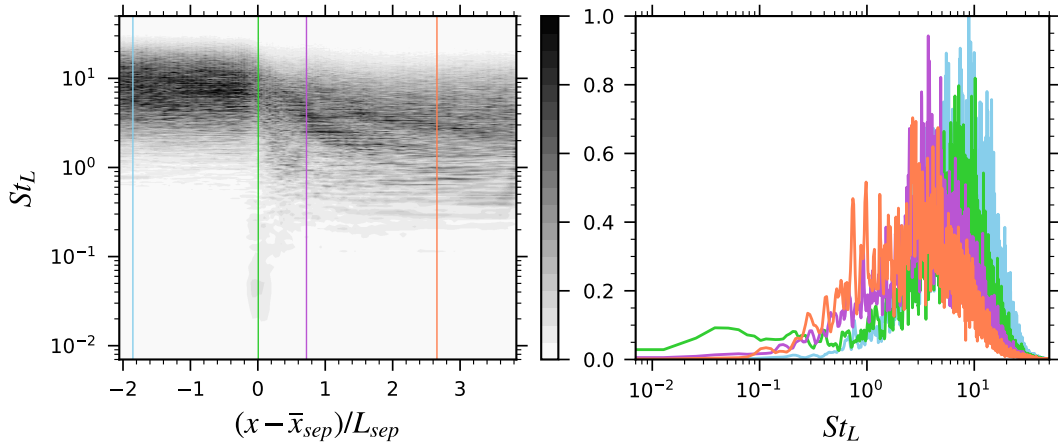


Figure 4.9. Weighted premultiplied Power Spectral Density of wall pressure - streamwise evolution (*left*) and four selected stations (*right*) corresponding to the upstream boundary layer (*blue*), the separation point (*green*), the minimum of friction coefficient (*purple*) and the relaxation zone (*orange*).

broadband low-frequency region is observed, witnessing the low-frequency motion of the reflected shock. As expected, the associated Strouhal number is two orders of magnitude lower than in the incoming boundary layer. Then, in the interaction region, intermediate frequencies develop in the detached shear layer. Finally, this intermediate range remains in the relaxation zone, downstream of the interaction. The *right* figure illustrates the PSDs at four selected stations, corresponding to the upstream boundary layer, the mean separation point, the minimum of friction coefficient and the relaxation region. The low-frequency content of the PSD near the mean separation point clearly stands out. It is widespread, with a peak located at $St_L \approx 0.04$. The intermediate frequency range emerges for the two downstream locations at $St_L \approx 1$.

To further understand how the reflected shock interacts with other regions of the flow, correlation coefficients are examined. As an indicator for the reflected shock, the wall-normal component of the velocity v is considered. It is indeed a direct image of the shock location since it will decrease for a more downstream position of the shock and vice versa. For a quantity of interest q , the coefficient is therefore computed following

$$R_{q,v_{ref}}(x, y) = \frac{\overline{q'(x, y, t) \cdot v'(x_{ref}, y_{ref}, t)}}{\sigma_q(x, y) \cdot \sigma_v(x_{ref}, y_{ref})} \quad (4.3)$$

where σ is the standard deviation. The reference point is located at $y/\delta_0 = 1.5$ and its streamwise position corresponds to the maximum of wall-normal velocity mean gradient in the streamwise direction $\partial \bar{v}/\partial x$ at the reflected shock. Figure 4.10 depicts the correlation coefficients with respect to the streamwise and the wall-normal velocity components as well as the pressure. Streamwise velocity is exactly anti-correlated with the wall-normal velocity at the reflected shock. The level of anti-correlation decreases as the shock penetrates the boundary layer. However, the start of the mixing layer is noticed and exhibits a fair amount of anti-correlation,

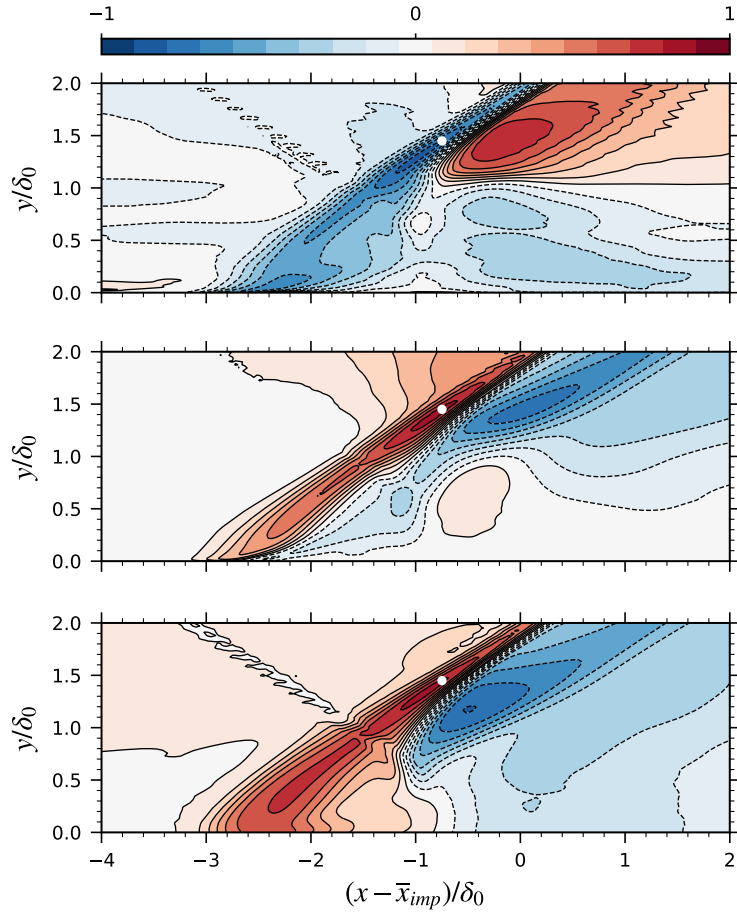


Figure 4.10. Spatial distribution of correlation coefficients - $R_{u,v_{ref}}$ (top), $R_{v,v_{ref}}$ (center) and $R_{p,v_{ref}}$ (bottom).

around -0.7. Weak negative correlation (≈ -0.3) is found in the downstream region. For the pressure, the correlation found at the reference point is almost completely transmitted into the boundary layer and down to the wall. It seems logical considering that, contrary to velocity fluctuations, pressure fluctuations do not cancel at the wall. In any case, no correlation is found neither with the incident shock wave nor the upstream boundary layer.

4.3.2 Shock-capturing technique performance

The shock-capturing technique is a critical feature of a solver when dealing with both shocks and turbulence. The performance of the methodology proposed in this work, introduced in section 3.3, is assessed hereunder. To illustrate the principles of the technique in more details, figure 4.11 shows side views of the time- and span-averaged shock sensor, Ducros sensor and artificial viscosity fields. The *left* figure clearly indicates that the shock sensor value is high everywhere in the boundary layer and takes similar values as near shocks. More particularly, the interaction region and the downstream boundary layer exhibit near maximum values. With the set

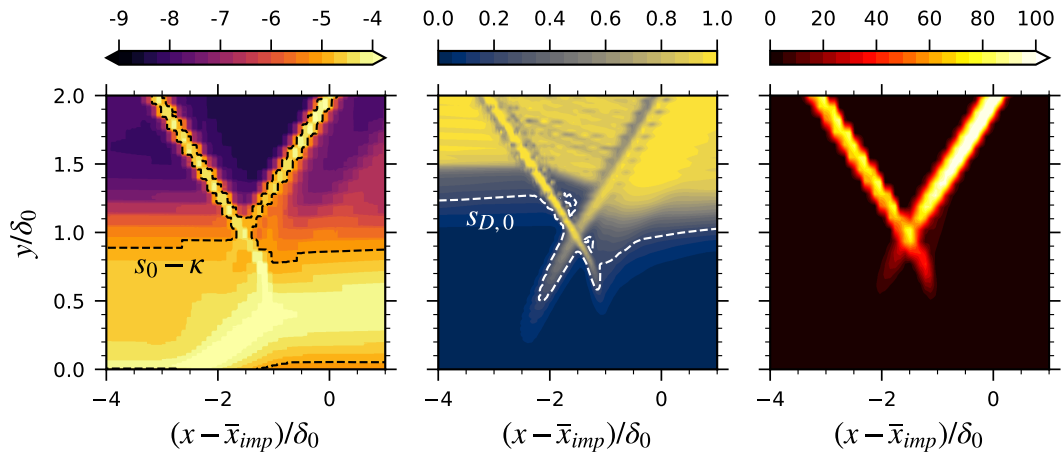


Figure 4.11. Averaged shock sensor s_e with $s_0 - \kappa = -5.0$ contour line (*left*), averaged Ducros sensor s_D with $s_{D,0} = 0.2$ contour line (*center*) and averaged artificial viscosity normalized by the local kinematic viscosity ε/ν (*right*).

of parameters used for this simulation, artificial viscosity would be triggered for any cells with a shock sensor value above $s_0 - \kappa = -5.0$ (see contour line) if the original method of Persson and Peraire (2006) was employed. A significant amount of artificial viscosity would be observed in the boundary layer and would damp the turbulence, resulting in an incorrect interaction with the shock system.

The solution proposed to circumvent this problem is to combine the method with the Ducros sensor (Ducros et al., 1999). The interest in using this sensor is illustrated in the *center* figure. As expected, the Ducros sensor exhibits very low values (close to zero) on average in the boundary layer whereas it is close to unity near shocks. It is therefore able to distinguish shocks from turbulence, whereas the shock sensor was not. The contour line indicates the threshold $s_{D,0}$ of the activation function (see figure 3.3, *right*), below which the artificial viscosity is explicitly set to zero. Only the boundary layer is affected.

As a result, the artificial viscosity field, depicted in the *right* figure, is focused around the shock system only. Note that the artificial viscosity is normalized by the local kinematic viscosity in order to compare the natural and the artificial viscous effects. Around the reflected shock in particular, the artificial viscosity is two orders of magnitude larger than the local kinematic viscosity.

To further investigate the behavior of the shock-capturing technique, figure 4.12 shows the streamwise evolution of the averaged shock sensor, Ducros sensor and artificial viscosity in the potential flow ($y/\delta_0 = 3.0$). The two peaks in the shock sensor correspond, respectively, to the incident and the reflected shock waves. These are the only features above the threshold value triggering artificial viscosity. The Ducros sensor is at each location much higher than its threshold but does not reach unity at the shocks. Artificial viscosity is therefore slightly attenuated around the shocks as a consequence of the activation function but still reaches orders of magnitude twice higher than the kinematic viscosity.

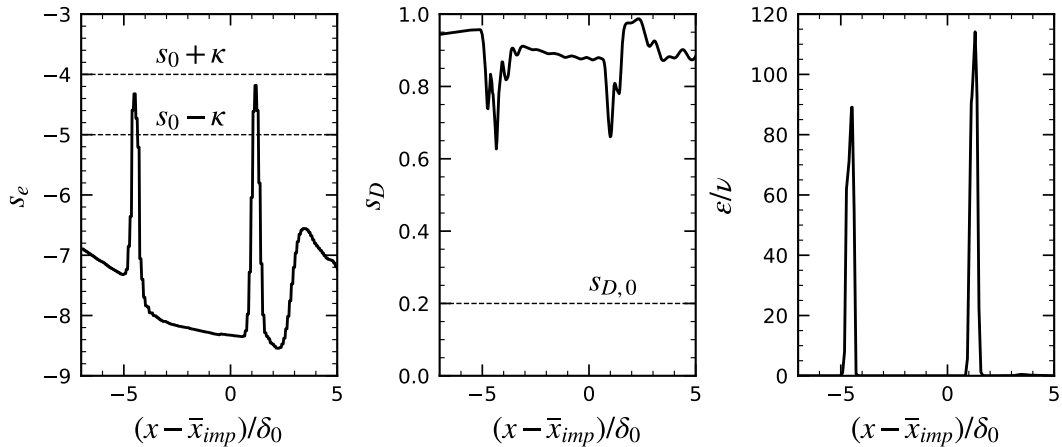


Figure 4.12. Streamwise evolution of the averaged shock sensor (*left*), Ducros sensor (*center*) and artificial viscosity (*right*) in the potential flow, at $y/\delta_0 = 3.0$. Threshold values for the shock sensor and Ducros sensor are indicated by *thin dashed* lines.

Figure 4.13 depicts the streamwise evolution of static pressure in the potential flow. The first objective of a shock-capturing technique is indeed to avoid any spurious oscillations of the solution around discontinuities. It is observed here that both shocks are properly resolved, with marginal oscillations around the incident shock and a perfectly smoothed reflected shock. The shocks are captured in approximately four cells, while the original shock-capturing technique is supposed to give a sub-cell resolution. This is simply a consequence of the C^0 -smoothing step.

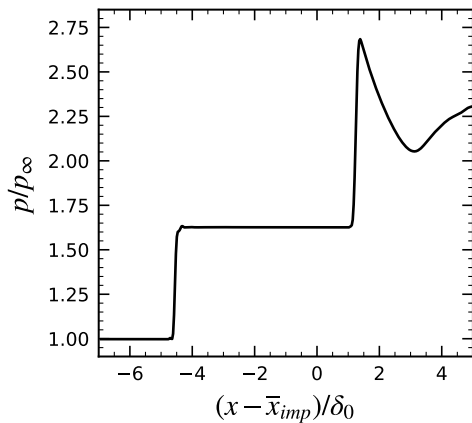


Figure 4.13. Averaged static pressure evolution in the potential flow, at $y/\delta_0 = 3.0$.

The second objective of a shock-capturing technique is to leave the turbulence untouched by the artificial viscosity. Figure 4.14 reports the streamwise evolution of the averaged shock sensor, Ducros sensor and artificial viscosity but within the boundary layer, at $y/\delta_0 = 0.2$. As stated previously, the shock sensor is high enough at all streamwise locations to trigger the artificial viscosity but none should be applied since the Ducros sensor is far below its threshold value. This is indeed the case for the vast majority of streamwise locations. Nevertheless, tiny amounts are still observed and correspond to the prints left by the shocks penetrating the boundary layer. These prints might originate from instantaneous events during which

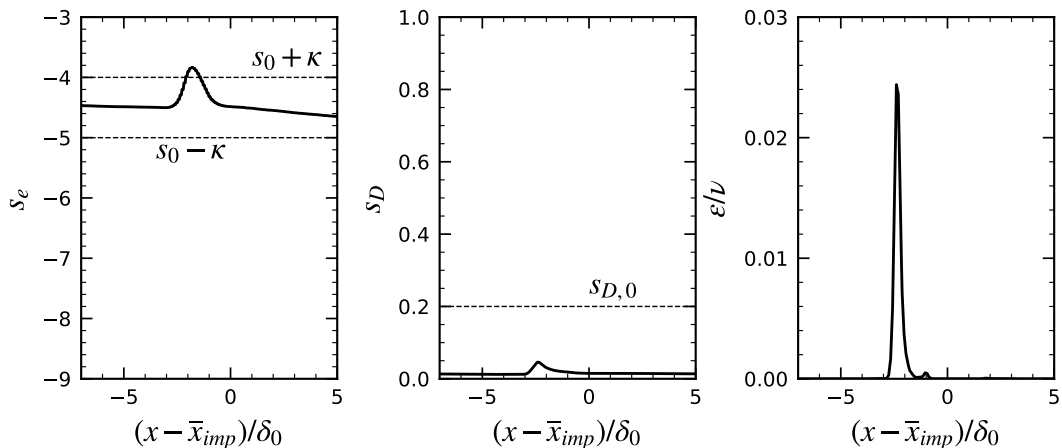


Figure 4.14. Streamwise evolution of the averaged shock sensor (*left*), Ducros sensor (*center*) and artificial viscosity (*right*) in the boundary layer, at $y/\delta_0 = 0.2$. Threshold values for the shock sensor and Ducros sensor are indicated by *thin dashed* lines.

no significant vortical structure is passing through the shocks, leading to a higher value of the Ducros sensor. As the order of magnitude of these remaining amounts is four times lower than what is needed to capture the shocks, these events are rare. This would also explain why practically nothing is detected near the incident shock. Turbulence is indeed promoted in the interaction region and it makes the occurrence even more uncommon. Considering the rarity of such events, they are believed to have no influence on the interaction.

4.3.3 Conditional averaging

The reflected shock exhibits a natural, large-scale, low-frequency behavior. It is therefore of interest to investigate how this motion is influencing the flow. A first step is to extract the coherent component of the flow from the high-fidelity data. In that regard, the triple decomposition of Reynolds and Hussain (1972), introduced in section 2.2, will be used. The separation of time scales required to perform such an analysis is clear in shock wave/boundary layer interactions. The low-frequency unsteadiness of the reflected shock is typically characterised by a Strouhal number two orders of magnitude lower than the Strouhal associated to the characteristic frequency of the incoming boundary layer. Figure 4.9 confirmed that for the present case.

The coherent component is usually isolated using phase averaging. In periodically forced flows, this notion is well defined as there is only one frequency involved, that is to say the perturbation frequency. However, the reflected shock motion involves a wide range of frequencies. It is not harmonic but broadband in nature, as again supported by the results presented in figure 4.9. Consequently, the notion of phase average is not straightforward if one wants to study this kind of unsteady behavior. Instead, it is suggested to use conditional average, meaning that the averaging is performed based on a certain condition. The position of the reflected shock foot will be used here as the criterion. A summary of this averaging process is provided

hereunder but the interested reader can refer to Touber (2010) to obtain more details.

Formally, the conditional average operator is defined as

$$\langle q \rangle_{\varepsilon_0, \Delta\sigma} = \frac{1}{\mathcal{N}(\mathcal{A}_{\varepsilon_0, \Delta\sigma})} \int_{\mathcal{A}_{\varepsilon_0, \Delta\sigma}} q(t) dt \quad (4.4)$$

where ε_0 is a particular reflected shock foot location, $\Delta\sigma$ is the range around ε_0 , $\mathcal{A}_{\varepsilon_0, \Delta\sigma}$ is the set of all instants t such that the reflected shock foot location lies between $[\varepsilon_0 - \Delta\sigma, \varepsilon_0 + \Delta\sigma]$ and finally \mathcal{N} is a measure of \mathcal{A} . A strong hypothesis to link the conditional average $\langle q \rangle$ (which is space-dependent) to its (time-dependent) coherent component \tilde{q} is that the flow field \tilde{q} is uniquely defined for a given reflected shock foot position if only the low-frequency motions are retained. It implies that the hysteresis, if there is any, is not significant. Whether the shock is moving upstream or downstream has no influence. Using this assumption, the conditional average resembles the phase average, giving directly

$$\langle q \rangle_{\varepsilon_0, \Delta\sigma} = \bar{q} + \tilde{q}(\varepsilon_0) + \mathcal{O}(\Delta\sigma) \quad (4.5)$$

and the coherent motion can be deduced knowing the time-averaged field.

The first step of the conditional averaging process is to extract the reflected shock foot position. For this purpose, a series of 10000 snapshots of the span-averaged flow field has been collected at a sampling rate of 500kHz. The shock system is extracted using a suitable threshold of velocity divergence. The efficiency of the method is demonstrated in figure 4.15 on a snapshot of the instantaneous flow field at mid-span. Both the incident and reflected shocks are nicely highlighted. The extraction is, however, not performed close to or within the boundary layer as it becomes more difficult due to the unsteadiness of the flow.

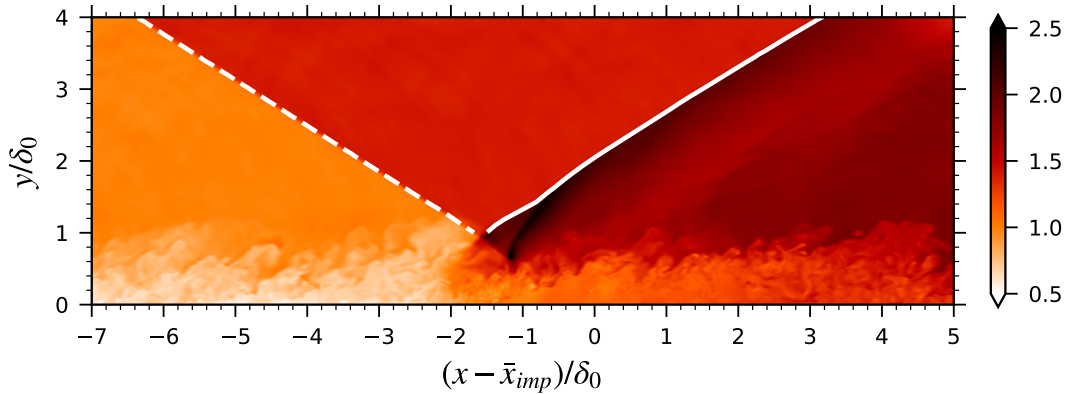


Figure 4.15. Mid-span slice of instantaneous density ρ/ρ_∞ with extracted incident shock (dashed white) and reflected shock (solid white).

For each snapshot, the extracted reflected shock is then approximated by its best-fit line and extrapolated down to the wall to obtain the temporal evolution of the reflected shock foot position. The same procedure can be applied for the incident shock wave for comparison. The obtained signals are depicted in figure 4.16. The

displacement extent of the reflected shock foot is much larger than for the incident shock foot, a difference of one order of magnitude. From the filtered signals, the low-frequency content of the reflected shock foot motion appears more clearly. To further investigate this latter point, Power Spectral Densities have been computed and the results are reported in figure 4.17. A dominant contribution is found at $St_L \approx 0.01$ for the reflected shock foot, while it is not present for the incident shock foot. It is of the same order as the Strouhal found from the PSDs of wall pressure signals (see figure 4.9).

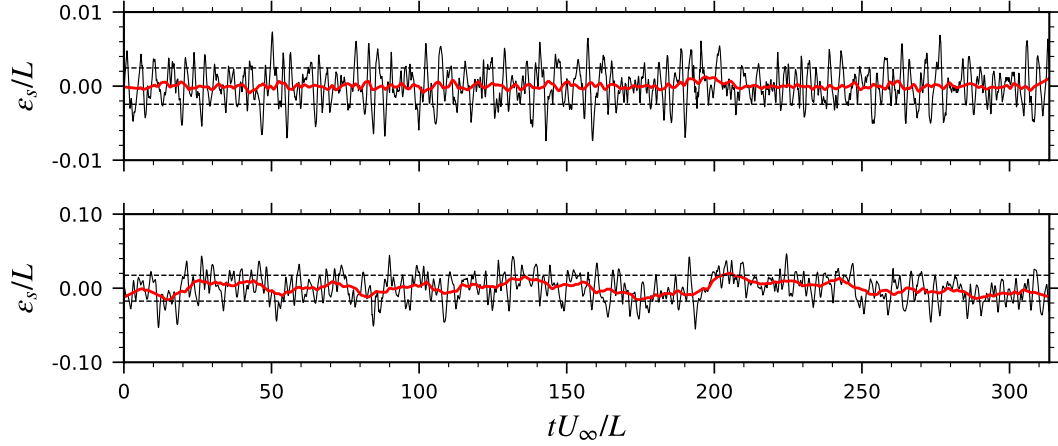


Figure 4.16. Temporal evolution of incident shock foot displacement (*top*) and reflected shock foot displacement (*bottom*). *red* lines are obtained by applying a Savitzky-Golay filter with a window length corresponding to $10L/U_\infty$. *dashed* lines represent the standard deviations.

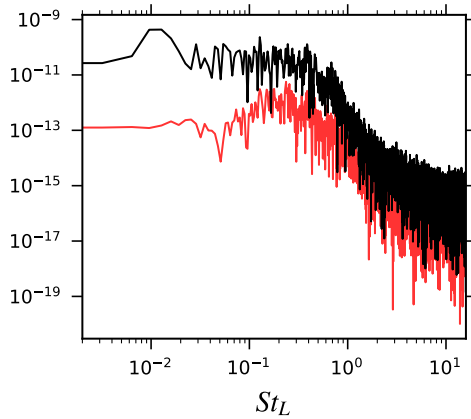


Figure 4.17. Comparison of Power Spectral Densities of the reflected shock foot displacement (*black*) and incident shock foot displacement (*red*).

The snapshots are then classified into several bins. Following Touber (2010), twelve bins of equal width between \pm three standard deviations around the mean are used. Figure 4.18 (*left*) shows the probability density function of the reflected shock foot position, arising from this classification. A Gaussian distribution is superimposed to highlight the resemblance between the two. It further confirms that the movement of the reflected shock is not purely sinusoidal but more complex.

The conditional averages are finally obtained by averaging all the snapshots of the same bin together. The conditionally-averaged flow features of the oblique

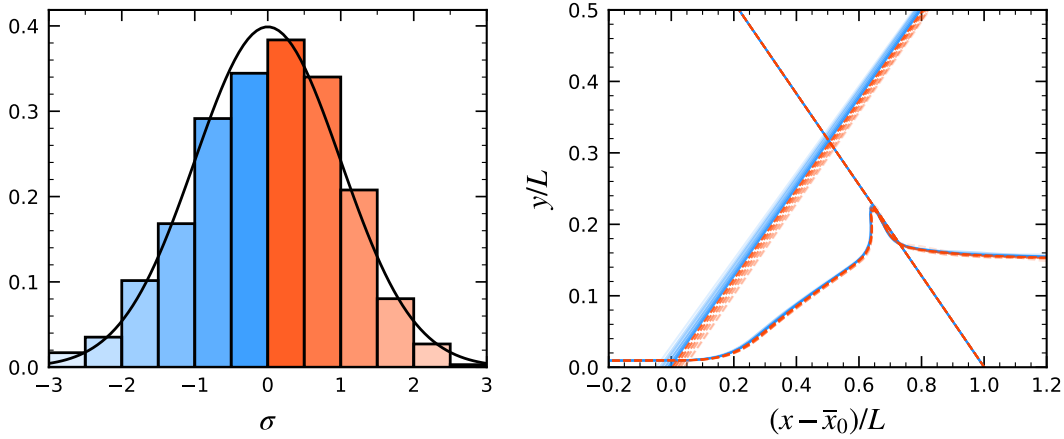


Figure 4.18. Probability density function of reflected shock foot position with superimposed Gaussian distribution (*left*) and conditional averages of the oblique shock wave/boundary layer interaction: best-fit lines of incident and reflected shock waves and sonic lines (*right*). \bar{x}_0 is the streamwise location of the mean reflected shock impingement point.

SWBLI are illustrated in figure 4.18 (*right*). For each bin, the best-fit lines of the incident shock and reflected shock are shown. They are extrapolated down to the wall even though in reality the shocks do not penetrate the subsonic region of the boundary layer. Also shown are the sonic lines. The results are drawn in *blue* for bins for which the reflected shock foot position is more upstream than its mean position and in (*dashed*) *orange* for more downstream positions. Moreover, the closer to the mean, the more opaque the lines are. While all the best-fit lines fall on top of each other for the incident shock wave, the larger amplitude of the reflected shock motion is clear. The best-fit lines of the reflected shock are diverging toward the wall, meaning that the streamwise excursion of the shock reduces away from the wall. This effect was already reported by Dupont et al. (2006) and Toubert (2010). The sonic lines illustrate that for a more upstream reflected shock position, the sonic region is bigger and a larger separation bubble can be expected (and vice versa).

From these conditional averages, the excursion length can be estimated for the present case, which gives $L_{ex}/L \approx 0.092$ at the wall. The same methodology leads to $L_{ex}/L \approx 0.115$ from the results reported by Toubert (2010). These are in rather good agreement compared to each other. Experimental values lie at $L_{ex}/L \approx 0.3$ (Dupont et al., 2005; Dupont et al., 2006; Dupont et al., 2008) but were obtained from pressure or velocity fluctuations using an arbitrarily defined threshold.

Figure 4.19 illustrates the spatial distribution of coherent streamwise velocity in the interaction region, for each bin. The mixing layer and the reflected shock itself clearly stand out, indicating a strong link between these two features. A similar result was reported by Van Oudheusden et al. (2011) for an oblique SWBLI at Mach 2 under incipient separation conditions. For more upstream positions of the shock, the streamwise velocity is lower than the mean in both structures and this tendency is nicely reversed as the shock moves downstream. An excellent match is observed between the structures from opposite bins, for example bins 2 and 9.

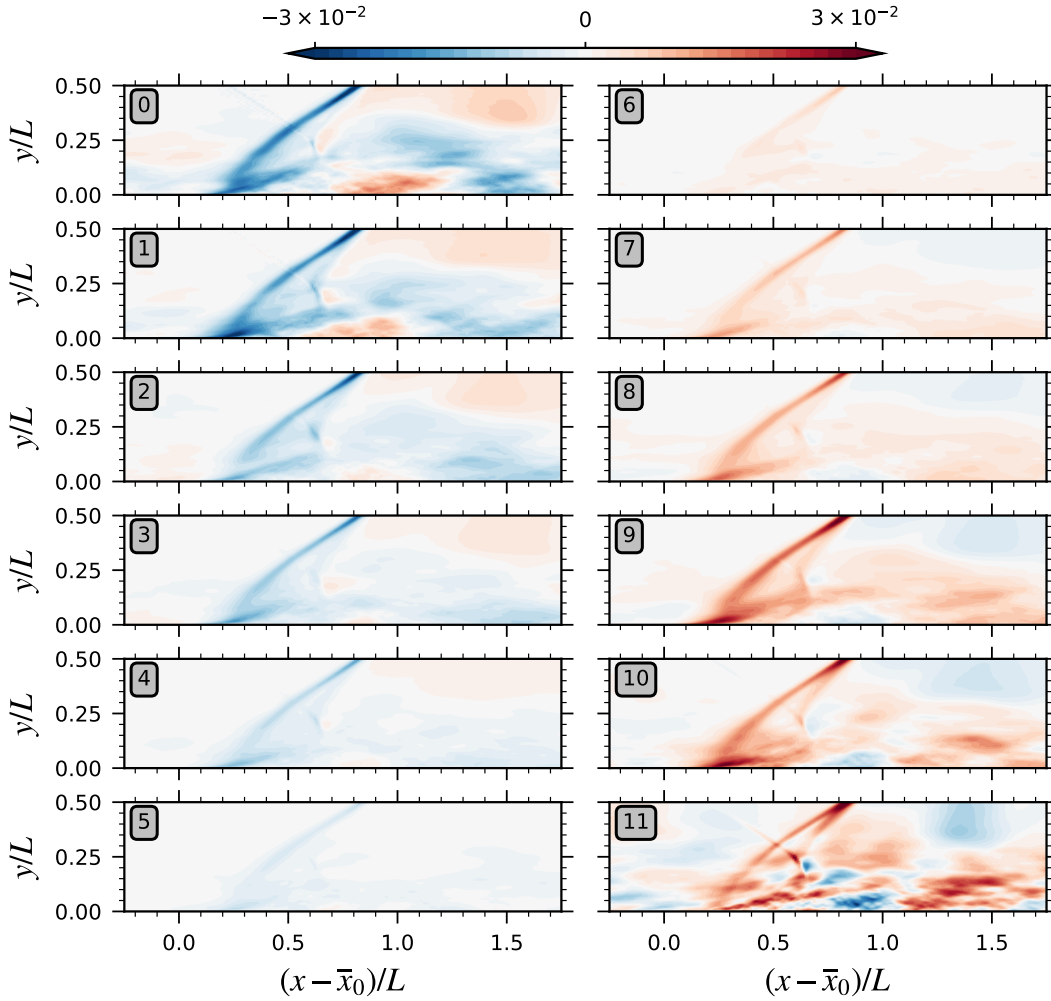


Figure 4.19. Coherent streamwise velocity \tilde{u}/U_∞ for each bin. The bin index is indicated in the top left corner of each subfigure.

Central bins (5 and 6) exhibit almost no coherent component. However, this is expected as they correspond to the locations of the reflected shock that are the closest to the mean. The conditional-averaged flow is therefore practically identical to the mean flow, resulting in a small coherent part. On the contrary, extreme bins (especially bin 11) suffer from a lack of convergence because of the insufficient number of samples. These observations reveal how impractical the study of natural shock oscillation can be. Because of the Gaussian distribution followed by the reflected shock foot position, the criterion used to perform the conditional averaging, the bins containing the coherent flow will be the least converged while the central bins, that are the best converged, will not show any oscillatory component. In the case of periodic forced oscillations, the samples are concentrated at the extremes and such impracticality does not exist.

To assess the effect of the low-frequency motion of the reflected shock on the turbulence in the interaction, the coherent turbulent stresses have been computed.

That is to say, using the triple decomposition,

$$u'_i u'_j = \overline{u'_i u'_j} + \widetilde{u'_i u'_j} + (u'_i u'_j)' = \langle u'_i u'_j \rangle + (u'_i u'_j)' \quad (4.6)$$

and the quantity of interest here is therefore the oscillatory component, $\widetilde{u'_i u'_j}$. The practical derivation is provided in appendix A. Figures 4.20 and 4.21 show the results for the turbulence kinetic energy and the shear stress, respectively. The *left* figures report the mean fields \overline{k}/U_∞^2 and $\overline{u'v'}/U_\infty^2$, as a comparison, whereas the *right* figures depict the coherent fields arising from the difference between two opposite bins $\Delta\widetilde{k}/U_\infty^2$ and $\Delta\widetilde{u'v'}/U_\infty^2$. In particular, bins 2 and 9 are selected as a good compromise to both capture the coherent field and avoid convergence issues.

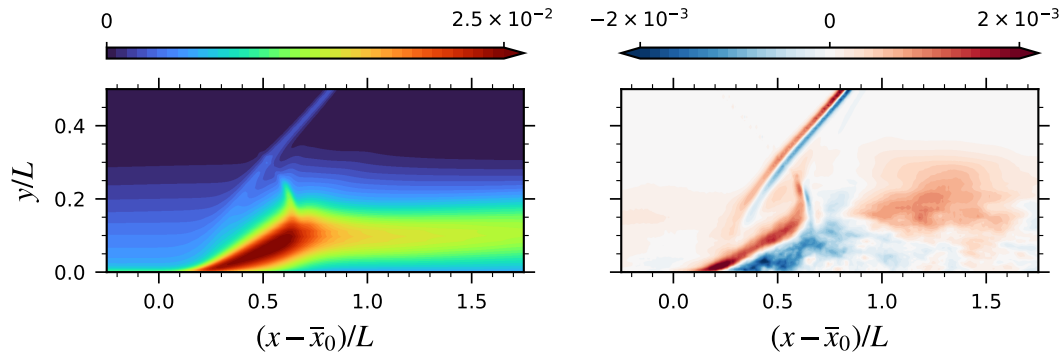


Figure 4.20. Mean turbulence kinetic energy \overline{k}/U_∞^2 (*left*) and differential coherent turbulence kinetic energy $\Delta\widetilde{k}/U_\infty^2$ between bins 2 and 9 (*right*).

Coherent turbulence kinetic is mostly generated in the mixing layer and two regions are discerned. A more detailed analysis reveals that they are distributed on each side of the maximum \overline{k} , meaning that the peak turbulence kinetic energy in the mixing layer remains constant over time (in a low-frequency perspective). Moreover, the two regions are strongly anti-correlated. A more upstream position of the reflected shock will enhance the amplification of turbulence in the front side of the mixing layer, while it will diminish it in the rear part. From a global point of view, coherent turbulence kinetic energy is one order of magnitude lower than the mean, which is not negligible. It becomes even less negligible when considering local values: $\Delta\widetilde{k}$ can indeed reach up to 20% of \overline{k} . Finally, these structures appear to fade downstream of the crossing point between the incident shock and the sonic line. A weak correlation is also pointed out with the upstream boundary layer and at the edge of the downstream boundary layer.

While the picture is rather clear for the turbulence kinetic energy, the shear stress is more complex to analyze. A weak correlation is again emphasized in the upstream boundary layer and at the edge of the downstream boundary layer. However, the interaction region does not exhibit any clear structure. A lack of convergence being put aside, it is most likely that the differential field between the two bins brings out noise. Consequently, it follows that the low-frequency motion of the shock does not influence the shear stress in the interaction region.

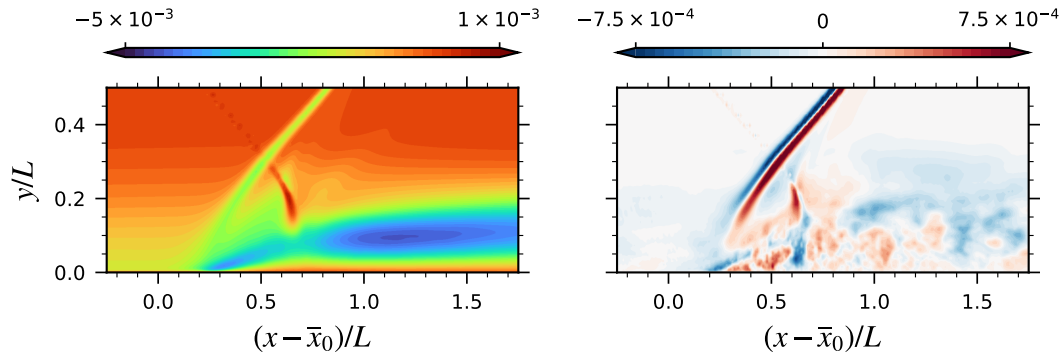


Figure 4.21. Mean shear stress $\overline{u'v'}/U_\infty^2$ (left) and differential coherent shear stress $\Delta \overline{u'v'}/U_\infty^2$ between bins 2 and 9 (right).

4.4 Summary

The canonical case of an oblique shock reflection on a supersonic, fully turbulent boundary layer was introduced in this chapter. It is indeed a relevant validation case for the high-order solver presented previously in order to assess its ability to perform high-fidelity simulations of shock wave/boundary layer interactions.

The results of an implicit Large-Eddy Simulation were then presented. The basic aspects of the flow have been first detailed and, by a systematic comparison, were shown to be consistent with the rich existing literature. In particular, the typical low-frequency unsteadiness of the reflected shock could be captured.

The shock-capturing technique was proven to be robust and efficient at distinguishing the shock system from the boundary layer. Consequently, the artificial viscosity was concentrated around the shocks and let the turbulence intact. A tiny amount of artificial was still perceptible in the interaction region due to the penetration of the shocks but was shown to be negligible. The set of parameters employed was demonstrated to be adequate as no spurious oscillations in the flow quantities were observed across the shocks.

Finally, the framework for the triple decomposition and the extraction of the coherent component of the flow was developed and applied to the acquired data. Coherent structures could be highlighted for the streamwise velocity and for the turbulence kinetic energy. The latter develop following the mixing layer, on each side of the maximum of mean turbulence kinetic energy.

These results give confidence in the high-order solver to be used as a tool to generate high-fidelity data in the context of shock wave/boundary layer interactions. The next chapter introduces the case of a periodically forced transonic flow over a bump, which is the main subject of this work.

Chapter 5

Transonic Bump

Now that the solver is able to handle canonical oblique shock wave/boundary layer interactions, the present chapter seeks to employ it to study the transonic flow over a bump. More particularly, in the framework of harmonic methods, the interest here lies in the periodically forced flow and the description of the resulting harmonic turbulent stresses in the region downstream of the bump.

After an introduction describing past studies related to transonic bumps, both in perturbed and unperturbed conditions, the case investigated is introduced. The analysis starts with an assessment of the influence of the Reynolds number on the flow, using Reynolds-Averaged Navier-Stokes (RANS) simulations. The results from the high-fidelity high-order solver are then presented. First, the undisturbed flow is described, followed by an analysis of the periodically perturbed flow at various forcing frequencies. The coherent flow is finally extracted and budgets of turbulent stresses are reported.

5.1 Introduction

The study of transonic flow over two-dimensional bumps dates back to the experimental works of Delery (1983) and X. Liu and Squire (1988). The flow conditions and bump geometry of the latter study were employed by Sandham et al. (2003) to demonstrate the feasibility of high-fidelity simulations for the fully turbulent transonic flow over a bump. The Reynolds number based on the bump length and free stream conditions $Re_{B_l} = B_l U_\infty / \nu$ was $\approx 2.3 \times 10^5$, around 7 times lower compared to the experiment. The boundary layer was found to separate over the bump much earlier than in the experiment, the peak Mach number was lower, and the results featured a steady shock. More recently, laminar and turbulent interactions in a transonic passage were studied by Priebe et al. (2020) using wall-resolved implicit Large-Eddy Simulation (ILES) on a custom geometry. The solver employed the flux reconstruction scheme for the spatial discretization.

Bron (2004) specifically designed a new two-dimensional bump to study basic flow interactions in turbomachinery and conducted both experiments and (unsteady)

RANS numerical investigations. Other authors employed high-fidelity methods. A summary of the flow conditions in these studies can be found in table 5.1. With fixed backpressure in time, Wollblad et al. (2006) presented the results of LES. The conditions were similar to the experiment with the exception of the Reynolds number, which had to be decreased by a factor of 11.25 to make the computation feasible, giving $Re_{B_l} \approx 3.1 \times 10^5$. A comparison with experimental results was made, even though the shock pattern was different as the boundary layer separates upstream of the position of the shock wave. Also, no large-scale movement of the shock was observed. Frequencies related to bursting events in the upstream boundary layer and to the separated region were detected but were apparently not triggering the shock motion. The effects of flow conditions and computational setup were further examined in Wollblad et al. (2010) in order to rule out possible explanations for the absence of shock motion. Four additional cases were introduced, with different combinations of domain height, outlet pressure and type of top boundary to examine the influence of choked/non-choked flow and/or elliptic leakage along the ceiling. The results showed again the absence of large-scale shock motion, although its innermost part was found to oscillate in some cases. It was argued to be due to elliptic leakage along the bump, the information coming from the separated region. More recently, Brouwer (2016) performed a Direct Numerical Simulation (DNS) but at a higher Mach number (0.79 against 0.7 in Bron (2004)) and at an even lower Reynolds number ($Re_{B_l} \approx 1.7 \times 10^5$). The domain was also twice the wind tunnel height, with a non-reflecting top boundary condition. Motion of the lower part of the shock was highlighted at low frequency. Spectral analysis led to a possible mechanism explaining this motion, connecting bursting events in the upstream boundary layer, the detachment of the recirculation bubble and the shock movement.

Table 5.1. Comparison of flow conditions for studies on the bump of Bron (2004). p_t and T_t are inlet total pressure and total temperature, respectively. p_o is the outlet static pressure. The integration time in convective time units n_{CTU} is given for high-fidelity simulations only.

	M	p_t [kPa]	T_t [K]	p_o [kPa]	Re_{B_l}	n_{CTU}
Bron (2004)	0.70	160	303	98-118	3.81×10^6	/
Wollblad et al. (2006)	0.70	160	303	103.5	3.10×10^5	3
Bodin and Fuchs (2008)	/	/	/	92-108	/	/
Brouwer (2016)	0.79	198	360	/	1.67×10^5	30
Present case	0.70	160	303	106	1.91×10^5	25

The budget of turbulence kinetic energy was analyzed in detail by Marquillie et al. (2008) and Laval and Marquillie (2011) from DNS data of incompressible turbulent flow in a converging-diverging channel, previously studied experimentally by Bernard et al. (2003). The Reynolds number Re_τ (based on the friction velocity and half the channel height) was decreased by an order of magnitude, from $Re_\tau \approx 6500$ in the experiment to $Re_\tau \approx 395$ and $Re_\tau \approx 617$ in the DNS. No shock was found to form, but the simulations still featured flow separation at the lower wall. A complex modification of the balance in the adverse pressure gradient region was described. In particular, turbulent transport was found to have a significant influence in the

presence of flow separation. Schiavo et al. (2015) reported the results from LES for the same configuration, at $Re_\tau \approx 615$ and $Re_\tau \approx 950$. Budgets for each individual turbulent stress were portrayed and illustrated the variation along the wall of their respective contribution to the turbulence kinetic energy budget. The turbulence kinetic energy budget was further investigated in Schiavo et al. (2017) by means of Proper Orthogonal Decomposition and spectral analysis. Turbulent transport was shown to be poorly reconstructed when the most energetic flow modes are considered.

Work was also done on forced transonic flow over a bump. Bur et al. (2006) performed an experimental and numerical study, using URANS. The perturbation was imposed downstream as a periodic pressure signal. The forcing frequencies investigated were low, such that the flow was quasi-steady. A phase lag between the core flow and the boundary layer was observed in the region downstream of the shock, but not in the shock oscillation region. Moroianu et al. (2005) reported the results of ILES on the same geometry, and observed the occurrence of a hysteresis cycle, during which the shock system varied significantly. Investigations of forced oscillation were also performed on the bump of Bron (2004). The unsteady conditions are summarized in table 5.2. Bron (2004) performed again both experiments and URANS simulations. The perturbation frequency reached up to 500Hz in the experiments or 1000Hz for the numerical study. The corresponding reduced frequencies (a parameter introduced by Lighthill (1954)) are $f_r = fB_l/U_\infty \approx 0.4-0.8$ and are particularly pertinent for turbomachinery flows. This range of values is indeed typically encountered in both low and high pressure turbines (Tucker, 2013) and means that convection and periodic fluctuations are two equally dominant mechanisms. The shock motion was found to decrease with increasing perturbation frequency. The latter also largely influenced the unsteady pressure distribution downstream of the shock and a substantial amplification was reported for strong shock wave/boundary layer interaction. Bodin and Fuchs (2008) performed an ILES on that bump geometry. Two frequencies were considered, 5Hz and 50Hz but correspond therefore to reduced frequencies one or two order(s) of magnitude lower than realistic values. The results showed that the shock position exhibits a hysteretic behavior regardless of the frequency. The amplitude of the fluctuation was 8% of the mean, leading to various shock patterns within the same cycle. None of these studies neither dealt with perturbation frequencies relevant for turbomachinery flows nor reported a detailed analysis of the influence of the forcing on the turbulent stresses.

Table 5.2. Comparison of unsteady flow conditions for studies on the bump of Bron (2004).

	Re_{B_l}	$A_{\tilde{p}_o}/\bar{p}_o$	f [Hz]
Bron (2004)	3.81×10^6	0.01/0.02	50/100/250/500(/1000)
Bodin and Fuchs (2008)	/	0.08	5/50
Present case	1.91×10^5	0.02	250/500/1000

5.2 Flow conditions and computational setup

The case under investigation is the transonic flow over a bump, the geometry of which is taken from the experiment of Bron (2004). The bump length B_l is 0.184m and its thickness B_h is 10.48mm, whereas the wind tunnel height L_y is 0.12m (see figure 5.1). The upstream conditions are a total pressure of 160kPa, a total temperature of 300K and a Mach number of 0.7. The ratio ρ_w/ρ_∞ is around 0.9 and is close enough to unity to assume that compressibility effects in the boundary layer are negligible, as also assumed by Sartor et al. (2012). Whereas various levels of backpressure were imposed in the experiment, the focus is here for the case with a mean static pressure \bar{p}_o of 106kPa. At these conditions, a shock wave develops in the rear part of the bump, promoting flow separation. Various cases will be considered in this work depending on the way the backpressure evolves in time. Broadly speaking, the outlet static pressure p_o follows equation 5.1

$$p_o(t) = \bar{p}_o + A_{\tilde{p}_o} \sin(2\pi ft) . \quad (5.1)$$

The case with steady backpressure ($A_{\tilde{p}_o} = 0$) will be referred to as the baseline case. Then, three cases with fluctuating backpressure will be presented. In the context of turbomachinery, this perturbation mimics the potential effects of a rotor/stator interaction (Korakianitis, 1993). The amplitude is fixed at 2% of the mean ($A_{\tilde{p}_o}/\bar{p}_o = 0.02$) and the frequency is either 250Hz, 500Hz or 1000Hz. The corresponding reduced frequencies $f_r = fB_l/U_\infty$ are, respectively, ≈ 0.2 , ≈ 0.4 and ≈ 0.8 . As mentioned in the introduction, these are values commonly met in low and high pressure turbines (Tucker, 2013) and are consequently relevant for turbomachinery applications. The Reynolds number based on the bump length Re_{B_l} amounts to $\approx 1.9 \times 10^5$, which is 20 times lower in comparison to the experiment. The fluid is therefore air assumed as a perfect gas but with a reference dynamic viscosity (see equation 2.11) multiplied by the same factor. Tables 5.1 and 5.2 summarize the different flow conditions and compare them with the available literature on this bump.

The choice of perturbation frequency and amplitude is rather limited. Reducing the frequency will increase the computing time since a sufficiently large number of periods has to be performed to get a correct convergence of the results. On the other side, increasing the frequency will weaken the effects of the perturbation as the experiments showed (Bron, 2004). Decreasing the amplitude will have the same impact as an increase in frequency, whereas the amplitude cannot be increased too much as, in the context of the Non-Linear Harmonic method, the linearity assumption requires a small amplitude.

The computational domain, depicted in figure 5.1, is a rectangular box with the bump geometry as bottom boundary. With respect to the bump, the beginning of which is located at $x = 0$ m, the domain extends from $30\delta_0$ upstream to $20\delta_0$ downstream. In the spanwise direction, the domain is $4\delta_0$ wide. Following the experimental measurements of Sigfrids (2003), the reference boundary layer thickness δ_0 is here 8.95mm, measured at $x = -0.1$ m. This value was also considered in other numerical studies (Wollblad et al., 2006). The dimensions of the domain (L_x , L_y and

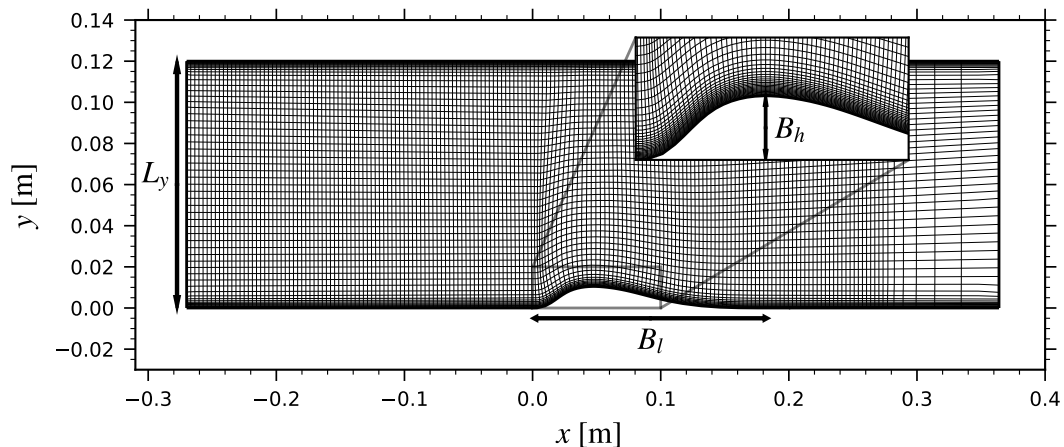


Figure 5.1. Computational domain and mesh. One gridline out of two is represented in the full domain view.

L_z , respectively) and inlet location x_{in} are summarized in table 5.3 and compared with other high-fidelity simulation setups of this bump from the literature.

Table 5.3. Comparison of domain size and inlet location for high-fidelity simulations of the bump of Bron (2004).

	L_x [m]	L_y [m]	L_z [m]	x_{in} [m]
Wollblad et al. (2006)	0.36	0.1186	0.039	-0.09
Bodin and Fuchs (2008)	1.15	0.12	0.2	/
Brouwer (2016)	0.86	0.2186	0.078	-0.2
Present case	0.634	0.12	0.036	-0.27

The mesh consists of hexahedra only and is also illustrated in figure 5.1. Using the high-order flux reconstruction approach, the target grid resolution is evaluated by considering a uniform distribution of the solution points within the cell, here with polynomial order three. In the streamwise direction, the grid spacing is initially constant, with $\Delta x^+ = 16$, in wall units based on the upstream conditions. Over the last $10\delta_0$, the mesh is progressively coarsened to $\Delta x^+ = 160$ to dampen high-frequency reflected waves. In the spanwise direction, $\Delta z^+ = 12$. The mesh is stretched in the wall-normal direction. Bottom and top boundary layers comprise 100 solution points each, the first one targeting $y^+ = 1$. The exact distribution of the solution points leads in fact to $y_w^+ \approx 0.28$. From the edge of the boundary layers and in the free stream, $\Delta y^+ = 16$. The total number of degrees of freedom rises to approximately 80 million. Finally, as observed in the zoomed-in view, the orthogonality of the cells near the bump wall is ensured over a layer of $\approx \delta_0$. A comparison of number of degrees of freedom and grid resolution with the literature is provided in table 5.4.

The inlet boundary is fully subsonic, with total pressure, total temperature and velocity direction imposed. These profiles, as well as Reynolds stress profiles (needed for the digital filtering approach), are taken from the averaged solution of

Table 5.4. Comparison of number of degrees of freedom and grid resolution for high-fidelity simulations of the bump of Bron (2004). ^avalues taken from figures 11 and 12 in Wollblad et al. (2006). ^bvalues estimated using the Blasius law.

	N_x	N_y	N_z	N	Δx^+	Δz^+	y_w^+
Wollblad et al. (2006)	306	131	171	7.0×10^6	100^a	20^a	0.5
Bodin and Fuchs (2008)	/	/	/	/	/	/	/
Brouwer (2016)	1920	576	176	1.9×10^8	20^b	20^b	0.64-0.93
Present case	1416	452	120	7.7×10^7	16	12	0.3

a precursor ILES of a turbulent boundary layer in the same flow conditions. The digital filtering parameters are $I_x/\delta_0 = 0.5$ and $I_z/\delta_0 = 0.375$. I_y is varying in the wall-normal direction such that $I_y = I_z$ at the edge of the boundary layer and the number of neighbors in the filter is practically constant and around 350. The velocity to evaluate the Lagrangian time scale is taken as $0.9U_\infty$. The top and bottom boundaries are no-slip adiabatic walls and periodic boundary conditions are imposed in the spanwise direction. A spatially constant static pressure is imposed along the fully subsonic outlet boundary.

The parameters of the shock-capturing technique (see subsection 3.3) are $s_0 = -4.5$, $\kappa = 1.5$, $C_T = 0.01$ and $s_{D,0} = 0.2$. Density is used as the sensor variable.

The explicit time step is 4×10^{-8} s and corresponds to a CFL number of around 2.5. The simulation is initially restarted from an initial RANS solution for a duration of around 45 convective time units (CTU) to set up the flow for the baseline case. One CTU is evaluated here with respect to the bump length and is therefore equal to B_l/U_∞ . For the forced cases, the perturbation is then applied for 30 additional CTUs so that the periodic flow can develop. The duration of the transient phases was checked to be sufficiently long by monitoring the shock location. The latter was considered at its mid-height since upstream propagating waves travel slower in the potential flow and the effect of the perturbation will be felt later there compared to the boundary layer. The initial transient was deemed to be over when the shock had stabilized for long enough. Indeed, the shock position is dependent on the inlet and outlet conditions and is therefore an image of the viscous losses in the top and bottom wall boundary layers. Consequently, a stable shock will indicate that boundary layers are developed properly. The duration of the periodic transient allowed the shock to describe multiple cycles at the forcing frequency and is independent of the forcing frequency since the mean propagation velocity is identical. After the transient phase(s), all the cases are finally run over the same physical time which corresponds to exactly ten periods at 500Hz or approximately 25 CTUs. This is summarized in table 5.2.

The data are extracted starting from the transient phase(s) and are collected every 50 iterations at the bump wall and on a slice at mid-span. The associated sampling rate is 500kHz, sufficiently high to capture the frequencies of the energy-carrying eddies of the upstream boundary layer ($\mathcal{O}(U_\infty/\delta_0) \approx 25$ kHz). Both instantaneous data and instantaneous span-averaged data are available. The latter is employed to benefit from the homogeneity of the flow in that direction, which greatly helps

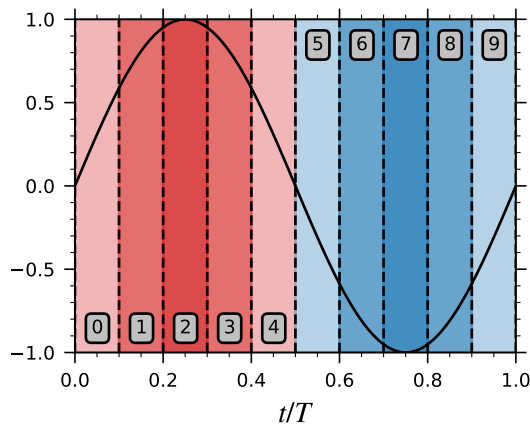


Figure 5.2. Labeling of the bins with respect to a reference oscillator

to improve the convergence of the results. Finally, probes are placed at various locations and record the primitive variables at every iteration (the sampling rate being therefore 25MHz).

Two averaging operators are needed when using the triple decomposition. Time-averaging is performed to obtain the mean component of the flow and phase-averaging is employed to extract the mean and the coherent components together. The difference between the two therefore allows to isolate the coherent component. Each period is decomposed here into ten bins of equal width. The corresponding labeling of the bins, with respect to a reference oscillator, is illustrated in figure 5.2. The choice of the reference oscillator will be discussed in the results section. The assumption for the triple decomposition to be valid is verified since several orders of magnitude separate one period at the forcing frequency (which is in the worst case 4×10^{-3} s) and the characteristic time scale of the incoming boundary layer ($\mathcal{O}(\delta_0/U_\infty) \approx 3.8 \times 10^{-5}$ s).

5.3 Results

5.3.1 Influence of Reynolds number

Reducing the Reynolds number is not without consequences and therefore, before having a look at the results from ILES, this short digression aims at describing the effects that could be expected from this modification. Because an ILES would be too computationally expensive at the reference conditions, the results from RANS simulations are presented. The simulations are performed using Cadence FINE™/Turbo flow solver, initially developed by Rizzi et al. (1993). The three-dimensional (U)RANS equations are discretized following a finite volume approach in which the spatial derivatives are evaluated with a centered second-order scheme in combination with a Jameson-type artificial dissipation (Jameson et al., 1981) while a 4-stages explicit Runge-Kutta scheme is used for the temporal discretization. Convergence is improved by means of multigrid, local time-stepping and implicit residual smoothing. For unsteady computations, a dual-time stepping method is employed, the temporal derivative being evaluated with a second-order backward

Euler difference. To highlight the influence of the Reynolds number, the simulations are performed in both the reference conditions ($Re_{B_1} = 3.81 \times 10^6$) from the experiments and the modified conditions ($Re_{B_1} = 1.91 \times 10^5$), used for the ILES. In the first instance, turbulence is accounted for with the $k - \omega$ model from Wilcox (2006). Each flow conditions has its own mesh to ensure that in any case y_w^+ is ≈ 1 .

Figure 5.3 shows the friction and pressure coefficients on the bump wall for both the reference conditions and the reduced Reynolds number conditions. For validation purposes, a comparison with the results from Bron (2004) is provided for the pressure coefficient. The latter were obtained from a two-dimensional RANS simulation at the same operating point, in the reference conditions and using the $k - \omega$ turbulence model as well. The curves being practically on top of each others, this gives confidence in the numerical setup employed here for the RANS simulations. At the reduced Reynolds number, the friction coefficient clearly exhibits a longer separation bubble, with the separation and reattachment points more upstream and more downstream, respectively. As indicated by the pressure coefficient, the shock is located more upstream and the pressure gradient is more diffused.

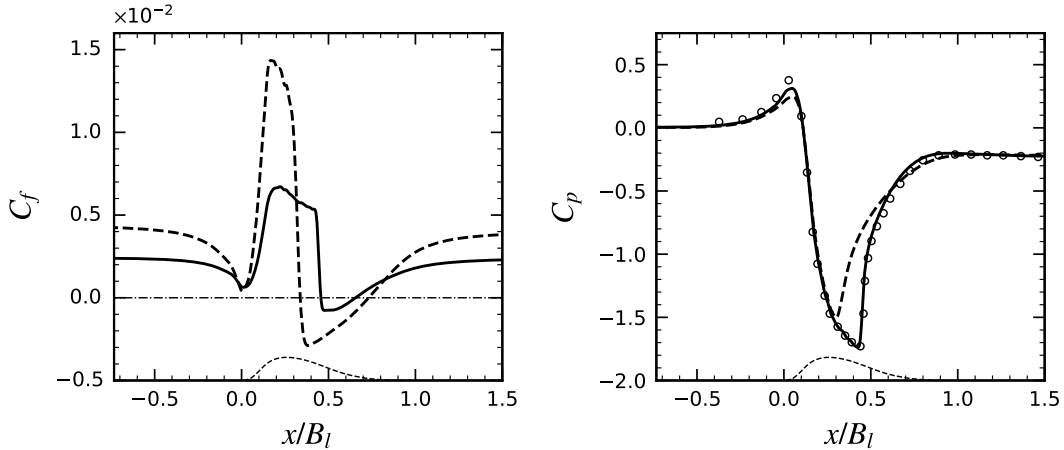


Figure 5.3. Comparison of mean friction coefficient (*left*) and mean wall pressure coefficient (*right*) on the bump wall from RANS simulations - $Re_{B_1} = 3.81 \times 10^6$ (*solid*), $Re_{B_1} = 1.91 \times 10^5$ (*dashed*) and results from Bron (2004) (*symbols*). The *thin dashed* line represents the bump geometry.

To obtain further insights on the evolution of the shock pattern, figure 5.4 depicts density contours over the bump. In the reference conditions, a strong shock wave is observed from the bump to the top wall. The flow is choked and the boundary layer separates at the shock impingement location. When the Reynolds number is reduced, separation occurs much earlier and the resulting thickening of the boundary layer leads to an upstream displacement of the shock because of the reduced cross section. Near the bump, the strong shock is replaced by a lambda shock, which explains the more gradual pressure rise reported previously. Also, the flow is not choked anymore as the shock has vanished at the top wall. The maximum Mach number decreases from 1.44 in the reference conditions to 1.29 in the modified conditions.

Finally, a sensitivity analysis is performed regarding the turbulence model. For both flow conditions, table 5.5 lists the location of the separation and reattachment

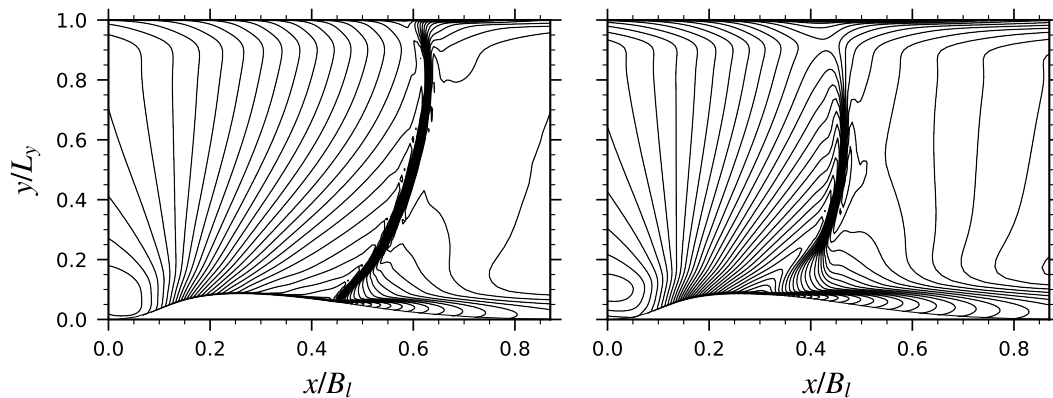


Figure 5.4. Mean ρ/ρ_∞ from RANS simulations, 40 equally-spaced contours between 0.4 and 1.1 - $Re_{B_l} = 3.81 \times 10^6$ (left) and $Re_{B_l} = 1.91 \times 10^5$ (right).

points for the Spalart-Allmaras model (Spalart & Allmaras, 1992), the $k - \omega$ model (Wilcox, 2006), the $k - \omega$ SST model (Menter, 1992) and the Explicit Algebraic Reynolds-Stress model (EARSM) implemented in Mehdizadeh et al. (2012). The extension of the separation bubble at the modified conditions is systematic and therefore not an effect of the modeling of turbulence. However, none of the models agree on the same location of separation and reattachment. The EARSM consistently shows the smallest separation bubble with, in particular, the most upstream reattachment. On the opposite lies the Spalart-Allmaras model, which exhibits the longest separation bubble and the most downstream reattachment. Finally, the $k - \omega$ SST model always displays the earliest separation. The shock locations are also reported. Whereas in the reference conditions this could be directly obtained from the pressure coefficient, the picture is not as clear in the modified conditions because of the diffused pressure gradient. To avoid any ambiguity, the shock location is therefore computed at mid-height. It is observed that it evolves in accordance with the separation point.

Table 5.5. Comparison of separation and reattachment points location as well as shock position at mid-height for various turbulence models.

Turbulence model	Reference conditions $Re_{B_l} = 3.81 \times 10^6$			Modified conditions $Re_{B_l} = 1.91 \times 10^5$		
	x_{sep}/B_l	x_{rea}/B_l	x_s/B_l	x_{sep}/B_l	x_{rea}/B_l	x_s/B_l
Spalart-Allmaras	0.416	0.931	0.582	0.298	0.947	0.443
$k - \omega$	0.456	0.655	0.595	0.337	0.731	0.461
$k - \omega$ SST	0.379	0.863	0.552	0.296	0.872	0.401
EARSM	0.422	0.626	0.582	0.310	0.663	0.431

The short investigation performed here using RANS simulations indicates that the main effect of the reduced Reynolds number is the upstream displacement of the separation point. As a result, the reattachment point moves downstream and the separation bubble grows. The shock is therefore located more upstream and is smeared near the bump wall, leading to a more progressive pressure rise. The

turbulence model sensitivity study illustrates that no agreement is found on the location of these flow phenomena regardless of the flow conditions. These results are nevertheless purely qualitative because of the known shortcomings of low-fidelity methods for such configurations. For the rest of the analysis, the high-fidelity setup introduced earlier is employed and should give more accurate insights on the physics of the flow.

5.3.2 Baseline flow

To start with an overall description of the flow field, figure 5.5 shows instantaneous contours of density gradient magnitude at mid-span and streamwise velocity near the bump wall, at $y^+ \approx 10$. A fully turbulent boundary layer is observed upstream of the bump, with its characteristic streaks. Approaching the bump, the flow slightly decelerates on the concave part and then quickly accelerates as it evolves on its convex part. The boundary layer undergoes partial re-laminarization due to the favorable pressure gradient there, which is also witnessed as the structures are widening in the spanwise direction. An oblique compression wave is generated when the flow separates and forms a large lambda pattern as it joins the normal shock standing downstream, responsible for the remaining compression. The separated shear layer is unstable, breaks down to turbulence and as a consequence, additional weak oblique compression waves are observed at the root of the normal shock. Finally, the boundary layer slowly recovers its initial, unperturbed state while reaching the end of the domain as thin and elongated structures appear again.

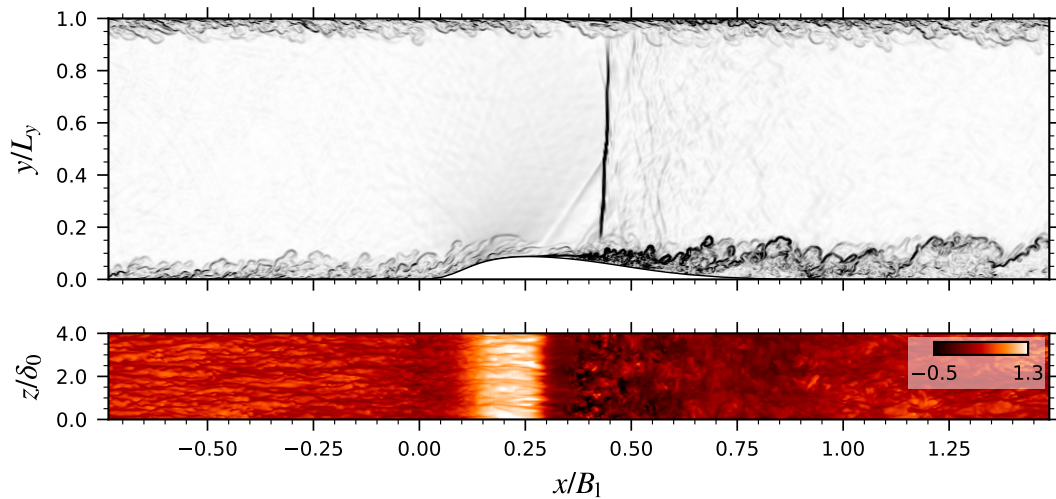


Figure 5.5. Instantaneous density gradient magnitude at mid-span (*top*) and instantaneous streamwise velocity u/U_∞ near the bump wall, $y^+ \approx 10$ (*bottom*).

Before proceeding further with the analysis of the flow, a sanity check of the computational setup is performed. The grid resolution is first assessed. As the solver employs the flux reconstruction approach, the actual resolution is based on the distance between the solution points and not the cell size. Hereunder, Δx^+ and Δz^+ are evaluated using the respective grid spacing divided by the number of

solution points in one direction (that is to say the polynomial order + 1). Since the solution points are not equally spaced within a cell, this provides an averaged resolution. For y_w^+ , however, the actual location of the first solution point off the wall is considered. Figure 5.6 shows the streamwise evolution of these quantities, in wall units calculated at the bump wall. Upstream of the bump, the resolution is close to the expected values $\Delta x^+ = 16$ and $\Delta z^+ = 12$. In the wall-normal direction, the very first solution point stands at a distance of $y_w^+ \approx 0.3$ from the wall. It is observed that the resolution remains around the target values or below, exception made of a short part of the bump over which it slightly worsens. At maximum, $\Delta x^+ \approx 30$, $\Delta z^+ \approx 20$ and $y_w^+ \approx 0.5$. Nevertheless, the resolution is still adequate for wall-resolved implicit large-eddy simulations. The resolution at the top wall (not illustrated here) shows less variation and is practically constant, equal to the target values.

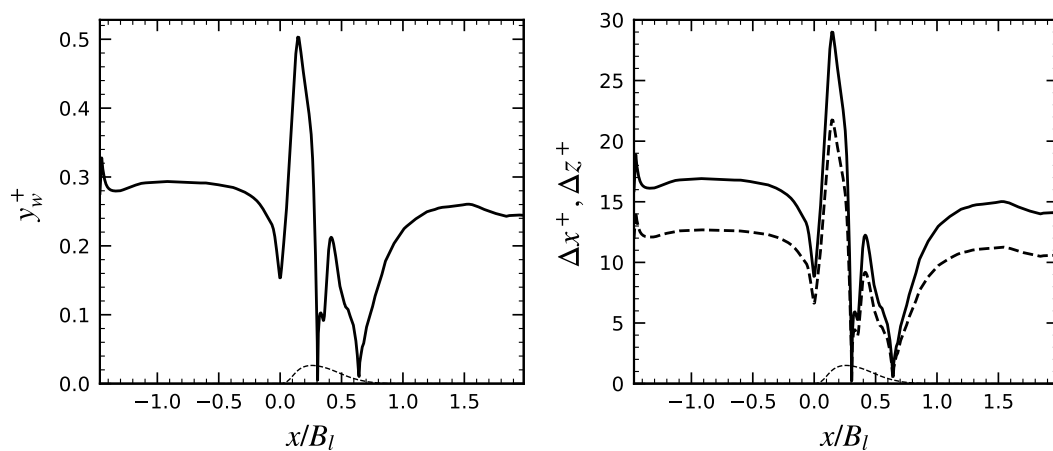


Figure 5.6. Mesh resolution at the bump wall - y_w^+ (left), Δx^+ and Δz^+ , respectively, solid and dashed lines (right). The thin dashed line represents the bump geometry.

Another assessment of the grid resolution is presented in figure 5.7. The effective mesh spacing $\Delta = (\Delta x \cdot \Delta y \cdot \Delta z)^{1/3}$, again in terms of solution point, is compared to the estimated local Kolmogorov scale η . The latter being most likely under-predicted, as dissipation is under-predicted, the results give an optimistic perspective. However, they still inform about the areas of the flow that are the most affected by the under-resolution. The highest ratio is found on the downstream part of the bump, but barely exceeds eight. In the boundary layer upstream of the bump, the ratio does not go above seven in the near-wall region. A value of five is typically taken as reference to state that all the relevant scales of turbulent motion are appropriately resolved (Pirozzoli & Bernardini, 2011). A slight under-estimation of dissipation is therefore expected here, especially on the downstream part of the bump, but the resolution is still acceptable.

The sanity check is pursued by looking at the quality of the boundary layer upstream of the bump. Since synthetic turbulence is generated at the inflow (using the digital filtering technique), it is indeed necessary to ensure that realistic turbulence can develop before reaching the bump. Figure 5.8 (left) shows the mean velocity profile in wall units, at the station $x/\delta_0 = -15$. This station is located $15\delta_0$

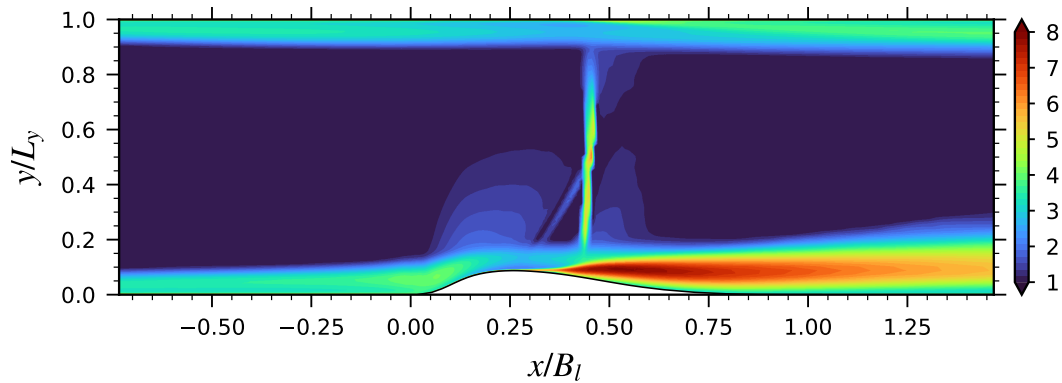


Figure 5.7. Ratio between local grid size and estimated Kolmogorov length scale Δ/η in the region downstream of the bump.

downstream of the inflow plane and $15\delta_0$ upstream of the start of the bump, that is to say sufficiently far away from the inlet to get rid of its unrealistic effect and sufficiently far away from the bump in order to avoid any upstream influence. The results have been interpolated back on the actual solution points and DNS data for incompressible boundary layers (Schlatter & Örlü, 2010) at the same Re_θ are used as a reference. The *dashed black* line indicates the Van Driest transformed velocity profile and is in perfect agreement with the incompressible normalization (*solid blue* line) in the viscous sub-layer and the logarithmic layer. However, a slight difference is observed in the defect layer, leading to a free stream velocity 1.4% lower with the incompressible normalization. The same agreement is found with respect to the DNS data. The free stream velocity is this time 1.9% lower. Figure 5.8 (*right*) depicts the normalized mean Reynolds stress profiles at the same station, again compared with DNS data from Schlatter and Örlü (2010), and shows a very good fit. The overestimation of the peak $\overline{u'u'}$ is an effect of the under-resolution (Poggie et al., 2015). These results show that the upstream boundary layer is properly developed and has recovered from the treatment at the inlet plane. Also, compressibility effects are small in this case, even if the bulk Mach number is 0.7. This was also highlighted in Wenzel et al. (2017) by performing DNS of compressible turbulent boundary layers at varying subsonic Mach numbers.

The assumption of incompressibility is finally supported by considering the turbulence Mach number, defined by $M_t = \overline{u'_i u'_i}^{1/2} / \bar{a}$. For strong turbulent fluctuations, that is to say that are comparable to the mean speed of sound, it is expected that compressibility effects will modify the properties of turbulence. The distribution of turbulence Mach number in this case is illustrated in figure 5.9, and shows, however, that its values remain small. In the upstream boundary layer, it does not exceed 0.1, while it can reach 0.4 very locally on the downstream part of the bump. With the latter value, the difference between Favre and Reynolds averages for an adiabatic flat plate is of a few percents (Smits & Dussauge, 2006) only, hence compressibility effects in the boundary layer can be assumed to be negligible.

Another aspect to take into consideration when simulating statistically two-dimensional flows is the spanwise extent of the domain, which should be sufficient to

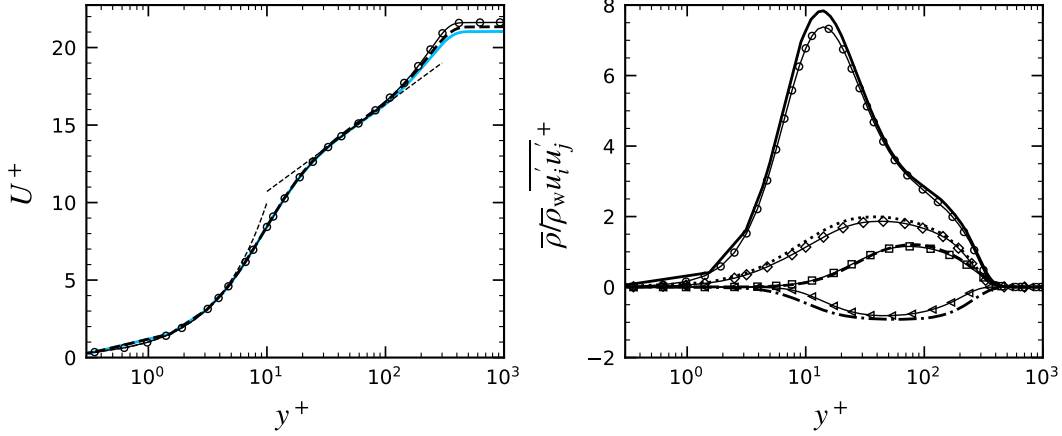


Figure 5.8. Boundary layer profiles at $x/\delta_0 = -15$ - Streamwise velocity, incompressible (solid blue) and Van Driest normalization (dashed black) (left) and Reynolds stresses (right), compared to DNS data for incompressible boundary layers from Schlatter and Örlü (2010) at $Re_\theta = 1000$ (symbols).

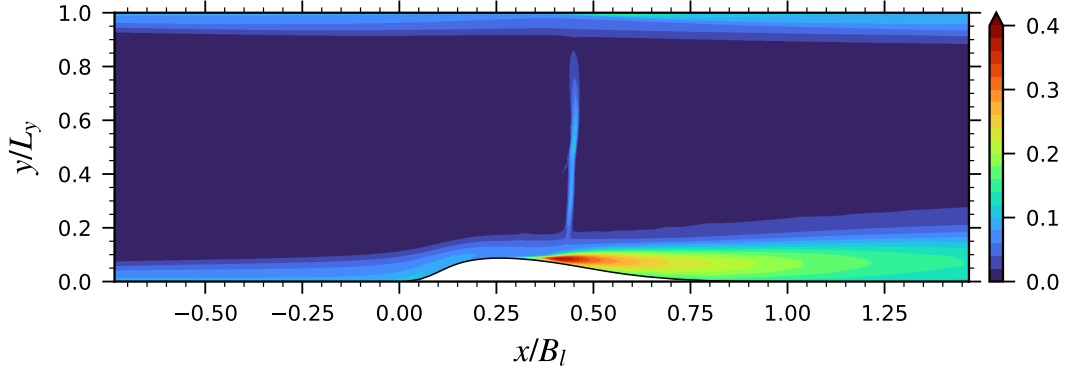


Figure 5.9. Distribution of turbulence Mach number M_t .

accommodate even the widest flow structures. This is usually verified by means of two-point streamwise velocity correlation in the spanwise direction. More precisely, the correlation coefficient is defined by

$$C_{uu}(x, y, \Delta z) = \overline{u'(x, y, z)u'(x, y, z + \Delta z)} / \overline{u'(x, y, z)u'(x, y, z)}, \quad (5.2)$$

and figure 5.10 shows the results for two stations, one upstream of the bump ($x/\delta_0 = -15$) and one downstream of the interaction ($x/\delta_0 = 16.67$). For both stations, the streamwise velocity is taken at a distance $y/\delta_0 = 0.5$ off the bump wall. It is observed that the correlation coefficient quickly drops to zero for the upstream station, at a distance $\Delta z/L_z \approx 0.08$. Downstream of the interaction, larger structures are expected because of the thickening of the boundary layer. This explains that the zero-crossing point of the correlation coefficient lies at a further distance, $\Delta z/L_z \approx 0.25$. In any case, this occurs within half the domain width and therefore the latter is deemed to be sufficiently large.

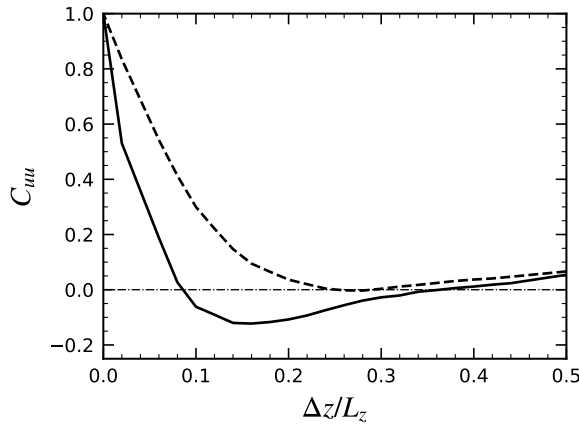


Figure 5.10. Two-point streamwise velocity correlation coefficient in the spanwise direction at $y/\delta_0 = 0.5$ - upstream of the bump, $x/\delta_0 = -15$ (*solid*) and downstream of the interaction, $x/\delta_0 = 16.67$ (*dashed*).

As for the validation case of the oblique shock wave/boundary layer interaction, the performance of the shock-capturing technique is finally assessed. Averaged shock sensor, Ducros sensor and artificial viscosity are depicted in a similar manner in figure 5.11. The shock sensor is able to detect the normal shock but is also considering the entire downstream region as well as the upstream boundary layer, close to the wall. The original method would have applied artificial viscosity since $s_e > s_0 - \kappa$ as the contour line indicates. Because of high levels of vorticity, both the upstream boundary layer and the downstream region show value under the threshold $s_{D,0}$, and as a consequence, the resulting artificial viscosity is concentrated only around the normal shock. This is another proof that the proposed method is efficient when it comes to stabilize flows in which shock waves and turbulence are interacting. Shocks are properly captured and the turbulent regions are left untouched.

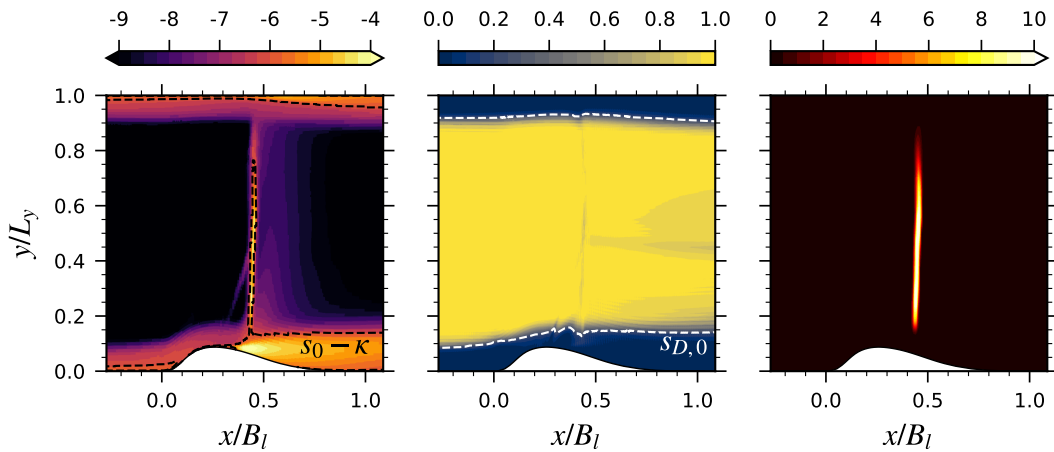


Figure 5.11. Averaged shock sensor s_e with $s_0 - \kappa = -6.0$ contour line (*left*), averaged Ducros sensor s_D with $s_{D,0} = 0.2$ contour line (*center*) and averaged artificial viscosity normalized by the local kinematic viscosity ε/ν (*right*).

Figure 5.12 (*left*) illustrates the mean friction coefficient with its Probability Density Function (PDF). As the incoming flow is subsonic, the bump has an upstream influence that is observed up to $x/B_l \approx -0.45$. Nevertheless, the friction coefficient steadily decreases already before, further confirming that the inflow is far

enough from the bump for the turbulence to develop properly. Over the bump, the friction coefficient reaches its maximum 1.47×10^{-2} at $x/B_l \approx 0.15$, in the favorable pressure gradient region. The flow then separates at $x/B_l \approx 0.3$ and reattaches at $x/B_l \approx 0.65$. It is noted that the first location is slightly downstream the section throat ($x/B_l \approx 0.26$). In between, the distribution is typical of thin separated zones (Sandham et al., 2003) with first a short region over which the skin friction is barely negative, and a second, longer region with larger negative values. The minimum is -3.2×10^{-3} and is found at $x/B_l \approx 0.4$. The superimposed PDF shows moreover that the first part is associated with a low variance. It is actually referred to as the region of stable recirculation (Brouwer, 2016). On very rare occasions, the flow almost reattaches (at $x/B_l \approx 0.35$). The second part exhibits a much higher variance that is linked to the vortex shedding occurring at the breakdown of the shear layer. Similar descriptions are provided in previous studies on the same bump geometry, even though the flow conditions were different (Brouwer, 2016; Wollblad et al., 2006) but also for other configurations with (Sandham et al., 2003) or without shock wave interaction (Laval & Marquillie, 2011; Schiavo et al., 2015; Schiavo et al., 2017). It is also noted that among the turbulence models presented in the results of section 5.3.1, the EARSM is by far the closest in terms of separation and reattachment locations (reported in table 5.5). Nevertheless, it is not able to predict the correct pattern of friction coefficient in the separated region. As for the $k - \omega$ model (see figure 5.3, left), it indeed exhibits a single, global minimum. This further illustrates the inability of lower fidelity methods to accurately represent the physics of the complex flow phenomena featured in this configuration, and therefore the need for high-fidelity simulations.

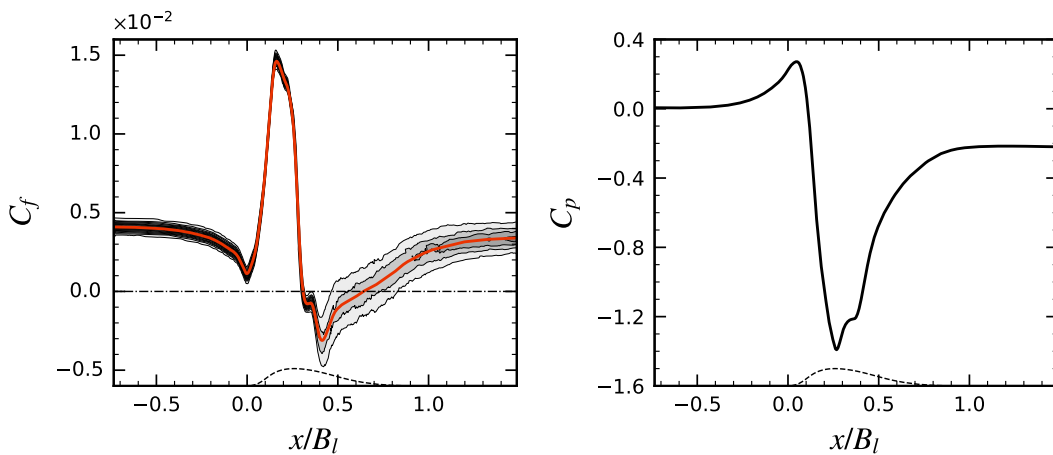


Figure 5.12. Mean friction coefficient (*solid red*) with superimposed PDF, 8 equally-spaced contours between 0.02 and 0.40 (*left*) and mean wall pressure coefficient (*right*) on the bump wall. The *dashed* line represents the bump geometry.

Regarding the pressure coefficient on the bump wall (see figure 5.12, *right*), the upstream influence of the bump is observed too. The favorable pressure gradient region starts at $x/B_l \approx 0.05$ and extends up to $x/B_l \approx 0.25$, which coincides with the location of the minimum C_p . This is located right after at the section throat. Downstream, pressure first rises as the flow undergoes compression from the

weak oblique wave and reaches a plateau that corresponds to the region of stable recirculation. Further downstream, pressure rises again due to the effect of the normal shock and finally recovers to reach the imposed outlet value. This is again not predicted by the turbulence models presented earlier (see figure 5.3, *right*).

The attention is now focused on turbulence, and the way it evolves over the bump. Figure 5.13 shows the contours of the three components of turbulence intensity, normalized by the upstream friction velocity. The highest intensities are found in the downstream part of the bump, as a consequence of the vortex shedding occurring there. u' is produced as soon as the boundary layer separates whereas v' and w' shows higher intensities starting from the end of the region of stable recirculation ($x/B_l \approx 0.35$). On the upstream convex part of the bump, u' decreases as an effect of the favorable pressure gradient. A thin contour of v' is observed from the top of the bump and is related to the separation of the flow. Finally, higher intensity of w' is shown upstream and on the first part of the bump, which is in line with the spanwise expansion of the structures already highlighted in figure 5.5. This description is in very good agreement with previous works, especially Brouwer (2016).

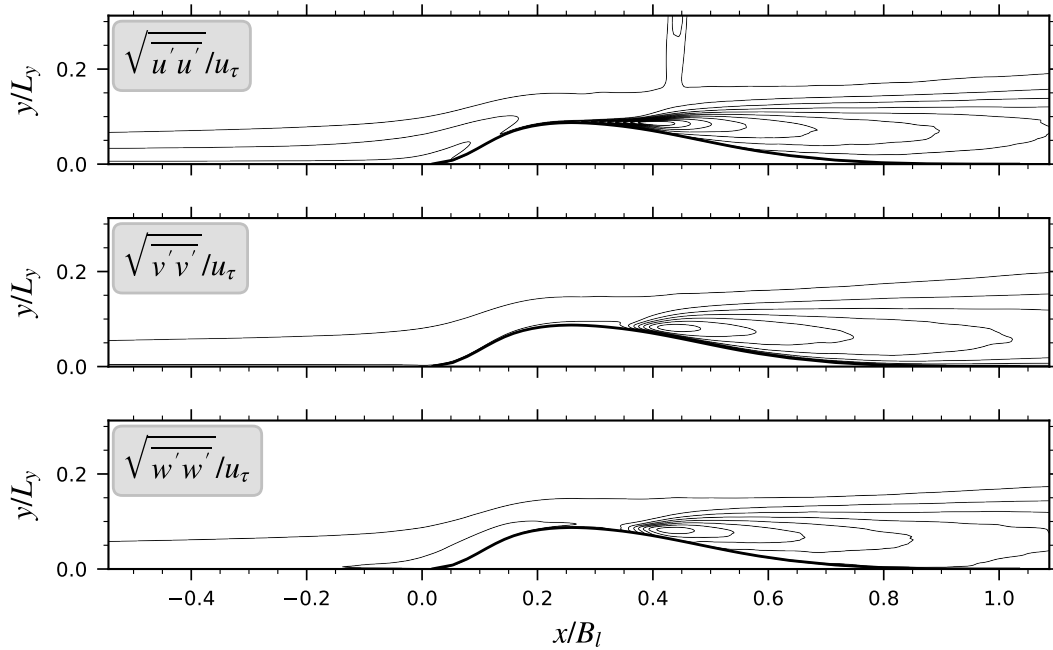


Figure 5.13. Mean turbulence intensities, 15 equally-spaced contours between 0 and 15. The friction velocity u_τ is evaluated based on upstream conditions.

The drop in turbulence intensity depicted above is due to the re-laminarization process that the boundary layer is undergoing over the upstream convex part of the bump. Depending on the state of the boundary layer, the interaction with the shock will behave differently and it is therefore of interest to investigate this further. A way to proceed is to look at the acceleration parameter, an indicator of re-laminarization, introduced by Jones and Launder (1972) and given by

$$K = \frac{\nu_e}{U_e^2} \frac{\partial U_e}{\partial s}, \quad (5.3)$$

where U_e is the streamwise velocity at the edge of the boundary layer, s is the curvilinear coordinate and ν_e the kinematic viscosity, also evaluated at the edge of the boundary layer. The streamwise evolution of this parameter is illustrated in figure 5.14 (*left*). The edge of the boundary layer has been chosen as the distance from the wall at which the averaged Ducros sensor is 0.2. The *dashdot* horizontal line indicates the typical threshold value $K_{lim} = 3.2 \times 10^{-6}$, over which it is stated that the flow re-laminarizes (Jones & Launder, 1972). It is observed that a large portion of the bump exhibits higher values, with a peak value of $\approx 2.4 \times 10^{-5}$ at $x/B_l \approx 0.15$, that is to say when the friction coefficient peaks as well. The boundary layer is therefore re-laminarizing there but it remains difficult to tell from this if a partial or a full re-laminarization occurs, as it depends on its extent.

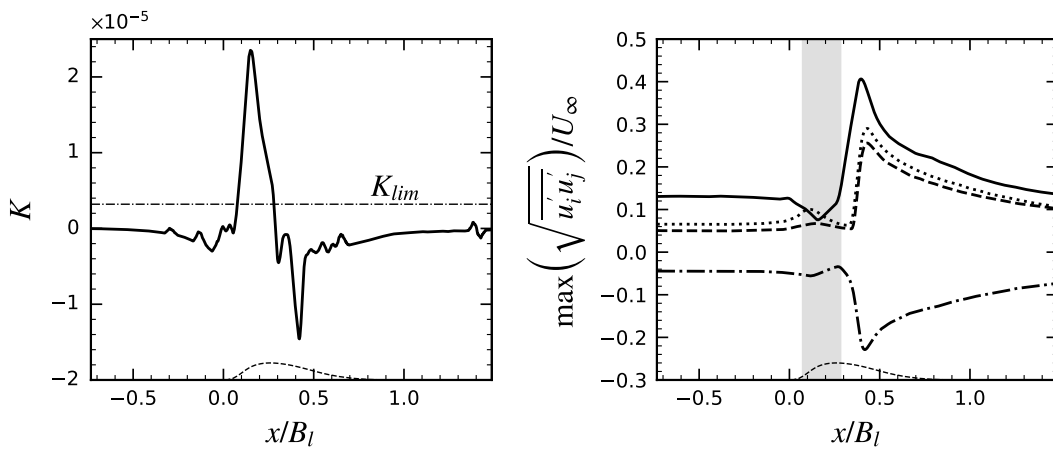


Figure 5.14. (*left*) Streamwise evolution of the acceleration parameter (*solid*) with threshold value (*dashdot*) and (*right*) streamwise evolution of maximum of mean turbulent stresses ($u'u'$ *solid*, $v'v'$ *dashed*, $w'w'$ *dotted* and $u'v'$ *dashdot*), the grey area represents the extent over which the acceleration parameter is higher than the threshold. On both figures, the *thin dashed* line represents the bump geometry.

Figure 5.14 (*right*) shows the streamwise evolution of the maximum turbulent stresses in the boundary layer. The grey area indicates the region over which $K > K_{lim}$. $u'u'$ is reduced by half in the re-laminarization region and reaches its minimum value when the acceleration parameter peaks. On the other side, $v'v'$ and $w'w'$ increase, which is in agreement with the expansion of the structures depicted in figure 5.5. It is also observed that before the separation, the maximum values of turbulent stresses are identical to the ones upstream of the bump. There is therefore still a non-negligible turbulence kinetic energy and it is concluded that the boundary layer is turbulent before separating. In other words, the streamwise extent over which the re-laminarization process occurs is not long enough for the boundary layer to become fully laminar. Previous numerical studies (Brouwer, 2016; Wollblad et al., 2006) came to the same conclusion with, respectively, a lower and a higher Reynolds number.

Finally, a comparison with the experimental results of Bron (2004) is not an easy task. As previously illustrated in section 5.3.1 using RANS simulations, the reduction of Reynolds number strongly modifies the flow and in particular the

location of the separation point. The use of high-fidelity methods allows now to give an explanation for this. The boundary layer is subjected to a partial re-laminarization process over the bump, in the favorable pressure gradient region. This provokes a modification of the structure of the turbulence in the boundary layer, even though the level of maximum of turbulent stresses is recovered before the separation. Moreover, an increase in viscosity, as it is the case in this simulation, enhances the re-laminarization and therefore the structural change of the turbulence. As a consequence, the boundary layer is more prone to separation, which therefore occurs earlier as it undergoes the adverse pressure gradient imposed by the geometry. In the experiment, the boundary layer is stronger and separates due to the interaction with the shock, more downstream. This premature separation in high-fidelity simulation compared to experimental results was also reported by Sandham et al. (2003). To further comment on this aspect, table 5.6 lists the locations of separation and reattachment points for the present case as well as for literature results on the same bump geometry. The height of the separation bubble h_{sep} is also indicated and is taken as the maximum height of the dividing streamline. It is clear that for reduced Reynolds number, the separation point moves upstream whereas the reattachment point moves downstream. As a consequence, the separation bubble is longer and taller.

Table 5.6. Comparison of separation bubble characteristics.

	Re_{B_l}	x_{sep}/B_l	x_{rea}/B_l	L_{sep}/δ_0	h_{sep}/δ_0
Wollblad et al. (2006)	3.10×10^5	0.320	0.476	3.2	0.057
Brouwer (2016)	1.67×10^5	0.280	0.890	12.5	0.132
Baseline	1.91×10^5	0.306	0.640	6.9	0.095
Forced - 250Hz	1.91×10^5	0.308	0.635	6.7	0.090
Forced - 500Hz	1.91×10^5	0.307	0.647	7.0	0.098
Forced - 1000Hz	1.91×10^5	0.306	0.646	7.0	0.097

The question whether the shock exhibits a large-scale motion is always of interest in shock wave/boundary layer interactions. For this purpose, the shock position has been monitored during the simulation. For each horizontal gridline, it is taken as the location of the maximum of pressure gradient magnitude. The mean shock position is illustrated in figure 5.15 (*left*) on averaged static pressure contours. The results are bounded to the range of height for which the shock detection is successful. This is obviously not the case near the walls due to the boundary layers. Even though not captured by the shock detection, the pressure contours highlight the front leg of the lambda shock, that joins the normal shock at $y/L_y \approx 0.5$, and also the weak compression waves at the root of the normal shock, consequence of the breakdown of the separated shear layer. These are reaching the normal shock at $y/L_y \approx 0.25$. The weighted premultiplied Power Spectral Density map of shock position, obtained from FFT and further normalized by its global maximum, is shown in figure 5.15 (*right*). This representation allows to emphasize the frequencies contributing the most to the variance of the signal. Dominant contributions are observed at $St_{\delta_0} \approx 0.0077$ and $St_{\delta_0} \approx 0.0135$ (200Hz and 350Hz, respectively). The emergence of two distinct low-frequency peaks is an artifact due to the relatively short simulation time with

respect to those frequencies. Another, weaker, contribution is captured at $St_{\delta_0} \approx 0.03$ (800Hz) and seems more active near the edges. Especially, its influence starts to rise below $y/L_y \approx 0.3$, which correlates well with the weak compression waves. High frequencies are not involved at all in the shock motion, which is in agreement with their well-known low-pass filter behavior.

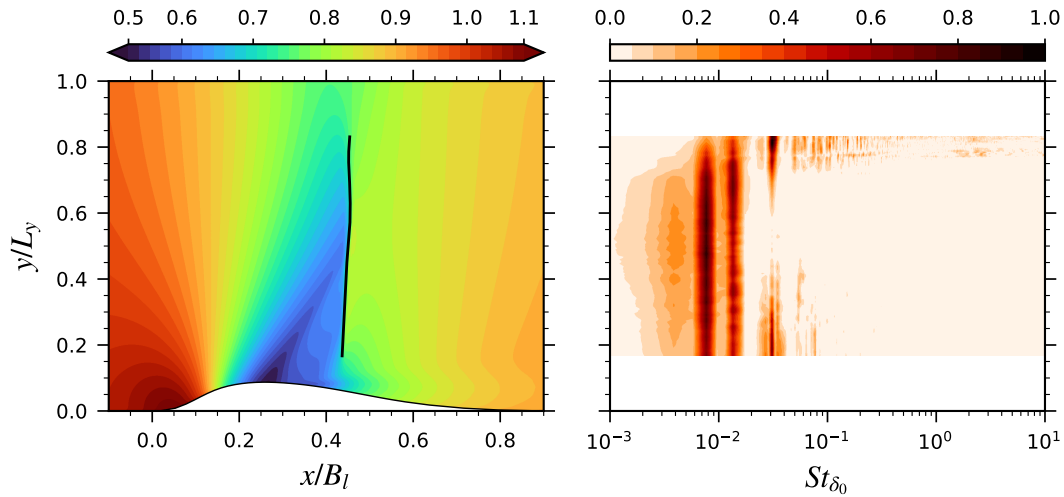


Figure 5.15. Mean shock position superimposed on mean p/p_∞ contours (*left*) and weighted premultiplied Power Spectral Density map of shock position (*right*).

To further comment on the two major contributions to the shock motion, figure 5.16 shows their amplitude and their phase as a function of the height. In terms of amplitude, the contributions at 200Hz and 350Hz exhibits a steadily increasing amplitude. For the higher frequency contribution at 800Hz, amplitude first decreases to reach a plateau from $y/L_y \approx 0.3$ to $y/L_y \approx 0.6$. Then, amplitude sharply rises. The evolution of phase indicates that the shock behaves differently below and above $y/L_y \approx 0.5$. Indeed, the three contributions have a more or less constant phase in the lower part, meaning that the shock is moving as a whole. From $y/L_y \approx 0.5$

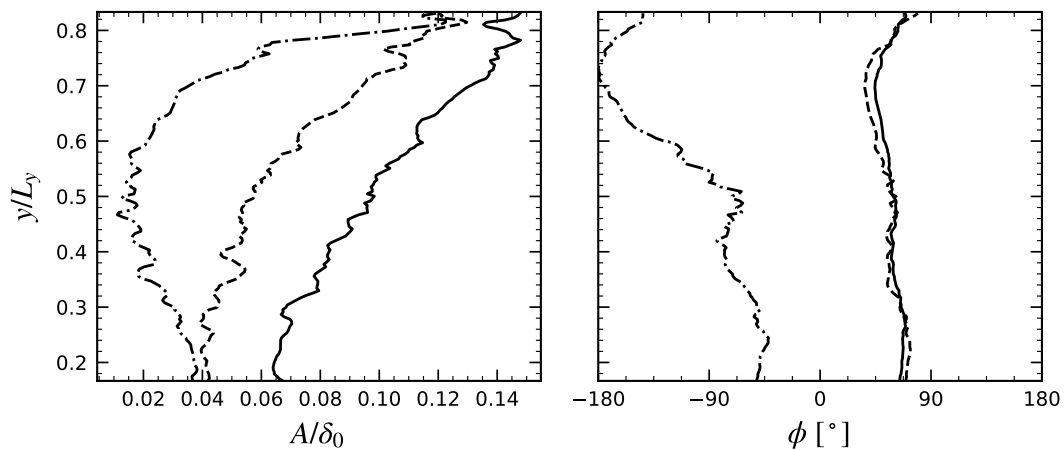


Figure 5.16. Shock motion amplitude (*left*) and phase (*right*) of dominant contributions for the baseline case - 200Hz (*solid*), 350Hz (*dashed*) and 800Hz (*dashdot*).

and above, the phase first decreases to reach a minimum around $y/L_y \approx 0.75$ and then finally increases. This is more marked at 800Hz. The result is a global wavy motion of the shock. This different behavior is due to the oblique compression wave joining the normal shock at around mid-height and which brings additional stability through the mean flow gradients.

The cause of the shock motion in the unperturbed case is not established. However, a legitimate question to raise is whether the purely reflective outlet boundary condition has an influence or not. To assess this issue, the streamwise evolution in the free stream of the static pressure amplitude $A_{\tilde{p}}$ and phase $\phi_{\tilde{p}}$ of the three frequencies contributing the most to the shock motion are depicted in figure 5.17. For consistency, the amplitude is normalized by the amplitude of the outlet disturbance of the forced cases $A_{\tilde{p}_o}$ to give the amplification factor, even if the flow is unperturbed here. Between $x/B_l \approx 0.55$ and the outlet, only the wave at 800Hz is traveling upstream since the phase is decreasing from downstream to upstream. The two other contributions show a practically constant or slightly increasing phase and therefore are propagated downstream. The sudden phase jumps are related to the nodes of the perturbations as the amplitude indicates. These results seem to indicate that the 800Hz contribution comes from the purely reflective outlet boundary.

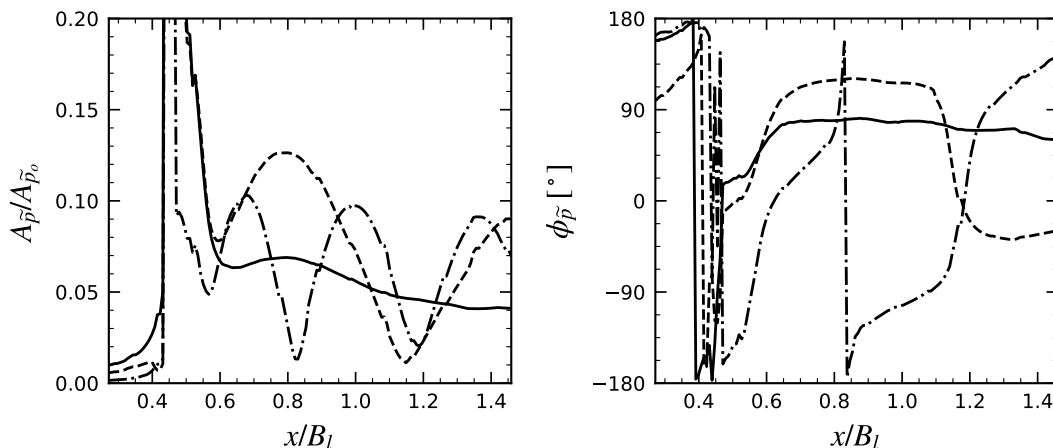


Figure 5.17. Streamwise evolution, at $y/L_y = 0.5$, of static pressure amplitude (*left*) and phase (*right*) of the three most dominant frequencies contributing to the shock motion - 200Hz (*solid*), 350Hz (*dashed*) and 800Hz (*dashdot*).

Figure 5.18 shows the weighted premultiplied Power Spectral Density map of wall pressure, normalized by its global maximum. The PSDs have been evaluated using the Welch periodogram method (Welch, 1967). The idea is to segment the full time series into shorter ones (called blocks) and average the PSDs obtained on each shorter segment to get a better convergence of the PSD over the full time series. A compromise has to be found between the number of blocks and the frequency resolution. By increasing the number of blocks, a better convergence of the PSD is obtained with the disadvantage that the frequency bin increases, which also means that the lowest frequency that can be captured increases as well. Here, the time series is segmented into 7 blocks with 50% overlap. The frequency bin and the lowest frequency resolvable are therefore 200Hz. Hamming windows have been employed.

Various locations are highlighted by vertical lines to ease the analysis. Solid lines refer to geometrical stations whereas dashed lines are related to physical phenomena. These locations are, from left to right, the beginning of the bump, the bump throat, the end of the region of stable recirculation, the reattachment point and the end of the bump.

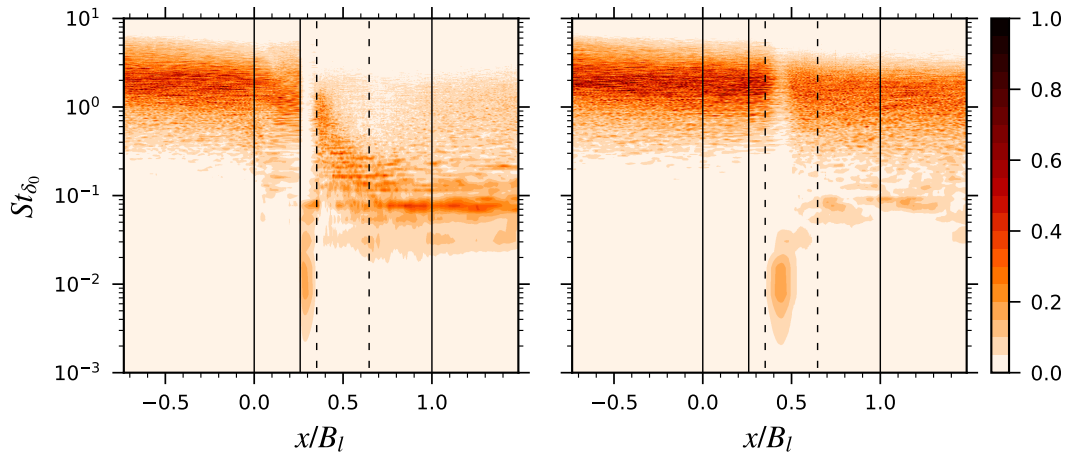


Figure 5.18. Weighted premultiplied PSD maps of bottom (*left*) and top (*right*) wall pressure for the baseline case - $N_{bl} = 7$ with 50% overlap. The *vertical* lines indicate from left to right the beginning of the bump, the bump throat, the end of the region of stable recirculation, the reattachment point and the end of the bump.

The upstream boundary layer is characterized by the ridge centered at $St_{\delta_0} \approx 1$. A broadband low-frequency energetic contribution is observed at both walls, around $St_{\delta_0} = 0.01$. At the bottom wall, this contribution starts from the separation point and is consequently associated to the front leg of the lambda shock. It is moreover contained within the region of stable recirculation. At the top wall, this contribution is located at $x/B_l \approx 0.45$, and is therefore related to the normal shock (see figure 5.5). These results, together with the analysis made from figure 5.15, indicate that the entire shock system is naturally oscillating. Actually, observing a low-frequency unsteadiness at a Strouhal number that is two orders of magnitude lower than the incoming boundary layer is typical for shock wave/boundary layer interactions with separation (Clemens & Narayanaswamy, 2014). The spurious contribution of the shock motion, at $St_{\delta_0} \approx 0.03$ and originating from the reflective outlet, is not influencing the wall pressure significantly. At the bottom wall, the upstream ridge is progressively shifted toward $St_{\delta_0} \approx 0.1$ in the interaction region. These intermediate frequencies develop as a consequence of the vortex shedding occurring at the breakdown of the shear layer and persist in the downstream boundary layer, from the reattachment point onward. Some contributions at intermediate frequencies are also captured at the top wall, downstream of the interaction, but most of the variance of the signal is due to the barely perturbed boundary layer.

Finally, time history of separation and reattachment point locations have been obtained, using wall data. Figure 5.19 shows the amplitude of motion based on FFT of the separation point and reattachment point. Whereas many contributions are observed, the separation point still exhibits the frequencies related to the shock

motion. The picture becomes less obvious for the reattachment point. Additional contributions are, however, found around $St_{\delta_0} \approx 0.077$ and $St_{\delta_0} \approx 0.13$. The amplitude of the separation point motion is one order of magnitude lower than for the reattachment point. The latter lies indeed in a region which exhibits a high variance of friction coefficient as described in figure 5.12.

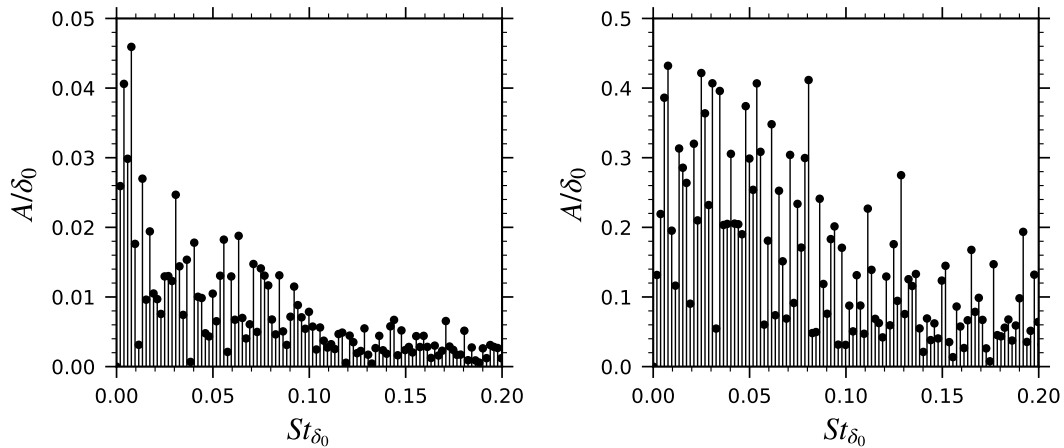


Figure 5.19. Amplitude of motion of separation point (*left*) and the reattachment point (*right*) for the baseline case.

5.3.3 Forced flow

To mimic the presence of rotor/stator interaction as in the blade passage of a turbomachine, the flow has been forced by imposing a fluctuating static pressure at the outlet boundary. It is first required to check if this perturbation is correctly applied. To assess the effectiveness of the forcing, the FFT of the static pressure signal acquired by a probe located at the center of the outlet cell, in the free stream ($y/L_y = 0.5$), has been performed and the results are summarized in table 5.7 for all the forced cases. In general, there is an excellent match between the prescribed amplitude and the amplitude of the first harmonic (that is to say the forcing frequency) obtained from FFT. Practically no deviation (less than 1%) is observed at 250Hz and 500Hz. The discrepancy is slightly higher at 1000Hz, case for which the amplitude of the perturbation is 5% higher than the prescribed one. Nevertheless, in all the cases, this first harmonic accounts for more than 96% of the total energy content while the second contribution corresponds to less than 0.4%, which is negligible. It is therefore concluded that the forcing is effective.

Table 5.7. Comparison of the effectiveness of the forcing conditions at the outlet boundary.

	$A_{p,1}^{\sim}/A_{p,o}^{\sim}$	$E_{p,1}^{\sim}/E_{p,t}^{\sim}$	$E_{p,2}^{\sim}/E_{p,t}^{\sim}$
Forced - 250 Hz	1.00	0.966	< 0.0004
Forced - 500 Hz	1.01	0.965	< 0.0004
Forced - 1000 Hz	1.05	0.968	< 0.0004

To further describe how the forcing is transmitted into the domain, figure 5.20 shows the streamwise evolution of the three first harmonics of static pressure at mid-height, both in terms of amplitude and energy, for the case at 500Hz. It is noted that the figure stops right before the coarsened part of the domain. The most downstream location does therefore not correspond to the actual outlet boundary. The first harmonic accounts for most of the energy content, between around 80% and 90%, regardless of the streamwise position. Due to non-linear effects, higher order harmonics are generated as the wave is traveling upstream. A second harmonic is already present at the most downstream location, representing a few percents of the total harmonic content. The third harmonic is noticeable starting from $x/B_l \approx 1.1$. Generally speaking, pressure perturbations are amplified as they move toward the shock, an effect of the acoustic blockage theory (Bron, 2004). Waves are progressively slowed down and stagnate as the Mach number tends toward one. Close to the shock, the first harmonic amplitude has been multiplied by a factor two compared to the prescribed forcing, and the second harmonic amplitude rises to half of it. The shock location is clearly identified by the sudden and sharp increase in pressure perturbation amplitudes. The first harmonic is there amplified by a factor of almost seven.

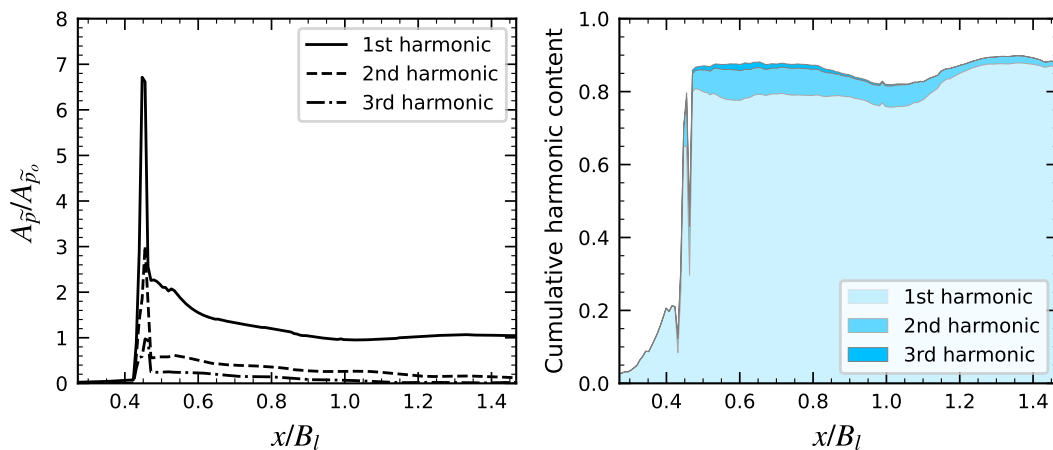


Figure 5.20. Streamwise evolution of the amplification factor (*left*) and cumulative harmonic content (*right*) of the three first harmonics at mid-height, for the forced case at 500Hz.

For the other perturbation frequencies (not shown here), the appearance of higher order harmonics as the waves are traveling upstream is delayed if the frequency is reduced. At 250Hz, the second harmonic is barely discernible at $x/B_l = 0.8$ and corresponds to less than 2% of the total energy content while for the 1000Hz case, it rises to 10%. Moreover, the amplification of pressure perturbation at the shock is drastically reduced as the frequency increases. This is clearly illustrated in figure 5.21, which reports the amplification factor for all the harmonics up to 3kHz. Twelve, six and three harmonics are thus considered for the 250Hz, 500Hz and 1000Hz cases, respectively. The data is well predicted by a quadratic logarithmic equation, its coefficient of determination reaches 0.89.

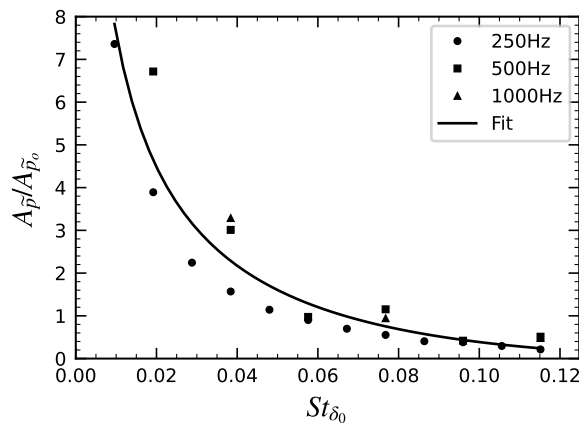


Figure 5.21. Evolution of the amplification level of harmonics at the shock as a function of the frequency.

Now that the forcing has been proven to be effective, various features of the flow are analyzed in order to highlight its effect. First, a comparison of mean friction and pressure coefficients is provided in figure 5.22. No distinction can be made between the baseline and the three forced cases. It indicates first that the harmonic disturbance has no effect on these mean quantities which is explained by the low perturbation amplitude that has been prescribed. Moreover, the frequency has no impact neither. Nevertheless, a slight difference in the length of the separation bubble is observed when the flow is perturbed. Table 5.6 summarizes the mean positions of the separation and reattachment points as well as the mean height of the separation bubble for all the cases. The separation point does not vary but the reattachment point moves upstream compared to the baseline case when the flow is forced at 250Hz and moves downstream at higher frequencies. As a consequence, a change in the height of the separation bubble is observed compared to the baseline case (-4.7% and $\approx +2.9\%$, respectively) but remains marginal.

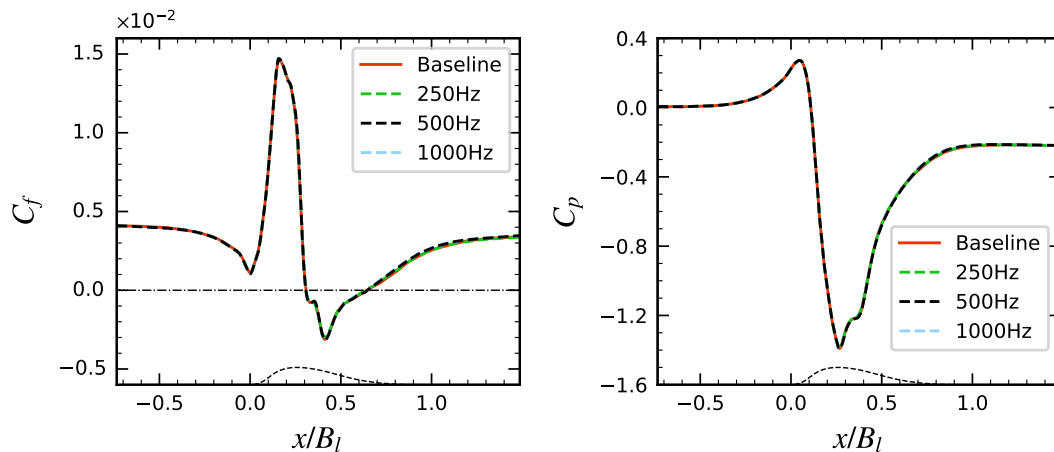


Figure 5.22. Comparison of mean friction coefficient (*left*) and mean wall pressure coefficient (*right*) on the bump wall between the baseline and the forced cases. The *dashed* line represents the geometry.

The response of the shock to the forcing is assessed hereunder. In a similar manner as for the baseline case, figure 5.23 displays the weighted premultiplied Power

Spectral Density map of the shock position, in the range of height for which the shock detection is successful. In all the cases, the forcing frequency clearly stands out at all heights as the main contributor to the variance of the signal. Whereas higher order harmonics of static pressure have been detected at mid-height in the free stream (see figure 5.20), they do not participate to the shock motion. Their influence is, however, felt above $y/L_y \approx 0.65$. Furthermore, a modification of the behavior is observed for the lower part of the shock. Indeed, at 1000Hz, a low-frequency contribution at St_{δ_0} comes at play, whereas nothing is highlighted for the lower perturbation frequency cases. It acts up to $y/L_y \approx 0.6$ and corresponds rather well to the extent of the lambda foot. This low-frequency range has also been pointed out for the natural motion of the shock (see figure 5.15). Its appearance at high forcing frequency could be explained by the diminished sensitivity of shock waves to high frequencies. A decoupling between the natural and the forced motions therefore occurs if the forcing frequency increases. This would be in agreement with the limit case of an infinitely high forcing frequency, to which the shock would not be able to adapt and would therefore oscillate at its natural frequencies. Finally, the baseline contribution at $St_{\delta_0} \approx 0.03$, which seems to be caused by the reflective outlet boundary condition, is completely obscured when the flow is perturbed.

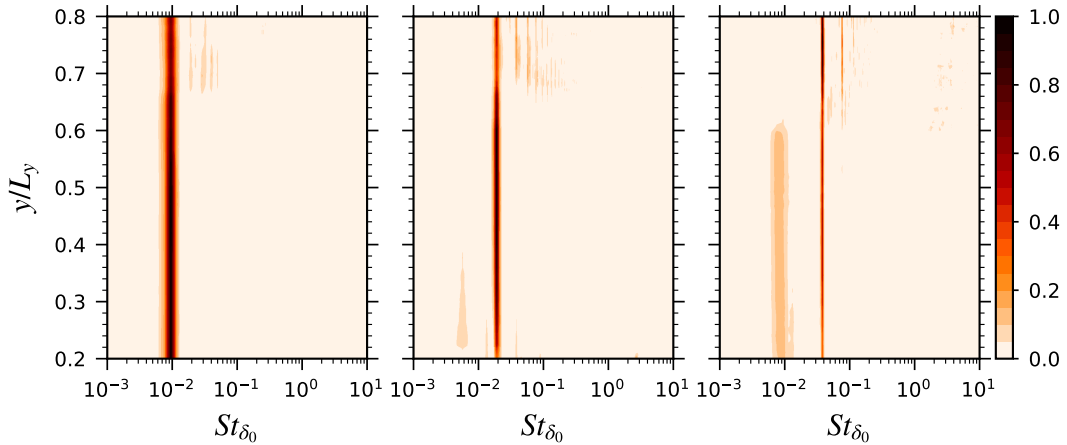


Figure 5.23. Weighted pre-multiplied Power Spectral Density map of shock motion for the forced cases - 250Hz (*left*), 500Hz (*center*) and 1000Hz (*right*).

The amplitude and phase of the shock position at the forcing frequencies are depicted in figure 5.24 as a function of height. The evolution of amplitude occurs differently depending on the frequency. At 250Hz, amplitude first increases and reaches a plateau above $y/L_y \approx 0.6$. At higher frequencies, the amplitude grows almost monotonically. However, the growth is very slow at 1000Hz below $y/L_y \approx 0.6$. Globally, amplitude is lower for a higher forcing frequency, which is an expected result (Bron, 2004; Bruce et al., 2011). The inset in the *left* figure further illustrates the evolution of amplitude at $y/L_y = 0.4$ as a function of frequency. The evolution of phase further confirms the change of dynamics above a certain height as it has been demonstrated in the baseline case. In the lower part of the shock, the phase is more or less constant, meaning that it moves in phase. The three cases show a similar evolution until the upper part is reached. At 500Hz and 1000Hz, the phase

then increases and therefore the upper part of the shock is in advance with respect to the lower one. It results in a wavy global motion of the shock. The change occurs slightly higher for the case at 500Hz, which is in line with the description given for the weighted premultiplied PSD maps (see figure 5.23). For the lowest frequency case (250Hz), the phase remains, however, more or less constant. As it will be shown later, the shock system is much more disturbed at that frequency and the upper part of the shock actually vanishes during a short part of the oscillation period. The shock detection is then not successful and it is believed to be the cause of the discrepancy.

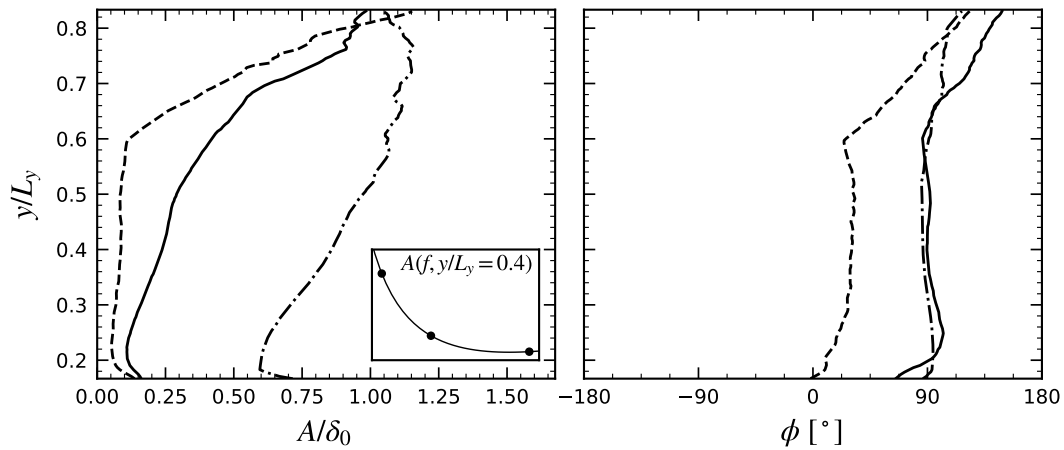


Figure 5.24. Amplitude (*left*) and phase (*right*) of shock motion at the forcing frequencies - 250Hz (*dashdot*), 500Hz (*solid*) and 1000Hz (*dashed*). The inset shows the evolution of amplitude depending on the frequency at $y/L_y = 0.4$.

The evolution of the shock position at $y/L_y = 0.4$, as a function of the outlet static pressure, is illustrated in figure 5.25. It exhibits clearly 5, 10 and 20 periods for the 250Hz, 500Hz and 1000Hz case, respectively. In any case, the trace of the shock motion is well centered around the mean shock position of the undisturbed case (see the *black dot*). For each period independently, the lowest backpressure corresponds to the most downstream location of the shock and vice versa. This is the expected behavior from nozzle theory. Hysteresis is highlighted: the shock does not take the same path with increasing or decreasing outlet pressure. The trace of shock motion is inclined by a lower angle as the frequency increases, which is in agreement with a smaller shock excursion at higher frequencies. The extent of the shock motion, for any given backpressure and regardless of the perturbation frequency, is constant. Bodin and Fuchs (2008) reported a decreasing extent as the backpressure increases. However, with a perturbation amplitude of 8% and a frequency of 5Hz, various shock patterns were allowed to appear within one period, from a weak shock and a small supersonic pocket to a strong shock that is even reflected at the top wall. In the present case, the shock system remains the same within each period and therefore the hysteresis extent is practically constant regardless of the backpressure.

To give a visual idea on how the shock evolves in time, figure 5.26 depicts the numerical Schlieren at mid-span for eight regularly spaced instants over a period for the 250Hz case. Following the analysis presented above, these conditions are the most

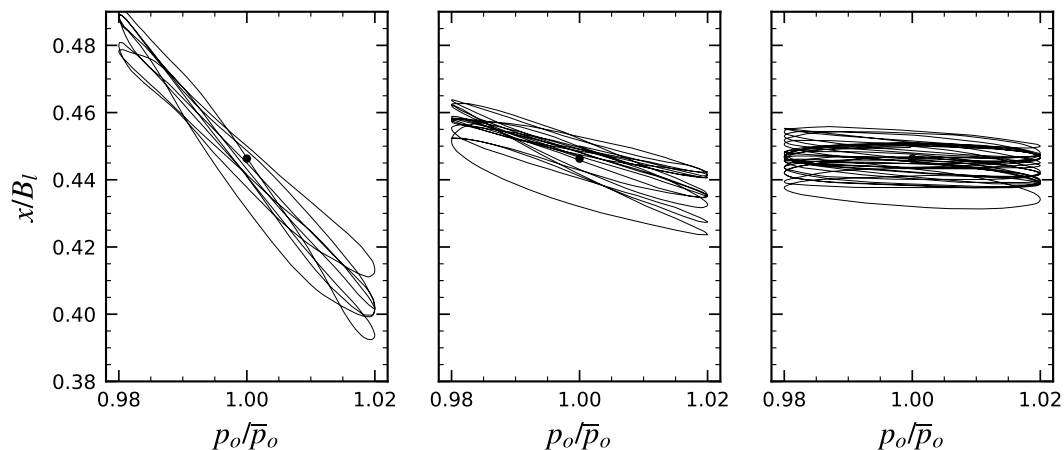


Figure 5.25. Evolution of the shock position at $y/L_y = 0.4$ with respect to the outlet static pressure - forced case 250Hz (*left*), 500Hz (*center*) and 1000Hz (*right*). The *black dot* is the mean shock position from the baseline case.

disrupting among the different frequencies investigated. Hysteresis is again pointed out as the shock takes much more time to move upstream, around 5 frames, against 3 frames to recover its downstream position. The normal shock is strongly modified within one period. At its most upstream position (frame $3T/8$), the shock stops at around mid-height in the channel and the flow is not choked anymore. Moreover, the shock is strong down to the separated shear layer. At its most downstream position (frame $7T/8$), the shock occupies the entire channel height. At the same time, its lower part clearly exhibits a lambda foot and the normal shock is therefore weaker. The occurrence of this lambda foot is linked to the instability of the separated shear layer, which results in a vortex shedding phenomenon. As the flow is supersonic, the generation of these vortices provokes weak oblique compression waves. When the normal shock is located upstream enough compared to the location of the instability ($x/B_l \approx 0.4$), the compression is performed only due to the shock and therefore a strong shock is observed. For more downstream positions of the shock, a part of the compression is operated by the weak compression waves and the remaining compression for the normal shock is not sufficient for a strong shock to appear.

Figure 5.27 shows the weighted premultiplied Power Spectral Density maps of wall pressure for each case. As for the baseline case, the PSDs have been obtained by using the Welch method. When the flow is perturbed at 250Hz or 500Hz (*left* and *center* figures, respectively), a strong influence of the forcing is perceived at the as soon as the flow separates at the bottom wall. In particular, the region of stable recirculation only receives a contribution corresponding to the forcing frequency. This influence persists further downstream and at some locations it conceals the contribution from the intermediate frequencies related to vortex shedding. At the top wall, the perturbation frequency is virtually the sole contributor in the region downstream of the interaction. The extent of the gap between the ridges corresponding to the upstream and downstream boundary layers (the latter being barely detectable) is larger at lower forcing frequency, and is directly reflecting the amplitude of the shock motion. When the flow is forced at 1000Hz (see *right* figures),

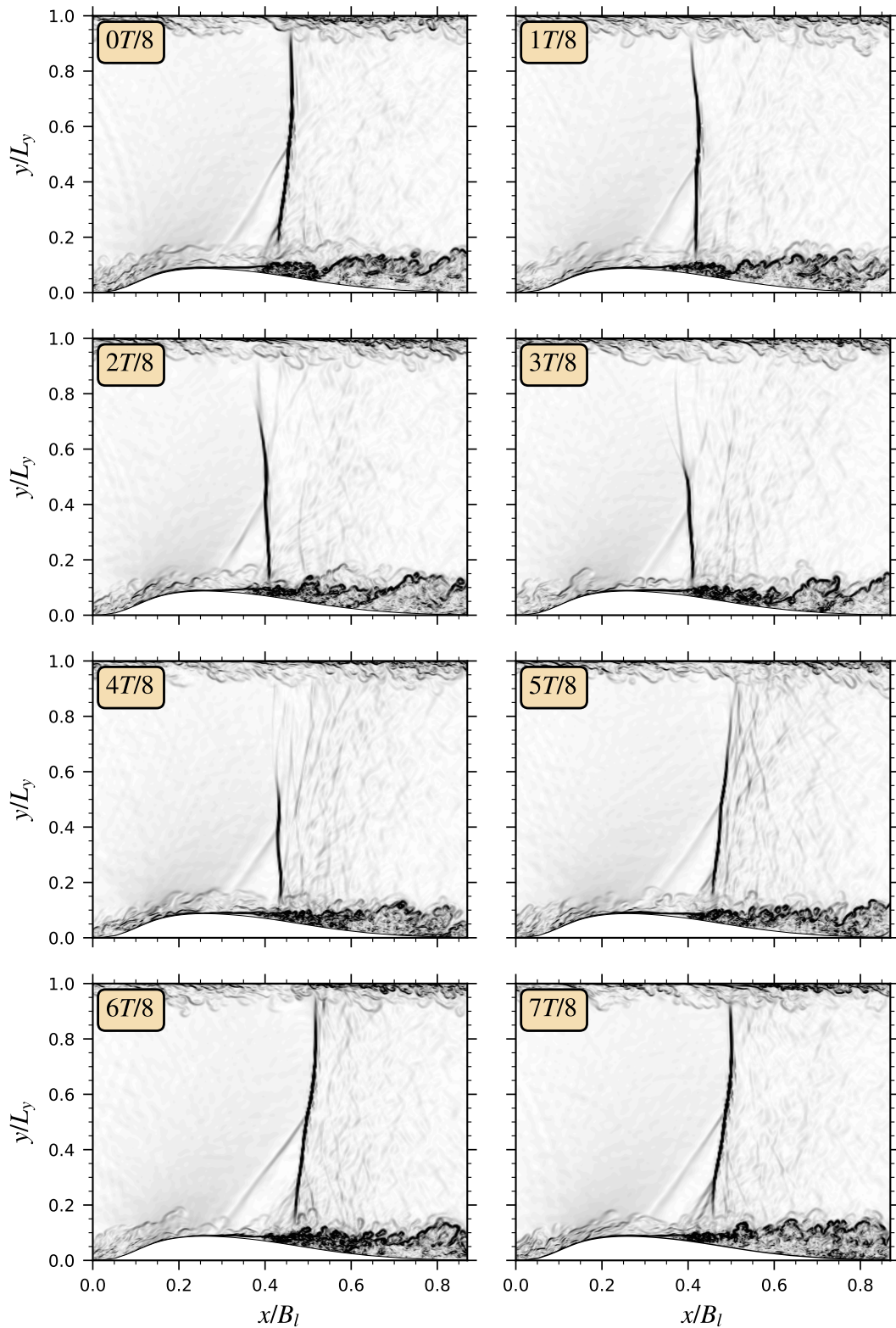


Figure 5.26. Instantaneous density gradient magnitude at mid-span at eight regularly spaced instants over a period for the forced case at 250Hz.

the similarity with the baseline case is striking (see figure 5.18). At the bottom wall, the contribution from the forcing frequency is almost indistinguishable from the vortex shedding contribution. Approaching the separation bubble, its influence vanishes and the broadband low-frequency energetic region is retrieved at $St_{\delta_0} \approx 0.01$ in the region of stable recirculation. At the top wall, the perturbation frequency stands out but the contribution from the natural shock oscillation is also detected.

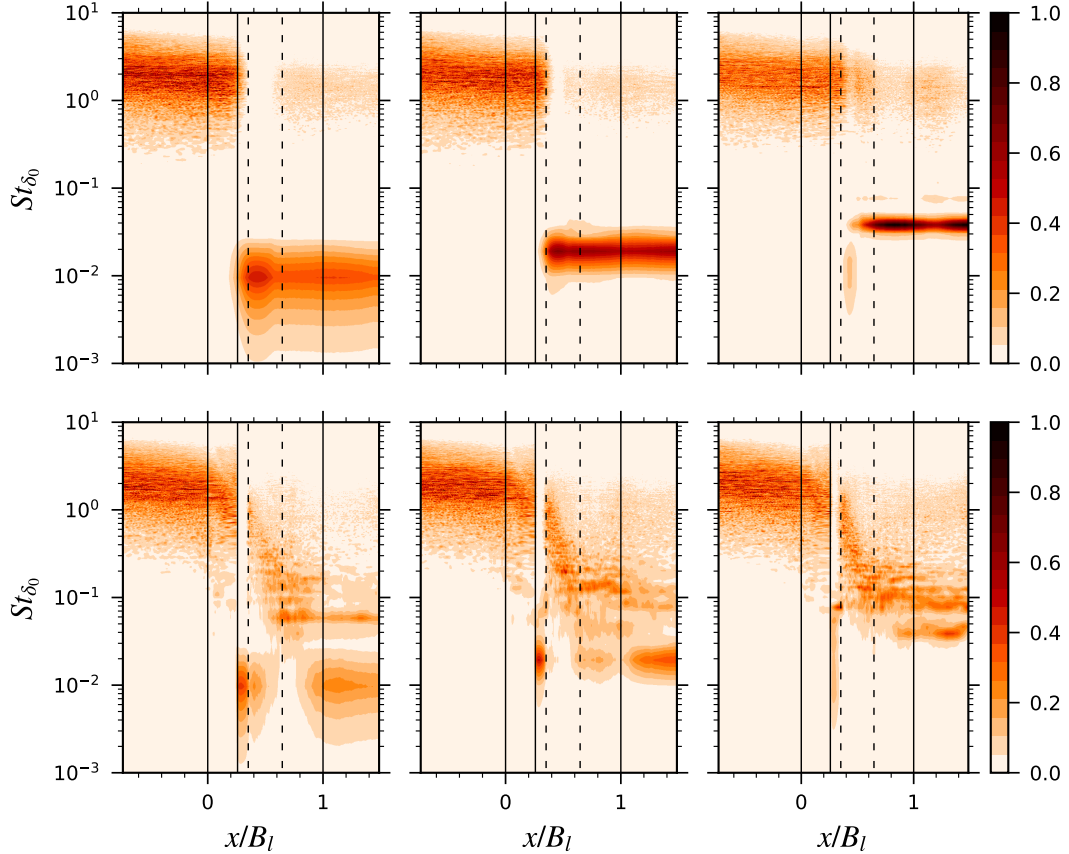


Figure 5.27. Weighted pre-multiplied PSD maps of top (*top*) and bottom (*bottom*) wall pressure for the forced cases - 250Hz, $N_b l = 9$ with 50% overlap (*left*), 500Hz, $N_b l = 9$ with 50% overlap (*center*) and 1000Hz, $N_b l = 7$ with 50% overlap (*right*). The *vertical* lines indicate from left to right the beginning of the bump, the bump throat, the end of the region of stable recirculation, the reattachment point and the end of the bump.

The streamwise evolution of the wall pressure amplification factor (A_{pw}/A_{po}) at the forcing frequencies is illustrated in figure 5.28. A complex pattern of pressure fluctuations amplification and attenuation is depicted. For all the cases, the three first local extrema are co-located. Indeed, the first and second amplification peaks are positioned at $x/B_l \approx 0.3$ and $x/B_l \approx 0.4$ and are caused by the oscillation of the weak oblique compression wave emanating from the separation point and by the oscillation of the normal shock, respectively. In between, the first attenuation peak is related to the end of the region of stable recirculation ($x/B_l \approx 0.35$). Further downstream, in the subsonic boundary layer, a succession of lobes is observed. With increasing frequency, these lobes are shrunk and shifted toward more upstream

locations, indicating upstream traveling waves. The ratio between the size of the first lobe (equal to half of the wavelength) and the period is constant for all frequencies and gives a propagation velocity of $\approx 87.5\text{m/s}$. The frequency insensitivity of the pattern under the shock region compared to the downstream boundary layer is in line with the conclusions of Bur et al. (2006). Acoustic waves are damped as they propagate upstream, because of viscous effects, and therefore the strong pressure amplification is due to the oscillation of the shock system in the region beneath. The shock system position being, on average, independent of the frequency, so are the locations of the three first extrema.

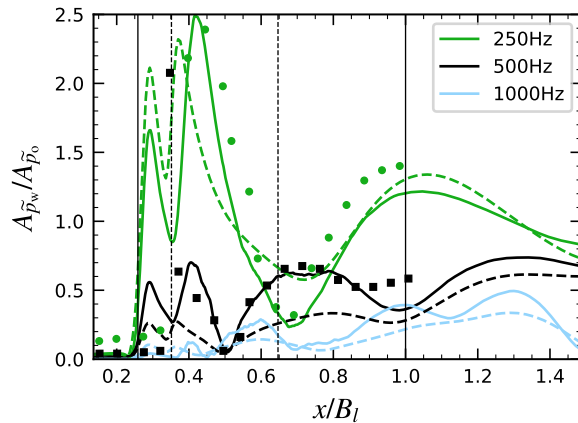


Figure 5.28. Normalized wall pressure amplitude at the forcing frequencies - *left*, comparison of stream-wise evolution between ILES (*solid*), URANS (*dashed*) and experiments (*symbols*) from Bron (2004). The *vertical* lines indicate from left to right the bump throat, the end of the region of stable recirculation, the reattachment point and the end of the bump.

As a comparison, the results of URANS simulations are shown as well, using the same computational setup as introduced in section 5.3.1. The trends predicted from the URANS corroborate qualitatively well those provided by the ILES. However, large discrepancies are noticed in terms of amplitude, and the first extrema are not correctly located, which can be explained as a shortcoming of URANS in resolving time-dependent phenomena. The available experimental results from Bron (2004) at the reference Reynolds number are represented as well. Because of the different shock structure and separation bubble topology, no agreement is expected for the first extrema, which are related to these features. Nonetheless, the first downstream lobe is reasonably well captured, revealing that the upstream propagation of pressure waves inside the boundary layer is not subject to Reynolds number effects. It also gives further confidence in the computational setup for the investigation performed in this work.

While the pattern is independent of the frequency beneath the shock region, the magnitude of the amplification factor is strongly affected and clearly decreases with increasing frequency. It actually reflects the extent of the shock system displacement. For a larger displacement (and therefore for a lower forcing frequency, see figure 5.24), a bigger portion of the pressure gradient will be felt by a fixed point on the wall, resulting in a higher pressure amplitude.

The effect of the perturbation on the separation bubble is investigated by looking at the behavior of the separation and reattachment points. The Power Spectral Densities are compared for the three forced cases in figure 5.29. It is clear that for the 250Hz and 500Hz cases, the forcing frequency stands out in the results whereas this contribution is completely absent for the 1000Hz case. However, the separation point

exhibits a peak at $St_{\delta_0} \approx 0.01$. These observations are in line with the description of the wall pressure made from figure 5.27.

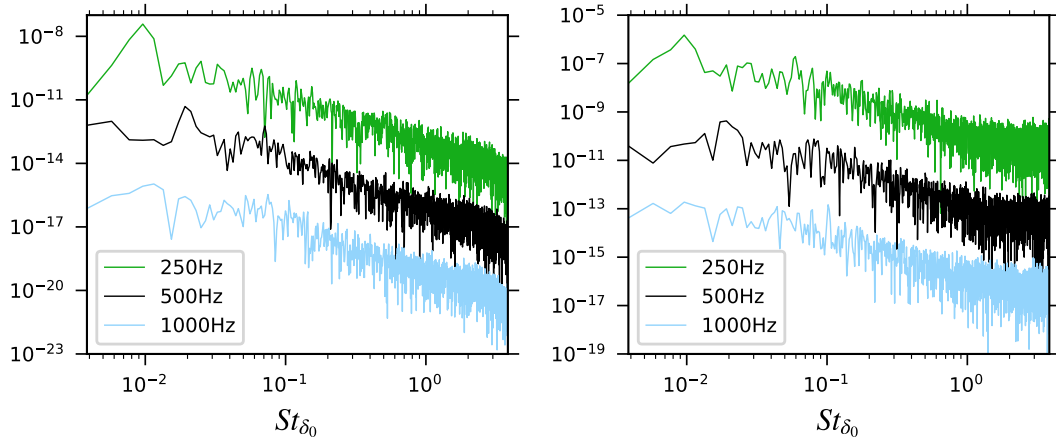


Figure 5.29. Comparison of Power Spectral Densities of the separation point (*left*) and reattachment point (*right*).

5.3.4 Coherent flow

The attention is now focused on the extraction of the coherent (or harmonic) component of the flow, using phase averaging. The choice of the reference oscillator is first discussed. Then, the effect of the coherent flow on the mean flow is assessed. Finally, the coherent streamwise velocity and turbulent stresses are presented, together with a detailed analysis of the coherent turbulent stress budgets.

5.3.4.1 Reference oscillator

Phase-average requires first the definition of a reference oscillator. For the forced cases at 250Hz and 500Hz, it has been shown previously that the dominant contribution to the evolution of the separation point position comes from the perturbation frequency (see figure 5.29). A reference oscillator is then obtained by reconstructing the signal with the sole contribution of the forcing frequency, its magnitude and phase being obtained from FFT of the original signal. The resulting reconstructed signals are illustrated in figure 5.30 on top of the original ones. With respect to the labeling introduced in figure 5.2, bins 2 and 7 correspond therefore to the most downstream and most upstream locations of the separation point, respectively.

The choice of the separation point location as a reference is justified first by the fact that the major contribution to that signal is from the forcing frequency. In addition, it seems more natural because the separation point is expected to be the point of formation of coherent structures, if they exist. This methodology does, however, not apply at 1000Hz since the separation point does not follow the perturbation. To allow a comparison, the prescribed outlet static pressure will be therefore used for the 1000Hz case. Using the outlet static pressure as a reference led to negligible changes in the results for the 250Hz and 500Hz cases, exception made

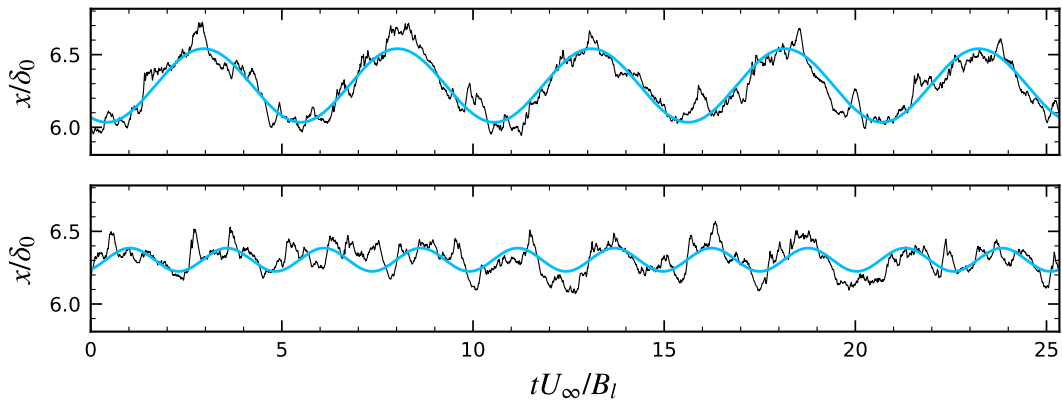


Figure 5.30. Time evolution of separation point (*solid black*) and reconstructed signal at the forcing frequency (*solid blue*) for the 250Hz (*top*) and 500Hz (*bottom*) cases.

of a shift in the bin number due to the phase difference between the two references. The computation of amplitude and phase is not affected by this change and these quantities can therefore be compared between the different cases, even though the reference oscillator is different.

5.3.4.2 Effect on the mean flow

Due to the triple decomposition, additional terms are introduced in the momentum equation of the mean flow (see equation 2.15). Representing the feedback of the coherent flow on the mean flow, it is checked here whether or not these terms are of importance. Figure 5.31 depicts profiles of the various contributions of the mean x - and y -momentum equations for the 500Hz case at two stations downstream the mean separation point, $x/B_l = 0.33$ and $x/B_l = 0.38$, respectively. The reason for choosing these stations is related to the coherent turbulence kinetic energy and is given in a subsequent subsection. d^+ is here the height from the bump wall, normalized with the upstream wall units. The turbulent force has been explicitly split into the contribution from the Reynolds stress $-u'_i u'_j$ and the contribution from the wave Reynolds stress $-\overline{\tilde{u}_i \tilde{u}_j}$. Both \tilde{u} and \tilde{v} are significant at the two stations chosen here and, therefore, an effect of the coherent flow on the mean flow should be noticeable through the wave Reynolds stress. The latter is, however, found to be practically identical to zero at both stations and for both equations, meaning that the organized motion has no effect on the mean flow. The forced mean flow is therefore indistinguishable from the baseline mean flow, without fluctuating backpressure. The results are shown here for the perturbation frequency of 500Hz. The exact same budgets were found for the 250Hz and 1000Hz cases, indicating that the mean flow is also insensitive to the forcing frequency. These effects had been already highlighted in the comparison of friction and pressure coefficients (see figure 5.22).

The different terms of the mean momentum equations are seen to balance each other perfectly. As these equations have been derived using the assumption that the flow is incompressible (see the detailed derivation in appendix A), it constitutes another proof that compressibility effects are negligible. In the near-wall region,

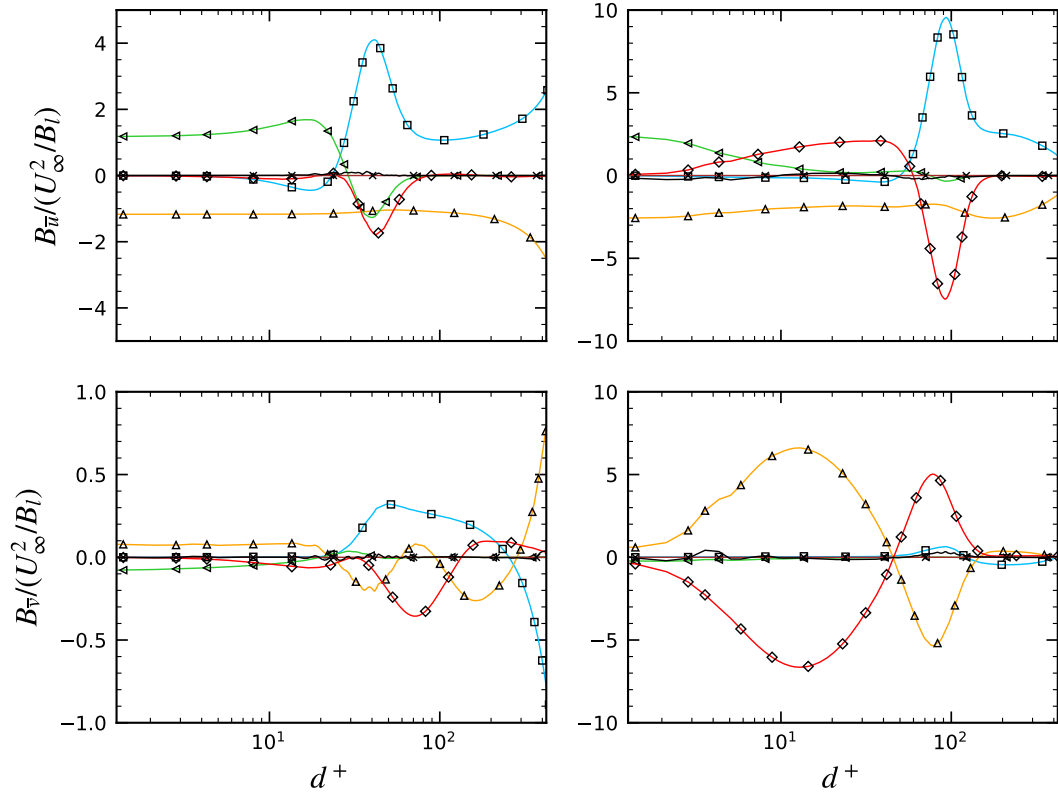


Figure 5.31. Budgets of mean x - (*top*) and y -momentum (*bottom*) equations for the 500Hz case at $x/B_l = 0.33$ (*left*) and $x/B_l = 0.38$ (*right*) - Convection (\square), pressure force (\triangle), viscous force (\diamond), turbulent force from $-\overline{u_i' u_j'}$ (\diamond), turbulent force from $-\overline{u_i u_j}$ (\times) and balance (*solid black line*).

viscous and pressure forces counterbalance each other, with the only exception of the y -momentum at the second station, where pressure and turbulent forces are by far hiding the effects of all the other contributions. For the x -momentum, pressure force is practically constant as the distance from the wall increases. Convection and turbulent force are then coming into play as viscous force disappears. This is also observed for the y -momentum terms at $x/B_l = 0.33$, even though the evolution of pressure force is more complex.

5.3.4.3 Streamwise velocity

Figure 5.32 shows the time history of the coherent streamwise velocity, that is to say \tilde{u} for each bin arising from the phase-average, for the 500Hz case. In the free stream, an upstream propagating wave is clearly discerned, which is the result of the forcing. This wave is actually of opposite sign compared to the pressure wave. The momentum equation in the streamwise direction for the coherent motion can be indeed simplified such that

$$\overline{u} \frac{\partial \tilde{u}}{\partial x} = -\frac{1}{\rho} \frac{\partial \tilde{p}}{\partial x} \quad (5.4)$$

and therefore pressure force balances convection, in the same way as for the mean flow (see figure 5.31). Starting from the separation point, a massive coherent structure develops in the line of the shear layer, and is further convected downstream as it changes of sign. When the separation point lies at its most downstream (bin 2) location, this structure exhibits highly positive values and changes sign as the separation point moves upstream. The weak oblique compression wave emanating from the separation point behaves in the same way.

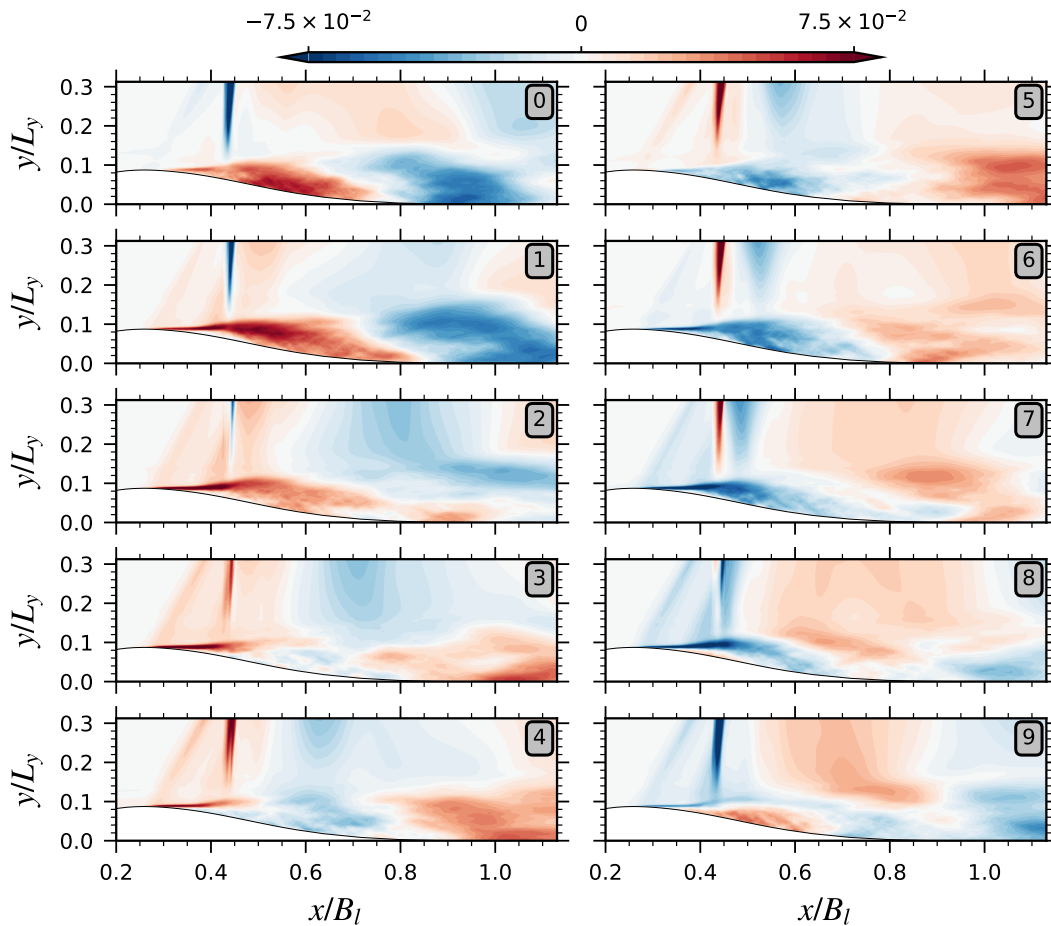


Figure 5.32. Time history of \tilde{u}/U_∞ for the case forced at 500Hz. The bin index is indicated in the top right corner of each subfigure.

Any coherent quantity \tilde{a} can be described by the amplitude and phase of the successive Fourier modes, which are obtained by Fourier transform of the phase-averaged data. Figure 5.33 compares the amplitude $A_{\tilde{u},1}/U_\infty$ and the phase $\phi_{\tilde{u},1}$ of the first harmonic of \tilde{u} for the three forced cases. At the lowest frequency, a single structure is highlighted. It starts from the separation point, develops following the shear layer and then goes down to the bump wall further downstream. An analogous structure is also observed at 500Hz. With increasing frequency (or decreasing wavelength), the structure extent is smaller and the amplitude drops to zero at $x/B_l \approx 0.75$. A second structure therefore shows up at $x/B_l \approx 1.1$ which, at 250Hz, actually lies outside the figure. Amplitude is larger at lower frequencies.

The maximum value of \tilde{u}/U_∞ at 500Hz is around 0.1, which corresponds to a large portion of the structure at 250Hz, as illustrated by the *black* contour. For the forced case at 1000Hz, coherent structures can be guessed at regularly-spaced intervals on the bump wall and in the shear layer, at, respectively, $x/B_l \approx 0.65$, $x/B_l \approx 0.875$ and finally $x/B_l \approx 0.1.1$ but are not well defined, while no structure at all is found near the separation point.

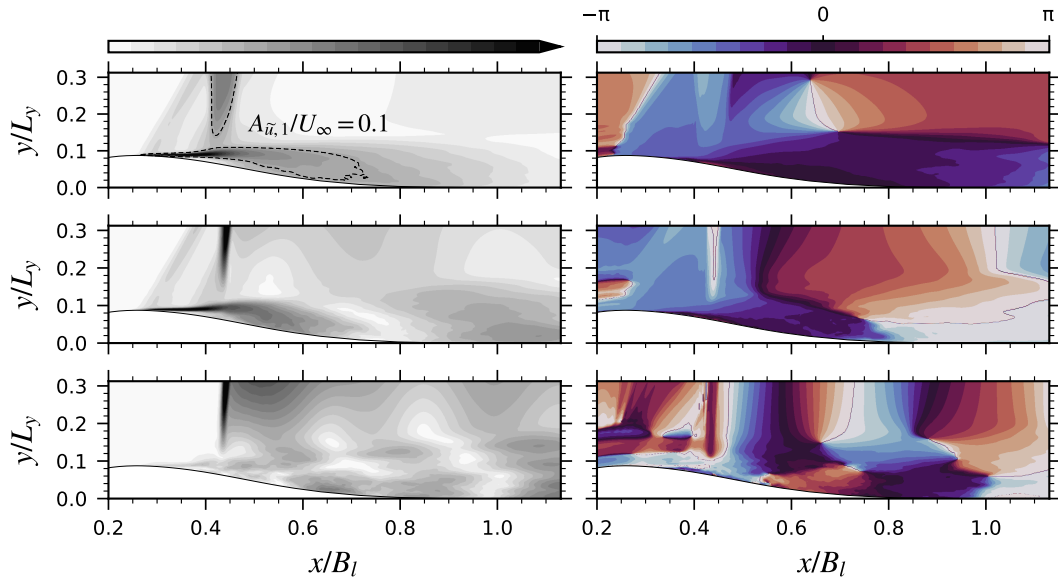


Figure 5.33. Amplitude $A_{\tilde{u},1}/U_\infty$ (left) and phase $\phi_{\tilde{u},1}$ (right) of the first harmonic of \tilde{u} - 250Hz (top), 500Hz (center) and 1000Hz (bottom). Amplitude is bounded between 0 and, respectively, 0.3, 0.1 and 0.05.

In order to check the harmonic content of the phase-averages, it is interesting to compare the phase-averaged or coherent flow variables to their smooth reconstruction from Fourier series. As an example, figure 5.34 shows the coherent streamwise velocity at a point in the shear layer ($x/B_l \approx 0.4$, $y/L_y \approx 0.09$) and the reconstruction using the first harmonic of its Fourier transform. A low scatter between the data points and the reconstruction is observed for the 250Hz and 500Hz cases. The first mode corresponds indeed to 99.5% and 97.4% of the total harmonic content, respectively. For the 1000Hz case, the agreement is rather poor. Only 51.4% of the total harmonic content is at the forcing frequency, while 40% comes from the second harmonic (2000Hz). The latter corresponds to $St_{\delta_0} \approx 0.1$ and is actually linked to vortex shedding (see figure 5.27). Because the downstream boundary layer is less sensitive to higher perturbation frequencies, the harmonic content at the forcing frequency diminishes as the forcing frequency increases. As a consequence, the harmonic content at natural frequencies of the flow increases. The time shift observed for the 1000Hz case is due to the phase difference between the reference oscillators, as explained previously. Finally, for the 250Hz and 500Hz cases, the first mode has been found to be dominant in the coherent structures above-mentioned and within the lambda shock, with more than 90% of the total harmonic content.

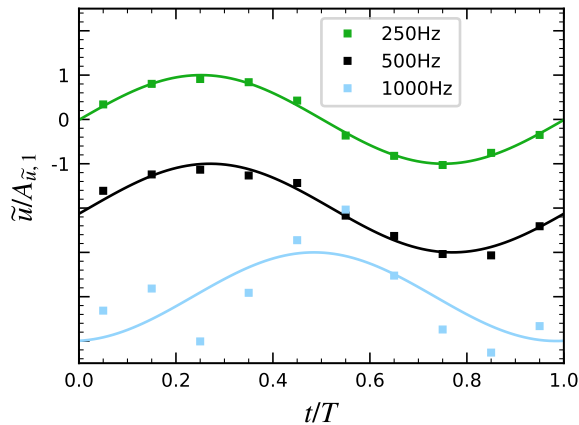


Figure 5.34. Evolution of the coherent streamwise velocity in the mixing layer over a period - Phase-averaged values (*symbols*) and first harmonic reconstruction (*solid*).

5.3.4.4 Turbulent stresses

In a similar manner, figure 5.35 compares the amplitude $A_{\tilde{k},1}/U_\infty^2$ and the phase $\phi_{\tilde{k},1}$ of the first harmonic of coherent turbulence kinetic energy \tilde{k} , for the three forced cases. Focusing first on the 250Hz case, various coherent structures are easily noticed. Starting from the separation point, two layers are discerned. The outer layer consists of a single, elongated and strong structure, following the shear layer, whereas below, the inner-layer develops as several, smaller and weaker structures, located at, respectively, $x/B_l \approx 0.33$, $x/B_l \approx 0.38$ and $x/B_l \approx 0.46$. The first of these is actually so weak that it is actually better seen on the phase. The phase moreover indicates that these inner layer structures are of alternating signs, the second being in phase with the outer layer structure. At 500Hz, this two-layers pattern is also discernible. Interestingly, the structure cores are co-located with the

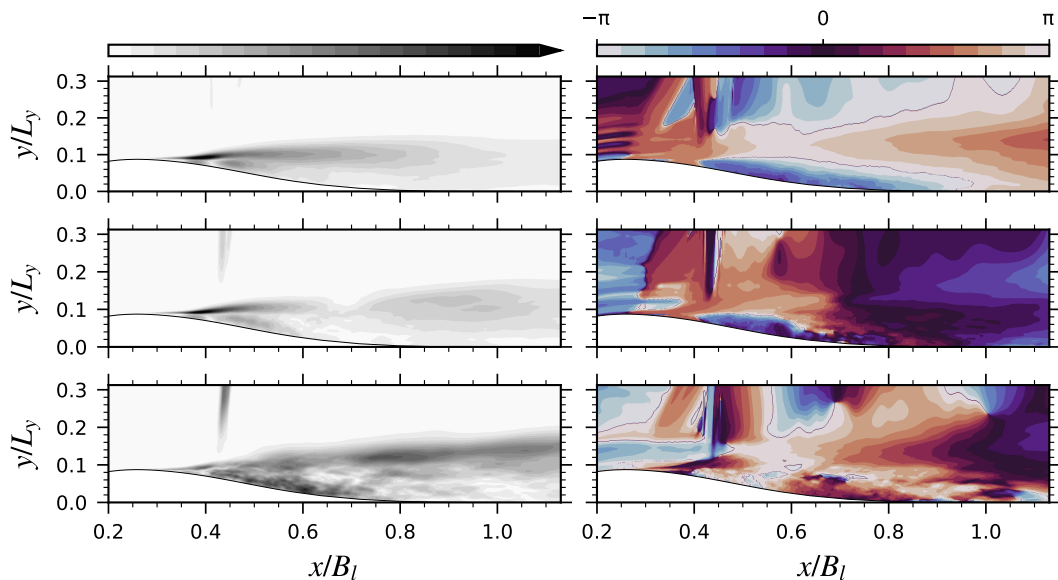


Figure 5.35. Amplitude $A_{\tilde{k},1}/U_\infty^2$ (*left*) and phase $\phi_{\tilde{k},1}$ (*right*) of the first harmonic of \tilde{k} - 250Hz (*top*), 500Hz (*center*) and 1000Hz (*bottom*). Amplitude is bounded between 0 and, respectively, 0.05, 0.02 and 0.005.

ones described at 250Hz, reminding the frequency insensitivity of the wall pressure amplification factor pattern beneath the shock system. Further downstream, the outer layer structure and the third inner layer structure have nevertheless shrunk because of the reduced wavelength. As a consequence, an additional structure is found at the edge of the downstream boundary layer (at $x/B_l \approx 0.9$). At 1000Hz, convergence is poorer but still allows to point out the outer structure and the second inner layer structure. The downstream boundary layer shows also a succession of structures which recalls the ones highlighted for the streamwise velocity.

No coherent structure is found upstream of the separation point, which indicates that it is the point of structure formation. A good convergence is obtained for structures in its vicinity whereas the identification becomes more difficult downstream and would require more samples of the flow. This is a direct consequence of the increasing dispersion in structure shape, size and strength as they are convected (Hussain, 1983).

To better highlight the different structures, figure 5.36 shows a zoomed-in view of the phase of the fundamental mode with superimposed contours of amplitude of \tilde{k} , for the 250Hz case. The cores of the four structures described above are pointed out by the *symbols*. The outer core structure will be called C_1 , while the inner layer structures will be refer to as C_2 to C_4 , from upstream to downstream. For the remaining analysis, two stations are defined at $x/B_l = 0.33$ and $x/B_l = 0.38$, such that they cross C_2 and $C_1 - C_3$, and are indicated by *thick solid white lines*. Table 5.8 reports the first harmonic energy content at the four cores, depending on the forcing frequency. At the lowest perturbation frequency, all structures exhibit at minimum 90% of their energy at the forcing frequency. At 500Hz, only the outer structure C_1 shows a very high level, more than 95%. This drops to around 70% for the cores of the inner layer. Finally, the low sensitivity of the flow for higher forcing frequency is again pointed out as at maximum 50% is obtained at 1000Hz.

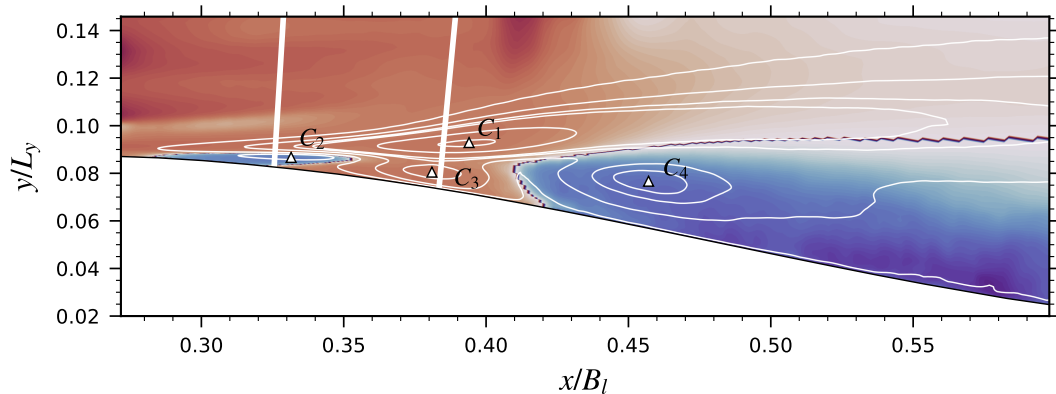


Figure 5.36. First harmonic phase of turbulence kinetic energy with superimposed contours of first harmonic amplitude of turbulence kinetic energy (250Hz case) - 6 contours at $A_{\tilde{k},1}/U_\infty^2 = \{0.004, 0.012, 0.018, 0.021, 0.036, 0.05\}$. The *solid straight white* lines indicate the stations $x/B_l = 0.33$ and $x/B_l = 0.38$, respectively. The *symbols* are located at the structure cores C_1 to C_4 .

f [Hz]	C_1	C_2	C_3	C_4
250	0.985	0.897	0.952	0.971
500	0.955	0.740	0.672	0.657
1000	0.443	0.514	0.142	0.337

Table 5.8. First harmonic energy content at the four structure cores depending on the forcing frequency.

Once again, the amplitude of the modulation is seen to increase as the frequency decreases, and the coherent turbulence kinetic energy is actually not negligible. At some stations, $A_{\tilde{k}}/\bar{k}$ can amount to almost 60% at 250Hz and to about 20% at 500Hz, when comparing the maximum values. Comparing the local values, these ratios can even be higher. Indeed, because of the periodic forcing, mean and harmonic components of turbulence kinetic energy do not necessarily peak at the same distance off the wall. To illustrate this, figure 5.37 (*top*) shows the profiles of the amplitude of the three first harmonics of \tilde{k} compared to the local mean value \bar{k} , at the two stations previously defined, for the 500Hz case. Close to the wall, the first harmonic accounts already for around 8% and 18% of the mean value, respectively. The peak ratio is reached in the outer layer at $d^+ \approx 40$ and $d^+ \approx 100$, with around 30% and 50%, respectively. The second harmonic is noticeable, whereas the third is negligible. The demarcation of the different structures that the first station goes across is clearly visible on the first harmonic phase (see *bottom left*). Very close to the wall, the

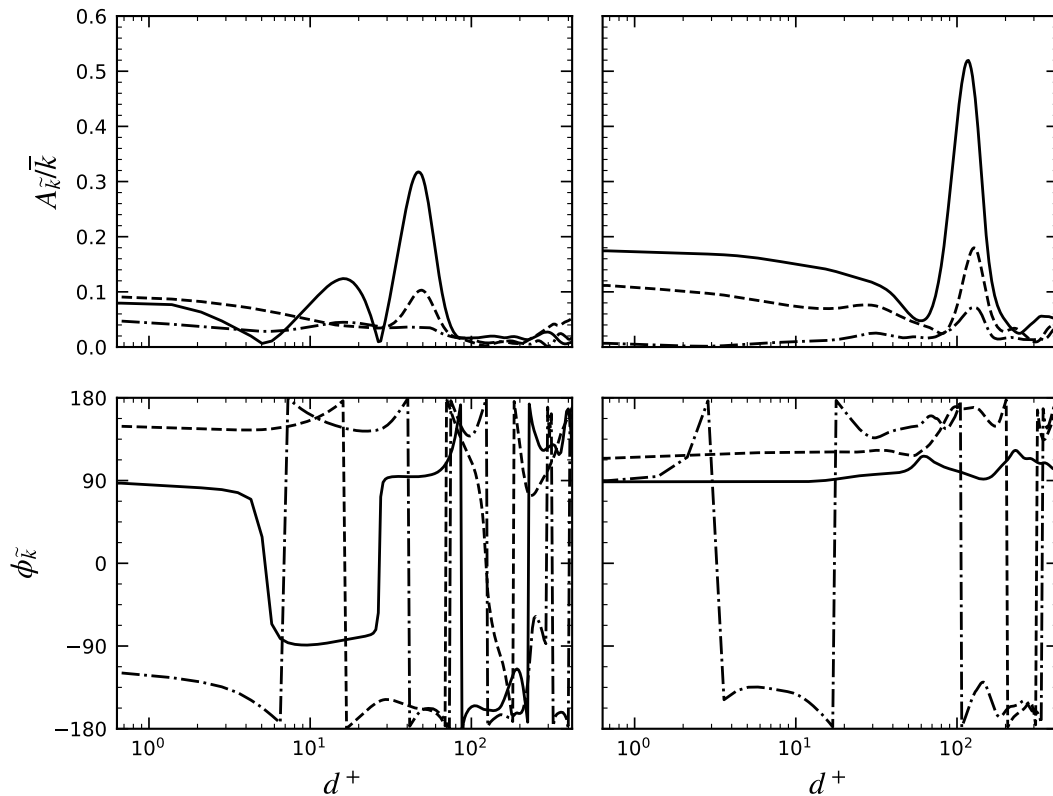


Figure 5.37. Profiles of the three first harmonics (first: *solid*, second: *dashed*, third: *dashdot*) of \tilde{k} for the 500Hz case - Amplitude (*top*) and phase (*bottom*) at stations $x/B_l = 0.33$ (*left*) and $x/B_l = 0.38$ (*right*).

second inner layer structure is already discerned, follow by the first inner layer and finally the outer structure. At the second station (*bottom right*), the first inner layer disappeared and therefore the phase of the fundamental is practically constant.

Figure 5.38 shows the profiles of the first harmonic amplitude for the different coherent turbulent stresses at the two stations for the 500Hz case. In the *top* figures, the curves are normalized by the free stream velocity to give an idea of each contribution to the turbulent stress tensor. At the first station, only $\widetilde{u'u'}$ is observable, whereas other stresses show up further downstream, at the second station. This is in agreement with the description of the mean turbulent stresses (see figure 5.13). Near the wall, both $\widetilde{u'u'}$ and $\widetilde{w'w'}$ are equally contributing to the coherent turbulence kinetic energy, whereas further away from the wall, $\widetilde{u'u'}$ becomes the dominant contributor. The peak is located at $d^+ \approx 100$. The *bottom* figures show the curves normalized using the local mean turbulent stresses. At the second station, the ratio is practically constant near the wall and is ≈ 0.15 except for $\widetilde{w'w'}$ for which it tends to ≈ 0.20 . It is also noticed that the peak of $\widetilde{u'u'}$ and $\widetilde{u'v'}$ coincides around $d^+ \approx 125$, the same for $\widetilde{v'v'}$ and $\widetilde{w'w'}$ at $d^+ \approx 100$. The peak $\widetilde{u'u'}$ is as high as 60% of the local mean value.

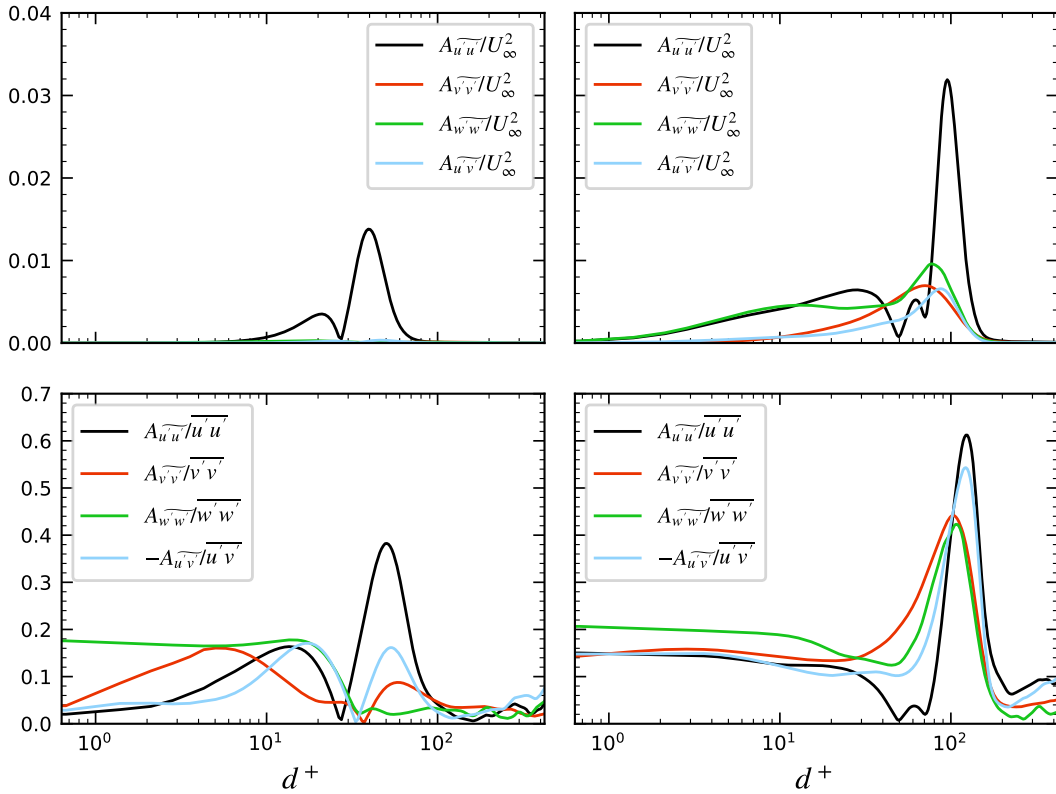


Figure 5.38. Profiles of the first amplitude of $\widetilde{u'_i u'_j}$ - normalized by reference velocity (*top*) and compared to local mean (*bottom*) at station $x/B_l = 0.33$ (*left*) and $x/B_l = 0.38$ (*right*) for the 500Hz case.

5.3.4.5 Mean turbulent stress budgets

The budgets of the mean turbulent stresses are first considered. Figure 5.39 depicts the budgets of the mean turbulence kinetic energy \bar{k} and the mean turbulent normal stresses $\overline{u'u'}$, $\overline{v'v'}$ and $\overline{w'w'}$. The first column refers to the station $x/B_l = 0.33$ and the second one to $x/B_l = 0.38$.

At the first station, the budget of \bar{k} is dictated only by $\overline{u'u'}$ since the terms for the other normal stresses are two orders of magnitude lower. The main area of activity is the mixing layer. Production is the dominant source term and peaks at $d^+ \approx 34$. The corresponding sink terms are convection, with the side contributions of dissipation, viscous diffusion and turbulent diffusion. Only pressure diffusion is inactive. Near the wall, all the contributions drastically decrease but a balance between viscous diffusion, pressure diffusion and dissipation is still perceived. Regarding $\overline{v'v'}$, pressure strain and pressure diffusion are balancing each other from the wall up to the mixing layer. Further away, previously inactive terms such as advection and turbulent diffusion come at play, whereas pressure strain drops to zero. Finally, the budget of $\overline{w'w'}$ shows two areas of activity. In the near-wall region, pressure strain, dissipation and viscous diffusion are the only actors, whereas in the mixing layer, viscous diffusion vanishes and convection comes to prominence. Last but not least, pressure strain is a sink term for $\overline{u'u'}$ (even though barely apparent) and redistributes the energy to $\overline{v'v'}$ and $\overline{w'w'}$, where it appears as a source term. It therefore plays the same role as typically observed in attached boundary layers (Pope, 2000).

Further downstream, at the second station, the behavior is modified regarding different points. First, the redistribution of energy due to the pressure strain term occurs differently. In the near-wall region, energy is transferred from $\overline{v'v'}$ to $\overline{u'u'}$ and $\overline{w'w'}$. In the mixing layer, the classical behavior is recovered, where $\overline{u'u'}$ acts as the only provider for the other normal stresses. Moreover, terms from $\overline{v'v'}$ and $\overline{w'w'}$ play now a role in turbulence kinetic energy budget. In particular, near-wall dissipation comes equally from $\overline{u'u'}$ and $\overline{w'w'}$ and pressure diffusion from $\overline{u'u'}$ and $\overline{v'v'}$. Finally, a second area of activity appears near the wall for $\overline{u'u'}$, which is also affecting the budget of \bar{k} . However, production is again the dominant term by far and peaks further away from the wall, at $d^+ \approx 74$, following the development of the shear layer. The maximum peak is actually located slightly more downstream, at the minimum of friction coefficient ($x/B_l \approx 0.4$), and rises to 6.2 (normalized by U_∞^3/B_l).

Distributions of mean turbulence kinetic energy budgets were also reported in Laval and Marquillie (2011), Marquillie et al. (2008), and Schiavo et al. (2017) on a bump without shock wave interaction, at the location of minimum of mean friction coefficient. Although the configurations are different, a very good agreement is noted with respect to the second station here. The latter is indeed very close to the minimum C_f , at $x/B_l \approx 0.4$ (see figure 5.22). Of particular interest is the three-peaks distribution of turbulent diffusion, showing two positive peaks (and therefore a gain of energy) around the production peak and acting as the main sink term where production is at its maximum. This was also highlighted experimentally in boundary layers subjected to strong adverse pressure gradients (Krogstad &

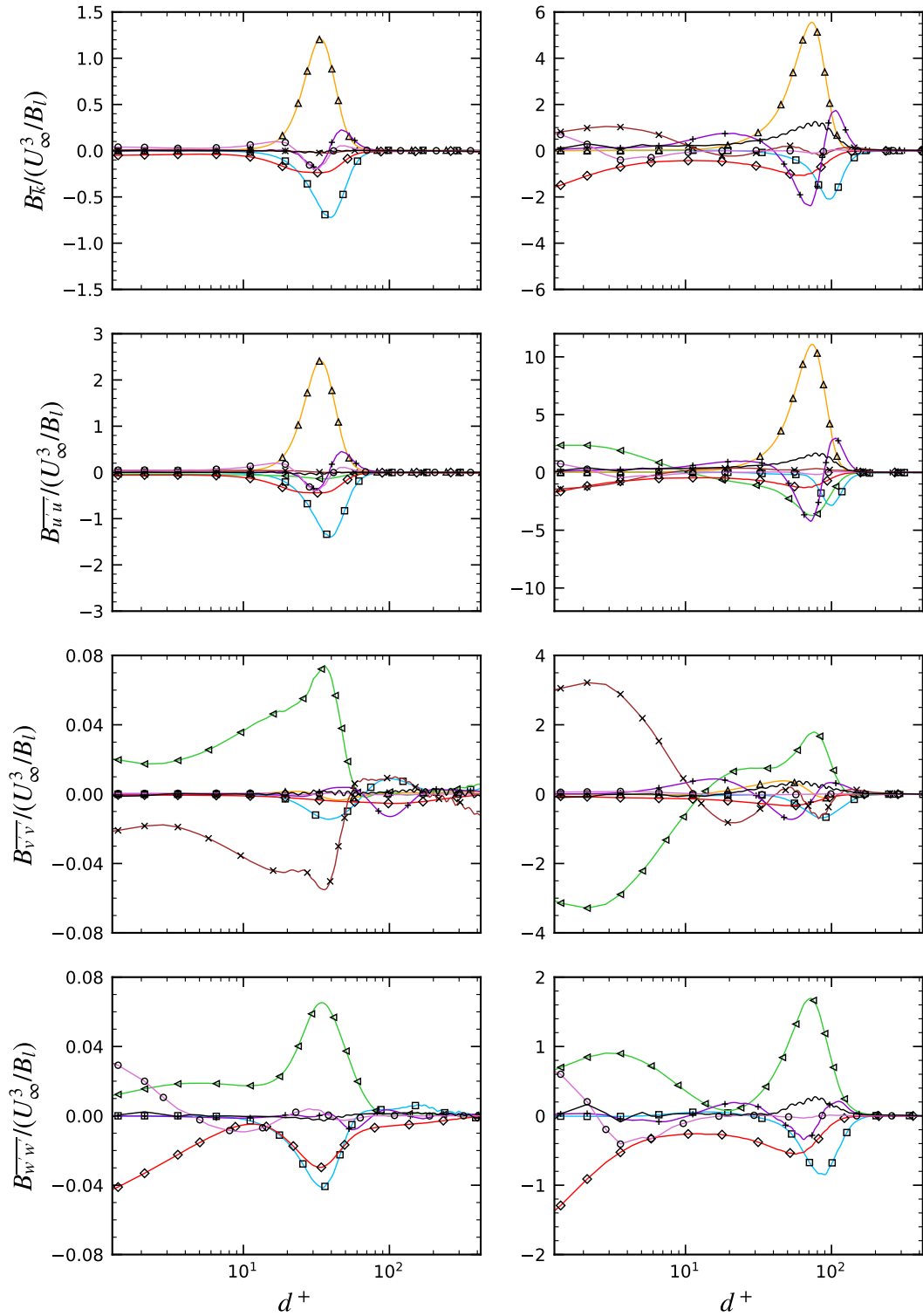


Figure 5.39. Budgets of mean turbulence kinetic energy and mean turbulent normal stresses at $x/B_l = 0.33$ (left) and $x/B_l = 0.38$ (right) for the 500Hz case - Convection (\square), production (\triangle), pressure strain (\diamond), dissipation (\circ), viscous diffusion (\circ), pressure diffusion (\times), turbulent diffusion ($+$) and balance (solid black).

Skåre, 1995). Finally, the near-wall equilibrium between pressure strain and pressure diffusion in the budget of $\overline{v'v'}$ was reported in Vyas et al. (2019a) for an oblique shock wave/boundary layer interaction.

The budgets of $-\overline{u'v'}$ are shown in figure 5.40 at the same two locations. The first station depicts mainly two actors, that is to say pressure strain and pressure diffusion, balancing each other regardless of the distance from the wall. Smaller contributions of convection and production are seen in the shear layer. At the second station, terms involving pressure are still present and balance each other almost perfectly. Again, this was documented in Vyas et al. (2019a). Furthermore, in the shear layer, production is now taking the lead and acts as a sink term. Turbulent diffusion, up to now benign, becomes active in this region and exhibits a similar threefold pattern as in the budget of turbulence kinetic energy, with one peak counterbalancing the maximum of production and two surrounding peaks of opposite sign.

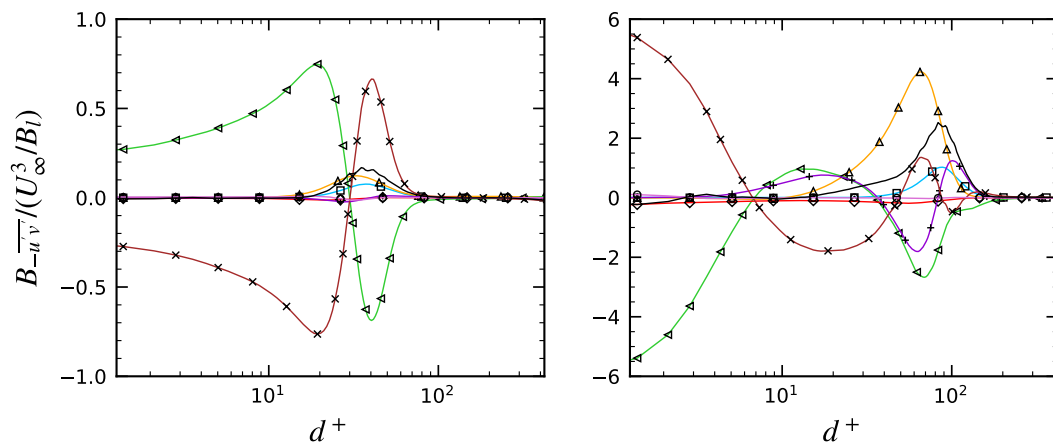


Figure 5.40. Budgets of mean turbulent shear stress at $x/B_l = 0.33$ (left) and $x/B_l = 0.38$ (right) for the 500Hz case - Convection (\square), production (\triangle), pressure strain (\triangleleft), dissipation (\diamond), viscous diffusion (\circ), pressure diffusion (\times), turbulent diffusion ($+$) and balance (solid black).

Figure 5.41 depicts the budgets of mean turbulence kinetic energy and mean turbulent shear stress downstream of the interaction, at $x/B_l = 1.05$. The formerly single production peak let place to two peaks. The farthest from the wall is actually the one detected at the more upstream stations but that has continued to move away from the wall, following the shear layer. It also became much weaker, almost two orders of magnitude smaller than the maximum peak. The inner peak, located at $d^+ \approx 10$ for \bar{k} , comes from the slow development of a turbulent boundary layer undergoing a zero pressure gradient. For both production peaks, turbulent transport shows the threefold pattern (positive-negative-positive). These observations were also reported in Marquillie et al. (2008). The budget of turbulent shear stress share the same features.

The sum of all terms (or the balance) is equivalent to the temporal derivative in the turbulent stress equations and should in principle be zero for the mean stresses. This is verified at $x/B_l = 0.33$ but it is not necessarily the case at the second station. The same unbalance was noted in Schiavo et al. (2015), Schiavo

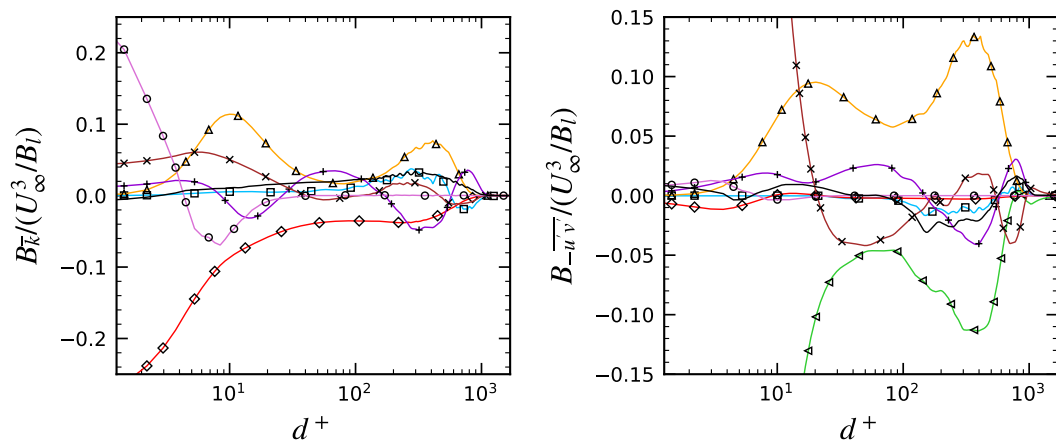


Figure 5.41. Budgets of mean turbulence kinetic energy (*left*) and turbulent shear stress (*right*) at $x/B_l = 1.05$ for the 500Hz case - Convection (\square), production (\triangle), pressure strain (\diamond), dissipation (\circ), viscous diffusion (\circ), pressure diffusion (\times), turbulent diffusion ($+$) and balance (*solid black*).

et al. (2017) for an incompressible flow over a bump, with a similar grid resolution ($\Delta x^+ \approx 16 - 21$, $y_w^+ \approx 0.11 - 0.17$ and $\Delta z^+ \approx 15 - 21$). Consequently, it is an effect of the mesh, and not of the neglected compressibility effects. The mesh is slightly under-resolved and dissipation is therefore under-estimated at the second station. These observations are in agreement with figure 5.7, showing that the ratio between the local grid resolution and the estimated Kolmogorov length scale is higher at the second station, and away from the wall.

The analysis performed here is based on the results from the forced simulations, with oscillating backpressure. As a consequence of the triple decomposition, convection and production terms contain additional contributions compared to the terms arising from the usual double decomposition (as shown in equations 2.19 and 2.20). These additional terms have been found to be two orders of magnitude smaller and, as a consequence, are negligible. The mean budgets obtained from the triple decomposition are virtually identical to the budgets computed from a double decomposition, without forcing. The results have been illustrated here for the 500Hz case, but have been found to be frequency independent. It constitutes another proof that the perturbation has no effect on the mean flow and more specifically here on the mean turbulent stresses. Consequently, the distribution of mean turbulent stresses is the same whether the flow is forced or not.

5.3.4.6 Coherent turbulent stress budgets

Coherent turbulent stresses budgets have also been computed from the data. In a similar manner as for the mean budgets, figure 5.42 illustrates the budgets of the coherent turbulence kinetic energy \tilde{k} and the coherent turbulent normal stresses $\widetilde{u'u'}$, $\widetilde{v'v'}$ and $\widetilde{w'w'}$ at the two stations defined previously. The results are shown only for bin 2, corresponding to the most downstream location of the separation point, of the 500Hz case.

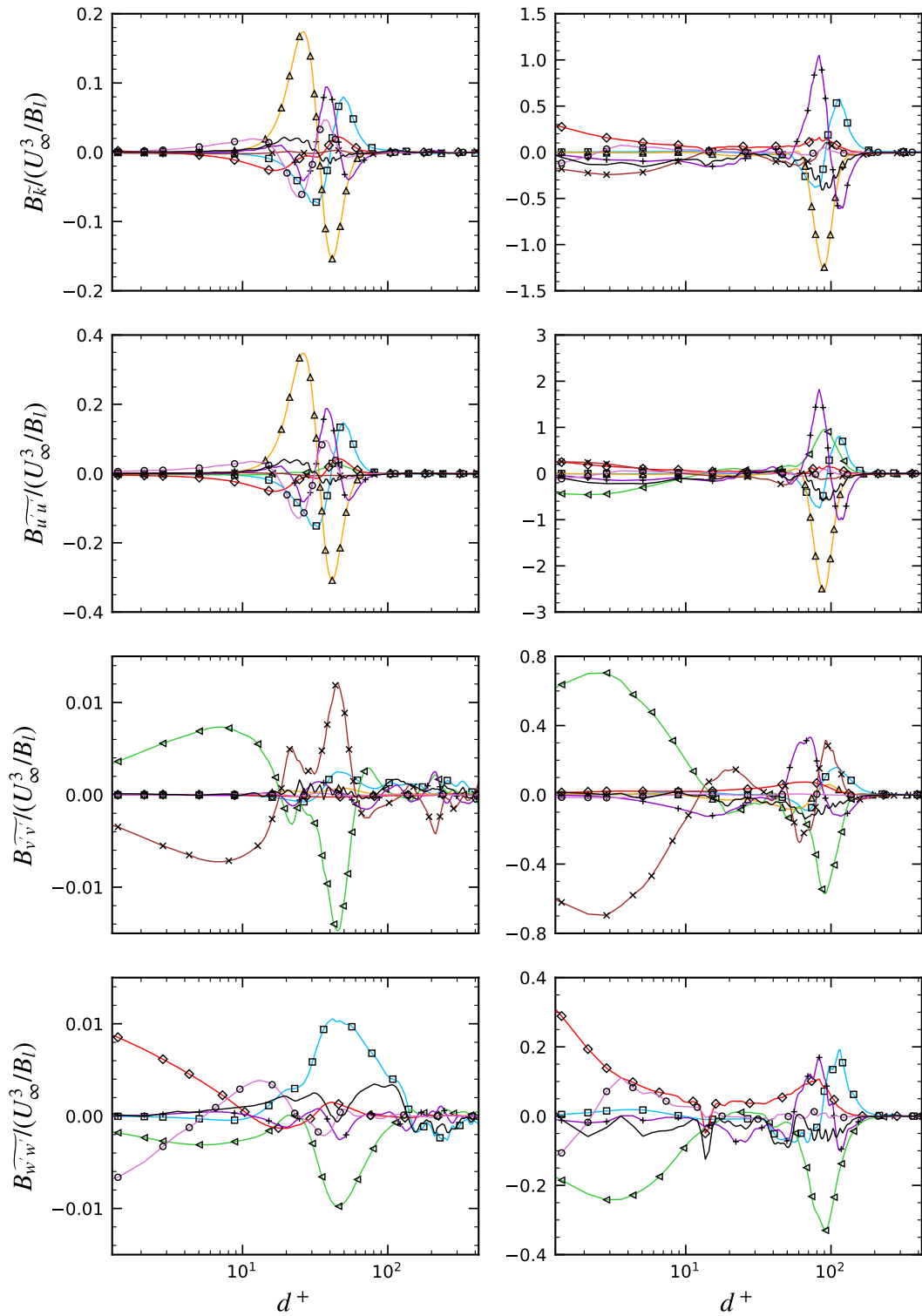


Figure 5.42. Budgets of coherent turbulence kinetic energy and coherent turbulent normal stresses for bin 2 at $x/B_l = 0.33$ (left) and $x/B_l = 0.38$ (right) for the 500Hz case - Convection (\square), production (\triangle), pressure strain (\diamond), dissipation (\diamond), viscous diffusion (\circ), pressure diffusion (\times), turbulent diffusion ($+$) and balance (solid black).

At the first station, the budget of \tilde{k} is controlled by $\widetilde{u'u'}$, as terms involved in the other normal stresses budgets are one order of magnitude lower. For $\widetilde{u'u'}$, production is again the most dominant contribution. However, instead of a single peak, it exhibits two peaks of opposite sign. The maximum is located at $d^+ \approx 25$ and the minimum at $d^+ \approx 42$. The fluctuation accounts for $\approx 25\%$ of the local mean production. In between, coherent production is null at the distance from the wall at which the mean production is maximum (see figure 5.39). Most of the production is either transported as the convection term is of importance or diffused by viscous or turbulent effects. Turbulent diffusion shows four peaks of alternating signs, which are actually two overlapping three-peaks distributions, one around each production extremum. Finally, dissipation and pressure strain have modest contributions. In the case of $\widetilde{v'v'}$, terms involving pressure are found to be prominent. Finally, the budget of $\widetilde{w'w'}$ is commanded by dissipation, pressure strain and viscous diffusion at the wall. Further away, convection and pressure strain are the active terms.

Moving to the second station, two areas of activity are discerned, similarly to the mean budgets. In the near-wall region, the budget of \tilde{k} is dominated by dissipation, pressure diffusion and viscous diffusion. The former comes from $\widetilde{u'u'}$ but also, and more importantly, from $\widetilde{w'w'}$. Pressure diffusion finds its origin in the budget of $\widetilde{v'v'}$. The second area is the shear layer. Production displays this time a single peak, coming only from $\widetilde{u'u'}$ and located slightly further away from the wall compared to the location of the mean peak production ($d^+ \approx 84$ for the coherent against $d^+ \approx 74$ for the mean). Compared to the first station, viscous diffusion is absent for the benefit of turbulent transport and convection. Turbulent diffusion shows again a three-peaks pattern. The modulation of turbulent diffusion is very high and reaches nearly 50% of the local mean value at the peaks.

The budgets of $-\widetilde{u'v'}$ are depicted in figure 5.43 for the two same stations. At the first station, pressure strain and pressure diffusion are the main contributions and cancel each other almost perfectly. The nodes correspond to the anti-nodes of

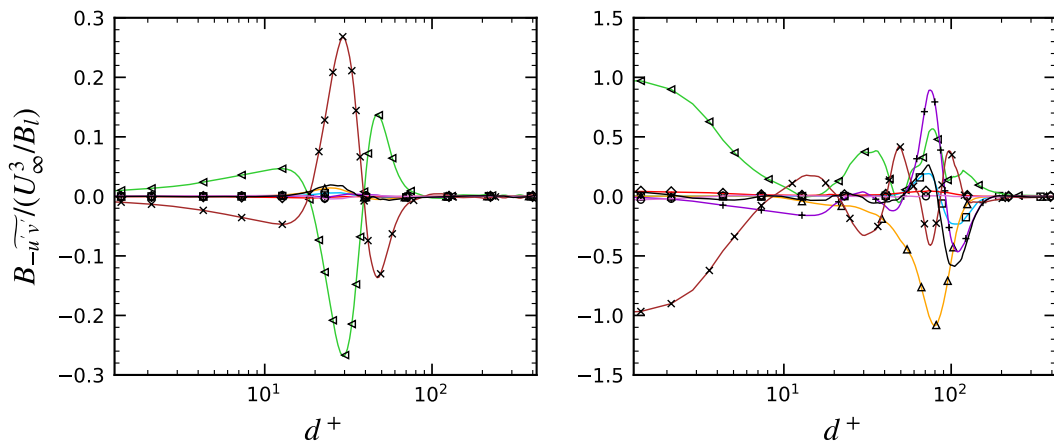


Figure 5.43. Budgets of coherent turbulent shear stress for bin 2 at $x/B_l = 0.33$ (left) and $x/B_l = 0.38$ (right) for the 500Hz case - Convection (\square), production (\triangle), pressure strain (\triangleleft), dissipation (\diamond), viscous diffusion (\circ), pressure diffusion (\times), turbulent diffusion ($+$) and balance (solid black).

the same contributions in the mean budget. Further downstream, terms involving pressure balance each other in the near-wall region. Away from the wall, production and turbulent diffusion become major contributors as well. Production shows again a single peak, co-located with the negative peak of turbulent diffusion at $d^+ \approx 78$. As for the mean budgets, two other peaks of turbulent diffusion are surrounding the production peak.

Figure 5.44 illustrates the budgets of the coherent turbulence kinetic energy and turbulent shear stress at $x/B_l = 1.05$. A complex evolution of the different contributions is depicted and the comparison with the mean budget is difficult. Nevertheless, coherent turbulence kinetic energy is ruled by the effects of turbulent transport and convection mostly, even though production and pressure diffusion can be of importance as well locally. For the coherent shear stress, pressure terms are again prominent, and smaller contributions from convection, production and turbulent diffusion are seen.

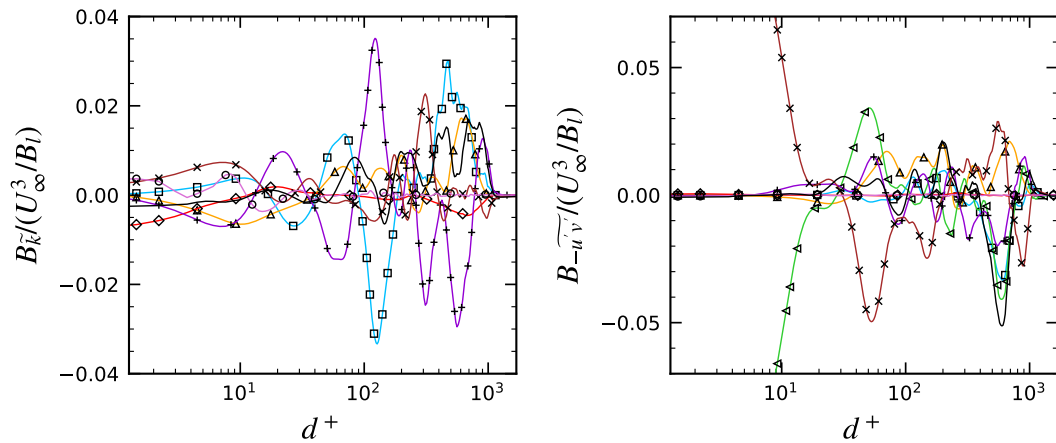


Figure 5.44. Budgets of coherent turbulence kinetic energy (*left*) and turbulent shear stress (*right*) for bin 2 at $x/B_l = 1.05$ for the 500Hz case - Convection (\square), production (\triangle), pressure strain (\diamond), dissipation (\circ), viscous diffusion (\circ), pressure diffusion (\times), turbulent diffusion ($+$) and balance (*solid black*).

No comment has been done so far regarding the closure of the coherent budgets. This is because the use of the word balance is actually not exact when analyzing coherent turbulent stresses. They are indeed quantities evolving in time and therefore the balance, which is actually the evaluation of the temporal derivative in the transport equation, should not necessarily be zero as it is the case for the mean turbulent stresses.

The analysis of the first harmonic amplitude of coherent turbulence kinetic energy $A_{k,1}^-$ revealed the existence of four coherent structures, the cores of which are co-located regardless of the perturbation frequency. It is therefore of interest to check if the budget distributions are also independent of the frequency. For that purpose, figure 5.45 compares the budgets of coherent turbulence kinetic energy for the 250Hz and 500Hz cases at the stations $x/B_l = 0.33$ and $x/B_l = 0.38$. Because of the weak sensitivity of the flow at 1000Hz, the latter case has been discarded.

The budgets are normalized as a function of the distance d such that the sum of the square of the terms is unity. It ensures that modulation effects, which are amplified at lower frequency, are not pointed out. For an easier interpretation, the figure has been split between the contributions of convection, production and dissipation (*top*) and the diffusion terms (*bottom*). The gray area marks the region of the flow for which there is practically no coherent turbulence kinetic energy. In reference to figure 5.36, the threshold has been taken as $A_{k,1}^{\sim}/U_{\infty}^2 = 0.004$. Apart from a few discrepancies, the agreement between both frequencies is remarkable.

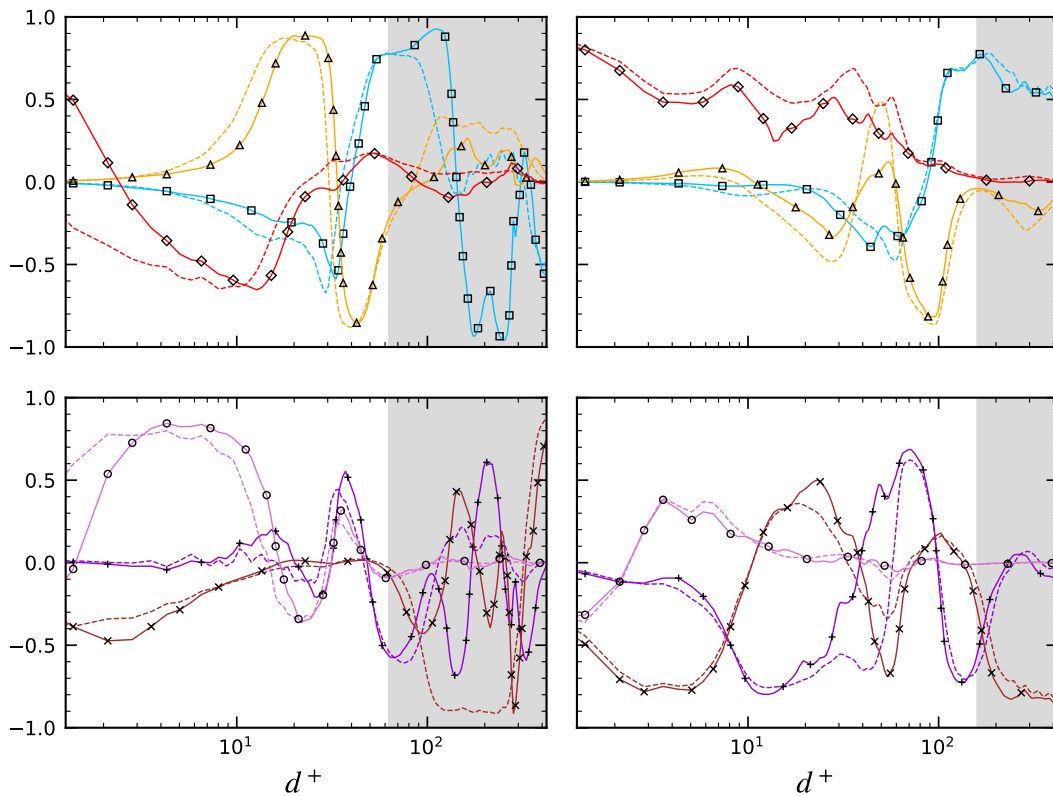


Figure 5.45. Comparison of budgets of coherent turbulence kinetic energy for bin 2 at $x/B_l = 0.33$ (left) and $x/B_l = 0.38$ (right) between the 250Hz (dashed) and the 500Hz (solid) cases - Convection (\square), production (\triangle), dissipation (\diamond) (*top*) and viscous diffusion (\circ), pressure diffusion (\times) and turbulent diffusion ($+$) (*bottom*). The gray area represents the region of the flow for which $A_{k,1}^{\sim}/U_{\infty}^2 < 0.004$.

5.3.4.7 Turbulence production

Production terms contain many different contributions. In this final subsection, the most dominant ones are emphasized. The detailed budgets of mean turbulent stresses showed significant production of $\overline{u'u'}$ and $\overline{u'v'}$. In a triple decomposition

framework, the complete production terms are written

$$\overline{P_{u'u'}} = -2\overline{u'u'}\frac{\partial\bar{u}}{\partial x} - \overline{2u'u'}\frac{\partial\bar{u}}{\partial x} - 2\overline{u'v'}\frac{\partial\bar{u}}{\partial y} - \overline{2u'v'}\frac{\partial\bar{u}}{\partial y} \quad (5.5)$$

$$\begin{aligned} \overline{P_{u'v'}} = & -\overline{u'u'}\frac{\partial\bar{v}}{\partial x} - \overline{u'u'}\frac{\partial\bar{v}}{\partial x} - \overline{u'v'}\frac{\partial\bar{u}}{\partial x} - \overline{u'v'}\frac{\partial\bar{u}}{\partial x} \\ & - \overline{u'v'}\frac{\partial\bar{v}}{\partial y} - \overline{u'v'}\frac{\partial\bar{v}}{\partial y} - \overline{v'v'}\frac{\partial\bar{u}}{\partial y} - \overline{v'v'}\frac{\partial\bar{u}}{\partial y}. \end{aligned} \quad (5.6)$$

In all cases, contributions involving a double product of coherent components, representing the feedback of the coherent flow on the mean, have been found to be negligible. This is consistent with previous observations, relating the insensitivity of the mean flow to the perturbation, regardless of the forcing frequency. Among the remaining terms, only $-2\overline{u'u'}\partial\bar{u}/\partial y$ and $-\overline{v'v'}\partial\bar{u}/\partial y$, for $\overline{u'u'}$ and $\overline{u'v'}$, respectively, are noticeable. It indicates that the flow is mostly dominated by shear and therefore the only mean velocity gradient of influence is $\partial\bar{u}/\partial y$.

Similarly, the coherent budgets pointed out active production terms for $\widetilde{u'u'}$ and $\widetilde{u'v'}$. In detail, they are written

$$\begin{aligned} \widetilde{P}_{u'u'} = & -2\widetilde{u'u'}\frac{\partial\bar{u}}{\partial x} - \overline{2u'u'}\frac{\partial\bar{u}}{\partial x} - 2\widetilde{u'u'}\frac{\partial\bar{u}}{\partial x} - 2\widetilde{u'u'}\frac{\partial\bar{u}}{\partial x} \\ & - 2\widetilde{u'v'}\frac{\partial\bar{u}}{\partial y} - \overline{2u'v'}\frac{\partial\bar{u}}{\partial y} - 2\widetilde{u'v'}\frac{\partial\bar{u}}{\partial y} - 2\widetilde{u'v'}\frac{\partial\bar{u}}{\partial y} \end{aligned} \quad (5.7)$$

$$\begin{aligned} \widetilde{P}_{u'v'} = & -\widetilde{u'u'}\frac{\partial\bar{v}}{\partial x} - \overline{u'u'}\frac{\partial\bar{v}}{\partial x} - \widetilde{u'u'}\frac{\partial\bar{v}}{\partial x} - \widetilde{u'u'}\frac{\partial\bar{v}}{\partial x} \\ & - \widetilde{u'v'}\frac{\partial\bar{u}}{\partial x} - \overline{u'v'}\frac{\partial\bar{u}}{\partial x} - \widetilde{u'v'}\frac{\partial\bar{u}}{\partial x} - \widetilde{u'v'}\frac{\partial\bar{u}}{\partial x} \\ & - \widetilde{u'v'}\frac{\partial\bar{v}}{\partial y} - \overline{u'v'}\frac{\partial\bar{v}}{\partial y} - \widetilde{u'v'}\frac{\partial\bar{v}}{\partial y} - \widetilde{u'v'}\frac{\partial\bar{v}}{\partial y} \\ & - \widetilde{v'v'}\frac{\partial\bar{u}}{\partial y} - \overline{v'v'}\frac{\partial\bar{u}}{\partial y} - \widetilde{v'v'}\frac{\partial\bar{u}}{\partial y} - \widetilde{v'v'}\frac{\partial\bar{u}}{\partial y}, \end{aligned} \quad (5.8)$$

with in total eight different contributions for the production of $\widetilde{u'u'}$ and sixteen for the production of $\widetilde{u'v'}$. Once again, all terms involving a double product of coherent components have been found to be negligible. Among the remaining terms, only the ones coming from the mean shear and its modulation are of importance. Indeed, the production of $\widetilde{u'u'}$ comes mainly from two terms (out of eight), $-2\widetilde{u'v'}\partial\bar{u}/\partial y$ and $-2\widetilde{u'v'}\partial\bar{u}/\partial y$. They are representing, respectively, the action of the coherent flow upon the mean component of the shear stress and the action of the mean flow upon the coherent component of the shear stress. Regarding production of $\widetilde{u'v'}$, two contributions (out of sixteen) are found to be dominant, which are $-\overline{v'v'}\partial\bar{u}/\partial y$ and $-\overline{v'v'}\partial\bar{u}/\partial y$. Even though these results have been obtained for a separated flow, these are in agreement with experimental observations on attached turbulent boundary layers subjected to oscillatory shear (Brereton & Reynolds, 1991).

These terms are compared all together for the two stations $x/B_l = 0.33$ and $x/B_l = 0.38$ for the flow perturbed at 500Hz, for $\widetilde{u'u'}$ in figure 5.46 and for $\widetilde{u'v'}$ in

figure 5.47. The sum of the two dominant terms alone is also represented in *light blue* to allow a direct comparison with the total production, in *solid black*. The figures illustrate an excellent match, showing that only two terms are sufficient to recover the total production. A slight discrepancy is observed for the production of $\widetilde{u'u'}$ at the first station. Taking into account the contributions from compressive/extensive strains ($-2\widetilde{u'u'}\partial\widetilde{u}/\partial x$ and $-2\widetilde{u'u'}\partial\bar{u}/\partial x$) helps to obtain a better match. Nevertheless, these are contributions that remain one order of magnitude lower.

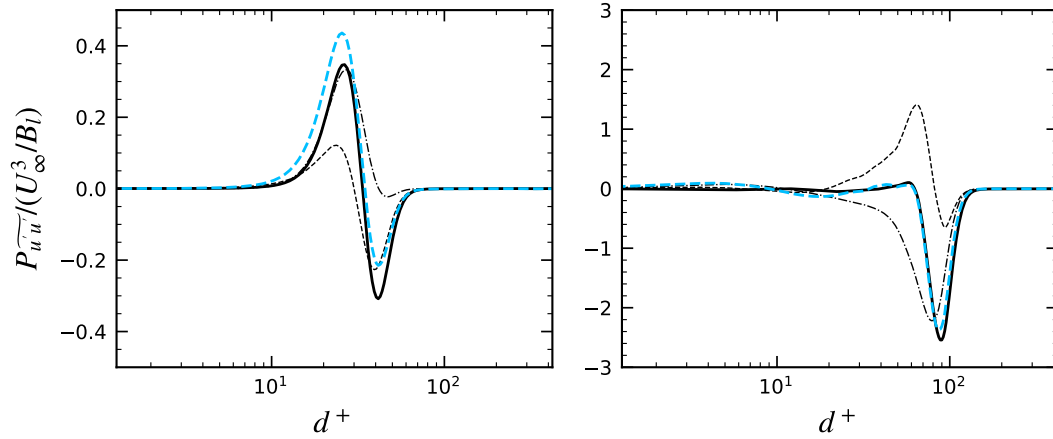


Figure 5.46. Coherent production of $\widetilde{u'u'}$ at $x/B_l = 0.33$ (left) and $x/B_l = 0.38$ (right) for the 500Hz case - Total production (solid), $-2\widetilde{u'u'}\partial\widetilde{u}/\partial y$ (dashed), $-2\widetilde{u'u'}\partial\bar{u}/\partial y$ (dashdot), $-2\widetilde{u'u'}\partial\widetilde{u}/\partial y - 2\widetilde{u'u'}\partial\bar{u}/\partial y$ (light blue).

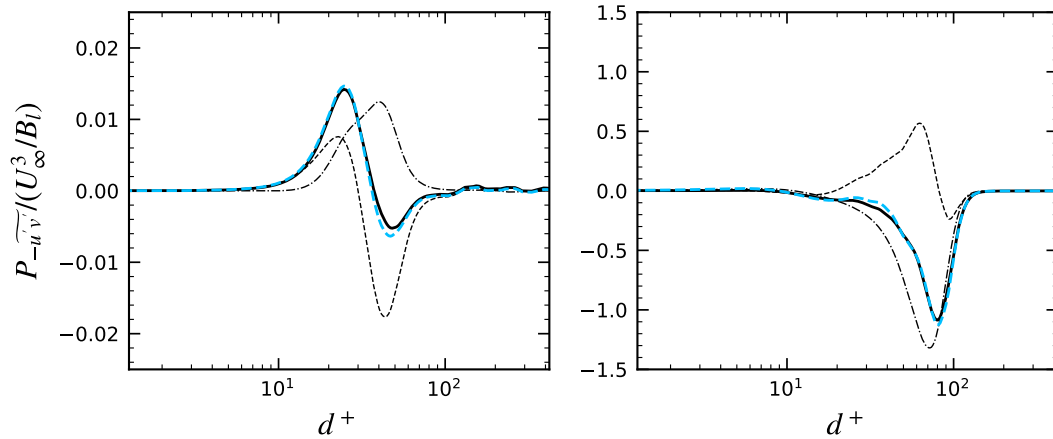


Figure 5.47. Coherent production of $-\widetilde{u'v'}$ at $x/B_l = 0.33$ (left) and $x/B_l = 0.38$ (right) for the 500Hz case - Total production (solid), $-\widetilde{v'v'}\partial\widetilde{u}/\partial y$ (dashed), $-\widetilde{v'v'}\partial\bar{u}/\partial y$ (dashdot), $-\widetilde{v'v'}\partial\widetilde{u}/\partial y - \widetilde{v'v'}\partial\bar{u}/\partial y$ (light blue).

5.4 Summary

Wall-resolved implicit large-eddy simulations of the transonic flow over a bump have been performed. The flow conditions were chosen to reproduce features encountered in transonic turbomachines: a shock wave develops in the passage and interacts with the boundary layer, and the potential effect of a rotor/stator interaction is accounted for by imposing a back pressure that is fluctuating in time periodically. Various realistic forcing frequencies were investigated.

To obtain an affordable computing cost, the Reynolds number was decreased by a factor of twenty compared to the experiments. The influence of such a modification was assessed using RANS simulations, which showed a drastic change in the shock pattern due to an early separation of the boundary layer.

The analysis of the results from ILES started with the unperturbed case, which highlighted a large lambda shock system with a massive flow separation on the downstream part of the bump. The shock system was found to oscillate naturally at a frequency corresponding to $St_{\delta_0} \approx 0.01$.

When the flow was subjected to a periodic forcing, no difference was observed between the mean unperturbed and the mean perturbed solutions. However, unsteady aspects were considerably modified and the sensitivity of the flow was shown to be higher for lower forcing frequencies. At 250Hz and 500Hz, the baseline behavior was completely obscured and the entire flow responded mainly to the perturbation. At the highest frequency (1000Hz), the influence of the forcing diminished. In particular, the separation bubble acted as in the baseline case and a decoupling between the natural and the forced shock oscillation was observed.

A complex pattern of wall pressure amplification factor is pointed out and reveals a twofold response of the downstream boundary layer. The three first extremum locations - beneath the shock region - are independent of the frequency. Their amplitude is nevertheless related to the sensitivity of the shock system to the forcing. Downstream lobes are linked to the upstream propagating pressure wave and their spatial extent is ruled by the wavelength of the signal. These lobes are moreover damped as the wave is traveling upstream.

To extract the harmonic component of the flow, phase-averaging has been carried out using a reference oscillator based on the separation point. Because of the higher sensitivity of the flow at low frequency, this was especially successful for the 250Hz and 500Hz cases. Coherent structures of streamwise velocity and turbulence kinetic energy were emphasized. Their layout is independent of the frequency in the region of influence of the shock system. More specifically, coherent turbulence kinetic energy is organized in a two-layers pattern starting from the separation point, with a single and strong outer-layer structure following the development of the shear layer and an inner layer comprising smaller structures with alternating sign.

Mean and coherent turbulent stress budgets were obtained and were analyzed at various stations. Convection, production and turbulent diffusion stand out as the major contributors to the budget of turbulence kinetic energy whereas pressure strain and pressure diffusion are prominent in the shear stress budget. A typical

pattern of mean turbulent diffusion for boundary layers in adverse pressure gradient was reproduced, that is to say a three-peaks distribution around the production peak. Results showed that this could be extended to the coherent turbulent transport regardless of the number of coherent production peaks. The decomposition of the coherent production terms allowed to isolate only two dominant contributions, coming from the mean and harmonic shears. Finally, the budgets were shown to be independent of the forcing frequency.

Chapter 6

Reduced-Order Modeling for the Non-Linear Harmonic Method

The motivation behind the development of harmonic methods for turbomachinery applications lies in the reduction of computing cost with respect to unsteady Reynolds-Averaged Navier-Stokes (URANS) simulations. By taking advantage of the inherent periodicity of turbomachinery flows, unsteady solutions can be obtained on a truncated computational domain consisting of a single blade passage, whereas full unsteady simulations need to be performed on the complete annulus. Various ways to benefit from this periodicity exist, and an overview of the resulting methods has been provided in the introduction (see section 1.1.1). The present work is concerned with the Non-Linear Harmonic (NLH) method, originally introduced by He and Ning (1998). It was later implemented by Vilmin et al. (2006) in Cadence FINE™/Turbo, the flow solver employed for the simulations performed in this chapter.

To begin with, the Non-Linear Harmonic method is presented, together with the assumption taken to account for turbulence. Then, its performance is assessed for the transonic flow over a bump already studied in chapter 5, and compared to URANS simulations. The chapter ends with an attempt to improve the predictions of the NLH method through the derivation of a model for the harmonic turbulence.

6.1 The Non-Linear Harmonic method

The procedure to derive the equations solved in the Non-Linear Harmonic method starts from the unsteady Reynolds-Averaged Navier-Stokes equations. Reusing the formulation introduced in section 3.1.3, these equations are given by

$$\frac{\partial \mathbf{W}}{\partial t} + \nabla \cdot \mathbf{F}(\mathbf{W}, \nabla \mathbf{W}) = 0, \quad (6.1)$$

where $\mathbf{W} = (\rho, \rho u, \rho v, \rho w, \rho E)$, with $E = e + u_i u_i / 2$, is the vector of conservative variables. The flux vector $\mathbf{F} = (F, G, H)$ is typically split into advective (or inviscid)

and viscous components, such that $(F, G, H) = (F_I - F_V, G_I - G_V, H_I - H_V)$, with

$$F_I = \begin{pmatrix} \rho u \\ \rho u^2 + p \\ \rho uv \\ \rho uw \\ \rho Eu + pu \end{pmatrix}, G_I = \begin{pmatrix} \rho v \\ \rho uv \\ \rho v^2 + p \\ \rho vw \\ \rho Ev + pv \end{pmatrix}, H_I = \begin{pmatrix} \rho w \\ \rho uw \\ \rho vw \\ \rho w^2 + p \\ \rho Ew + pw \end{pmatrix} \quad (6.2)$$

$$F_V = \begin{pmatrix} 0 \\ \sigma_{xx} \\ \sigma_{xy} \\ \sigma_{xz} \\ u_i \sigma_{ix} - q_x \end{pmatrix}, G_V = \begin{pmatrix} 0 \\ \sigma_{xy} \\ \sigma_{yy} \\ \sigma_{yz} \\ u_i \sigma_{iy} - q_y \end{pmatrix}, H_V = \begin{pmatrix} 0 \\ \sigma_{xz} \\ \sigma_{yz} \\ \sigma_{zz} \\ u_i \sigma_{iz} - q_z \end{pmatrix}. \quad (6.3)$$

As a result of Reynolds-averaging, the viscous stress tensor σ_{ij} contains a contribution arising from turbulence. Closure of the equations is performed here following the hypothesis of Boussinesq (Boussinesq, 1877). The (laminar) dynamic viscosity μ is supplemented by a (turbulent) eddy viscosity μ_T , the latter can be evaluated with any turbulence model. The viscous stress tensor is consequently computed with

$$\sigma_{ij} = 2(\mu + \mu_T) \left(s_{ij} - \frac{1}{3} \frac{\partial u_k}{\partial x_k} \delta_{ij} \right). \quad (6.4)$$

The conservative variables are now split into a mean component and a sum of N_p periodic perturbations, representing the multiple disturbances that turbomachinery flows may be subjected to. Each periodic perturbation is further decomposed into N harmonics, giving

$$\mathbf{W} = \overline{\mathbf{W}} + \sum_{l=1}^{N_p} \mathbf{W}'_l \quad (6.5a)$$

$$= \overline{\mathbf{W}} + \sum_{l=1}^{N_p} \sum_{k=1}^{N(l)} \left(\widetilde{\mathbf{W}}_{lk} \exp(Ik\omega_l t) + \widetilde{\mathbf{W}}_{-lk} \exp(-Ik\omega_l t) \right), \quad (6.5b)$$

where I is the imaginary unit, and the harmonic amplitudes $\widetilde{\mathbf{W}}_{lk}$ and $\widetilde{\mathbf{W}}_{-lk}$ are complex conjugates.

Introducing this decomposition into the URANS equations and taking the time average, the equations for the mean flow are obtained. They are given by

$$\nabla \cdot \overline{\mathbf{F}}(\overline{\mathbf{W}}, \nabla \overline{\mathbf{W}}, \mathbf{W}'_l, \nabla \mathbf{W}'_l) = 0, \quad (6.6)$$

with the components of the mean flux $\overline{\mathbf{F}}$ being of the form

$$\overline{F}_I = \begin{pmatrix} \overline{\rho u} \\ \overline{u \rho u} + \overline{p} + \overline{u'(\rho u)'} \\ \overline{v \rho u} + \overline{v'(\rho u)'} \\ \overline{w \rho u} + \overline{w'(\rho u)'} \\ \overline{u \rho E} + \overline{p} + \overline{u'(\rho E)'} + \overline{p'u'} \end{pmatrix}, \overline{F}_V = \begin{pmatrix} 0 \\ \overline{\sigma_{xx}} \\ \overline{\sigma_{xy}} \\ \overline{\sigma_{xz}} \\ \overline{u_i \sigma_{ix}} + \overline{u'_i \sigma'_{ix}} - \overline{q_x} \end{pmatrix} \quad (6.7)$$

$$\bar{G}_I = \begin{pmatrix} \bar{\rho v} \\ \bar{u} \bar{\rho v} + \overline{u'(\rho v)'} \\ \bar{v} \bar{\rho v} + \bar{p} + \overline{v'(\rho v)'} \\ \bar{w} \bar{\rho v} + \overline{w'(\rho v)'} \\ \bar{v} \bar{\rho E} + \bar{p} \bar{v} + \overline{v'(\rho E)'} + \overline{p'v'} \end{pmatrix}, \bar{G}_V = \begin{pmatrix} 0 \\ \bar{\sigma}_{xy} \\ \bar{\sigma}_{yy} \\ \bar{\sigma}_{yz} \\ \bar{u}_i \bar{\sigma}_{iy} + \overline{u'_i \sigma'_{iy}} - \bar{q}_y \end{pmatrix} \quad (6.8)$$

$$\bar{H}_I = \begin{pmatrix} \bar{\rho w} \\ \bar{u} \bar{\rho w} + \overline{u'(\rho w)'} \\ \bar{v} \bar{\rho w} + \overline{v'(\rho w)'} \\ \bar{w} \bar{\rho w} + \bar{p} + \overline{w'(\rho w)'} \\ \bar{w} \bar{\rho E} + \bar{p} \bar{w} + \overline{w'(\rho E)'} + \overline{p'w'} \end{pmatrix}, \bar{H}_V = \begin{pmatrix} 0 \\ \bar{\sigma}_{xz} \\ \bar{\sigma}_{yz} \\ \bar{\sigma}_{zz} \\ \bar{u}_i \bar{\sigma}_{iz} + \overline{u'_i \sigma'_{iz}} - \bar{q}_z \end{pmatrix}. \quad (6.9)$$

The non-linearity of the Navier-Stokes equations generated additional terms, usually called the deterministic stresses (Adamczyk, 1984), which account for the feedback of the perturbations on the mean flow. The deterministic stress from two fluctuations a' and b' being computed by

$$\overline{a'b'} = \sum_{l=1}^{N_p} \overline{a'_l b'_l} = 2 \sum_{l=1}^{N_p} \sum_{k=1}^{N(l)} \left(\tilde{a}_{lk,R} \tilde{b}_{lk,R} + \tilde{a}_{lk,I} \tilde{b}_{lk,I} \right), \quad (6.10)$$

the closure of the mean flow equations requires the evaluation of the real (R) and imaginary (I) parts of each harmonic of each perturbation.

The equations for the perturbations are derived by subtracting the time-averaged equations (6.6) from the basic equations (6.1), and then retaining the first-order terms only. Higher-order cross coupling terms can also be included following Vasanthakumar (2003) and have actually been implemented by Debrabandere (2014) in the present NLH solver for interactions between harmonics originating from the same perturbation. This feature is, however, not employed in the subsequent simulations. The temporal derivative is further evaluated in the frequency domain. The resulting system for each complex amplitude \mathbf{W}_k (dropping the dependence on the perturbation) is therefore written

$$Ik\omega \tilde{\mathbf{W}}_k + \nabla \cdot \tilde{\mathbf{F}}(\overline{\mathbf{W}}, \nabla \overline{\mathbf{W}}, \tilde{\mathbf{W}}_k, \nabla \tilde{\mathbf{W}}_k) = 0, \quad (6.11)$$

and the inviscid and viscous harmonic flux components of $\tilde{\mathbf{F}}$ are, respectively,

$$\tilde{F}_I = \begin{pmatrix} \tilde{\rho u} \\ \tilde{u} \tilde{\rho u} + \bar{u} \tilde{\rho u} + \tilde{p} \\ \tilde{v} \tilde{\rho u} + \bar{v} \tilde{\rho u} \\ \tilde{w} \tilde{\rho u} + \bar{w} \tilde{\rho u} \\ \tilde{u} \tilde{\rho E} + \bar{u} \tilde{\rho E} + \tilde{u} \tilde{p} + \bar{u} \tilde{p} \end{pmatrix}, \tilde{F}_V = \begin{pmatrix} 0 \\ \tilde{\sigma}_{xx} \\ \tilde{\sigma}_{xy} \\ \tilde{\sigma}_{xz} \\ \tilde{u}_i \tilde{\sigma}_{ix} + \bar{u}_i \tilde{\sigma}_{ix} - \tilde{q}_x \end{pmatrix} \quad (6.12)$$

$$\tilde{G}_I = \begin{pmatrix} \tilde{\rho v} \\ \tilde{u} \tilde{\rho v} + \bar{u} \tilde{\rho v} \\ \tilde{v} \tilde{\rho v} + \bar{v} \tilde{\rho v} + \tilde{p} \\ \tilde{w} \tilde{\rho v} + \bar{w} \tilde{\rho v} \\ \tilde{v} \tilde{\rho E} + \bar{v} \tilde{\rho E} + \tilde{v} \tilde{p} + \bar{v} \tilde{p} \end{pmatrix}, \tilde{G}_V = \begin{pmatrix} 0 \\ \tilde{\sigma}_{xy} \\ \tilde{\sigma}_{yy} \\ \tilde{\sigma}_{yz} \\ \tilde{u}_i \tilde{\sigma}_{iy} + \bar{u}_i \tilde{\sigma}_{iy} - \tilde{q}_y \end{pmatrix} \quad (6.13)$$

$$\tilde{H}_I = \begin{pmatrix} \tilde{\rho}\tilde{u} \\ \tilde{u}\tilde{\rho}\tilde{w} + \tilde{u}\tilde{\rho}\tilde{w} \\ \tilde{v}\tilde{\rho}\tilde{w} + \tilde{v}\tilde{\rho}\tilde{w} \\ \tilde{w}\tilde{\rho}\tilde{w} + \tilde{w}\tilde{\rho}\tilde{w} + \tilde{p} \\ \tilde{w}\tilde{\rho}\tilde{E} + \tilde{w}\tilde{\rho}\tilde{E} + \tilde{w}\tilde{p} + \tilde{w}\tilde{p} \end{pmatrix}, \tilde{H}_V = \begin{pmatrix} 0 \\ \tilde{\sigma}_{xz} \\ \tilde{\sigma}_{yz} \\ \tilde{\sigma}_{zz} \\ \tilde{u}_i\tilde{\sigma}_{iz} + \tilde{u}_i\tilde{\sigma}_{iz} - \tilde{q}_z \end{pmatrix}, \quad (6.14)$$

in the three spatial directions. Thanks to the linear nature of the perturbation equations, they can be solved independently for each harmonic of each disturbance.

Some questions remain on how to compute the viscous stress tensors. In the Non-Linear Harmonic method implemented by Vilmin et al. (2006), both the laminar viscosity μ and the eddy viscosity μ_T are computed from the averaged flow variables only. Consequently, the mean and harmonic viscous stress tensors are given by

$$\bar{\sigma}_{ij} = 2(\bar{\mu} + \bar{\mu}_T) \left(\bar{s}_{ij} - \frac{1}{3} \frac{\partial \bar{u}_k}{\partial x_k} \delta_{ij} \right) \quad (6.15)$$

$$\tilde{\sigma}_{ij} = 2(\bar{\mu} + \bar{\mu}_T) \left(\tilde{s}_{ij} - \frac{1}{3} \frac{\partial \tilde{u}_k}{\partial x_k} \delta_{ij} \right), \quad (6.16)$$

respectively. For the treatment of turbulence, such an approach is often referred to as the frozen turbulence assumption. The influence of the harmonic flow on the eddy viscosity is ignored, which corresponds therefore to consider that turbulence is frozen in time. That approach is simple as a single turbulence model is required (for the mean eddy viscosity $\bar{\mu}_T$) and is actually accurate enough in many cases (see references in section 1.1.1). However, when the unsteady fluctuations have non-negligible effects on turbulence, then the complete viscous stress tensors read

$$\bar{\sigma}_{ij} = 2(\bar{\mu} + \bar{\mu}_T) \left(\bar{s}_{ij} - \frac{1}{3} \frac{\partial \bar{u}_k}{\partial x_k} \delta_{ij} \right) + 2\overline{\tilde{\mu}_T} \left(\bar{s}_{ij} - \frac{1}{3} \frac{\partial \bar{u}_k}{\partial x_k} \delta_{ij} \right) \quad (6.17)$$

$$\tilde{\sigma}_{ij} = 2(\bar{\mu} + \bar{\mu}_T) \left(\tilde{s}_{ij} - \frac{1}{3} \frac{\partial \tilde{u}_k}{\partial x_k} \delta_{ij} \right) + 2\tilde{\mu}_T \left(\bar{s}_{ij} - \frac{1}{3} \frac{\partial \bar{u}_k}{\partial x_k} \delta_{ij} \right), \quad (6.18)$$

and a second turbulence model is needed for the harmonic eddy viscosity $\tilde{\mu}_T$. As discussed in the introduction (see section 1.1.1), the perturbation equation(s) corresponding to the turbulence model employed could be obtained following the same procedure described here above for the Navier-Stokes equations. The resulting linearized turbulence model then allows to evaluate $\tilde{\mu}_T$. However, this comes with a series of issues, among which the inherent non-linearity of turbulence.

6.2 Comparison between URANS and NLH

In this section, a comparison between URANS and NLH methodologies to solve the transonic flow over a bump introduced in chapter 5 is carried out. As a first step, the results in the conditions of the experiments, at $Re_{B_l} = 3.81 \times 10^6$, are presented. The simulations are performed on the same mesh as used in section 5.3.1 for the reference conditions, ensuring that $y_w^+ \approx 1$. The boundary conditions and flow conditions are also identical. The turbulence model considered to evaluate the eddy viscosity is the

Spalart-Allmaras model (Spalart & Allmaras, 1992). The pressure perturbation is imposed at the outlet boundary. For the URANS, it consists in a sinusoidally varying temporal signal with the appropriate amplitude and frequency, while for the NLH, the frequency and the imaginary part of the perturbation are prescribed. Furthermore, the Non-Linear Harmonic model employs a single perturbation consisting of a single harmonic, at the forcing frequency, and turbulence is assumed to be frozen. The simulations are completed for forcing frequencies of 500Hz and 1000Hz.

Figure 6.1 first compares the contours of mean density for the case forced at 500Hz. The two methodologies give remarkably identical results, with a choked flow and a boundary layer separating at the shock foot.

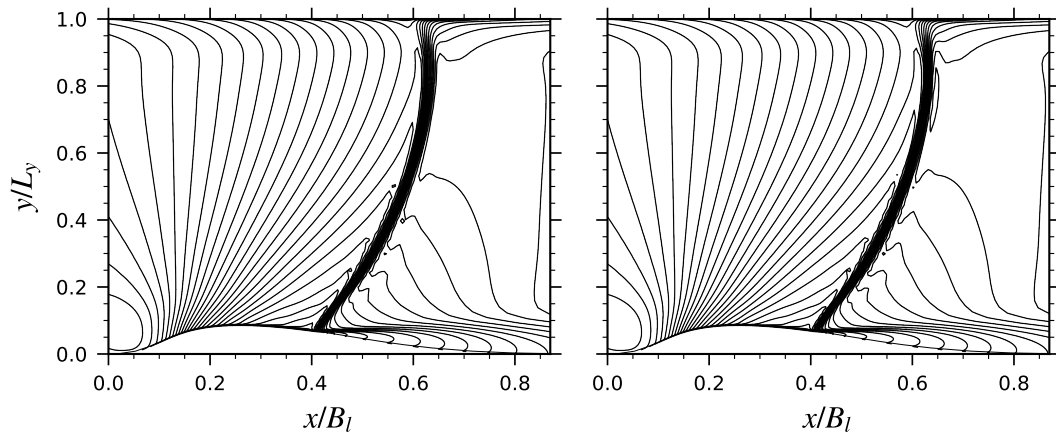


Figure 6.1. Mean ρ/ρ_∞ from URANS (*left*) and NLH (*right*) simulations at $Re_{B_1} = 3.81 \times 10^6$ and $f = 500\text{Hz}$, 40 equally-spaced contours between 0.4 and 1.1.

The mean friction and pressure coefficients at the bottom wall are given in figure 6.2. Similarly, the results are on top of each other, so that it is impossible to distinguish one from another. The same observations could be done for the case

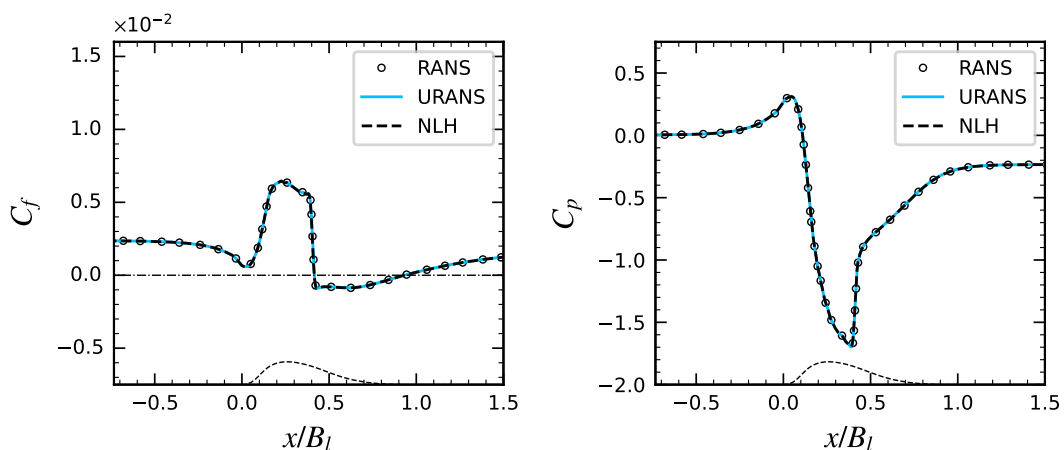


Figure 6.2. Comparison of mean friction coefficient (*left*) and mean wall pressure coefficient (*right*) on the bump wall between RANS, URANS and NLH simulations at $Re_{B_1} = 3.81 \times 10^6$. For the forced cases, $f = 500\text{Hz}$. The *thin dashed* line represents the bump geometry.

forced at 1000Hz but the results are not shown here since they are indistinguishable from the 500Hz case. Moreover, the perfect agreement with RANS tells that the perturbation itself has no effect on the mean flow. In the reference conditions, the NLH is therefore able to reproduce the same mean flow as RANS and URANS, regardless of the forcing frequency. Even though worth noticing, this capability is actually not surprising. It was indeed demonstrated in chapter 5, using ILES, that the mean flow was unaffected by the perturbation and that, independently of the perturbation frequency.

Of bigger interest is the ability of the NLH method to predict the unsteady features of the flow as URANS simulations can do. In that regard, figure 6.3 compares the amplitude and the phase of the first harmonic of \tilde{p} between the two methodologies, when the flow is forced at 500Hz. The phase clearly displays an upstream propagating wave since it decreases from downstream to upstream. This behavior extends similarly in the free stream up to the shock wave, but is somehow different in the bottom boundary layer upstream of $x/B_l \approx 1$. The maximum of amplitude is in both cases predicted along the upper part of the shock. Nevertheless, other discrepancies are observed in the bottom boundary layer.

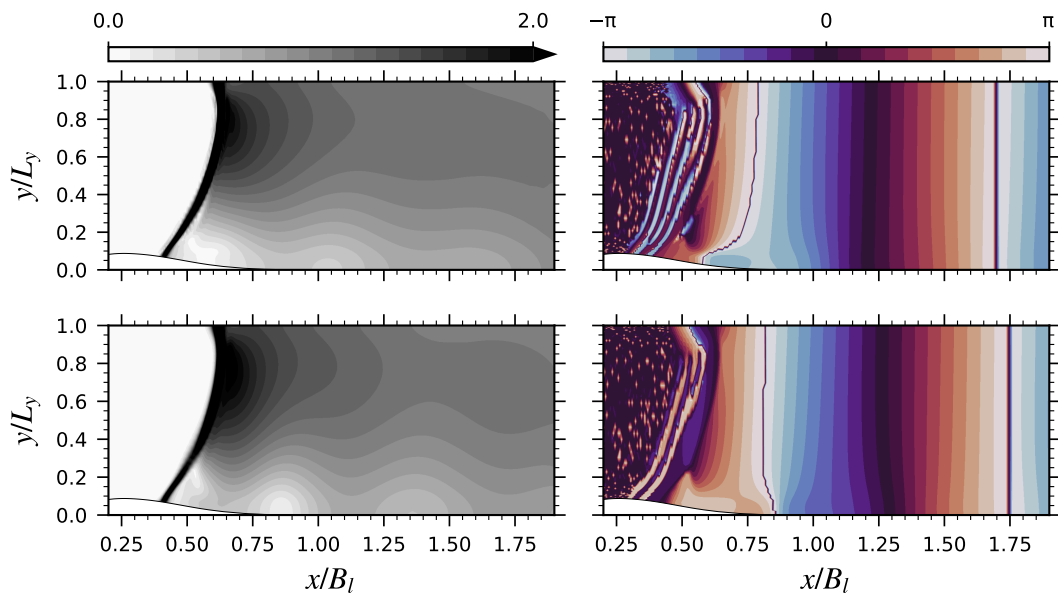


Figure 6.3. Amplitude $A_{p,1}/A_{p_o}$ (left) and phase $\phi_{p,1}$ (right) of the first harmonic of \tilde{p} at $Re_{B_l} = 3.81 \times 10^6$ and $f = 500\text{Hz}$ - URANS (top) and NLH (bottom) simulations.

To further illustrate these disagreements, the evolution of the first harmonic amplitude of pressure at the bottom wall is depicted in figure 6.4, for both the 500Hz and 1000Hz cases. The mismatch between NLH and URANS results is now clear, as the lobes downstream of the shock are shifted in the NLH and therefore not properly reproduced. Debrabandere (2013) ruled out several possible explanations for this. The inclusion of higher-order cross coupling terms, the non-reflecting treatment at the outlet boundary and the neglect of the deterministic stresses were indeed not found to yield better results. Such an inconsistency was also pointed out by Philit

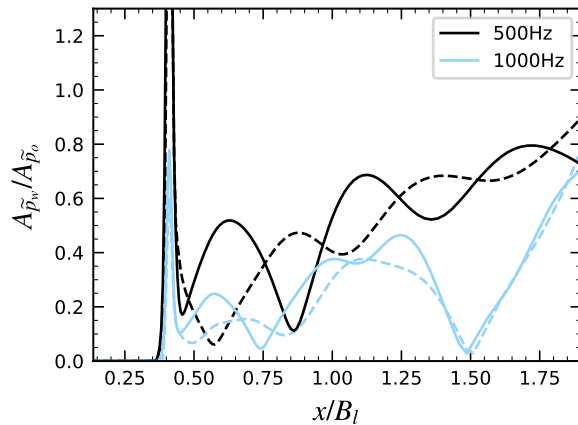


Figure 6.4. Normalized wall pressure amplitude at the forcing frequencies - comparison of streamwise evolution between URANS (*dashed*) and NLH (*solid*) simulations at $Re_{B_l} = 3.81 \times 10^6$.

et al. (2012) on the same configuration, using a fully-linearized harmonic solver. The $k - \omega$ turbulence model of Wilcox (2006) was employed, while the Spalart-Allmaras model is used here, showing that changing the type of turbulence closure does not solve the issue neither. However, their investigation demonstrated that taking into account harmonic turbulence allows to recover URANS results. In other words, the reason for the discrepancy lies in the freezing of the turbulence.

The ILES presented in chapter 5 were performed at a reduced Reynolds number, $Re_{B_l} = 1.91 \times 10^5$, to obtain an affordable computing cost. The comparison between URANS and NLH is therefore pursued considering the same conditions as in the ILES. Figure 6.5 shows the mean density contours for the case forced at 500Hz. By decreasing the Reynolds number, the flow is modified as described in section 5.3.1. The flow is indeed not choked anymore and the boundary layer separates upstream of the shock. Nevertheless, the NLH is able to reproduce the same mean flow as URANS. This is further demonstrated in figure 6.6, comparing the mean friction and pressure coefficients on the bottom wall, in which a perfect match between all the methodologies is reported.

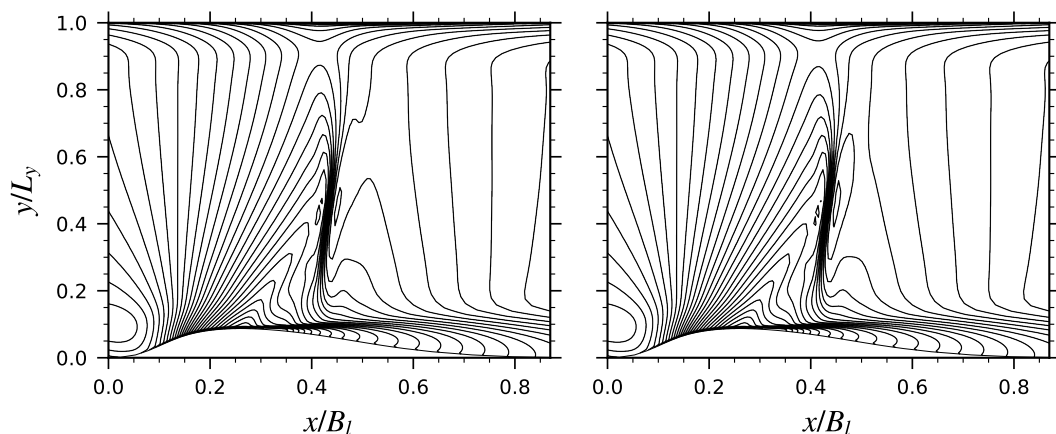


Figure 6.5. Mean ρ/ρ_∞ from URANS (*left*) and NLH (*right*) simulations at $Re_{B_l} = 1.91 \times 10^5$ and $f = 500\text{Hz}$, 40 equally-spaced contours between 0.4 and 1.1.

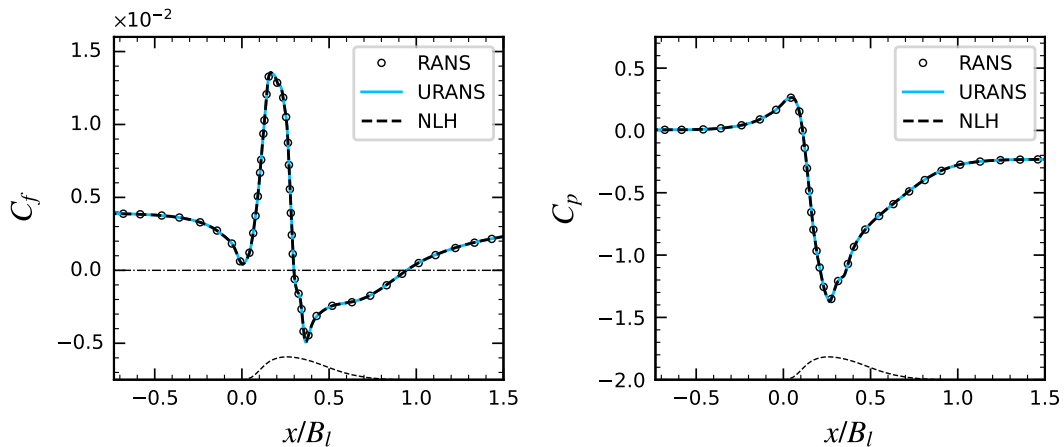


Figure 6.6. Comparison of mean friction coefficient (*left*) and mean wall pressure coefficient (*right*) on the bump wall between RANS, URANS and NLH simulations at $Re_{B_l} = 1.91 \times 10^5$. For the forced cases, $f = 500\text{Hz}$. The *thin dashed* line represents the bump geometry.

The evolution of the first harmonic amplitude of pressure along the bottom wall is portrayed in figure 6.7. The frozen turbulence approach of the NLH is again not able to predict the same evolution as in URANS. The ILES performed in chapter 5 are consequently relevant to study in order to correct this defect.

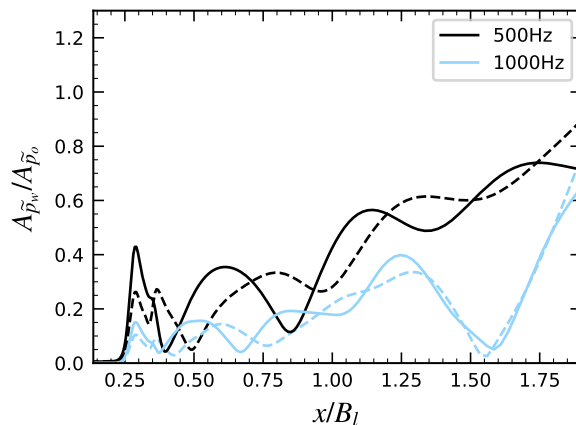


Figure 6.7. Normalized wall pressure amplitude at the forcing frequencies - comparison of streamwise evolution between URANS (*dashed*) and NLH (*solid*) simulations at $Re_{B_l} = 1.91 \times 10^5$.

6.3 A first model for the harmonic turbulence

The previous section illustrated the shortcomings related to the frozen turbulence assumption, that is to say to consider that only the mean flow is affecting turbulence. In this section, a first simple model is derived to account for the influence of the harmonic flow.

Assuming a turbulence model based on an eddy viscosity ν_T , turbulent stresses are generally written

$$-u'_i u'_j = 2\nu_T \left(s_{ij} - \frac{1}{3} \frac{\partial u_k}{\partial x_k} \delta_{ij} \right) \quad (6.19)$$

and, more particularly, in a shear-dominated flow, the shear stress is given by

$$-u'v' = \nu_T S, \quad (6.20)$$

with $S = \partial u / \partial y$ being the shear.

In the Non-Linear Harmonic method, the flow variables are decomposed into a mean and a sum of perturbations, each of them being assumed to be periodic and therefore represented by a sum of harmonics. Considering a single perturbation made of a single harmonic, the eddy viscosity and the shear are written

$$\nu_T = \bar{\nu}_T + \tilde{\nu}_T \quad (6.21)$$

$$S = \bar{S} + \tilde{S} \quad (6.22)$$

and, consequently, the shear stress is obtained with

$$-u'v' = (\bar{\nu}_T + \tilde{\nu}_T)(\bar{S} + \tilde{S}) \quad (6.23a)$$

$$= \bar{\nu}_T \bar{S} + \bar{\nu}_T \tilde{S} + \tilde{\nu}_T \bar{S} + \tilde{\nu}_T \tilde{S}. \quad (6.23b)$$

The mean shear stress follows from time averaging, such that,

$$-\overline{u'v'} = \bar{\nu}_T \bar{S} + \overline{\tilde{\nu}_T \tilde{S}} \quad (6.24a)$$

$$= \bar{\nu}_T \bar{S}, \quad (6.24b)$$

with the second term being dropped since the feedback effect of the harmonic flow on the mean flow was shown to be negligible. The phase-averaged shear stress is given by

$$-\langle u'v' \rangle = \bar{\nu}_T \bar{S} + \bar{\nu}_T \tilde{S} + \tilde{\nu}_T \bar{S} + \tilde{\nu}_T \tilde{S} \quad (6.25a)$$

$$= \bar{\nu}_T \bar{S} + \bar{\nu}_T \tilde{S} + \tilde{\nu}_T \bar{S}, \quad (6.25b)$$

where again the last term in equation 6.25a is supposed to be negligible. Finally, the harmonic shear stress is the difference between the phase average and the time average, therefore giving

$$-\widetilde{u'v'} = -\langle u'v' \rangle + \overline{u'v'} \quad (6.26a)$$

$$= \bar{\nu}_T \tilde{S} + \tilde{\nu}_T \bar{S}. \quad (6.26b)$$

In a frozen turbulence approach, the harmonic eddy viscosity $\tilde{\nu}_T$ is neglected and only the mean eddy viscosity $\bar{\nu}_T$ is computed. The latter simply comes from the turbulence model employed, with all the variables being evaluated from the mean flow.

The analysis of the harmonic turbulent stress budgets and, more specifically, turbulence production in section 5.3.4.7 showed that only two contributions are necessary to represent the full production term. A simple reduced-order model is derived by using this information. The flow is supposed to be dominated by shear

and therefore, an exact form of the production term of turbulence kinetic energy is given by

$$P_k = \frac{1}{2} P_{u'v'} \quad (6.27a)$$

$$= \frac{1}{2} \left(-2u'v' \frac{\partial u}{\partial y} \right) \quad (6.27b)$$

$$= -u'v' \frac{\partial u}{\partial y} \quad (6.27c)$$

$$= \nu_T S^2, \quad (6.27d)$$

which can be further expanded following the decomposition from the NLH and simplified by neglecting second order terms, such that

$$P_k = (\bar{\nu}_T + \tilde{\nu}_T)(\bar{S} + \tilde{S})^2 \quad (6.28a)$$

$$= (\bar{\nu}_T + \tilde{\nu}_T)(\bar{S}^2 + 2\bar{S}\tilde{S} + \tilde{S}^2) \quad (6.28b)$$

$$= (\bar{\nu}_T + \tilde{\nu}_T)(\bar{S}^2 + 2\bar{S}\tilde{S}) \quad (6.28c)$$

$$= \bar{\nu}_T \bar{S}^2 + 2\bar{\nu}_T \bar{S}\tilde{S} + \tilde{\nu}_T \bar{S}^2 + 2\tilde{\nu}_T \bar{S}\tilde{S} \quad (6.28d)$$

$$= \bar{\nu}_T \bar{S}^2 + 2\bar{\nu}_T \bar{S}\tilde{S} + \tilde{\nu}_T \bar{S}^2. \quad (6.28e)$$

Mean and harmonic turbulence kinetic energy production terms will finally correspond to, respectively,

$$\bar{P}_k = \bar{\nu}_T \bar{S}^2 \quad (6.29)$$

$$\tilde{P}_k = 2\bar{\nu}_T \bar{S}\tilde{S} + \tilde{\nu}_T \bar{S}^2. \quad (6.30)$$

From the analysis of the high-fidelity data, the coherent turbulence kinetic energy production comes mostly from the production of $\widetilde{u'v'}$. Moreover, the latter can be reduced to two dominant terms, that is to say

$$\tilde{P}_k = -\overline{u'v'} \tilde{S} - \widetilde{u'v'} \bar{S}. \quad (6.31)$$

It is now assumed that each term of the right-hand side of equation 6.30 can be identified to each term of the right-hand side of equation 6.31. An equation is therefore obtained for the mean eddy viscosity, as well as for the harmonic eddy viscosity, such that

$$\bar{\nu}_T = \frac{-\overline{u'v'}}{2\bar{S}} \quad (6.32)$$

$$\tilde{\nu}_T = \frac{-\widetilde{u'v'}}{\bar{S}}. \quad (6.33)$$

Eliminating \bar{S} leads to

$$\tilde{\nu}_T = 2\bar{\nu}_T \frac{\widetilde{u'v'}}{\overline{u'v'}}, \quad (6.34)$$

in which the mean and harmonic shear stresses can be replaced by the expressions from equations 6.24b and 6.26b to give

$$\tilde{\nu}_T = 2\bar{\nu}_T \frac{\widetilde{u'v'}}{\overline{u'v'}} \quad (6.35a)$$

$$= 2\bar{\nu}_T \frac{\bar{\nu}_T \tilde{S} + \tilde{\nu}_T \bar{S}}{\bar{\nu}_T \bar{S}} \quad (6.35b)$$

$$= 2\bar{\nu}_T \frac{\tilde{S}}{\bar{S}} + 2\tilde{\nu}_T \quad (6.35c)$$

and, solving for $\tilde{\nu}_T$, the final expression reads

$$\tilde{\nu}_T = -2\bar{\nu}_T \frac{\tilde{S}}{\bar{S}}. \quad (6.36)$$

Before actually implementing the model in the NLH solver, its accuracy is *a priori* assessed by looking at the results obtained from URANS simulations, which allow to derive all the quantities involved in equation 6.36. To evaluate the harmonic components, the flow variables are Fourier transformed and only the first harmonic is retained. Moreover, the harmonic eddy viscosity is limited to 20% of the mean eddy viscosity. The shear ratio \tilde{S}/\bar{S} can indeed become excessively high in regions in which the mean shear is close to zero, leading to unrealistic values of harmonic eddy viscosity.

Figure 6.8 reports the results for the various forced cases, at the reduced Reynolds number. Looking first at 500Hz, from the URANS simulation, three elongated structures of harmonic eddy viscosity are highlighted, following the edge of the downstream boundary layer. Their cores are located at $x/B_l \approx 0.6$, $x/B_l \approx 1.0$

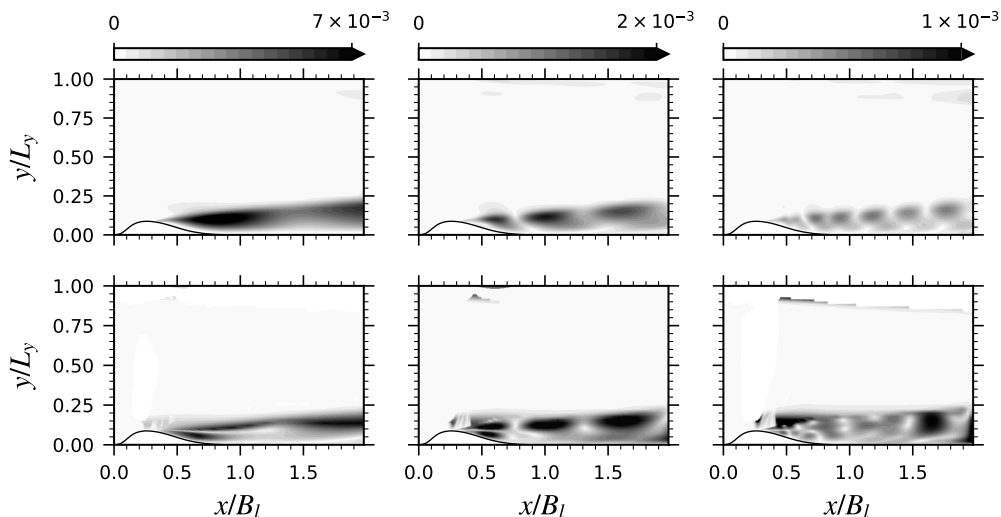


Figure 6.8. Comparison of harmonic eddy viscosity $\tilde{\nu}_T$ for the case at $Re_{B_l} = 1.91 \times 10^5$ with $f = 250\text{Hz}$ (*left*), $f = 500\text{Hz}$ (*center*) and $f = 1000\text{Hz}$ (*right*) - from URANS (*top*) and from the model (*bottom*).

and $x/B_l \approx 1.6$, respectively, which corresponds well to the local minima of wall pressure amplitude (see figure 6.7). The model is capturing qualitatively well the two most downstream structures, while the most upstream one is actually split into two structures. This actually means that $\tilde{\nu}_T$ is not following the harmonic shear in that region. The magnitude of harmonic eddy viscosity is slightly over-estimated by the model. At 250Hz, a satisfactory agreement is also observed. The most upstream structure pointed out in URANS is also broken down into two in the model, whereas the downstream structure is correctly predicted. At 1000Hz, the model is not accurate. None of the structures emphasized from URANS can be clearly discerned in the model. The reason for this discrepancy at high forcing frequency is not clear, but it seems to indicate that the harmonic eddy viscosity is not controlled by the shear.

Since this first simple model was derived from the high-fidelity data at the reduced Reynolds number, it is also of interest to check its prediction in the reference conditions. The harmonic eddy viscosity from URANS and from the model, at $Re_{B_l} = 3.81 \times 10^6$, are therefore compared in figure 6.9. The same agreement is found with respect to the lower Reynolds number configuration, regardless of the forcing frequency.

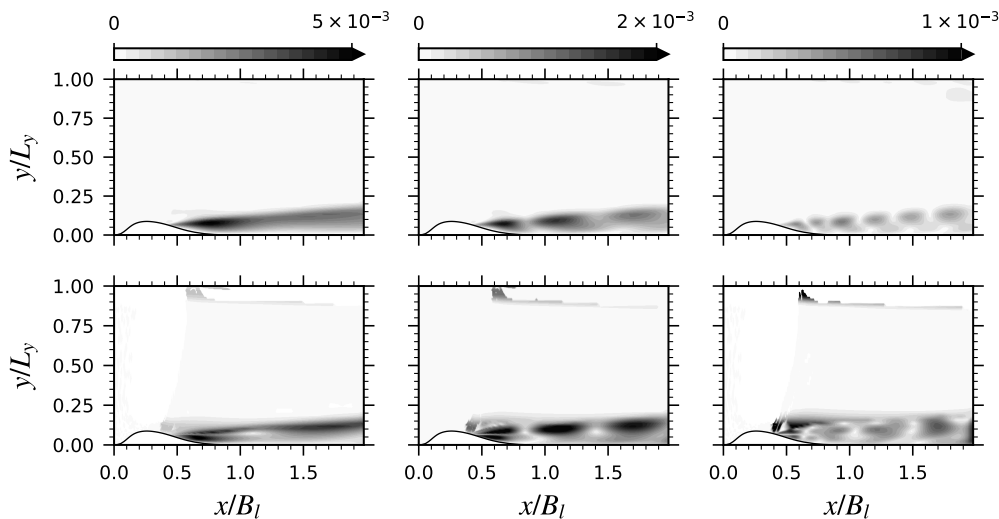


Figure 6.9. Comparison of harmonic eddy viscosity $\tilde{\nu}_T$ for the case at $Re_{B_l} = 3.81 \times 10^6$ with $f = 250\text{Hz}$ (left), $f = 500\text{Hz}$ (center) and $f = 1000\text{Hz}$ (right) - from URANS (top) and from the model (bottom).

6.4 Summary

In this last chapter, the attention was given to the Non-Linear Harmonic method. First, the derivation of the method has been recalled and the need for two turbulence models, one for the mean eddy viscosity and one for the harmonic eddy viscosity was expressed. A common assumption was presented, that is to say the frozen turbulence approach, in which the harmonic eddy viscosity is discarded.

The performance of the NLH method was then assessed on the transonic flow over a bump, studied in the previous chapter, and compared to the results obtained from URANS simulations. The mean solution given by the NLH is identical to the mean solution given by the URANS computations. However, discrepancies were found in the unsteady flow field. In particular, a mismatch was pointed out in the distribution of wall pressure amplitude downstream of the bump. These differences are attributed to the frozen turbulence assumption.

In an attempt to improve the NLH method regarding the treatment of turbulence, a simple model for the harmonic eddy viscosity was derived using the high-fidelity data presented in the previous chapter. The accuracy of the model has been tested *a priori* by comparing its predictions to the expected harmonic eddy viscosity given by URANS simulations.

For such a simple model, the results are encouraging. The agreement with URANS, both qualitatively and quantitatively, was found to be satisfactory, for different forcing frequencies and for different Reynolds numbers. While only aspects related to turbulence production were considered to develop the model, improved formulations could be obtained by incorporating other effects, such as convection or turbulent transport for example.

Chapter 7

Conclusions

In this dissertation is presented a methodology to employ high-fidelity high-order simulations, with the idea of improving turbulence modeling in reduced-order harmonic methods, in the context of turbomachinery applications featuring shock wave/boundary layer interactions. In that regard, three objectives were established. Starting *from high-fidelity high-order*, the first goal was to contribute to the development of a high-order solver to enhance its robustness regarding shock waves and its ability to deal with turbulent flows. Then, as a second objective, the intent was to use the solver as a numerical wind tunnel and generate high-fidelity data to study turbulence in periodically forced shock wave/boundary layer interactions. Finally, *to reduced-order modeling*, the last aim was to improve harmonic turbulence modeling in the framework of harmonic methods for turbomachinery applications. The contributions of the different chapters to meet these objectives are summarized hereunder.

- In chapters 3 and 4, the first goal has been addressed. In the former chapter, the numerical methods chosen to develop the solver were described. High-order spatial accuracy is obtained with a flux reconstruction scheme. Shock waves are resolved with the help of artificial viscosity, and further associated with the Ducros sensor. The generation of turbulent inflow conditions is managed with a digital filtering technique. In the latter chapter, the adequacy of these features was validated by assessing the ability of the solver to reproduce a well-known canonical case of an oblique shock wave/turbulent boundary layer interaction at Mach 2.3. The experimental Reynolds number ($Re_\theta \approx 5000$) is matched in a wall-resolved implicit large-eddy simulation, the results of which were analyzed in detail and found to be in excellent agreement with the numerous other works from the literature. The shock-capturing strategy put in place was shown to be robust enough to handle the complex and unsteady shock system. At the same time, the treatment applied at the inlet boundary allowed the development of a realistic turbulent boundary layer shortly downstream, which was furthermore not affected by the artificial viscosity.
- In chapter 5, the second objective has been completed. To study the harmonic turbulence, the periodically forced transonic flow over a bump at

$Re_{B_i} = 1.91 \times 10^5$ was examined by carrying out implicit large-eddy simulations. Care was taken to prescribe perturbation frequencies that are representative of the conditions encountered in turbomachinery due to rotor/stator interactions. Three forcing frequencies were investigated, corresponding to reduced frequencies of 0.2, 0.4 and 0.8. A meticulous comparison was performed between the unperturbed and forced cases. It showed first that the mean flow is insensitive to the forcing. However, unsteady aspects are considerably influenced. For low forcing frequencies, the flow is fully locked at the forcing frequency. At the highest forcing frequency, a decoupling between the baseline and forced flows starts to appear. The natural oscillation of the shock, highlighted in the baseline case, is indeed recovered. To extract the harmonic component of the flow, phase-averaging was employed, which was found to be particularly efficient for the two lowest forcing frequencies. Coherent structures of streamwise velocity and turbulence kinetic energy were identified. Their layout is identical in the region beneath the shock system, while it is function of the forcing frequency in the downstream boundary layer. Further insights on harmonic turbulence was gained by the detailed description of the harmonic turbulent stress budgets. Only two contributions from the mean and harmonic shears were found to be dominant for the harmonic production term.

- In chapter 6, the third goal has been achieved. The ineptitude of the Non-Linear Harmonic method to accurately predict the transonic flow over a bump presented earlier was formalized and attributed to the lack of a harmonic turbulence model. A simple analytical model for the harmonic eddy viscosity was then derived, by taking advantage of the observations made about the harmonic production. Its *a priori* performance was assessed using the results from URANS simulations as ground truth. Albeit imperfect, the model features a satisfactory agreement, both qualitatively and quantitatively, at reduced frequencies of 0.2 and 0.4.

Even though the progress made on the harmonic eddy viscosity model is encouraging, additional work would be needed to bring it to maturity for industrial applications of the Non-Linear Harmonic method. At last, a series of actions going in that direction are suggested.

- The simple analytical model for the harmonic eddy viscosity could be actually implemented in the Non-Linear Harmonic solver, so that its *a posteriori* performance could be assessed. This is the first next step to undertake.
- The model could be progressively supplemented by additional terms to include effects other than production, such as convection or turbulent transport, and improve its performance. This could potentially correct the defect of the model for the highest forcing frequency investigated. A deeper analysis of the harmonic budgets would be required to identify how relevant the different terms would be exactly.
- To take full advantage of the database, approaches using machine learning algorithms could be used to derive a model, with possibly the incorporation of

the knowledge gained with the previous analytical work. Genetic Programming based techniques, such as Gene Expression Programming or Multi-Expression Programming, are attractive in that regard, as they allow to derive analytical expressions that can be directly implemented in CFD solvers. They have been already applied to turbulence modeling (Miró et al., 2023; Weatheritt & Sandberg, 2016) and also, in that context, to phase-averaged data (Akolekar et al., 2019).

- The current study of periodically forced transonic flow is limited to a two-dimensional bump, with the only parameter investigated being the perturbation frequency. The study could be broadened to variation in perturbation amplitude and/or in Reynolds number, for example. Configurations of increasing complexity could be considered in order to get closer to actual turbomachinery flows and widen the range of application of the model. A linear cascade configuration would be the first step toward that objective. Then, full-span configurations would follow, to include three-dimensional effects into the model.
- In relation to the inclusion of three-dimensional effects, the eddy viscosity formulation could be abandoned in favor of more complex closures, as (explicit) algebraic Reynolds-stress models or non-linear eddy viscosity models. In a triple decomposition framework, the latter was employed for instance by Kitsios et al. (2010) to perform stability analysis of a turbulent channel.

Appendix A

Triple Decomposition for Incompressible Flows

In this appendix, the triple decomposition is introduced as a tool to study periodically forced flows. The first section defines the triple decomposition and a few useful properties. Then, the governing equations of the mean and the periodic flows, as well as the budgets of mean and periodic turbulent stresses, are derived in detail in the framework of the triple decomposition. Finally, practical aspects for the obtainment of the coherent budgets are covered in the last section.

A.1 Definitions and properties

The triple decomposition of Reynolds and Hussain (1972) states that any flow variable a may be decomposed as the sum of three components, such that

$$a(x, y, z, t; T) = \bar{a}(x, y, z) + \tilde{a}(x, y, z, t/T) + a'(x, y, z, t) \quad (\text{A.1})$$

where \bar{a} is the mean component, \tilde{a} is the coherent (also called periodic or harmonic) component and a' is the incoherent (or random) component. x, y and z are the spatial coordinates, t is the time and T is the period. Both the coherent and incoherent components depend on time and therefore, for this decomposition to be meaningful, the period T must be several orders of magnitude higher than the time scale of the random component.

Two averaging operators are required to retrieve the different components. Time averaging will directly give the mean component \bar{a} whereas phase averaging or ensemble averaging, if there is indeed a separation of time scales, will filter out the random component, giving

$$\langle a \rangle = \bar{a} + \tilde{a} . \quad (\text{A.2})$$

Consequently, the coherent and incoherent components are obtained following

$$\tilde{a} = \langle a \rangle - \bar{a} \quad (\text{A.3})$$

$$a' = a - \langle a \rangle . \quad (\text{A.4})$$

Some useful properties can be derived. They are summarized hereunder.

$$\bar{\tilde{a}} = 0, \quad \overline{a'} = 0, \quad \overline{\tilde{a}b} = \bar{a}\bar{b} \quad (\text{A.5})$$

$$\langle a' \rangle = 0, \quad \langle \tilde{a}b \rangle = \tilde{a}\langle b \rangle, \quad \langle \tilde{a}b \rangle = \bar{a}\langle b \rangle \quad (\text{A.6})$$

$$\overline{\langle a \rangle} = \bar{a}, \quad \langle \bar{a} \rangle = \bar{a}, \quad \overline{\tilde{a}b'} = \langle \tilde{a}b' \rangle = 0 \quad (\text{A.7})$$

These properties further allow to write that

$$\overline{ab} = \bar{a}\bar{b} + \overline{\tilde{a}b} + \overline{a'b'} \quad (\text{A.8})$$

$$\langle ab \rangle = \bar{a}\bar{b} + \tilde{a}\bar{b} + \bar{a}\tilde{b} + \tilde{a}\tilde{b} + \langle a'b' \rangle . \quad (\text{A.9})$$

A.2 Mean and coherent governing equations

After introduction of the triple decomposition into the incompressible Navier-Stokes equations, the governing equations for the mean component of the flow are directly obtained by time averaging. The equations governing the coherent motion are derived by subtracting the time-averaged equations from the phase-averaged ones. In the following, the convention of repeated indices is employed.

For the equation of conservation of mass, starting from equation 2.1, it gives

$$\frac{\partial \rho}{\partial t} + \frac{\partial}{\partial x_i}(\rho u_i) = 0 \quad (\text{A.10})$$

and using the incompressible assumption,

$$\frac{\partial u_i}{\partial x_i} = 0 . \quad (\text{A.11})$$

Introducing the triple decomposition for u_i and time averaging,

$$\overline{\frac{\partial}{\partial x_i} (\bar{u}_i + \tilde{u}_i + u'_i)} = 0 \quad (\text{A.12})$$

simplifying into

$$\frac{\partial \bar{u}_i}{\partial x_i} = 0 \quad (\text{A.13})$$

whereas the phase-average gives

$$\left\langle \frac{\partial}{\partial x_i} (\bar{u}_i + \tilde{u}_i + u'_i) \right\rangle = 0 \quad (\text{A.14a})$$

$$\frac{\partial}{\partial x_i} (\bar{u}_i + \tilde{u}_i) = 0 . \quad (\text{A.14b})$$

Subtracting time-average from phase-average (A.14b – A.13) finally gives (see equation 2.3b of Reynolds and Hussain (1972))

$$\frac{\partial \tilde{u}_i}{\partial x_i} = 0 . \quad (\text{A.15})$$

For the equation of conservation of mass, starting from equation 2.2, it gives

$$\frac{\partial}{\partial t}(\rho u_i) + \frac{\partial}{\partial x_j}(\rho u_i u_j) = -\frac{\partial p}{\partial x_i} + \frac{\partial \sigma_{ij}}{\partial x_j} \quad (\text{A.16})$$

which can be further simplified thanks to the incompressibility assumption, such that

$$\rho \frac{\partial u_i}{\partial t} + \rho u_j \frac{\partial u_i}{\partial x_j} + \rho u_i \frac{\partial u_j}{\partial x_j} = -\frac{\partial p}{\partial x_i} + \frac{\partial \sigma_{ij}}{\partial x_j} . \quad (\text{A.17})$$

Moreover,

$$\sigma_{ij} = 2\mu \left(s_{ij} - \frac{1}{3} \frac{\partial u_k}{\partial x_k} \delta_{ij} \right) \quad (\text{A.18a})$$

$$= 2\mu s_{ij} \quad (\text{A.18b})$$

from which it follows that

$$\frac{\partial \sigma_{ij}}{\partial x_j} = 2\mu \frac{\partial s_{ij}}{\partial x_j} \quad (\text{A.19a})$$

$$= \mu \left(\frac{\partial^2 u_i}{\partial x_j^2} + \frac{\partial^2 u_j}{\partial x_i \partial x_j} \right) \quad (\text{A.19b})$$

$$= \mu \left[\frac{\partial^2 u_i}{\partial x_j^2} + \frac{\partial}{\partial x_i} \left(\frac{\partial u_j}{\partial x_j} \right) \right] \quad (\text{A.19c})$$

$$= \mu \frac{\partial^2 u_i}{\partial x_j^2} \quad (\text{A.19d})$$

and therefore, the equation of conservation of momentum for incompressible flows is

$$\rho \frac{\partial u_i}{\partial t} + \rho u_j \frac{\partial u_i}{\partial x_j} = -\frac{\partial p}{\partial x_i} + \mu \frac{\partial^2 u_i}{\partial x_j^2} . \quad (\text{A.20})$$

Only the second term of the left-hand side needs attention, the time-average gives

$$\overline{u_j \frac{\partial u_i}{\partial x_j}} = \overline{(\bar{u}_j + \tilde{u}_j + u'_j) \frac{\partial}{\partial x_j} (\bar{u}_i + \tilde{u}_i + u'_i)} \quad (\text{A.21a})$$

$$\begin{aligned} &= \overline{\bar{u}_j \frac{\partial \bar{u}_i}{\partial x_j}} + \overline{\bar{u}_j \frac{\partial \tilde{u}_i}{\partial x_j}} + \overline{\bar{u}_j \frac{\partial u'_i}{\partial x_j}} \\ &+ \overline{\tilde{u}_j \frac{\partial \bar{u}_i}{\partial x_j}} + \overline{\tilde{u}_j \frac{\partial \tilde{u}_i}{\partial x_j}} + \overline{\tilde{u}_j \frac{\partial u'_i}{\partial x_j}} \\ &+ \overline{u'_j \frac{\partial \bar{u}_i}{\partial x_j}} + \overline{u'_j \frac{\partial \tilde{u}_i}{\partial x_j}} + \overline{u'_j \frac{\partial u'_i}{\partial x_j}} \end{aligned} \quad (\text{A.21b})$$

$$= \overline{\bar{u}_j \frac{\partial \bar{u}_i}{\partial x_j}} + \overline{\tilde{u}_j \frac{\partial \tilde{u}_i}{\partial x_j}} + \overline{u'_j \frac{\partial u'_i}{\partial x_j}} \quad (\text{A.21c})$$

$$= \overline{\bar{u}_j \frac{\partial \bar{u}_i}{\partial x_j}} + \overline{\frac{\partial}{\partial x_j} (\tilde{u}_i \tilde{u}_j)} - \overline{\tilde{u}_i \frac{\partial \tilde{u}_j}{\partial x_j}} + \overline{\frac{\partial}{\partial x_j} (u'_i u'_j)} - \overline{u'_i \frac{\partial u'_j}{\partial x_j}} \quad (\text{A.21d})$$

$$= \overline{\bar{u}_j \frac{\partial \bar{u}_i}{\partial x_j}} + \overline{\frac{\partial}{\partial x_j} (\tilde{u}_i \tilde{u}_j + u'_i u'_j)} \quad (\text{A.21e})$$

while the phase-average gives

$$\left\langle u_j \frac{\partial u_i}{\partial x_j} \right\rangle = \left\langle (\bar{u}_j + \tilde{u}_j + u'_j) \frac{\partial}{\partial x_j} (\bar{u}_i + \tilde{u}_i + u'_i) \right\rangle \quad (\text{A.22a})$$

$$\begin{aligned} &= \left\langle \bar{u}_j \frac{\partial \bar{u}_i}{\partial x_j} \right\rangle + \left\langle \bar{u}_j \frac{\partial \tilde{u}_i}{\partial x_j} \right\rangle + \left\langle \bar{u}_j \frac{\partial u'_i}{\partial x_j} \right\rangle \\ &+ \left\langle \tilde{u}_j \frac{\partial \bar{u}_i}{\partial x_j} \right\rangle + \left\langle \tilde{u}_j \frac{\partial \tilde{u}_i}{\partial x_j} \right\rangle + \left\langle \tilde{u}_j \frac{\partial u'_i}{\partial x_j} \right\rangle \\ &+ \left\langle u'_j \frac{\partial \bar{u}_i}{\partial x_j} \right\rangle + \left\langle u'_j \frac{\partial \tilde{u}_i}{\partial x_j} \right\rangle + \left\langle u'_j \frac{\partial u'_i}{\partial x_j} \right\rangle \end{aligned} \quad (\text{A.22b})$$

$$= \left\langle \bar{u}_j \frac{\partial \bar{u}_i}{\partial x_j} \right\rangle + \left\langle \bar{u}_j \frac{\partial \tilde{u}_i}{\partial x_j} \right\rangle + \left\langle \tilde{u}_j \frac{\partial \bar{u}_i}{\partial x_j} \right\rangle + \left\langle \tilde{u}_j \frac{\partial \tilde{u}_i}{\partial x_j} \right\rangle + \left\langle u'_j \frac{\partial u'_i}{\partial x_j} \right\rangle \quad (\text{A.22c})$$

$$\begin{aligned} &= \left\langle \bar{u}_j \frac{\partial \bar{u}_i}{\partial x_j} \right\rangle + \left\langle \bar{u}_j \frac{\partial \tilde{u}_i}{\partial x_j} \right\rangle + \left\langle \tilde{u}_j \frac{\partial \bar{u}_i}{\partial x_j} \right\rangle \\ &+ \left\langle \frac{\partial}{\partial x_j} (\tilde{u}_i \tilde{u}_j) \right\rangle - \left\langle \tilde{u}_i \frac{\partial \tilde{u}_j}{\partial x_j} \right\rangle + \left\langle \frac{\partial}{\partial x_j} (u'_i u'_j) \right\rangle - \left\langle u'_i \frac{\partial u'_j}{\partial x_j} \right\rangle \end{aligned} \quad (\text{A.22d})$$

$$= \bar{u}_j \frac{\partial \bar{u}_i}{\partial x_j} + \bar{u}_j \frac{\partial \tilde{u}_i}{\partial x_j} + \tilde{u}_j \frac{\partial \bar{u}_i}{\partial x_j} + \frac{\partial}{\partial x_j} (\langle \tilde{u}_i \tilde{u}_j \rangle + \langle u'_i u'_j \rangle) \quad (\text{A.22e})$$

$$= \bar{u}_j \frac{\partial \bar{u}_i}{\partial x_j} + \bar{u}_j \frac{\partial \tilde{u}_i}{\partial x_j} + \tilde{u}_j \frac{\partial \bar{u}_i}{\partial x_j} + \frac{\partial}{\partial x_j} (\tilde{u}_i \tilde{u}_j + \langle u'_i u'_j \rangle) . \quad (\text{A.22f})$$

Subtracting time average from phase average (A.22f – A.21e) therefore gives

$$\begin{aligned} \left\langle u_j \frac{\partial u_i}{\partial x_j} \right\rangle - \overline{u_j \frac{\partial u_i}{\partial x_j}} &= \overline{u_j} \frac{\partial \tilde{u}_i}{\partial x_j} + \tilde{u}_j \frac{\partial \overline{u_i}}{\partial x_j} \\ &+ \frac{\partial}{\partial x_j} \left(\tilde{u}_i \tilde{u}_j + \langle u'_i u'_j \rangle - \overline{\tilde{u}_i \tilde{u}_j} - \overline{u'_i u'_j} \right) \end{aligned} \quad (\text{A.23a})$$

$$= \overline{u_j} \frac{\partial \tilde{u}_i}{\partial x_j} + \tilde{u}_j \frac{\partial \overline{u_i}}{\partial x_j} + \frac{\partial}{\partial x_j} \left(\tilde{u}_i \tilde{u}_j - \overline{\tilde{u}_i \tilde{u}_j} + \widetilde{u'_i u'_j} \right). \quad (\text{A.23b})$$

Accounting for all the terms, the final equations for the conservation of momentum for both the mean and the coherent motion are written

$$\rho \overline{u_j} \frac{\partial \overline{u_i}}{\partial x_j} = -\frac{\partial \overline{p}}{\partial x_i} + \mu \frac{\partial^2 \overline{u_i}}{\partial x_j^2} - \rho \frac{\partial}{\partial x_j} \left(\overline{\tilde{u}_i \tilde{u}_j} + \overline{u'_i u'_j} \right) \quad (\text{A.24})$$

$$\rho \frac{\partial \tilde{u}_i}{\partial t} + \rho \overline{u_j} \frac{\partial \tilde{u}_i}{\partial x_j} + \rho \tilde{u}_j \frac{\partial \overline{u_i}}{\partial x_j} = -\frac{\partial \tilde{p}}{\partial x_i} + \mu \frac{\partial^2 \tilde{u}_i}{\partial x_j^2} - \rho \frac{\partial}{\partial x_j} \left(\tilde{u}_i \tilde{u}_j - \overline{\tilde{u}_i \tilde{u}_j} + \widetilde{u'_i u'_j} \right) \quad (\text{A.25})$$

with the latter corresponding to equation 2.6 of Reynolds and Hussain (1972).

The derivation of the equations for the coherent component of the turbulent stresses $\widetilde{u'_i u'_j}$ starts by the derivation of the equation of conservation of momentum for the incoherent component of the velocity, u'_i . This is obtained by subtracting the phase-averaged equation from the Navier-Stokes equation of conservation of momentum. The equation of conservation of momentum is written (see equation A.20)

$$\rho \frac{\partial u_i}{\partial t} + \rho u_j \frac{\partial u_i}{\partial x_j} = -\frac{\partial p}{\partial x_i} + \mu \frac{\partial^2 u_i}{\partial x_j^2} \quad (\text{A.26})$$

and its phase-average is

$$\begin{aligned} \rho \frac{\partial \tilde{u}_i}{\partial t} + \rho \overline{u_j} \frac{\partial \tilde{u}_i}{\partial x_j} + \rho \tilde{u}_j \frac{\partial \overline{u_i}}{\partial x_j} + \rho \tilde{u}_j \frac{\partial \overline{u_i}}{\partial x_j} \\ + \rho \frac{\partial}{\partial x_j} \left(\tilde{u}_i \tilde{u}_j + \langle u'_i u'_j \rangle \right) = -\frac{\partial \langle p \rangle}{\partial x_i} + \mu \frac{\partial^2 \langle u_i \rangle}{\partial x_j^2} \end{aligned} \quad (\text{A.27})$$

so that the difference between the two (A.26 – A.27) gives

$$\begin{aligned} \rho \frac{\partial u'_i}{\partial t} + \rho \overline{u_j} \frac{\partial u'_i}{\partial x_j} + \rho \tilde{u}_j \frac{\partial u'_i}{\partial x_j} + \rho u'_j \frac{\partial \overline{u_i}}{\partial x_j} \\ + \rho u'_j \frac{\partial \tilde{u}_i}{\partial x_j} = -\frac{\partial p'}{\partial x_i} + \mu \frac{\partial^2 u'_i}{\partial x_j^2} + \rho \frac{\partial}{\partial x_j} \left(\langle u'_i u'_j \rangle - u'_i u'_j \right) \end{aligned} \quad (\text{A.28})$$

and corresponds to equation 2.8 of Reynolds and Hussain (1972).

The equation for $u'_i u'_j$ is obtained by summing equation A.28 for u'_i multiplied by u'_j and the same but for u'_j multiplied by u'_i . The equation for the coherent

component $\widetilde{u'_i u'_j}$ is finally the difference between the phase and time averages while the budget of the mean component $\overline{u'_i u'_j}$ is simply arising from the time average. The derivation for the coherent component is now detailed.

For the first term of the left-hand side, it gives

$$\rho u'_j \frac{\partial u'_i}{\partial t} + \rho u'_i \frac{\partial u'_j}{\partial t} = \rho \frac{\partial}{\partial t} (u'_i u'_j) \quad (\text{A.29})$$

and the difference between phase and time averages leads to

$$\rho \frac{\partial \langle u'_i u'_j \rangle}{\partial t} - \rho \frac{\partial \overline{u'_i u'_j}}{\partial t} = \rho \frac{\partial \overline{u'_i u'_j}}{\partial t} + \rho \frac{\partial \widetilde{u'_i u'_j}}{\partial t} - \rho \frac{\partial \overline{u'_i u'_j}}{\partial t} \quad (\text{A.30a})$$

$$= \rho \frac{\partial \widetilde{u'_i u'_j}}{\partial t}. \quad (\text{A.30b})$$

For the second term of the left-hand side, it gives

$$\rho \overline{u'_k} u'_j \frac{\partial u'_i}{\partial x_k} + \rho \overline{u'_k} u'_i \frac{\partial u'_j}{\partial x_k} = \rho \overline{u'_k} \frac{\partial u'_i u'_j}{\partial x_k} \quad (\text{A.31})$$

and the difference between phase and time averages leads to

$$\rho \left\langle \overline{u'_k} \frac{\partial u'_i u'_j}{\partial x_k} \right\rangle - \rho \overline{u'_k} \frac{\partial \overline{u'_i u'_j}}{\partial x_k} = \rho \overline{u'_k} \frac{\partial \langle u'_i u'_j \rangle}{\partial x_k} - \rho \overline{u'_k} \frac{\partial \overline{u'_i u'_j}}{\partial x_k} \quad (\text{A.32a})$$

$$= \rho \overline{u'_k} \frac{\partial \overline{u'_i u'_j}}{\partial x_k} + \rho \overline{u'_k} \frac{\partial \widetilde{u'_i u'_j}}{\partial x_k} - \rho \overline{u'_k} \frac{\partial \overline{u'_i u'_j}}{\partial x_k} \quad (\text{A.32b})$$

$$= \rho \overline{u'_k} \frac{\partial \widetilde{u'_i u'_j}}{\partial x_k}. \quad (\text{A.32c})$$

For the third term of the left-hand side, it gives

$$\rho \widetilde{u'_k} u'_j \frac{\partial u'_i}{\partial x_k} + \rho \widetilde{u'_k} u'_i \frac{\partial u'_j}{\partial x_k} = \rho \widetilde{u'_k} \frac{\partial u'_i u'_j}{\partial x_k} \quad (\text{A.33})$$

and the difference between phase and time averages leads to

$$\rho \left\langle \widetilde{u'_k} \frac{\partial u'_i u'_j}{\partial x_k} \right\rangle - \rho \widetilde{u'_k} \frac{\partial \overline{u'_i u'_j}}{\partial x_k} = \rho \widetilde{u'_k} \frac{\partial \langle u'_i u'_j \rangle}{\partial x_k} - \rho \widetilde{u'_k} \frac{\partial \overline{u'_i u'_j}}{\partial x_k} \quad (\text{A.34a})$$

$$= \rho \widetilde{u'_k} \frac{\partial \overline{u'_i u'_j}}{\partial x_k} + \rho \widetilde{u'_k} \frac{\partial \widetilde{u'_i u'_j}}{\partial x_k} - \rho \widetilde{u'_k} \frac{\partial \overline{u'_i u'_j}}{\partial x_k} \quad (\text{A.34b})$$

$$= \rho \widetilde{u'_k} \frac{\partial \overline{u'_i u'_j}}{\partial x_k} + \rho \widetilde{u'_k} \frac{\partial \widetilde{u'_i u'_j}}{\partial x_k} - \rho \widetilde{u'_k} \frac{\partial}{\partial x_k} (\overline{u'_i u'_j} + \widetilde{u'_i u'_j} + (\overline{u'_i u'_j})') \quad (\text{A.34c})$$

$$= \rho \widetilde{u'_k} \frac{\partial \overline{u'_i u'_j}}{\partial x_k} + \rho \widetilde{u'_k} \frac{\partial \widetilde{u'_i u'_j}}{\partial x_k} - \rho \widetilde{u'_k} \frac{\partial \widetilde{u'_i u'_j}}{\partial x_k}. \quad (\text{A.34d})$$

For the fourth term of the left-hand side, it gives

$$\rho u'_j u'_k \frac{\partial \bar{u}_i}{\partial x_k} + \rho u'_i u'_k \frac{\partial \bar{u}_j}{\partial x_k} = \rho u'_j u'_k \frac{\partial \bar{u}_i}{\partial x_k} + \rho u'_i u'_k \frac{\partial \bar{u}_j}{\partial x_k} \quad (\text{A.35})$$

and the difference between phase and time averages leads to

$$\begin{aligned} \rho \left\langle u'_j u'_k \frac{\partial \bar{u}_i}{\partial x_k} \right\rangle + \rho \left\langle u'_i u'_k \frac{\partial \bar{u}_j}{\partial x_k} \right\rangle - \overline{\rho u'_j u'_k \frac{\partial \bar{u}_i}{\partial x_k}} - \overline{\rho u'_i u'_k \frac{\partial \bar{u}_j}{\partial x_k}} \\ = \overline{\rho u'_j u'_k \frac{\partial \bar{u}_i}{\partial x_k}} + \overline{\rho u'_i u'_k \frac{\partial \bar{u}_j}{\partial x_k}} + \overline{\rho u'_i u'_k \frac{\partial \bar{u}_j}{\partial x_k}} \\ + \overline{\rho u'_i u'_k \frac{\partial \bar{u}_j}{\partial x_k}} - \overline{\rho u'_j u'_k \frac{\partial \bar{u}_i}{\partial x_k}} - \overline{\rho u'_i u'_k \frac{\partial \bar{u}_j}{\partial x_k}} \end{aligned} \quad (\text{A.36a})$$

$$= \overline{\rho u'_j u'_k \frac{\partial \bar{u}_i}{\partial x_k}} + \overline{\rho u'_i u'_k \frac{\partial \bar{u}_j}{\partial x_k}}. \quad (\text{A.36b})$$

For the fifth term of the left-hand side, it gives

$$\rho u'_j u'_k \frac{\partial \tilde{u}_i}{\partial x_k} + \rho u'_i u'_k \frac{\partial \tilde{u}_j}{\partial x_k} = \rho u'_j u'_k \frac{\partial \tilde{u}_i}{\partial x_k} + \rho u'_i u'_k \frac{\partial \tilde{u}_j}{\partial x_k} \quad (\text{A.37})$$

and the difference between phase and time averages leads to

$$\begin{aligned} \rho \left\langle u'_j u'_k \frac{\partial \tilde{u}_i}{\partial x_k} \right\rangle + \rho \left\langle u'_i u'_k \frac{\partial \tilde{u}_j}{\partial x_k} \right\rangle - \overline{\rho u'_j u'_k \frac{\partial \tilde{u}_i}{\partial x_k}} - \overline{\rho u'_i u'_k \frac{\partial \tilde{u}_j}{\partial x_k}} \\ = \overline{\rho u'_j u'_k \frac{\partial \tilde{u}_i}{\partial x_k}} + \overline{\rho u'_i u'_k \frac{\partial \tilde{u}_j}{\partial x_k}} + \overline{\rho u'_i u'_k \frac{\partial \tilde{u}_j}{\partial x_k}} \\ + \overline{\rho u'_i u'_k \frac{\partial \tilde{u}_j}{\partial x_k}} - \overline{\rho u'_j u'_k \frac{\partial \tilde{u}_i}{\partial x_k}} - \overline{\rho u'_i u'_k \frac{\partial \tilde{u}_j}{\partial x_k}}. \end{aligned} \quad (\text{A.38})$$

For the first term of the right-hand side, it gives

$$-u'_i \frac{\partial p'}{\partial x_j} - u'_j \frac{\partial p'}{\partial x_i} \quad (\text{A.39})$$

and the difference between phase and time averages leads to

$$-\left\langle u'_i \frac{\partial p'}{\partial x_j} \right\rangle - \left\langle u'_j \frac{\partial p'}{\partial x_i} \right\rangle + \overline{u'_i \frac{\partial p'}{\partial x_j}} + \overline{u'_j \frac{\partial p'}{\partial x_i}}. \quad (\text{A.40})$$

For the second term of the right-hand side, it gives

$$\mu \left(u'_j \frac{\partial^2 u'_i}{\partial x_k^2} + u'_i \frac{\partial^2 u'_j}{\partial x_k^2} \right) = \mu \left[\frac{\partial}{\partial x_k} \left(u'_j \frac{\partial u'_i}{\partial x_k} \right) + \frac{\partial}{\partial x_k} \left(u'_i \frac{\partial u'_j}{\partial x_k} \right) - 2 \frac{\partial u'_i}{\partial x_k} \frac{\partial u'_j}{\partial x_k} \right] \quad (\text{A.41a})$$

$$= \mu \left(\frac{\partial^2 u'_i u'_j}{\partial x_k^2} - 2 \frac{\partial u'_i}{\partial x_k} \frac{\partial u'_j}{\partial x_k} \right) \quad (\text{A.41b})$$

and the difference between phase and time averages leads to

$$\begin{aligned} \mu \left(\frac{\partial^2 \langle u'_i u'_j \rangle}{\partial x_k^2} - 2 \left\langle \frac{\partial u'_i}{\partial x_k} \frac{\partial u'_j}{\partial x_k} \right\rangle \right) - \mu \left(\frac{\partial^2 \overline{u'_i u'_j}}{\partial x_k^2} + 2 \overline{\frac{\partial u'_i}{\partial x_k} \frac{\partial u'_j}{\partial x_k}} \right) \\ = \mu \left[\frac{\partial^2 \widetilde{u'_i u'_j}}{\partial x_k^2} - 2 \left(\widetilde{\frac{\partial u'_i}{\partial x_k} \frac{\partial u'_j}{\partial x_k}} \right) \right]. \end{aligned} \quad (\text{A.42})$$

For the third term of the right-hand side, it gives

$$\begin{aligned} \rho u'_j \frac{\partial}{\partial x_k} \langle u'_i u'_k \rangle + \rho u'_i \frac{\partial}{\partial x_k} \langle u'_j u'_k \rangle = \rho u'_j \frac{\partial}{\partial x_k} \left(\overline{u'_i u'_k} + \widetilde{u'_i u'_k} \right) \\ + \rho u'_i \frac{\partial}{\partial x_k} \left(\overline{u'_j u'_k} + \widetilde{u'_j u'_k} \right) \end{aligned} \quad (\text{A.43})$$

and both phase and time averages of this term are zero.

For the fourth term of the right-hand side, it gives

$$-\rho u'_j \frac{\partial u'_i u'_k}{\partial x_k} - \rho u'_i \frac{\partial u'_j u'_k}{\partial x_k} = -\rho u'_j u'_k \frac{\partial u'_i}{\partial x_k} - \rho u'_i u'_k \frac{\partial u'_j}{\partial x_k} \quad (\text{A.44a})$$

$$= -\rho u'_j u'_k \frac{\partial u'_i}{\partial x_k} - \rho u'_i u'_k \frac{\partial u'_j}{\partial x_k} - \rho u'_i u'_j \frac{\partial u'_k}{\partial x_k} \quad (\text{A.44b})$$

$$= -\rho \frac{\partial u'_i u'_j u'_k}{\partial x_k} \quad (\text{A.44c})$$

and the difference between phase and time averages leads to

$$-\rho \frac{\partial \langle u'_i u'_j u'_k \rangle}{\partial x_k} + \rho \frac{\partial \overline{u'_i u'_j u'_k}}{\partial x_k} = -\rho \frac{\partial \widetilde{u'_i u'_j u'_k}}{\partial x_k}. \quad (\text{A.45})$$

Gathering the terms from equations A.30b, A.32c, A.34d, A.36b, A.38, A.40, A.42 and A.45 all together, it gives

$$\begin{aligned} \rho \frac{\partial \widetilde{u'_i u'_j}}{\partial t} + \rho \overline{u_k} \frac{\partial \widetilde{u'_i u'_j}}{\partial x_k} + \rho \widetilde{u_k} \frac{\partial \overline{u'_i u'_j}}{\partial x_k} + \rho \widetilde{u_k} \frac{\partial \widetilde{u'_i u'_j}}{\partial x_k} - \rho \overline{u_k} \frac{\partial \overline{u'_i u'_j}}{\partial x_k} \\ + \rho \widetilde{u'_j u'_k} \frac{\partial \overline{u'_i}}{\partial x_k} + \rho \overline{u'_i u'_k} \frac{\partial \widetilde{u'_j}}{\partial x_k} + \rho \overline{u'_j u'_k} \frac{\partial \widetilde{u'_i}}{\partial x_k} + \rho \widetilde{u'_j u'_k} \frac{\partial \widetilde{u'_i}}{\partial x_k} \\ + \rho \overline{u'_i u'_k} \frac{\partial \widetilde{u'_j}}{\partial x_k} + \rho \widetilde{u'_i u'_k} \frac{\partial \widetilde{u'_j}}{\partial x_k} - \rho \overline{u'_j u'_k} \frac{\partial \widetilde{u'_i}}{\partial x_k} - \rho \widetilde{u'_i u'_k} \frac{\partial \widetilde{u'_j}}{\partial x_k} \\ = - \left\langle u'_i \frac{\partial p'}{\partial x_j} \right\rangle - \left\langle u'_j \frac{\partial p'}{\partial x_i} \right\rangle + \overline{u'_i \frac{\partial p'}{\partial x_j}} + \overline{u'_j \frac{\partial p'}{\partial x_i}} \\ + \mu \left[\frac{\partial^2 \widetilde{u'_i u'_j}}{\partial x_k^2} - 2 \left(\widetilde{\frac{\partial u'_i}{\partial x_k} \frac{\partial u'_j}{\partial x_k}} \right) \right] + \rho \frac{\partial}{\partial x_k} \left(\overline{u'_i u'_j u'_k} - \langle u'_i u'_j u'_k \rangle \right) \end{aligned} \quad (\text{A.46})$$

and it can re-arranged as in equation 2.9 of Reynolds and Hussain (1972) to give

$$\begin{aligned}
& \rho \frac{\partial \widetilde{u'_i u'_j}}{\partial t} + \rho \overline{u'_k} \frac{\partial \widetilde{u'_i u'_j}}{\partial x_k} + \rho \widetilde{u'_k} \frac{\partial \widetilde{u'_i u'_j}}{\partial x_k} + \rho \overline{u'_k} \frac{\partial \widetilde{u'_i u'_j}}{\partial x_k} \\
& + \rho \widetilde{u'_j u'_k} \frac{\partial \widetilde{u'_i}}{\partial x_k} + \rho \widetilde{u'_i u'_k} \frac{\partial \widetilde{u'_j}}{\partial x_k} + \rho \overline{u'_j u'_k} \frac{\partial \widetilde{u'_i}}{\partial x_k} + \rho \overline{u'_i u'_k} \frac{\partial \widetilde{u'_j}}{\partial x_k} \\
& = -\rho \widetilde{u'_j u'_k} \frac{\partial \widetilde{u'_i}}{\partial x_k} + \overline{\rho u'_j u'_k} \frac{\partial \widetilde{u'_i}}{\partial x_k} - \rho \widetilde{u'_i u'_k} \frac{\partial \widetilde{u'_j}}{\partial x_k} + \overline{\rho u'_i u'_k} \frac{\partial \widetilde{u'_j}}{\partial x_k} + \overline{\rho u'_k} \frac{\partial \widetilde{u'_i u'_j}}{\partial x_k} \\
& + \rho \frac{\partial}{\partial x_k} \left(\overline{u'_i u'_j u'_k} - \langle u'_i u'_j u'_k \rangle \right) \\
& - \left\langle u'_j \frac{\partial p'}{\partial x_i} \right\rangle + u'_j \frac{\partial \overline{p'}}{\partial x_i} - \left\langle u'_i \frac{\partial p'}{\partial x_j} \right\rangle + u'_i \frac{\partial \overline{p'}}{\partial x_j} \\
& + \mu \left[\frac{\partial^2 \widetilde{u'_i u'_j}}{\partial x_k^2} - 2 \left(\frac{\partial \widetilde{u'_i}}{\partial x_k} \frac{\partial \widetilde{u'_j}}{\partial x_k} \right) \right]. \tag{A.47}
\end{aligned}$$

The terms can now be re-arranged as in Brereton and Reynolds (1991) into the contributions of production, pressure strain, dissipation and diffusion, such that

$$\frac{\partial \widetilde{u'_i u'_j}}{\partial t} + \overline{u'_k} \frac{\partial \widetilde{u'_i u'_j}}{\partial x_k} + \widetilde{u'_k} \frac{\partial \widetilde{u'_i u'_j}}{\partial x_k} = \widetilde{P}_{ij} + \widetilde{T}_{ij} - \widetilde{D}_{ij} - \widetilde{J}_{ij,k}. \tag{A.48}$$

The production term \widetilde{P}_{ij} is obtained as follows. By taking from equation A.47 the last term of the left-hand side and the third and fourth terms of the right-hand side,

$$-\widetilde{u'_i u'_k} \frac{\partial \widetilde{u'_j}}{\partial x_k} + \overline{u'_i u'_k} \frac{\partial \widetilde{u'_j}}{\partial x_k} - \overline{u'_i u'_k} \frac{\partial \widetilde{u'_j}}{\partial x_k} = -\langle u'_i u'_k \rangle \frac{\partial \widetilde{u'_j}}{\partial x_k} + \overline{u'_i u'_k} \frac{\partial \widetilde{u'_j}}{\partial x_k} \tag{A.49a}$$

$$= -\left\langle u'_i u'_k \frac{\partial \widetilde{u'_j}}{\partial x_k} \right\rangle + \overline{u'_i u'_k} \frac{\partial \widetilde{u'_j}}{\partial x_k} \tag{A.49b}$$

$$= -\left\langle u'_i u'_k \frac{\partial \widetilde{u'_j}}{\partial x_k} \right\rangle + \overline{u'_i u'_k} \frac{\partial \widetilde{u'_j}}{\partial x_k} \tag{A.49c}$$

$$= -\widetilde{u'_i u'_k} \frac{\partial \widetilde{u'_j}}{\partial x_k} \tag{A.49d}$$

and similarly, by taking from equation A.47 the second to last term of the left-hand side and the first and second terms of the right-hand side,

$$-\widetilde{u'_j u'_k} \frac{\partial \widetilde{u'_i}}{\partial x_k} + \overline{u'_j u'_k} \frac{\partial \widetilde{u'_i}}{\partial x_k} - \overline{u'_j u'_k} \frac{\partial \widetilde{u'_i}}{\partial x_k} = -\widetilde{u'_j u'_k} \frac{\partial \widetilde{u'_i}}{\partial x_k}. \tag{A.50}$$

Finally, by adding to equations A.49d and A.50 the fifth and sixth terms of the left-hand side of equation A.47, the production term is given by

$$\widetilde{P}_{ij} = - \left(\widetilde{u'_i u'_k} \frac{\partial \widetilde{u'_j}}{\partial x_k} + \widetilde{u'_i u'_k} \frac{\partial \widetilde{u'_j}}{\partial x_k} \right) - \left(\widetilde{u'_j u'_k} \frac{\partial \widetilde{u'_i}}{\partial x_k} + \widetilde{u'_i u'_k} \frac{\partial \widetilde{u'_j}}{\partial x_k} \right). \tag{A.51}$$

The pressure strain term \widetilde{T}_{ij} is obtained by using the eighth to eleventh terms of equation A.47, such that

$$-\frac{1}{\rho} \left\langle u'_j \frac{\partial p'}{\partial x_i} \right\rangle + \frac{1}{\rho} \overline{u'_j \frac{\partial p'}{\partial x_i}} - \frac{1}{\rho} \left\langle u'_i \frac{\partial p'}{\partial x_j} \right\rangle + \frac{1}{\rho} \overline{u'_i \frac{\partial p'}{\partial x_j}}$$

$$= -\frac{1}{\rho} \left(\widetilde{u'_j \frac{\partial p'}{\partial x_i}} + \widetilde{u'_i \frac{\partial p'}{\partial x_j}} \right) \quad (\text{A.52a})$$

$$= -\frac{1}{\rho} \left(\frac{\partial \widetilde{u'_j p'}}{\partial x_i} - \widetilde{p' \frac{\partial u'_j}{\partial x_i}} + \frac{\partial \widetilde{u'_i p'}}{\partial x_j} - \widetilde{p' \frac{\partial u'_i}{\partial x_j}} \right) \quad (\text{A.52b})$$

$$= \frac{1}{\rho} \left(2\widetilde{p' S'_{ij}} - \frac{\partial \widetilde{u'_j p'}}{\partial x_i} - \frac{\partial \widetilde{u'_i p'}}{\partial x_j} \right) \quad (\text{A.52c})$$

with

$$s'_{ij} = \frac{1}{2} \left(\frac{\partial u'_i}{\partial x_j} + \frac{\partial u'_j}{\partial x_i} \right). \quad (\text{A.53})$$

To follow Breerton and Reynolds (1991),

$$\widetilde{T}_{ij} = \frac{2}{\rho} \widetilde{p' s'_{ij}} \quad (\text{A.54})$$

and the remaining terms are the pressure contributions to the diffusion term $\widetilde{J}_{ij,k}$.

The dissipation term \widetilde{D}_{ij} is simply the last term of the right-hand side of equation A.47 and therefore,

$$\widetilde{D}_{ij} = 2\nu \frac{\partial \widetilde{u'_i \frac{\partial u'_j}{\partial x_k}}}{\partial x_k}. \quad (\text{A.55})$$

The diffusion term $\widetilde{J}_{ij,k}$ is made of different contributions. The turbulent transport is obtained by taking the sixth and seventh terms of the right-hand side of equation A.47, such that

$$\frac{\partial}{\partial x_k} \left(\overline{u'_i u'_j u'_k} - \langle u'_i u'_j u'_k \rangle \right) = -\frac{\partial \widetilde{u'_i u'_j u'_k}}{\partial x_k}. \quad (\text{A.56})$$

The remaining terms coming from the derivation of the pressure strain term gives the contribution of pressure diffusion,

$$-\frac{1}{\rho} \left(\frac{\partial \widetilde{u'_j p'}}{\partial x_i} + \frac{\partial \widetilde{u'_i p'}}{\partial x_j} \right) = -\frac{1}{\rho} \frac{\partial}{\partial x_k} \left(\widetilde{u'_j p'} \delta_{ik} + \widetilde{u'_i p'} \delta_{jk} \right) \quad (\text{A.57})$$

and the last contribution, the molecular diffusion, comes from the second to last term of the right-hand side of equation A.47, giving

$$\nu \frac{\partial^2 \widetilde{u'_i u'_j}}{\partial x_k^2}. \quad (\text{A.58})$$

The sum of equations A.56, A.57 and A.58 gives the full diffusion term,

$$\widetilde{J}_{ij,k} = \frac{\partial}{\partial x_k} \left(\widetilde{u'_i u'_j u'_k} + \frac{1}{\rho} \widetilde{u'_j p'} \delta_{ik} + \frac{1}{\rho} \widetilde{u'_i p'} \delta_{jk} - \nu \frac{\partial \widetilde{u'_i u'_j}}{\partial x_k} \right). \quad (\text{A.59})$$

Finally, the attentive reader will notice that some terms of equation A.47 have not been used to derive the budgets. It comes from a different definition of the substantial derivative between Reynolds and Hussain (1972) and Brereton and Reynolds (1991). Indeed, in Brereton and Reynolds (1991),

$$\frac{\mathcal{D} \widetilde{u'_i u'_j}}{\mathcal{D}t} = \frac{\partial \widetilde{u'_i u'_j}}{\partial t} + \widetilde{u_k} \frac{\partial \widetilde{u'_i u'_j}}{\partial x_k} + \widetilde{u_k} \frac{\partial \widetilde{u'_i u'_j}}{\partial x_k} \quad (\text{A.60})$$

whereas in Reynolds and Hussain (1972), the last term is not taken into account, giving

$$\frac{\mathcal{D} \widetilde{u'_i u'_j}}{\mathcal{D}t} = \frac{\partial \widetilde{u'_i u'_j}}{\partial t} + \widetilde{u_k} \frac{\partial \widetilde{u'_i u'_j}}{\partial x_k}. \quad (\text{A.61})$$

By recombining the remaining terms, that is to say the third and fourth terms of the left-hand side and the fifth term of the right-hand side, it gives (similarly to the derivation of the production terms)

$$\widetilde{u_k} \frac{\partial \widetilde{u'_i u'_j}}{\partial x_k} + \widetilde{u_k} \frac{\partial \widetilde{u'_i u'_j}}{\partial x_k} - \overline{\widetilde{u_k} \frac{\partial \widetilde{u'_i u'_j}}{\partial x_k}} = \widetilde{u_k} \frac{\partial \widetilde{u'_i u'_j}}{\partial x_k} \quad (\text{A.62})$$

which is the additional term of Brereton and Reynolds (1991) in the substantial derivative.

The mean turbulent stress budgets are obtained by collecting the time-averaged terms, which can be re-arranged in a similar fashion, giving

$$\overline{\widetilde{u_k} \frac{\partial \widetilde{u'_i u'_j}}{\partial x_k}} + \overline{\widetilde{u_k} \frac{\partial \widetilde{u'_i u'_j}}{\partial x_k}} = \overline{P_{ij}} + \overline{T_{ij}} - \overline{D_{ij}} - \overline{J_{ij,k}} \quad (\text{A.63})$$

with

$$\bar{P}_{ij} = - \left(\overline{u'_j u'_k \frac{\partial \bar{u}_i}{\partial x_k}} + \overline{u'_i u'_k \frac{\partial \bar{u}_j}{\partial x_k}} + \overline{u'_j u'_k \frac{\partial \bar{u}_i}{\partial x_k}} + \overline{u'_i u'_k \frac{\partial \bar{u}_j}{\partial x_k}} \right) \quad (\text{A.64})$$

$$\bar{T}_{ij} = \frac{2}{\rho} \overline{p' s'_{ij}} \quad (\text{A.65})$$

$$\bar{D}_{ij} = 2\nu \overline{\frac{\partial u'_i}{\partial x_k} \frac{\partial u'_j}{\partial x_k}} \quad (\text{A.66})$$

$$\bar{J}_{ij,k} = \frac{\partial}{\partial x_k} \left(\overline{u'_i u'_j u'_k} + \frac{1}{\rho} \overline{u'_j p'} \delta_{ik} + \frac{1}{\rho} \overline{u'_i p'} \delta_{jk} - \nu \overline{\frac{\partial u'_i u'_j}{\partial x_k}} \right). \quad (\text{A.67})$$

A.3 Practical computation of the turbulent stress budgets

A.3.1 Double and triple correlations

As for the classical Reynolds, double decomposition, practical formulations for the double and triple correlations can be derived in the framework of the triple decomposition. These are detailed in this section.

For the double correlation, considering two variables a and b , the time average of the double product is given by equation A.8,

$$\overline{ab} = \bar{a}\bar{b} + \widetilde{a\bar{b}} + \overline{a'b'} \quad (\text{A.68})$$

and therefore

$$\overline{a'b'} = \bar{a}\bar{b} - \widetilde{a\bar{b}} - \widetilde{\bar{a}b}. \quad (\text{A.69})$$

Moreover, the phase average is written following equation A.9,

$$\langle ab \rangle = \bar{a}\bar{b} + \widetilde{a\bar{b}} + \widetilde{\bar{a}b} + \widetilde{a'b'} \quad (\text{A.70})$$

and therefore

$$\langle a'b' \rangle = \langle ab \rangle - \bar{a}\bar{b} - \widetilde{a\bar{b}} - \widetilde{\bar{a}b} - \widetilde{a'b'} \quad (\text{A.71})$$

This leads to the expression of the coherent component of the double correlation,

$$\widetilde{a'b'} = \langle a'b' \rangle - \overline{a'b'} \quad (\text{A.72a})$$

$$= \langle ab \rangle - \bar{a}\bar{b} - \widetilde{a\bar{b}} - \widetilde{\bar{a}b} - \widetilde{a'b'} + \widetilde{\bar{a}b} \quad (\text{A.72b})$$

and finally,

$$\widetilde{a'b'} = \widetilde{a\bar{b}} - \widetilde{\bar{a}b} - \widetilde{a'b'} + \widetilde{\bar{a}b}. \quad (\text{A.73})$$

For the triple correlation, a bit more work has to be performed. Indeed, considering three variables a , b and c , the time average of the triple product is written

$$\begin{aligned} \overline{abc} &= \overline{a\bar{b}\bar{c}} + \overline{a\bar{b}\bar{c}} + \overline{b\bar{a}\bar{c}} + \overline{c\bar{a}\bar{b}} + \overline{a\bar{b}'c'} + \overline{b\bar{a}'c'} + \overline{c\bar{a}'b'} + \overline{a\bar{b}\bar{c}} + \overline{a'b'c'} \\ &+ \overline{a\bar{b}c'} + \overline{a\bar{c}b'} + \overline{b\bar{c}a'} + \overline{a\bar{b}'c'} + \overline{b\bar{a}'c'} + \overline{c\bar{a}'b'} \end{aligned} \quad (\text{A.74})$$

and the last six terms require further effort. It can be pursued by developing

$$\overline{abc} = \overline{a\bar{c}\bar{b}} + \overline{a\bar{b}\bar{c}} + \overline{a\bar{b}\bar{c}} + \overline{a\bar{b}c'} + \overline{a\bar{c}b'} + \overline{a\bar{b}'c'} \quad (\text{A.75})$$

and therefore

$$\overline{a'b'c'} = \overline{abc} - \overline{a\bar{c}\bar{b}} - \overline{a\bar{b}\bar{c}} - \overline{a\bar{b}\bar{c}} - \overline{a\bar{b}c'} - \overline{a\bar{c}b'} . \quad (\text{A.76})$$

Adapting for $\overline{b'a'c'}$ and $\overline{c'a'b'}$, and replacing in equation A.74, it gives

$$\begin{aligned} \overline{abc} &= \overline{a\bar{b}\bar{c}} + \overline{a\bar{b}\bar{c}} + \overline{a\bar{b}'c'} + \overline{b\bar{a}\bar{c}} + \overline{c\bar{a}\bar{b}} + \overline{a\bar{b}\bar{c}} + \overline{b\bar{a}'c'} + \overline{c\bar{a}'b'} + \overline{a'b'c'} \\ &+ \overline{a\bar{b}c'} - \overline{a\bar{c}\bar{b}} - \overline{a\bar{b}\bar{c}} - \overline{a\bar{b}\bar{c}} - \overline{a\bar{b}c'} - \overline{a\bar{c}b'} \\ &+ \overline{b\bar{a}c'} - \overline{b\bar{c}\bar{a}} - \overline{a\bar{b}\bar{c}} - \overline{a\bar{b}\bar{c}} - \overline{a\bar{b}c'} - \overline{b\bar{c}a'} \\ &+ \overline{c\bar{a}b} - \overline{b\bar{c}\bar{a}} - \overline{a\bar{c}\bar{b}} - \overline{a\bar{b}\bar{c}} - \overline{b\bar{c}a'} - \overline{a\bar{c}b'} \\ &+ \overline{a\bar{b}c'} + \overline{a\bar{c}b'} + \overline{b\bar{c}a'} . \end{aligned} \quad (\text{A.77})$$

It can also be found that

$$\overline{a\bar{b}\bar{c}} = \overline{a\bar{b}\bar{c}} + \overline{a\bar{b}\bar{c}} + \overline{a\bar{b}c'} \quad (\text{A.78})$$

which leads to

$$\overline{a\bar{b}c'} = \overline{a\bar{b}\bar{c}} - \overline{a\bar{b}\bar{c}} - \overline{a\bar{b}\bar{c}} . \quad (\text{A.79})$$

Adapting for $\overline{a\bar{c}b'}$ and $\overline{b\bar{c}a'}$, and replacing in equation A.77, it gives

$$\begin{aligned} \overline{abc} &= \overline{a\bar{b}\bar{c}} + \overline{a\bar{b}'c'} + \overline{b\bar{a}'c'} + \overline{c\bar{a}'b'} + \overline{a'b'c'} \\ &+ \overline{a\bar{b}\bar{c}} + \overline{b\bar{a}c'} + \overline{c\bar{a}b} - \overline{b\bar{c}\bar{a}} - \overline{a\bar{c}\bar{b}} - \overline{a\bar{b}\bar{c}} - 2\overline{a\bar{b}\bar{c}} \\ &- \overline{a\bar{b}\bar{c}} + \overline{a\bar{b}\bar{c}} + \overline{a\bar{b}\bar{c}} \\ &- \overline{a\bar{c}b'} + \overline{a\bar{c}\bar{b}} + \overline{a\bar{b}\bar{c}} \\ &- \overline{b\bar{c}a'} + \overline{b\bar{c}\bar{a}} + \overline{a\bar{b}\bar{c}} \end{aligned} \quad (\text{A.80})$$

which is finally written

$$\begin{aligned} \overline{abc} &= \overline{a\bar{b}\bar{c}} + \overline{a\bar{b}'c'} + \overline{b\bar{a}'c'} + \overline{c\bar{a}'b'} + \overline{a'b'c'} \\ &+ \overline{a\bar{b}\bar{c}} + \overline{b\bar{a}c'} + \overline{c\bar{a}b} - \overline{a\bar{b}\bar{c}} - \overline{a\bar{c}b'} - \overline{b\bar{c}a'} + \overline{a\bar{b}\bar{c}} . \end{aligned} \quad (\text{A.81})$$

Isolating the triple correlation therefore gives

$$\begin{aligned} \overline{a'b'c'} &= \overline{abc} - \overline{a\bar{b}\bar{c}} - \overline{\bar{a}b'c'} - \overline{\bar{b}a'c'} - \overline{\bar{c}a'b'} \\ &\quad - \overline{\bar{a}\bar{b}c} - \overline{\bar{b}\bar{a}c} - \overline{\bar{c}\bar{a}b} + \overline{\bar{a}\bar{b}c} + \overline{\bar{a}\bar{c}b} + \overline{\bar{b}\bar{c}a} - \overline{\bar{a}\bar{b}\bar{c}}. \end{aligned} \quad (\text{A.82})$$

The phase average of the triple product contains less terms and is written

$$\begin{aligned} \langle a'b'c' \rangle &= \langle abc \rangle - \overline{a\bar{b}\bar{c}} - \overline{\bar{a}b\bar{c}} - \overline{\bar{a}\bar{c}b} - \overline{\bar{b}\bar{c}a} - \overline{\bar{a}\bar{b}\bar{c}} - \overline{\bar{b}\bar{a}\bar{c}} - \overline{\bar{c}\bar{a}\bar{b}} - \overline{\bar{a}\bar{b}\bar{c}} \\ &\quad - \overline{\bar{a}b'c'} - \overline{\bar{b}a'c'} - \overline{\bar{c}a'b'} - \overline{\bar{a}\langle b'c' \rangle} - \overline{\bar{b}\langle a'c' \rangle} - \overline{\bar{c}\langle a'b' \rangle}. \end{aligned} \quad (\text{A.83})$$

Finally, the expression of the coherent component of the triple correlation can be obtained and is written

$$\widetilde{a'b'c'} = \langle a'b'c' \rangle - \overline{a'b'c'} \quad (\text{A.84a})$$

$$\begin{aligned} &= \langle abc \rangle - \overline{abc} - \overline{a\bar{b}\bar{c}} - \overline{\bar{a}b\bar{c}} - \overline{\bar{a}\bar{c}b} - \overline{\bar{b}\bar{c}a} - \overline{\bar{a}\bar{b}\bar{c}} - \overline{\bar{b}\bar{a}\bar{c}} - \overline{\bar{c}\bar{a}\bar{b}} \\ &\quad - \overline{\bar{a}\bar{b}\bar{c}} - \overline{\bar{b}\bar{a}\bar{c}} - \overline{\bar{c}\bar{a}\bar{b}} - \overline{\bar{a}\bar{b}\bar{c}} + \overline{\bar{a}\bar{b}\bar{c}} \\ &\quad - \overline{\bar{a}\langle b'c' \rangle} - \overline{\bar{b}\langle a'c' \rangle} - \overline{\bar{c}\langle a'b' \rangle} \\ &\quad + \overline{\bar{a}\bar{b}\bar{c}} + \overline{\bar{b}\bar{a}\bar{c}} + \overline{\bar{c}\bar{a}\bar{b}} - \overline{\bar{a}\bar{b}\bar{c}} - \overline{\bar{a}\bar{c}\bar{b}} - \overline{\bar{b}\bar{c}\bar{a}}. \end{aligned} \quad (\text{A.84b})$$

Contrary to the double correlation, the triple correlation requires two accumulation steps, to obtain the last six terms.

A.3.2 Application to the coherent turbulent stress budgets

The practical algorithm to compute the coherent turbulent stress budgets is finally described. The data consist of a series of instantaneous (or, if the flow is statistically two-dimensional, span-averaged) solutions containing ρ , μ , p , u_i , pu_i , $u_i u_j$, $u_i u_j u_k$, $\partial u_i / \partial x_j$, $p \partial u_i / \partial x_j$ and $\partial u_i / \partial x_k \cdot \partial u_j / \partial x_k$. The algorithm is the following.

1. Perform a first loop over the samples to compute the time average and the phase averages.
2. Compute the coherent components by subtracting the time average from the phase averages.
3. Loop over the phases to accumulate the double and triple products \widetilde{ab} and \widetilde{abc} . The latter is needed for the turbulent transport term only. Compute their time average at the end of the loop.
4. Loop over the phases and for each phase, loop over the corresponding samples to accumulate the terms \widetilde{abc} , \widetilde{bac} , \widetilde{cab} , \widetilde{abc} , \widetilde{acb} and \widetilde{bca} . Compute their time average at the end of the loops. These are needed for the turbulent transport term only.

5. Compute the coherent double and triple correlations following equations A.73 and A.84b.
6. Form the different budget terms. For the convection and diffusion terms, it implies the (*a posteriori*) evaluation of the gradients of coherent double and triple correlations.

Appendix B

Turbulent Boundary Layer at Mach 2

As a first test case for the solver, this appendix presents the results of an ILES of a fully turbulent boundary layer developing over a flat plate at Mach 2. The main objective is to validate the implementation of the turbulent inflow generator, using the digital filtering technique described in section 3.5. Additionally, an estimate of the adaptation length needed to obtain a realistic turbulent boundary layer should be obtained.

B.1 Flow conditions and computational setup

The case under investigation is a fully turbulent boundary layer developing over a flat plate. The inflow conditions are given as Mach number $M_\infty = 2$, static temperature $T_\infty = 169.44\text{K}$, Reynolds number based on the reference boundary layer thickness $Re_{\delta_0} = 12662$ and Reynolds number based on the friction velocity $Re_\tau = 250$. The choice of the reference boundary layer thickness δ_0 is arbitrary and has been taken equal to 0.01m.

The computational domain is a simple rectangular box. Its dimensions in the streamwise, wall-normal and spanwise directions are, respectively, $L_x/\delta_0 = 20$, $L_y/\delta_0 = 8.3$ and $L_z/\delta_0 = 9.6$. The mesh is entirely composed of hexahedra. The number of solution points, at polynomial order 3, is $N_x \times N_y \times N_z = 312 \times 240 \times 200 \approx 15 \times 10^6$. The grid resolution, with respect to the solution points and expressed in wall units based on the inflow conditions, is constant in the streamwise and spanwise directions, with $\Delta x^+ = 16$ and $\Delta z^+ = 12$. In the wall-normal direction, the cells are stretched following a hyperbolic tangent law and such that $y_w^+ < 1$. The boundary layer counts 100 solution points. In the freestream, $\Delta y^+ = 16$.

The inlet boundary condition is fully supersonic, with prescribed mean velocity components, static temperature and static pressure profiles. The digital filtering employed to provide a turbulent inflow is setup as follows. Turbulence length scales in the streamwise and spanwise directions are constant across the inlet plane

and taken as $I_x/\delta_0 = 0.5$ and $I_z/\delta_0 = 0.3$, respectively. I_y is varying in the wall-normal direction, such that $I_y = I_z$ at the edge of the boundary layer (a reasonable assumption in the outer layer (Adler et al., 2018)) and the number of flux points in the filter is constant across the inlet plane and equal to approximately 275. Keeping a constant filter size has indeed been found to give the best results. While in the general case, turbulence length scales can be specified independently for each velocity components, Adler et al. (2018) specified that these are unnecessary complications. For the present simulation, these length scales are therefore identical for each velocity component. The Lagrangian time scale (see equation 3.59) is evaluated considering a velocity taken as $0.9U_\infty$, with U_∞ being the mean streamwise velocity. Finally, the perturbations are scaled based on prescribed profiles of Reynolds stresses. All the imposed profiles at the inflow are coming from a reference DNS. As demonstrated by Adler et al. (2018), providing a higher fidelity of mean quantities and Reynolds stresses to initialize the digital filter results in a shorter adaptation length.

The outflow is supersonic with a specific treatment for the subsonic part of the boundary layer. If the Mach number is detected to be less than unity, then static pressure is imposed at the same value as for the inlet. The bottom boundary is a no-slip adiabatic and the top boundary is external and uses Riemann invariants.

The shock-capturing feature of the solver is disabled for the simulation since no shock wave is expected to develop. The explicit time step is 5×10^{-8} s, corresponding to a CFL number of around 2.5. The simulation is restarted from an initial RANS solution and run for about 25 convective time units (defined as L_x/U_∞) to get rid of the transient. The accumulation of data then takes place for 65 convective time units.

B.2 Results


A systematic comparison will be undertaken with DNS results kindly generated and provided by Alessandro Ceci  (0000-0001-6664-1677). The solver used to this effect is STREAmS, a description of which can be found in Bernardini et al. (2021). For the DNS, the flow conditions and domain dimensions are kept identical. The mesh has a finer resolution in the streamwise and spanwise coordinates, with, respectively, $\Delta x^+ = 6.4$ and $\Delta z^+ = 5.4$. The first point lies at a distance from the wall $y_w^+ = 0.68$. Velocity perturbations at the inlet plane are also provided using a digital filter algorithm. The filter is built by a convolution a three one-dimensional filters encompassing 2×64 neighbors in each direction. For a two-dimensional filter, it would correspond to 256 neighbors, which is relatively close to the 275 the elliptical filter considered here. I_y and I_z are varying in the wall-normal direction and all turbulence length scales are specified differently for each velocity components. The details of the implementation can be found in Ceci et al. (2022).

Figure B.1 first illustrates instantaneous views of the flow field, that is to say the density at mid-span and the streamwise velocity component near the bottom wall, at $y^+ \approx 10$. The former figure shows clearly the boundary layer evolving. Also depicted are the spurious but weak pressure waves that are generated at the inlet, because of

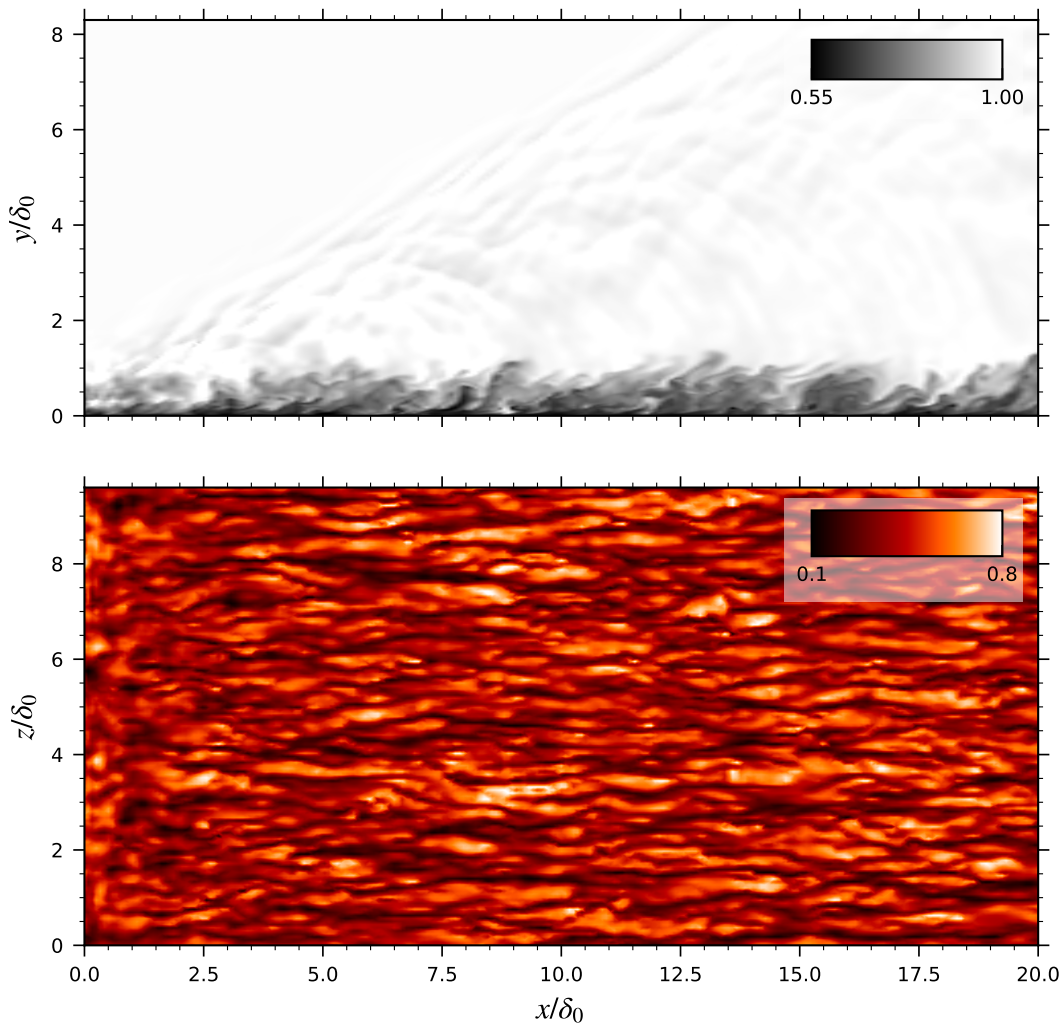


Figure B.1. Instantaneous density ρ/ρ_∞ at mid-span (*top*) and instantaneous streamwise velocity u/U_∞ near the bottom wall, $y^+ \approx 10$ (*bottom*).

the non-equilibrium conditions that are prescribed, and propagating downstream. They are reflected on the top boundary before leaving the computational domain. The latter figure highlights the characteristic thin and elongated structures developing in the boundary layer, known as streaks. They start to develop a few boundary layer thicknesses downstream of the inlet plane as the boundary layer recovers from the unrealistic inflow turbulent conditions.

The streamwise evolution of Reynolds numbers Re_τ and Re_θ , based, respectively, on the friction velocity and on the boundary layer momentum thickness, is depicted in figure B.2. A slight offset is noticed with respect to the DNS results but remains marginal. More importantly, the slopes are nicely matched, meaning that the growth of the boundary layer is correctly captured.

Another quantity of interest is the friction coefficient. Its streamwise evolution is shown in figure B.3 (*left*) whereas the *right* figure shows its dependence with respect to Re_θ . The *right* figure also reports the correlations established by Ceci

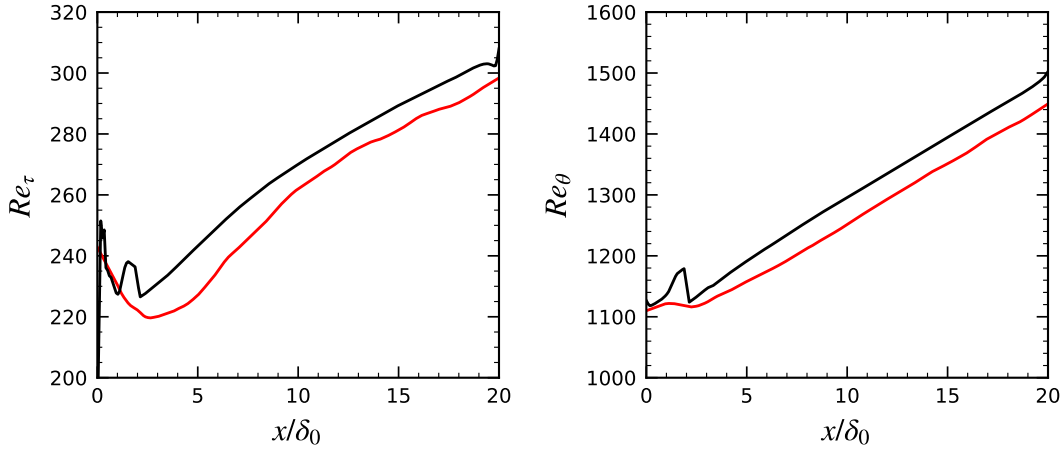


Figure B.2. Streamwise evolution of Reynolds numbers based on the friction velocity Re_τ (*left*) and on the boundary layer momentum thickness Re_θ (*right*), present case (*black*) and DNS results (*red*).

et al. (2022) with DNS of supersonic turbulent boundary layers at Mach 2, using very long streamwise domains ($L_x/\delta_0 > 100$). The friction coefficient is seen to need at least $10\delta_0$ to get rid of the effects from the inlet boundary. However, the correct slope, leading to a decreasing friction coefficient, is obtained before the end of the domain at $20\delta_0$. This is further confirmed by an additional simulation, performed on a domain twice longer, while keeping the same grid resolution, for which an excellent match is obtained with respect to the corresponding DNS. In both cases, an undesired effect of the outlet boundary is pointed out and extends up to $2\delta_0$ upstream. For the extended domain simulation, the local bump at $x/\delta_0 \approx 26$ is due to the spurious pressure waves reflecting on the boundary layer after having been reflected on the top boundary at $x/\delta_0 \approx 13$ (as shown in figure B.1). In the region of decreasing friction coefficient, the error is of about 3% with respect to the correlation.

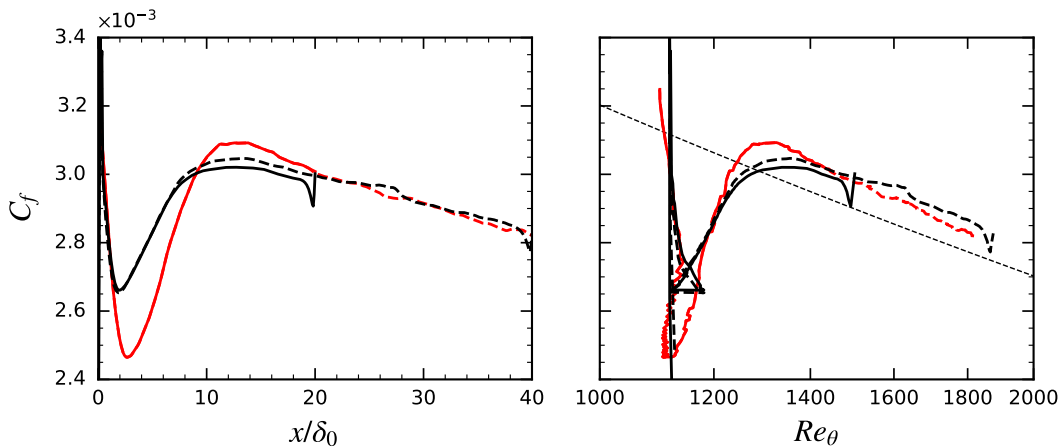


Figure B.3. Evolution of friction coefficient, present case (*black*) and DNS results (*red*). The results from simulations with an extended domain are shown in *dashed*. The *thin dashed* line represents the correlation from Ceci et al. (2022).

Figure B.4 reports the evolution of the peak $\overline{\rho u' u'}$ and $\overline{\rho u' v'}$. For the former, the DNS is able to reach the correlation within $20\delta_0$ while in the present case, the peak stagnates at a higher value. This over-prediction is a typical effect of the under-resolution (Poggie et al., 2015). Regarding the peak shear stress, comparable values are obtained tending toward more downstream locations, even though the DNS exhibits a quicker recovery.

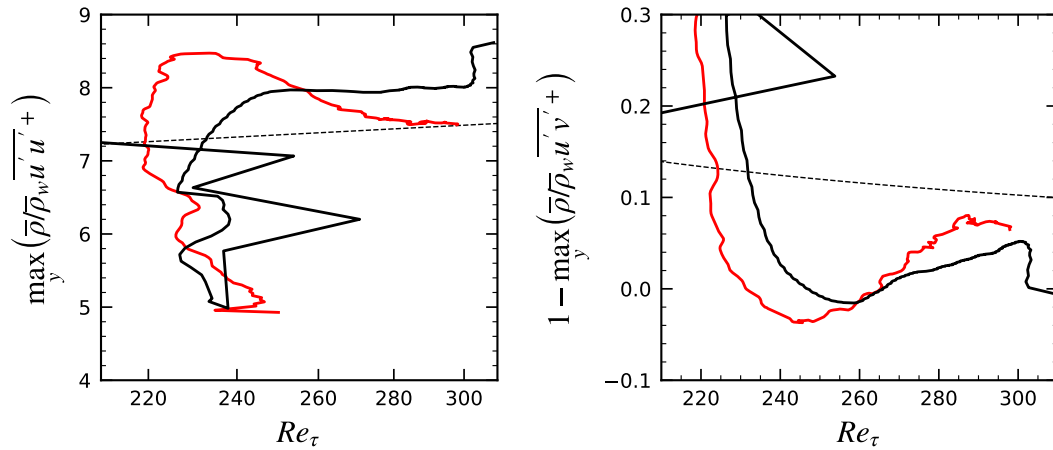


Figure B.4. Evolution of peak $\overline{\rho u' u'}$ (left) and peak $\overline{\rho u' v'}$ (right), present case (black) and DNS results (red). The thin dashed lines represent the correlations from Ceci et al. (2022).

Wall pressure variance distribution is depicted in figure B.5. The present case and the DNS show the same decreasing evolution as the friction Reynolds number (or, equivalently, the streamwise coordinate) increases. At the end of the domain, both simulations exhibit a normalized variance between 15 and 20, which is three times the variance predicted by the correlation. However, it is expected since Ceci et al. (2022) demonstrated that the level of pressure fluctuations is particularly over-predicted when using a *baseline* digital filtering technique. Some improved implementations were suggested and were shown to lead to reasonably correct results with respect to the correlation. These are, however, not considered in the high-order solver employed here.

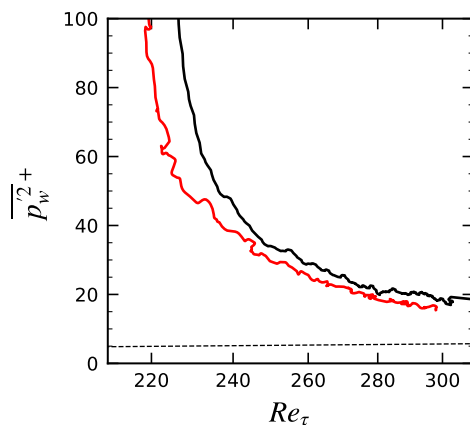


Figure B.5. Evolution of static pressure fluctuations, present case (black) and DNS results (red). The thin dashed line represents the correlations from Ceci et al. (2022).

Finally, figure B.6 shows the van Driest-transformed mean velocity profile and the density-scaled Reynolds stress profiles at the station $x/\delta_0 = 15$, in the region of decreasing friction coefficient. An excellent agreement is found for the velocity profile, especially in the viscous sublayer and in the logarithmic region. The law of the wall is matched, with $\kappa = 0.41$ and $C = 5.1$. An offset is observed in the defect layer, with an over-prediction of about 1.5% with respect to the DNS. The Reynolds stress profiles exhibit a good agreement as well. The slight over-prediction of the peak $\overline{u'u'}$, already reported above, is clearly discerned.

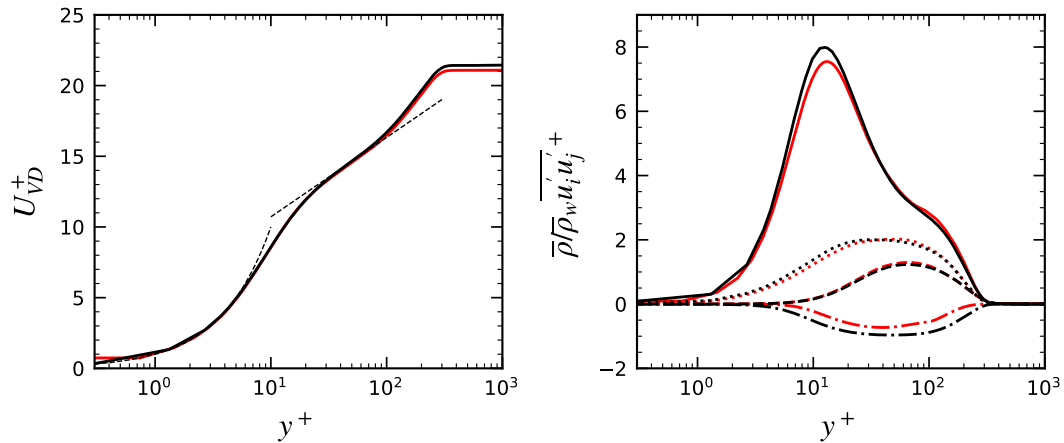


Figure B.6. Boundary layer profiles at $x/\delta_0 = 15$ - van Driest-transformed mean velocity profile (*left*) and density-scaled Reynolds stress profiles (*right*), present case (*black*) and DNS results (*red*).

B.3 Summary

This appendix presented the results of an ILES of a fully turbulent boundary layer developing over a flat plate at Mach 2. A systematic comparison with DNS results in the same conditions and using the same domain dimensions was performed and showed a good agreement, giving confidence in the implementation of the digital filtering technique. Moreover, a reasonably well-developed boundary layer is provided within a distance of $10\delta_0$ to $20\delta_0$ from the inlet, which is the typical adaptation length reported in the literature to recover the friction coefficient, inner scale mean velocity and Reynolds stress profiles (Adler et al., 2018; Dhamankar et al., 2018). The level of pressure fluctuations remains nevertheless high compared to reference data and this has to be taken into consideration for the subsequent analyses.

Bibliography

- Adamczyk, J. J. (1984). *Model Equation for Simulating Flows in Multistage Turbomachinery* (Report No. NASA-TM-86869). Retrieved July 13, 2023, from <https://ntrs.nasa.gov/api/citations/19850003728/downloads/19850003728.pdf>. (Cited on pages 6, 115)
- Adler, M. C., Gonzalez, D. R., Stack, C. M., & Gaitonde, D. V. (2018). Synthetic generation of equilibrium boundary layer turbulence from modeled statistics. *Computers & Fluids*, *165*, 127–143. <https://doi.org/10.1016/j.compfluid.2018.01.003> (Cited on pages 33–35, 145, 149)
- Agostini, L., Larchevêque, L., Dupont, P., Debiève, J.-F., & Dussauge, J.-P. (2012). Zones of Influence and Shock Motion in a Shock/Boundary-Layer Interaction. *AIAA Journal*, *50*(6), 1377–1387. <https://doi.org/10.2514/1.J051516> (Cited on pages 38–40, 49)
- Airbus. (2023). Global Market Forecast 2023. Retrieved July 20, 2023, from https://www.airbus.com/sites/g/files/jlcbta136/files/2023-06/GMF%202023-2042%20Presentation_0.pdf. (Cited on page 1)
- Akolekar, H., Sandberg, R., Hutchins, N., Michelassi, V., & Laskowski, G. (2019). Machine-learned turbulence closures for low-pressure turbines with unsteady inflow conditions. *Journal of Turbomachinery*, *141*(10), 101009. <https://doi.org/10.1115/1.4043907> (Cited on page 128)
- ATAG. (2020). Aviation: Benefits Beyond Borders. Retrieved August 18, 2023, from https://aviationbenefits.org/media/167517/aw-oct-final-atag_abbb-2020-publication-digital.pdf. (Cited on page 1)
- ATAG. (2021). Waypoint 2050. Retrieved August 18, 2023, from https://aviationbenefits.org/media/167417/w2050_v2021_27sept_full.pdf. (Cited on page 1)
- Aubard, G., Gloerfelt, X., & Robinet, J.-C. (2013). Large-Eddy Simulation of Broadband Unsteadiness in a Shock/Boundary-Layer Interaction. *AIAA Journal*, *51*(10), 2395–2409. <https://doi.org/10.2514/1.J052249> (Cited on pages 39–40)
- Barter, G. E., & Darmofal, D. L. (2010). Shock Capturing with PDE-Based Artificial Viscosity for DGFEM: Part I. Formulation. *Journal of Computational Physics*, *229*(5), 1810–1827. <https://doi.org/10.1016/j.jcp.2009.11.010> (Cited on page 29)
- Bassi, F., & Rebay, S. (1997). A high-order accurate discontinuous finite element method for the numerical solution of the compressible Navier–Stokes equations. *Journal of Computational Physics*, *131*(2), 267–279. <https://doi.org/10.1006/jcph.1996.5572> (Cited on page 8)

- Bermejo-Moreno, I., Larsson, J., & Bodart, J. (2014). Wall modeled large-eddy simulation of shock wave/turbulent boundary layer interaction with separation. *Center for Turbulence Research Annual Research Briefs*, 155–167. Retrieved July 24, 2023, from https://web.stanford.edu/group/ctr/ResBriefs/2014/16_bermejo.pdf (Cited on pages 39–41)
- Bernard, A., Foucaut, J.-M., Dupont, P., & Stanislas, M. (2003). Decelerating Boundary Layer: A New Scaling and Mixing Length Model. *AIAA Journal*, 41(2), 248–255. <https://doi.org/10.2514/2.1937> (Cited on page 63)
- Bernardini, M., Della Posta, G., Salvatore, F., & Martelli, E. (2023). Unsteadiness characterisation of shock wave/turbulent boundary-layer interaction at moderate Reynolds number. *Journal of Fluid Mechanics*, 954, A43. <https://doi.org/10.1017/jfm.2022.1038> (Cited on pages xi–xii, 32, 39–41, 45–49)
- Bernardini, M., Modesti, D., Salvatore, F., & Pirozzoli, S. (2021). STREAmS: A high-fidelity accelerated solver for direct numerical simulation of compressible turbulent flows. *Computer Physics Communications*, 263, 107906. <https://doi.org/10.1016/j.cpc.2021.107906> (Cited on page 145)
- Bodin, O., & Fuchs, L. (2008). Shock Unsteadiness and Shock Induced Separation at Transonic Flow over a Bump. *38th Fluid Dynamics Conference and Exhibit*, 4174. <https://doi.org/10.2514/6.2008-4174> (Cited on pages 63–64, 66–67, 87)
- Boeing. (2023). Commercial Market Outlook. Retrieved July 20, 2023, from https://www.boeing.com/resources/boeingdotcom/market/assets/downloads/2023-CMO_Hulst-Presentation.pdf. (Cited on page 1)
- Borm, O., & Kau, H.-P. (2012). Unsteady Aerodynamics of a Centrifugal Compressor Stage: Validation of Two Different CFD Solvers. *ASME Turbo Expo: Power for Land, Sea, and Air, Volume 8: Turbomachinery, Parts A, B, and C*, 2753–2764. <https://doi.org/10.1115/GT2012-69636> (Cited on page 7)
- Boussinesq, J. (1877). *Essai sur la théorie des eaux courantes* [Mémoires présentés par divers savants à l'Académie des Sciences de l'Institut de France. Extrait des T. 23 et 24]. Imprimerie Nationale (Paris). Retrieved September 29, 2023, from <https://catalogue.bnf.fr/ark:/12148/cb301489808>. (Cited on page 114)
- Box, G. E., & Muller, M. E. (1958). A Note on the Generation of Random Normal Deviates. *The Annals of Mathematical Statistics*, 29(2), 610–611. <https://doi.org/10.1214/aoms/1177706645> (Cited on page 34)
- Bravo-Mosquera, P. D., Catalano, F. M., & Zingg, D. W. (2022). Unconventional aircraft for civil aviation: A review of concepts and design methodologies. *Progress in Aerospace Sciences*, 131, 100813. <https://doi.org/10.1016/j.paerosci.2022.100813> (Cited on page 2)
- Brereton, G., & Reynolds, W. (1991). Dynamic response of boundary-layer turbulence to oscillatory shear. *Physics of Fluids A: Fluid Dynamics*, 3(1), 178–187. <https://doi.org/10.1063/1.857877> (Cited on pages 15, 109, 137–139)
- Bron, O. (2004). *Etude Expérimentale et Numérique de l'interaction Onde de Choc-Couche Limite en Écoulement Transsonique Instationnaire* (Doctoral dissertation). Ecole Centrale de Lyon. Retrieved July 12, 2023, from <https://bibli.ec-lyon.fr/exl-doc/obron.pdf>. (Cited on pages xiii, xv, xviii, 62–67, 69, 78, 84, 86, 91)
- Brouwer, J. (2016). *A Study of Transonic Shock-Wave/Boundary-Layer Interactions using Conservative, Skew-Symmetric Finite-Differences* (Doctoral dissertation)

- tion). Technische Universitaet Berlin, Germany. Retrieved July 12, 2023, from https://depositonce.tu-berlin.de/bitstream/11303/5318/4/brouwer_jens.pdf. (Cited on pages 63, 66–67, 76–79)
- Bruce, P., Babinsky, H., Tartinville, B., & Hirsch, C. (2011). Experimental and Numerical Study of Oscillating Transonic Shock Waves in Ducts. *AIAA Journal*, 49(8), 1710–1720. <https://doi.org/10.2514/1.J050944> (Cited on page 86)
- Bur, R., Benay, R., Galli, A., & Berthouze, P. (2006). Experimental and Numerical Study of Forced Shock-Wave Oscillations in a Transonic Channel. *Aerospace Science and Technology*, 10(4), 265–278. <https://doi.org/10.1016/j.ast.2005.12.002> (Cited on pages 64, 91)
- Carpenter, M. H., & Kennedy, C. A. (1994). *Fourth-Order 2N-Storage Runge-Kutta Schemes* (Report No. NASA-TM-109112). Retrieved May 8, 2023, from <https://ntrs.nasa.gov/api/citations/19940028444/downloads/19940028444.pdf>. (Cited on page 25)
- Castonguay, P., Williams, D., Vincent, P., & Jameson, A. (2013). Energy stable flux reconstruction schemes for advection–diffusion problems. *Computer Methods in Applied Mechanics and Engineering*, 267, 400–417. <https://doi.org/10.1016/j.cma.2013.08.012> (Cited on pages 9, 22)
- Castonguay, P., Vincent, P., & Jameson, A. (2011). Application of High-Order Energy Stable Flux Reconstruction Schemes to the Euler Equations. *49th AIAA Aerospace Sciences Meeting including the New Horizons Forum and Aerospace Exposition*, 686. <https://doi.org/10.2514/6.2011-686> (Cited on page 9)
- Castonguay, P., Vincent, P. E., & Jameson, A. (2012). A New Class of High-Order Energy Stable Flux Reconstruction Schemes for Triangular Elements. *Journal of Scientific Computing*, 51, 224–256. <https://doi.org/10.1007/s10915-011-9505-3> (Cited on page 9)
- Castonguay, P., Williams, D., Vincent, P. E., Lopez, M., & Jameson, A. (2011). On the Development of a High-Order, Multi-GPU Enabled, Compressible Viscous Flow Solver for Mixed Unstructured Grids. *20th AIAA Computational Fluid Dynamics Conference*, 3229. <https://doi.org/10.2514/6.2011-3229> (Cited on page 9)
- Ceci, A., Palumbo, A., Larsson, J., & Pirozzoli, S. (2022). Numerical tripping of high-speed turbulent boundary layers. *Theoretical and Computational Fluid Dynamics*, 1–22. <https://doi.org/10.1007/s00162-022-00623-0> (Cited on pages xvii, 145–148)
- Ceci, A., Palumbo, A., Larsson, J., & Pirozzoli, S. (2023). On low-frequency unsteadiness in swept shock wave–boundary layer interactions. *Journal of Fluid Mechanics*, 956, R1. <https://doi.org/10.1017/jfm.2023.2> (Cited on pages 39–41)
- Clark, W. S., & Hall, K. C. (2000). A Time-Linearized Navier-Stokes Analysis of Stall Flutter. *Journal of Turbomachinery*, 122(3), 467–476. <https://doi.org/10.1115/1.1303073> (Cited on page 7)
- Clemens, N. T., & Narayanaswamy, V. (2009). Shock/Turbulent Boundary Layer Interactions: Review of Recent Work on Sources of Unsteadiness. *39th AIAA*

- Fluid Dynamics Conference*, 3710. <https://doi.org/10.2514/6.2009-3710>
(Cited on pages xviii, 49)
- Clemens, N. T., & Narayanaswamy, V. (2014). Low-Frequency Unsteadiness of Shock Wave/Turbulent Boundary Layer Interactions. *Annual Review of Fluid Mechanics*, 46, 469–492. <https://doi.org/10.1146/annurev-fluid-010313-141346> (Cited on pages 2, 38, 82)
- Cockburn, B., & Shu, C.-W. (1989). TVB Runge-Kutta Local Projection Discontinuous Galerkin Finite Element Method for Conservation Laws. II. General Framework. *Mathematics of Computation*, 52(186), 411–435. <https://doi.org/10.1090/S0025-5718-1989-0983311-4> (Cited on page 26)
- Cockburn, B., & Shu, C.-W. (1998). The Local Discontinuous Galerkin Method for Time-Dependent Convection-Diffusion Systems. *SIAM Journal on Numerical Analysis*, 35(6), 2440–2463. <https://doi.org/10.1137/S0036142997316712>
(Cited on pages 8, 22)
- DeBonis, J. R., Oberkampf, W. L., Wolf, R. T., Orkwis, P. D., Turner, M. G., Babinsky, H., & Benek, J. A. (2012). Assessment of Computational Fluid Dynamics and Experimental Data for Shock Boundary-Layer Interactions. *AIAA Journal*, 50(4), 891–903. <https://doi.org/10.2514/1.J051341> (Cited on page 4)
- Debrabandere, F. (2013). *Comparison of NLH and full unsteady methods on the 2D bump* [Internal technical Report, NUMECA International]. (Cited on page 118).
- Debrabandere, F. (2014). *Computational method for industrial fluid-structure interactions* (Doctoral dissertation). University of Mons. (Cited on pages 6, 115).
- Debrabandere, F., Tartinville, B., Hirsch, C., & Coussement, G. (2013). Extension of the Non-Linear Harmonic Method to Flow Computations Around Moving and Deforming Structures. *International Forum on Aeroelasticity & Structural Dynamics 2013* (Cited on page 6).
- Delery, J. M. (1983). Experimental Investigation of Turbulence Properties in Transonic Shock/Boundary-Layer Interactions. *AIAA Journal*, 21(2), 180–185. <https://doi.org/10.2514/3.8052> (Cited on page 62)
- Denton, J., & Dawes, W. (1998). Computational fluid dynamics for turbomachinery design. *Proceedings of the Institution of Mechanical Engineers, Part C: Journal of Mechanical Engineering Science*, 213(2), 107–124. <https://doi.org/10.1243/0954406991522211> (Cited on page 3)
- Dhamankar, N. S., Blaisdell, G. A., & Lyrantzis, A. S. (2018). Overview of Turbulent Inflow Boundary Conditions for Large-Eddy Simulations. *AIAA Journal*, 56(4), 1317–1334. <https://doi.org/10.2514/1.J055528> (Cited on pages 31–32, 149)
- Di Renzo, M., Oberoi, N., Larsson, J., & Pirozzoli, S. (2022). Crossflow effects on shock wave/turbulent boundary layer interactions. *Theoretical and Computational Fluid Dynamics*, 36(2), 327–344. <https://doi.org/10.1007/s00162-021-00574-y> (Cited on pages 39–41)
- Dolling, D. S. (2001). Fifty Years of Shock-Wave/Boundary-Layer Interaction Research: What Next? *AIAA Journal*, 39(8), 1517–1531. <https://doi.org/10.2514/2.1476> (Cited on page 38)

- Du, J., Shu, C.-W., & Zhang, M. (2015). A simple weighted essentially non-oscillatory limiter for the correction procedure via reconstruction (CPR) framework. *Applied Numerical Mathematics*, 95, 173–198. <https://doi.org/10.1016/j.apnum.2014.01.006> (Cited on page 26)
- Duan, Z., & Wang, Z. J. (2022). A Turbulent Inflow Generation Approach for High Order Implicit Large Eddy Simulation. *AIAA SciTech Forum*, 1202. <https://doi.org/10.2514/6.2022-1202> (Cited on page 33)
- Ducros, F., Ferrand, V., Nicoud, F., Weber, C., Darracq, D., Gacherieu, C., & Poinso, T. (1999). Large-Eddy Simulation of the Shock/Turbulence Interaction. *Journal of Computational Physics*, 152(2), 517–549. <https://doi.org/10.1006/jcph.1999.6238> (Cited on pages 27, 29, 53)
- Dupont, P., Haddad, C., Ardisson, J., & Debieve, J. (2005). Space and time organisation of a shock wave/turbulent boundary layer interaction. *Aerospace Science and Technology*, 9(7), 561–572. <https://doi.org/10.1016/j.ast.2004.12.009> (Cited on pages 37, 41, 49, 58)
- Dupont, P., Haddad, C., & Debieve, J. (2006). Space and time organization in a shock-induced separated boundary layer. *Journal of Fluid Mechanics*, 559, 255–277. <https://doi.org/10.1017/S0022112006000267> (Cited on pages xii, 37, 47–48, 58)
- Dupont, P., Piponniau, S., Sidorenko, A., & Debiève, J. (2008). Investigation by Particle Image Velocimetry Measurements of Oblique Shock Reflection with Separation. *AIAA Journal*, 46(6), 1365–1370. <https://doi.org/10.2514/1.30154> (Cited on pages xi–xii, xviii, 37, 45, 50, 58)
- Dussauge, J.-P., Dupont, P., & Debiève, J.-F. (2006). Unsteadiness in shock wave boundary layer interactions with separation. *Aerospace Science and Technology*, 10(2), 85–91. <https://doi.org/10.1016/j.ast.2005.09.006> (Cited on page 37)
- European Commission and Directorate-General for Mobility and Transport and Directorate-General for Research and Innovation. (2011). *Flightpath 2050: Europe's Vision for Aviation: Maintaining global leadership and serving society's needs*. Publications Office. <https://doi.org/10.2777/50266>. (Cited on page 1)
- European Commission and Directorate-General for Research and Innovation. (2022). *Fly the Green Deal: Europe's Vision for Sustainable Aviation*. Publications Office of the European Union. <https://doi.org/10.2777/732726>. (Cited on page 1)
- Fernandez, P., Nguyen, C., & Peraire, J. (2018). A physics-based shock capturing method for unsteady laminar and turbulent flows. *2018 AIAA Aerospace Sciences Meeting*, 0062. <https://doi.org/10.2514/6.2018-0062> (Cited on page 27)
- Flad, D., Beck, A., & Munz, C.-D. (2016). Simulation of underresolved turbulent flows by adaptive filtering using the high order discontinuous Galerkin spectral element method. *Journal of Computational Physics*, 313, 1–12. <https://doi.org/10.1016/j.jcp.2015.11.064> (Cited on page 26)
- Frey, C., Ashcroft, G., Kersken, H.-P., & Voigt, C. (2014). A Harmonic Balance Technique for Multistage Turbomachinery Applications. *ASME Turbo Expo*:

- Power for Land, Sea, and Air, Volume 2B: Turbomachinery*, V02BT39A005. <https://doi.org/10.1115/GT2014-25230> (Cited on page 6)
- Fu, L. (2023). Review of the High-Order TENO Schemes for Compressible Gas Dynamics and Turbulence. *Archives of Computational Methods in Engineering*, 30(4), 2493–2526. <https://doi.org/10.1007/s11831-022-09877-7> (Cited on page 26)
- Gaitonde, D. V., & Adler, M. C. (2023). Dynamics of Three-Dimensional Shock-Wave/Boundary-Layer Interactions. *Annual Review of Fluid Mechanics*, 55, 291–321. <https://doi.org/10.1146/annurev-fluid-120720-022542> (Cited on page 2)
- Gao, H., & Wang, Z. J. (2009). A High-Order Lifting Collocation Penalty Formulation for the Navier-Stokes Equations on 2D Mixed Grids. *19th AIAA Computational Fluid Dynamics*, 3784. <https://doi.org/10.2514/6.2009-3784> (Cited on page 9)
- Garnier, E., Sagaut, P., & Deville, M. (2002). Large Eddy Simulation of Shock/Boundary-Layer Interaction. *AIAA Journal*, 40(10), 1935–1944. <https://doi.org/10.2514/2.1552> (Cited on pages 38–40)
- Gaviglio, J. (1987). Reynolds analogies and experimental study of heat transfer in the supersonic boundary layer. *International Journal of Heat and Mass Transfer*, 30(5), 911–926. [https://doi.org/10.1016/0017-9310\(87\)90010-X](https://doi.org/10.1016/0017-9310(87)90010-X) (Cited on page 35)
- Glaubitz, J., Nogueira, A., Almeida, J. L., Cantão, R., & Silva, C. (2019). Smooth and Compactly Supported Viscous Sub-Cell Shock Capturing for Discontinuous Galerkin Methods. *Journal of Scientific Computing*, 79(1), 249–272. <https://doi.org/10.1007/s10915-018-0850-3> (Cited on pages 29–30)
- Goffart, N., Tartinville, B., Hirsch, C., & Pirozzoli, S. (2022). Coherent Turbulent Stresses in Transonic Nozzle with Shock-Wave/Turbulent Boundary Layer Interaction. *ERCOfTAC Direct and Large-Eddy Simulation Workshop 13* (Cited on page 11).
- Goffart, N., Tartinville, B., Hirsch, C., & Pirozzoli, S. (2023). Investigation of Forced Shock-Induced Separation in a Transonic Channel. *15th European Conference on Turbomachinery Fluid Dynamics and \mathcal{E} Thermodynamics*. <https://doi.org/10.29008/ETC2023-155> (Cited on page 12)
- Goffart, N., Tartinville, B., & Pirozzoli, S. (2023). Coherent Turbulent Stresses in Unsteady Forced Transonic Nozzle with Shock-Induced Separation. *ASME Turbo Expo: Power for Land, Sea, and Air, Volume 13D: Turbomachinery — Multidisciplinary Design Approaches, Optimization, and Uncertainty Quantification; Radial Turbomachinery Aerodynamics; Unsteady Flows in Turbomachinery*, V13DT36A009. <https://doi.org/10.1115/GT2023-101925> (Cited on page 12)
- Goffart, N., Tartinville, B., & Pirozzoli, S. (2024). Harmonic Turbulent Stress Budgets in Forced Transonic Flow over a Bump. *AIAA Journal*, 62(3), 940–955. <https://doi.org/10.2514/1.J063417> (Cited on page 11)
- Goffart, N., Tartinville, B., Puri, K., Hirsch, C., & Pirozzoli, S. (2022). High-Order, High-Fidelity Simulation of Unsteady Shock-Wave/Boundary Layer Interaction Using Flux Reconstruction. *8th European Congress on Computational*

- Methods in Applied Sciences and Engineering*. <https://doi.org/10.23967/eccomas.2022.138> (Cited on page 11)
- Hadjadj, A. (2012). Large-Eddy Simulation of Shock/Boundary-Layer Interaction. *AIAA Journal*, 50(12), 2919–2927. <https://doi.org/10.2514/1.J051786> (Cited on pages 39–41)
- Haga, T., Gao, H., & Wang, Z. J. (2011). A High-Order Unifying Discontinuous Formulation for the Navier-Stokes Equations on 3D Mixed Grids. *Mathematical Modelling of Natural Phenomena*, 6(3), 28–56. <https://doi.org/10.1051/mmnp/20116302> (Cited on page 9)
- Hall, K. C., & Lorence, C. B. (1993). Calculation of Three-Dimensional Unsteady Flows in Turbomachinery Using the Linearized Harmonic Euler Equations. *Journal of Turbomachinery*, 115(4), 800–809. <https://doi.org/10.1115/1.2929318> (Cited on page 6)
- Hall, K. C., Thomas, J. P., & Clark, W. S. (2002). Computation of Unsteady Nonlinear Flows in Cascades Using a Harmonic Balance Technique. *AIAA Journal*, 40(5), 879–886. <https://doi.org/10.2514/2.1754> (Cited on page 6)
- Hammond, J., Pepper, N., Montomoli, F., & Michelassi, V. (2022). Machine Learning Methods in CFD for Turbomachinery: A Review. *International Journal of Turbomachinery, Propulsion and Power*, 7(2), 16. <https://doi.org/10.3390/ijtp7020016> (Cited on page 5)
- Harten, A., Engquist, B., Osher, S., & Chakravarthy, S. R. (1987). Uniformly High Order Accurate Essentially Non-oscillatory Schemes, III. *Journal of Computational Physics*, 71(2), 231–303. [https://doi.org/10.1016/0021-9991\(87\)90031-3](https://doi.org/10.1016/0021-9991(87)90031-3) (Cited on page 26)
- He, L. (2010). Fourier methods for turbomachinery applications. *Progress in Aerospace Sciences*, 46(8), 329–341. <https://doi.org/10.1016/j.paerosci.2010.04.001> (Cited on page 5)
- He, L., & Ning, W. (1998). Efficient Approach for Analysis of Unsteady Viscous Flows in Turbomachines. *AIAA Journal*, 36(11), 2005–2012. <https://doi.org/10.2514/2.328> (Cited on pages 6, 113)
- Hembera, M., Loos, A., Kau, H.-P., & Johann, E. (2009). Comparing a 40 Mio Gridpoints Full-Annulus Computation with a 7 Mio Gridpoints Nonlinear Harmonic Computation. *47th AIAA Aerospace Sciences Meeting including The New Horizons Forum and Aerospace Exposition*, 930. <https://doi.org/10.2514/6.2009-930> (Cited on page 7)
- Hildebrandt, T., Thiel, P., Albert, S., & Vilmin, S. (2014). Applying an Extended Non Linear Harmonic Method to a CROR Configuration With Emphasis on the Acoustic Signature. *ASME Turbo Expo: Power for Land, Sea, and Air, Volume 2A: Turbomachinery*, V02AT41A001. <https://doi.org/10.1115/GT2014-25061> (Cited on page 7)
- Holmes, D. G., & Lorence, C. B. (1998). Three Dimensional Linearized Navier-Stokes Calculations for Flutter and Forced Response. *Unsteady Aerodynamics and Aeroelasticity of Turbomachines: Proceedings of the 8th International Symposium*, 211–224. https://doi.org/10.1007/978-94-011-5040-8_14 (Cited on page 7)

- Hussain, A. F. (1983). Coherent Structures—Reality and Myth. *The Physics of Fluids*, 26(10), 2816–2850. <https://doi.org/10.1063/1.864048> (Cited on page 98)
- Huynh, H. T. (2007). A Flux Reconstruction Approach to High-Order Schemes Including Discontinuous Galerkin Methods. *18th AIAA Computational Fluid Dynamics Conference*, 4079. <https://doi.org/10.2514/6.2007-4079> (Cited on pages 8–9, 22)
- Huynh, H. T. (2009). A Reconstruction Approach to High-Order Schemes Including Discontinuous Galerkin for Diffusion. *47th AIAA Aerospace Sciences Meeting Including The New Horizons Forum and Aerospace Exposition*, 403. <https://doi.org/10.2514/6.2009-403> (Cited on page 9)
- Huynh, H. T. (2011). High-Order Methods Including Discontinuous Galerkin by Reconstructions on Triangular Meshes. *49th AIAA Aerospace Sciences Meeting including the New Horizons Forum and Aerospace Exposition*, 44. <https://doi.org/10.2514/6.2011-44> (Cited on page 9)
- Huynh, H. T. (2020). Discontinuous Galerkin via Interpolation: The Direct Flux Reconstruction Method. *Journal of Scientific Computing*, 82(3), 75. <https://doi.org/10.1007/s10915-020-01175-3> (Cited on page 9)
- ICCT. (2020). CO₂ Emissions from Commercial Aviation. Retrieved August 18, 2023, from <https://theicct.org/wp-content/uploads/2021/06/CO2-commercial-aviation-oct2020.pdf>. (Cited on page 1)
- Iyer, A., Abe, Y., Vermeire, B., Bechlars, P., Baier, R., Jameson, A., Witherden, F., & Vincent, P. (2021). High-order accurate direct numerical simulation of flow over a MTU-T161 low pressure turbine blade. *Computers & Fluids*, 226, 104989. <https://doi.org/10.1016/j.compfluid.2021.104989> (Cited on page 10)
- Jameson, A. (2010). A Proof of the Stability of the Spectral Difference Method for All Orders of Accuracy. *Journal of Scientific Computing*, 45, 348–358. <https://doi.org/10.1007/s10915-009-9339-4> (Cited on page 9)
- Jameson, A., Schmidt, W., & Turkel, E. (1981). Numerical Solution of the Euler Equations by Finite Volume Methods Using Runge Kutta Time Stepping Schemes. *14th Fluid and Plasma Dynamics Conference*, 1259. <https://doi.org/10.2514/6.1981-1259> (Cited on page 68)
- Jones, W. P., & Launder, B. E. (1972). The Prediction of Laminarization with a Two-Equation Model of Turbulence. *International Journal of Heat and Mass Transfer*, 15(2), 301–314. [https://doi.org/10.1016/0017-9310\(72\)90076-2](https://doi.org/10.1016/0017-9310(72)90076-2) (Cited on pages 77–78)
- Kempf, A. M., Wysocki, S., & Pettit, M. (2012). An efficient, parallel low-storage implementation of Klein’s turbulence generator for LES and DNS. *Computers & Fluids*, 60, 58–60. <https://doi.org/10.1016/j.compfluid.2012.02.027> (Cited on page 33)
- Kim, Y., Castro, I. P., & Xie, Z.-T. (2013). Divergence-free turbulence inflow conditions for large-eddy simulations with incompressible flow solvers. *Computers & Fluids*, 84, 56–68. <https://doi.org/10.1016/j.compfluid.2013.06.001> (Cited on page 35)
- Kitsios, V., Cordier, L., Bonnet, J.-P., Ooi, A., & Soria, J. (2010). Development of a nonlinear eddy-viscosity closure for the triple-decomposition stability

- analysis of a turbulent channel. *Journal of Fluid Mechanics*, 664, 74–107. <https://doi.org/10.1017/S0022112010003617> (Cited on page 128)
- Klein, M., Sadiki, A., & Janicka, J. (2003). A digital filter based generation of inflow data for spatially developing direct numerical or large eddy simulations. *Journal of Computational Physics*, 186(2), 652–665. [https://doi.org/10.1016/S0021-9991\(03\)00090-1](https://doi.org/10.1016/S0021-9991(03)00090-1) (Cited on pages 32–33, 35)
- Klöckner, A., Warburton, T., & Hesthaven, J. S. (2011). Viscous Shock Capturing in a Time-Explicit Discontinuous Galerkin Method. *Mathematical Modelling of Natural Phenomena*, 6(3), 57–83. <https://doi.org/10.1051/mmnp/20116303> (Cited on page 30)
- Kok, J. (2009). A high-order low-dispersion symmetry-preserving finite-volume method for compressible flow on curvilinear grids. *Journal of Computational Physics*, 228(18), 6811–6832. <https://doi.org/10.1016/j.jcp.2009.06.015> (Cited on page 8)
- Kopriva, D. A., & Koliass, J. H. (1996). A conservative staggered-grid Chebyshev multidomain method for compressible flows. *Journal of Computational Physics*, 125(1), 244–261. <https://doi.org/10.1006/jcph.1996.0091> (Cited on page 8)
- Korakianitis, T. (1993). On the Propagation of Viscous Wakes and Potential Flow in Axial-Turbine Cascades. *Journal of Turbomachinery*, 115(1), 118–127. <https://doi.org/10.1115/1.2929196> (Cited on page 65)
- Krogstad, P.-Å., & Skåre, P. E. (1995). Influence of a strong adverse pressure gradient on the turbulent structure in a boundary layer. *Physics of Fluids*, 7(8), 2014–2024. <https://doi.org/10.1063/1.868513> (Cited on page 101)
- Larsson, J., Kumar, V., Oberoi, N., Renzo, M. D., & Pirozzoli, S. (2022). Large-Eddy Simulations of Idealized Shock/Boundary-Layer Interactions with Crossflow. *AIAA Journal*, 60(5), 2767–2779. <https://doi.org/10.2514/1.J061060> (Cited on pages 25, 32, 39–41)
- Laval, J.-P., & Marquillie, M. (2011). Direct Numerical Simulations of Converging–Diverging Channel Flow. *Progress in Wall Turbulence: Understanding and Modeling: Proceedings of the WALLTURB International Workshop held in Lille, France, April 21–23, 2009*, 203–209. https://doi.org/10.1007/978-90-481-9603-6_21 (Cited on pages 63, 76, 101)
- Lighthill, M. J. (1954). The Response of Laminar Skin Friction and Heat Transfer to Fluctuations in the Stream Velocity. *Proceedings of the Royal Society of London. Series A. Mathematical and Physical Sciences*, 224(1156), 1–23. <https://doi.org/10.1098/rspa.1954.0137> (Cited on page 64)
- Liu, X., & Squire, L. C. (1988). An Investigation of Shock/Boundary-Layer Interactions on Curved Surfaces at Transonic Speeds. *Journal of Fluid Mechanics*, 187, 467–486. <https://doi.org/10.1017/S0022112088000527> (Cited on page 62)
- Liu, X.-D., Osher, S., & Chan, T. (1994). Weighted Essentially Non-Oscillatory Schemes. *Journal of computational physics*, 115(1), 200–212. <https://doi.org/10.1006/jcph.1994.1187> (Cited on page 26)
- Liu, Y., Wei, X., & Tang, Y. (2023). Investigation of Unsteady Rotor–Stator Interaction and Deterministic Correlation Analysis in a Transonic Compressor Stage. *Journal of Turbomachinery*, 145(7), 071004. <https://doi.org/10.1115/1.4056716> (Cited on page 7)

- Liu, Y., Vinokur, M., & Wang, Z. J. (2006). Spectral difference method for unstructured grids I: Basic formulation. *Journal of Computational Physics*, 216(2), 780–801. <https://doi.org/10.1016/j.jcp.2006.01.024> (Cited on page 8)
- Lund, T. S., Wu, X., & Squires, K. D. (1998). Generation of Turbulent Inflow Data for Spatially-Developing Boundary Layer Simulations. *Journal of Computational Physics*, 140(2), 233–258. <https://doi.org/10.1006/jcph.1998.5882> (Cited on page 34)
- Mani, A., Larsson, J., & Moin, P. (2009). Suitability of artificial bulk viscosity for large-eddy simulation of turbulent flows with shocks. *Journal of Computational Physics*, 228(19), 7368–7374. <https://doi.org/10.1016/j.jcp.2009.06.040> (Cited on page 29)
- Marlier, J., Barbieux, V., & Tartinville, B. (2016). Unsteady Rotating Radial Load of a Single Stage Radial Inflow Turbine. *ASME Turbo Expo: Power for Land, Sea, and Air, Volume 2D: Turbomachinery*, V02DT42A021. <https://doi.org/10.1115/GT2016-56983> (Cited on page 7)
- Marquillie, M., Laval, J.-P., & Dolganov, R. (2008). Direct Numerical Simulation of a Separated Channel Flow with a Smooth Profile. *Journal of Turbulence*, 9, N1. <https://doi.org/10.1080/14685240701767332> (Cited on pages 63, 101, 103)
- Mathison, R. M., Wishart, M. B., Haldeman, C. W., & Dunn, M. G. (2011). Temperature Predictions and Comparison With Measurements for the Blade Leading Edge and Platform of a 1 1/2 Stage Transonic HP Turbine. *Journal of Turbomachinery*, 134(1), 011016. <https://doi.org/10.1115/1.4002992> (Cited on page 7)
- McMullen, M., Jameson, A., & Alonso, J. J. (2001). Acceleration of Convergence to a Periodic Steady State in Turbomachinery Flows. *39th AIAA Aerospace Sciences Meeting & Exhibit*, 152. <https://doi.org/10.2514/6.2001-152> (Cited on page 6)
- Mehdizadeh, O. Z., Temmerman, L., Tartinville, B., & Hirsch, C. (2012). Applications of EARSM Turbulence Models to Internal Flows. *ASME Turbo Expo: Power for Land, Sea, and Air, Volume 8: Turbomachinery, Parts A, B, and C*, 2079–2086. <https://doi.org/10.1115/GT2012-68886> (Cited on page 70)
- Mehdizadeh, O. Z., Vilmin, S., Tartinville, B., & Hirsch, C. (2017). Nonlinear Harmonic Method Applied to Turbine Conjugate Heat Transfer Analysis for Efficient Simulation of Hot Streak Clocking and Unsteady Heat Transfer. *ASME Turbo Expo: Power for Land, Sea, and Air, Volume 5A: Heat Transfer*, V05AT10A003. <https://doi.org/10.1115/GT2017-63622> (Cited on page 6)
- Menter, F. R. (1992). *Improved Two-Equation $k - \omega$ Turbulence Models for Aerodynamic Flows* (Report No. NASA-TM-103975). Retrieved May 8, 2023, from <https://ntrs.nasa.gov/api/citations/19930013620/downloads/19930013620.pdf>. (Cited on page 70)
- Miró, A., Wallin, S., Colombo, A., Temmerman, L., Wunsch, D., & Lehmkuhl Barba, O. (2023). Towards a Machine Learning Model for Explicit Algebraic Reynolds Stress Modelling Using Multi-Expression Programming. *14th International ERCOFTAC Symposium on Engineering, Turbulence, Modelling and Measurements*. Retrieved October 19, 2023, from <https://upcommons>.

- upc.edu/bitstream/handle/2117/394814/AC_ETMM_ML_EARSM.pdf
(Cited on page 128)
- Morgan, B., Duraisamy, K., Nguyen, N., Kawai, S., & Lele, S. (2013). Flow physics and RANS modelling of oblique shock/turbulent boundary layer interaction. *Journal of Fluid Mechanics*, 729, 231–284. <https://doi.org/10.1017/jfm.2013.301> (Cited on pages xii, 25, 38–40, 46–49)
- Moroianu, D., Caraeni, D., & Fuchs, L. (2005). Large Eddy Simulation of a Shock Boundary Layer Interaction in a Transonic Internal Flow. *43rd AIAA Aerospace Sciences Meeting and Exhibit*, 312. <https://doi.org/10.2514/6.2005-312> (Cited on page 64)
- Ou, K., Vincent, P., & Jameson, A. (2011). High-Order Methods for Diffusion Equation with Energy Stable Flux Reconstruction Scheme. *49th AIAA Aerospace Sciences Meeting Including the New Horizons Forum and Aerospace Exposition*, 46. <https://doi.org/10.2514/6.2011-46> (Cited on page 9)
- Park, J. S., Witherden, F. D., & Vincent, P. E. (2017). High-Order Implicit Large-Eddy Simulations of Flow over a NACA0021 Aerofoil. *AIAA Journal*, 55(7), 2186–2197. <https://doi.org/10.2514/1.J055304> (Cited on page 10)
- Persson, P.-O. (2013). Shock Capturing for High-Order Discontinuous Galerkin Simulation of Transient Flow Problems. *21st AIAA Computational Fluid Dynamics Conference*, 3061. <https://doi.org/10.2514/6.2013-3061> (Cited on pages 29–30)
- Persson, P.-O., & Peraire, J. (2006). Sub-Cell Shock Capturing for Discontinuous Galerkin Methods. *44th AIAA Aerospace Sciences Meeting and Exhibit*, 112. <https://doi.org/10.2514/6.2006-112> (Cited on pages 27, 29–30, 53)
- Philit, M., Ferrand, P., Labit, S., Chassaing, J., Aubert, S., & Fransson, T. (2012). Derivated Turbulence Model to Predict Harmonic Loads in Transonic Separated Flows over a Bump. *28th International Congress of Aeronautical Sciences*. Retrieved July 11, 2023, from https://www.icas.org/ICAS_ARCHIVE/ICAS2012/PAPERS/773.pdf (Cited on pages 7, 118)
- Piponnier, S., Dussauge, J.-P., Debieve, J.-F., & Dupont, P. (2009). A simple model for low-frequency unsteadiness in shock-induced separation. *Journal of Fluid Mechanics*, 629, 87–108. <https://doi.org/10.1017/S0022112009006417> (Cited on pages xviii, 38, 41, 45)
- Pirozzoli, S. (2010). Generalized conservative approximations of split convective derivative operators. *Journal of Computational Physics*, 229(19), 7180–7190. <https://doi.org/10.1016/j.jcp.2010.06.006> (Cited on page 8)
- Pirozzoli, S., & Bernardini, M. (2011). Direct Numerical Simulation Database for Impinging Shock Wave/Turbulent Boundary-Layer Interaction. *AIAA Journal*, 49(6), 1307–1312. <https://doi.org/10.2514/1.J050901> (Cited on pages 38–40, 72)
- Pirozzoli, S., & Grasso, F. (2006). Direct numerical simulation of impinging shock wave/turbulent boundary layer interaction at $M = 2.25$. *Physics of Fluids*, 18(6), 065113. <https://doi.org/10.1063/1.2216989> (Cited on pages 38–40)
- Poggie, J., Bisek, N. J., & Gosse, R. (2015). Resolution Effects in Compressible, Turbulent Boundary Layer Simulations. *Computers & Fluids*, 120, 57–69. <https://doi.org/10.1016/j.compfluid.2015.07.015> (Cited on pages 73, 148)

- Pope, S. B. (2000). *Turbulent flows*. Cambridge University Press. <https://doi.org/10.1017/CBO9780511840531>. (Cited on pages 32, 101)
- Priebe, S., Wilkin, I., Daniel, Breeze-Stringfellow, A., Jothiprasad, G., & Cheung, L. C. (2020). Large Eddy Simulation of Laminar and Turbulent Shock/Boundary Layer Interactions in a Transonic Passage. *ASME Turbo Expo: Power for Land, Sea, and Air, Volume 2A: Turbomachinery*. <https://doi.org/10.1115/GT2020-14244> (Cited on pages 10, 62)
- Rahmani, S. K., & Wang, Z. J. (2022). Large Eddy Simulation of the Sandia Axisymmetric Transonic Hump Using a High-Order Method. *AIAA Scitech 2022 Forum*, 1534. <https://doi.org/10.2514/6.2022-1534> (Cited on page 10)
- Reed, W. H., & Hill, T. R. (1973). *Triangular Mesh Methods for the Neutron Transport Equation* (Report No. LA-UR-73-479). Retrieved August 31, 2023, from <https://www.osti.gov/servlets/purl/4491151>. (Cited on page 8)
- Reynolds, W., & Hussain, A. (1972). The Mechanics of an Organized Wave in Turbulent Shear Flow. Part 3. Theoretical Models and Comparisons with Experiments. *Journal of Fluid Mechanics*, 54(2), 263–288. <https://doi.org/10.1017/S0022112072000679> (Cited on pages 14, 55, 129, 131, 133, 137, 139)
- Rizzi, A., Eliasson, P., Lindblad, I., Hirsch, C., Lacor, C., & Haeuser, J. (1993). The Engineering of Multiblock/Multigrid Software for Navier-Stokes Flows on Structured Meshes. *Computers & Fluids*, 22(2), 341–367. [https://doi.org/10.1016/0045-7930\(93\)90065-H](https://doi.org/10.1016/0045-7930(93)90065-H) (Cited on page 68)
- Roe, P. L. (1981). Approximate Riemann Solvers, Parameter Vectors, and Difference Schemes. *Journal of Computational Physics*, 43(2), 357–372. [https://doi.org/10.1016/0021-9991\(81\)90128-5](https://doi.org/10.1016/0021-9991(81)90128-5) (Cited on page 22)
- Romero, J., Asthana, K., & Jameson, A. (2016). A Simplified Formulation of the Flux Reconstruction Method. *Journal of Scientific Computing*, 67, 351–374. <https://doi.org/10.1007/s10915-015-0085-5> (Cited on page 9)
- Romero, J., Crabill, J., Watkins, J. E., Witherden, F. D., & Jameson, A. (2020). ZEFR: A GPU-accelerated high-order solver for compressible viscous flows using the flux reconstruction method. *Computer Physics Communications*, 250, 107169. <https://doi.org/10.1016/j.cpc.2020.107169> (Cited on page 10)
- Romero, J., Witherden, F. D., & Jameson, A. (2017). A Direct Flux Reconstruction Scheme for Advection-Diffusion Problems on Triangular Grids. *Journal of Scientific Computing*, 73, 1115–1144. <https://doi.org/10.1007/s10915-017-0472-1> (Cited on page 9)
- Rumsey, C., & Coleman, G. (2022). *NASA Symposium on Turbulence Modeling: Roadblocks, and the Potential for Machine Learning* (Report No. NASA-TM-20220015595). Retrieved October 17, 2023, from <https://ntrs.nasa.gov/api/citations/20220015595/downloads/NASA-TM-20220015595final.pdf>. (Cited on page 4)
- Sandham, N., Yao, Y., & Lawal, A. (2003). Large-Eddy Simulation of Transonic Turbulent Flow Over a Bump. *International Journal of Heat and Fluid Flow*, 24(4), 584–595. [https://doi.org/10.1016/S0142-727X\(03\)00052-3](https://doi.org/10.1016/S0142-727X(03)00052-3) (Cited on pages 62, 76, 79)
- Sartor, F., Losfeld, G., & Bur, R. (2012). PIV Study on a Shock-Induced Separation in a Transonic Flow. *Experiments in Fluids*, 53, 815–827. <https://doi.org/10.1007/s00348-012-1330-4> (Cited on page 65)

- Sbardella, L., & Imregun, M. (2001). Linearized Unsteady Viscous Turbomachinery Flows Using Hybrid Grids. *Journal of Turbomachinery*, 123(3), 568–582. <https://doi.org/10.1115/1.1371777> (Cited on pages 6–7)
- Schiavo, L. A., Jesus, A. B., Azevedo, J. L., & Wolf, W. R. (2015). Large Eddy Simulations of Convergent–Divergent Channel Flows at Moderate Reynolds Numbers. *International Journal of Heat and Fluid Flow*, 56, 137–151. <https://doi.org/10.1016/j.ijheatfluidflow.2015.07.006> (Cited on pages 64, 76, 103)
- Schiavo, L. A., Wolf, W. R., & Azevedo, J. L. F. (2017). Turbulent Kinetic Energy Budgets in Wall Bounded Flows with Pressure Gradients and Separation. *Physics of Fluids*, 29(11), 115108. <https://doi.org/10.1063/1.4992793> (Cited on pages 64, 76, 101, 103)
- Schlatter, P., & Örlü, R. (2010). Assessment of Direct Numerical Simulation Data of Turbulent Boundary Layers. *Journal of Fluid Mechanics*, 659, 116–126. <https://doi.org/10.1017/S0022112010003113> (Cited on pages xiii, 73–74)
- Sheshadri, A. (2016). *An Analysis of Stability of the Flux Reconstruction Formulation with Applications to Shock Capturing* (Doctoral dissertation). Stanford University. Retrieved August 15, 2023, from http://aero-comlab.stanford.edu/Papers/Abhishek_thesis_hc_Aug26.pdf. (Cited on page 26)
- Sicot, F. (2009). *Simulation efficace des écoulements instationnaires périodiques en turbomachines* (Doctoral dissertation). Ecole Centrale de Lyon. Retrieved July 12, 2023, from https://acoustique.ec-lyon.fr/publi/sicot_thesis.pdf. (Cited on page 5)
- Sicot, F., Guédeney, T., & Dufour, G. (2013). Time-domain harmonic balance method for aerodynamic and aeroelastic simulations of turbomachinery flows. *International Journal of Computational Fluid Dynamics*, 27(2), 68–78. <https://doi.org/10.1080/10618562.2012.740021> (Cited on page 6)
- Sigfrids, T. (2003). *Hot Wire and PIV Studies of Transonic Turbulent Wall-Bounded Flows* (Licentiate Thesis). Royal Institute of Technology, Sweden. Retrieved July 12, 2023, from <https://www.diva-portal.org/smash/get/diva2:7500/FULLTEXT01.pdf>. (Cited on page 65)
- Smits, A. J., & Dussauge, J.-P. (2006). *Turbulent Shear Layers in Supersonic Flow*. Springer New York, NY. <https://doi.org/10.1007/b137383>. (Cited on page 73)
- Spalart, P., & Allmaras, S. (1992). A One-Equation Turbulence Model for Aerodynamic Flows. *30th Aerospace Sciences Meeting and Exhibit*, 439. <https://doi.org/10.2514/6.1992-439> (Cited on pages 70, 117)
- Sugimoto, T., Kawanishi, T., Kumamaru, H., & Tohbe, Y. (2014). Performance Investigation Into Supersonic Diffuser for a High Pressure Centrifugal Compressor. *ASME Turbo Expo: Power for Land, Sea, and Air, Volume 2D: Turbomachinery*, V02DT42A004. <https://doi.org/10.1115/GT2014-25104> (Cited on page 7)
- Tartinville, B., & Hirsch, C. (2015). Investigation of Stator Induced Unsteadiness on a Centrifugal Impeller Using a Mach-Independent Non-Linear Harmonic Method. *ASME Turbo Expo: Power for Land, Sea, and Air, Volume 2C: Turbomachinery*, V02CT44A001. <https://doi.org/10.1115/GT2015-42042> (Cited on page 6)

- Tartinville, B., & Vilmin, S. (2023). Efficient Unsteady Simulations of Multistage Turbines Using a Flexible Frequency-Domain Approach. *ASME Turbo Expo: Power for Land, Sea, and Air, Volume 13C: Turbomachinery — Deposition, Erosion, Fouling, and Icing; Design Methods and CFD Modeling for Turbomachinery; Ducts, Noise, and Component Interactions*, V13CT32A007. <https://doi.org/10.1115/GT2023-101108> (Cited on page 7)
- Tonicello, N., Lodato, G., & Vervisch, L. (2020). Entropy preserving low dissipative shock capturing with wave-characteristic based sensor for high-order methods. *Computers & Fluids*, 197, 104357. <https://doi.org/10.1016/j.compfluid.2019.104357> (Cited on page 28)
- Touber, E. (2010). *Unsteadiness in Shock-Wave/Boundary Layer Interactions* (Doctoral dissertation). University of Southampton. (Cited on pages 32, 35, 38–40, 42, 45–47, 49, 56–58).
- Tucker, P. (2013). Trends in turbomachinery turbulence treatments. *Progress in Aerospace Sciences*, 63, 1–32. <https://doi.org/10.1016/j.paerosci.2013.06.001> (Cited on pages 4, 64–65)
- Tyacke, J., Vadlamani, N., Trojak, W., Watson, R., Ma, Y., & Tucker, P. (2019). Turbomachinery simulation challenges and the future. *Progress in Aerospace Sciences*, 110, 100554. <https://doi.org/10.1016/j.paerosci.2019.100554> (Cited on pages 4, 10)
- Van Oudheusden, B., Jöbbsis, A., Scarano, F., & Souverein, L. (2011). Investigation of the unsteadiness of a shock-reflection interaction with time-resolved particle image velocimetry. *Shock Waves*, 21, 397–409. <https://doi.org/10.1007/s00193-011-0304-4> (Cited on page 58)
- Vasanthakumar, P. (2003). *Three dimensional frequency-domain solution method for unsteady turbomachinery flows* (Doctoral dissertation). Durham University. Retrieved October 20, 2023, from http://etheses.dur.ac.uk/3089/1/3089_1114.pdf?UkUDh:CyT. (Cited on page 115)
- Vermeire, B. C., Nadarajah, S., & Tucker, P. G. (2016). Implicit large eddy simulation using the high-order correction procedure via reconstruction scheme. *International Journal for Numerical Methods in Fluids*, 82(5), 231–260. <https://doi.org/10.1002/flid.4214> (Cited on pages 10, 25)
- Vermeire, B. C., Witherden, F. D., & Vincent, P. E. (2017). On the utility of GPU accelerated high-order methods for unsteady flow simulations: A comparison with industry-standard tools. *Journal of Computational Physics*, 334, 497–521. <https://doi.org/10.1016/j.jcp.2016.12.049> (Cited on page 10)
- Vilmin, S., Lorrain, E., & Hirsch, C. (2009). Application of a Nonlinear Harmonic Method to the Simulation of Clocking Effects. *ASME Turbo Expo: Power for Land, Sea, and Air*, 48883, 1601–1609. <https://doi.org/10.1115/GT2009-59475> (Cited on page 6)
- Vilmin, S., Lorrain, E., Hirsch, C., & Swoboda, M. (2006). Unsteady Flow Modeling Across the Rotor/Stator Interface Using the Nonlinear Harmonic Method. *ASME Turbo Expo: Power for Land, Sea, and Air, Volume 6: Turbomachinery, Parts A and B*, 1227–1237. <https://doi.org/10.1115/GT2006-90210> (Cited on pages 6, 113, 116)
- Vilmin, S., Lorrain, E., & Hirsch, C. (2007). The Nonlinear Harmonic Method for Rotor-Stator Interactions Applied to Thermally Perfect Gas. *8th Interna-*

- tional Symposium on Experimental and Computational Aerothermodynamics of Internal Flows*, (ISAI8-0066) (Cited on page 6).
- Vilmin, S., Lorrain, É., Tartinville, B., Capron, A., & Hirsch, C. (2013). The nonlinear harmonic method: from single stage to multi-row effects. *International Journal of Computational Fluid Dynamics*, 27(2), 88–99. <https://doi.org/10.1080/10618562.2012.752074> (Cited on page 6)
- Vincent, P. E., Castonguay, P., & Jameson, A. (2011a). A New Class of High-Order Energy Stable Flux Reconstruction Schemes. *Journal of Scientific Computing*, 47, 50–72. <https://doi.org/10.1007/s10915-010-9420-z> (Cited on page 9)
- Vincent, P. E., Castonguay, P., & Jameson, A. (2011b). Insights from von Neumann analysis of high-order flux reconstruction schemes. *Journal of Computational Physics*, 230(22), 8134–8154. <https://doi.org/10.1016/j.jcp.2011.07.013> (Cited on page 25)
- VonNeumann, J., & Richtmyer, R. D. (1950). A Method for the Numerical Calculation of Hydrodynamic Shocks. *Journal of Applied Physics*, 21(3), 232–237. <https://doi.org/10.1063/1.1699639> (Cited on page 26)
- Vyas, M. A., Yoder, D. A., & Gaitonde, D. V. (2019a). Reynolds-Stress Budgets in an Impinging Shock-Wave/Boundary-Layer Interaction. *AIAA Journal*, 57(11), 4698–4714. <https://doi.org/10.2514/1.J058487> (Cited on pages 25, 32, 39–41, 49, 103)
- Vyas, M. A., Yoder, D. A., & Gaitonde, D. V. (2019b). Sidewall Effects on Exact Reynolds-Stress Budgets in an Impinging Shock Wave/Boundary Layer Interaction. *AIAA Scitech 2019 Forum*, 1890. <https://doi.org/10.2514/6.2019-1890> (Cited on pages 39–41, 49)
- Wang, C., Zhang, X., Shu, C. W., & Ning, J. (2012). Robust high order discontinuous Galerkin schemes for two-dimensional gaseous detonations. *Journal of Computational Physics*, 231(2), 653–665. <https://doi.org/10.1016/j.jcp.2011.10.002> (Cited on page 31)
- Wang, Z. J., & Gao, H. (2009). A unifying lifting collocation penalty formulation including the discontinuous Galerkin, spectral volume/difference methods for conservation laws on mixed grids. *Journal of Computational Physics*, 228(21), 8161–8186. <https://doi.org/10.1016/j.jcp.2009.07.036> (Cited on page 9)
- Wang, Z. J., & Rahmani, S. (2021). Implicit large eddy simulation of the NASA CRM high-lift configuration near stall. *Computers & Fluids*, 220, 104887. <https://doi.org/10.1016/j.compfluid.2021.104887> (Cited on page 10)
- Wang, Z. (2014). High-order computational fluid dynamics tools for aircraft design. *Philosophical Transactions of the Royal Society A: Mathematical, Physical and Engineering Sciences*, 372(2022), 20130318. <https://doi.org/10.1098/rsta.2013.0318> (Cited on page 10)
- Weatheritt, J., & Sandberg, R. (2016). A novel evolutionary algorithm applied to algebraic modifications of the RANS stress-strain relationship. *Journal of Computational Physics*, 325, 22–37. <https://doi.org/10.1016/j.jcp.2016.08.015> (Cited on page 128)
- Welch, P. (1967). The Use of Fast Fourier Transform for the Estimation of Power Spectra: a Method Based on Time Averaging Over Short, Modified Peri-

- odograms. *IEEE Transactions on Audio and Electroacoustics*, 15(2), 70–73. <https://doi.org/10.1109/TAU.1967.1161901> (Cited on pages 49, 81)
- Wenzel, C., Selent, B., Kloker, M., & Rist, U. (2017). DNS of Compressible Turbulent Boundary Layers at Varying Subsonic Mach Numbers. *47th AIAA Fluid Dynamics Conference*, 3116. <https://doi.org/10.2514/6.2017-3116> (Cited on page 73)
- Wilcox, D. (2006). *Turbulence Modeling for CFD*. DCW Industries. (Cited on pages 69–70, 119).
- Williams, D., Castonguay, P., Vincent, P., & Jameson, A. (2011). An Extension of Energy Stable Flux Reconstruction to Unsteady, Non-Linear, Viscous Problems on Mixed Grids. *20th AIAA Computational Fluid Dynamics Conference*, 3405. <https://doi.org/10.2514/6.2011-3405> (Cited on page 9)
- Williams, D., Castonguay, P., Vincent, P., & Jameson, A. (2013). Energy stable flux reconstruction schemes for advection-diffusion problems on triangles. *Journal of Computational Physics*, 250, 53–76. <https://doi.org/10.1016/j.jcp.2013.05.007> (Cited on page 9)
- Williams, D., & Jameson, A. (2014). Energy Stable Flux Reconstruction Schemes for Advection-Diffusion Problems on Tetrahedra. *Journal of Scientific Computing*, 59, 721–759. <https://doi.org/10.1007/s10915-013-9780-2> (Cited on page 9)
- Witherden, F. D., Farrington, A. M., & Vincent, P. E. (2014). PyFR: An open source framework for solving advection-diffusion type problems on streaming architectures using the flux reconstruction approach. *Computer Physics Communications*, 185(11), 3028–3040. <https://doi.org/10.1016/j.cpc.2014.07.011> (Cited on page 10)
- Witherden, F. D., Vermeire, B. C., & Vincent, P. E. (2015). Heterogeneous computing on mixed unstructured grids with PyFR. *Computers & Fluids*, 120, 173–186. <https://doi.org/10.1016/j.compfluid.2015.07.016> (Cited on page 10)
- Wollblad, C., Davidson, L., & Eriksson, L.-E. (2006). Large Eddy Simulation of Transonic Flow with Shock Wave/Turbulent Boundary Layer Interaction. *AIAA Journal*, 44(10), 2340–2353. <https://doi.org/10.2514/1.20358> (Cited on pages xviii, 63, 65–67, 76, 78–79)
- Wollblad, C., Davidson, L., & Eriksson, L.-E. (2010). Investigation of Large Scale Shock Movement in Transonic Flow. *International Journal of Heat and Fluid Flow*, 31(4), 528–535. <https://doi.org/10.1016/j.ijheatfluidflow.2010.02.009> (Cited on page 63)
- Wu, X. (2017). Inflow Turbulence Generation Methods. *Annual Review of Fluid Mechanics*, 49, 23–49. <https://doi.org/10.1146/annurev-fluid-010816-060322> (Cited on page 31)
- Xie, Z. T., & Castro, I. P. (2008). Efficient Generation of Inflow Conditions for Large Eddy Simulation of Street-Scale Flows. *Flow, Turbulence and Combustion*, 81(3), 449–470. <https://doi.org/10.1007/s10494-008-9151-5> (Cited on pages 33–35)
- Yang, G., Yao, Y., Fang, J., Gan, T., Li, Q., & Lu, L. (2016). Large-eddy simulation of shock-wave/turbulent boundary layer interaction with and without SparkJet control. *Chinese Journal of Aeronautics*, 29(3), 617–629. <https://doi.org/10.1016/j.cja.2016.04.001> (Cited on pages 39–41)

- Zhang, X., & Shu, C.-W. (2010). On positivity-preserving high order discontinuous Galerkin schemes for compressible Euler equations on rectangular meshes. *Journal of Computational Physics*, 229(23), 8918–8934. <https://doi.org/10.1016/j.jcp.2010.08.016> (Cited on pages 30–31)